MANIPULATION OF HOST CELLULAR PROCESSES BY POSITIVE-STRANDED RNA VIRUSES



Sophie Wilhelmina van Leur
Somerville College
Sir William Dunn School of Pathology
University of Oxford

A thesis submitted for the degree of

Doctor of Philosophy

in Molecular Cell Biology in Health and Disease

August 26th, 2024

Supervisor: Prof. Sumana Sanyal
Second Supervisor: Dr. Ivan Ahel
College Advisor: Dr. Robin Klemm
Assessors: Prof. Benedikt Kessler, Prof. Mirko Cortese



Somerville College
University of Oxford



Statement of Authorship

I declare that this thesis is entirely my own work, unless otherwise stated. Experiments conducted by core facilities or collaborators have been clearly indicated.

Specifically, sections of **Chapter 5** have been adapted or reproduced from publications of which I am co-first author and have gotten permission from the co-authors to include this material in my thesis. Section 5.1 is adapted from a publication and review where I was co-first author: *Nature Communications* (van Leur et al., 2023) and *Virulence* (van Leur et al., 2021), as indicated by references 178 and 194. Particularly, the data presented in this chapter has been previously published under the title “Viral subversion of selective autophagy is critical for biogenesis of virus replication organelles.” in *Nature Communications* (reference 178). Section 1.3 has been adapted from a review of which I was co-first author, published in *The FEBS Journal* (reference 106). Moreover, data from Chapters 2, 3, and 4 are being prepared as manuscripts for publication.

I have included relevant data in this thesis that was produced by Prof Sumana Sanyal, Dr Yun Lan, Dr. Deeksha Munnur and Asmaa Hachim (all members of the Sanyal lab) to provide a fuller picture of these research projects. S.S. performed Figures 2.1B, 2.2B, 2.3, 5.10B-C, 5.12C; A.H. performed Figure 2.2B, D.M performed Figure 4.1B and Y.L. performed Figures 5.3D-F; 5.4E-G; 5.8G-H; 5.11; 5.12; 5.13D, -E; 5.14E and 5.15. Together with Tiaan Heunis Figure 2.4 was established.

Word count: 43 / 50k (excluding bibliography, appendices, acknowledgements)

Abstract

The rapid spread and immune pressure on SARS-CoV-2 have led to the emergence of variant strains that challenge global health. As SARS-CoV-2 becomes endemic, understanding its pathogenesis and adaptation mechanisms is crucial. This thesis investigates the multifaceted role of ORF8, a protein recognized for its immunodominance and hypervariability. ORF8 was indicated to modulate the immune response by downregulating MHC-I through autophagy and to act as a viral cytokine, contributing to the "cytokine storm" seen in COVID-19 patients.

A central focus of this thesis is exploring the role of ORF8 in autophagy modulation. Positive-sense RNA viruses, including SARS-CoV-2, exploit this process for their replication and survival. By exploring how ORF8 fine-tunes autophagy and supports replication organelle formation, this study provides insights into potential antiviral strategies. We investigate two natural ORF8 variants—the Alpha strain (Q27stop) and the Gamma strain (E92K)—to assess their functional implications, including the impact of ORF8's ER localization, oligomerization, and glycosylation on cellular reprogramming. The modulation of the autophagy pathway will not only be addressed in relation to SARS-CoV2 ORF8, but in general for its role in replication organelle formation in +RNA virus infection, utilizing SARS-CoV2 and Zika virus as model systems.

Our findings, derived from live virus infections and stable expression in lung epithelial cells, reveal distinct modes of cellular reprogramming and immune interference by ORF8 variants. Moreover, we demonstrate that ORF8 plays a key role in replication organelle formation by cellular reprogramming, a process that we show in Zika infection to rely on Ube2g2 hijacking.

This thesis highlights the complex interplay between +RNA viruses and host cellular processes, showing how these viruses can reshape the endoplasmic reticulum, alter lipid metabolism and autophagy, modify secretory pathways, and interfere in the immune response. It offers crucial insights into host dependency factors and their potential as

targets for antiviral development, while also elucidating the impact of natural selection on SARS-CoV-2 ORF8.

Keywords: SARS-CoV2, Zika virus, autophagy, ER-phagy, MHC-I, Immune evasion, Ube2g2, replication organelle, DMV

Contents

Statement of Authorship 3
Abstract 4
Contents 6
List of Figures 8
List of Tables 10
List of Abbreviations 11
Chapter 1 Introduction 12
1.1 SARS-CoV2 12
1.1.1. Infection and disease 12
1.1.2. Variants of Concern 14
1.1.3. SARS-CoV2 virus life cycle 18
1.2. SARS-CoV2 ORF8 22
1.3. Viral subversion of cellular processes 25
1.3.1. ER Stress 25
1.3.2. UPR 25
1.3.3. Autophagy 27
1.4. Aims of the work described in this thesis 31
Chapter 2 Functional characterization of natural variants of SARS-CoV2 ORF8 and their impact on MHC-I expression 32
2.1. Introduction 32
2.1.1. Structural organization of ORF8 32
2.1.2. Immune interference by ORF8 33
2.2. Methods 35
2.3. Results 48
2.3.1. Ectopic expression of natural ORF8 variants leads to cell surface MHC-I downregulation 48
2.3.2. Stable cell lines expressing naturally occurring variants of ORF8 reveal differential mechanisms of MHC-I downregulation. 52
2.3.3. MHC-I interactome altered by expression of naturally occurring variants of ORF8 56
2.3.4. ORF8 variants differentially regulate autophagosomal compartments. 58
2.3.5. Deletion of ORF8 does not restrict primary infection in bronchial epithelial cells. 64
2.4. Discussion 67
Chapter 3 How SARS-CoV2 ORF8 reprograms lung epithelial cells 70
3.1. Introduction 70
3.2. Methods 72

3.3. Results 75
3.3.1. ORF8 variants are rapidly secreted in vesicles as glycosylated oligomerized proteins 75
3.3.2. ORF8 variants rewire the cell 77
3.3.3. ORF8 displays complex relationship with the immune response 80
3.3.4. ORF8*gamma* undergoes defective maturation and unconventional secretion via lamellar bodies 83
3.4. Discussion 88
Chapter 4 The role of SARS-CoV2 ORF8 in DMV formation 92
4.1. Introduction 92
4.1.1. SARS-CoV2 DMV biogenesis 92
4.1.2. DMV formation and the ER stress response 93
4.1.3. ER-phagy & DMV formation: a complex relationship 94
4.2. Methods 96
4.3. Results 105
4.3.1. SARS-CoV2 ORF8 facilitates DMV formation 105
4.3.2. DMV growth is restricted in absence of ORF8 in *live virus* infection 113
4.3.3. DMV components share interactions with ORF8 117
4.4. Discussion 123
Chapter 5 +RNA virus replication organelle formation requires intricate balance in selective autophagy 127
5.1. Introduction 127
5.2. Methods 134
5.3. Results 143
5.3.1. Ube2g2-deficiency restricts viral production of +RNA viruses 143
5.3.2. Ube2g2 is required for efficient viral replication 147
5.3.3. Viral replication organelle formation impaired in absence of Ube2g2 150
5.3.4. Ube2g2-deficiency induces Sec62-dependent ER-phagy in ZIKV-infection 155
5.3.5. NS3-induced cleavage of ER-chaperones requires Ube2g2 to prevent ER-phagy 160
5.3.6. Ube2g2-deficiency restricts viral release 161
5.3.7. ZIKV-induced lipophagy depends on Ube2g2 and is required for efficient viral release 163
5.4. Discussion 167
Chapter 6 Discussion 172
References 182
Appendices 194
Acknowledgements 219

List of Figures

Figure 1.1 Sequence analysis of natural SARS-CoV2 variants included in this thesis

Figure 1.2 The life cycle of SARS-CoV2 virus

Figure 1.3 Structure of ORF8*ancestral* with indicated multimerization and natural mutation sites

Figure 2.1 A549 stable cell lines were established expressing natural and structural variants of SARS-CoV2 ORF8

Figure 2.2 Stable overexpression of ORF8 in A549 leads to cell surface MHC-I downregulation

Figure 2.3 ORF8 secretion indicated to rely on lysosomal pathway and secretory pathway, while MHC-I downregulation relies on lysosomal pathway for ORF8*ancestral* and -C20S, but no other variant

Figure 2.4 Differential interactor enrichment of MHC-I heavy chain during ORF8-transfections in A549 cells

Figure 2.5 ORF8variants interfere in autophagosomal compartment abundance

Figure 2.6 Natural variants of ORF8 increase the abundance of lysosomal vesicles in A549 cells in homeostasis

Figure 2.7 Structural variants of ORF8 suggest that unconventional lysosome-dependent secretion might be induced in glycosylation-dependent manner

Figure 2.8 ORF8 deletion does not significantly compromise virus production nor immune signalling in Calu-3-infection

Figure 3.1 ORF8 variants are predominantly secreted in vesicles

Figure 3.2 Protein hits identified as unique interactor for extracellular ORF8 matched to intracellular log2 intensity data

Figure 3.3 Unique or significantly enriched interactors of ORF8 involved in secretion

Figure 3.4 The intra- and extracellular interactome of SARS-CoV2-ORF8*gamma* shows increased association with markers of acetylation, oxidoreductases and lamellar body markers

Figure 4.1 SARS-CoV2 DMV formation is impacted by ORF8 variant expression

Figure 4.2 ORF8 variant expression impacts DMV component expression

Figure 4.3 DMV formation and LD metabolism affected by ORF8 variant expression

Figure 4.4 DMV formation in overdrive in absence of SARS-CoV2 ORF8

Figure 4.5 SARS-CoV2 DMVs are significantly reduced in size in absence of ORF8

Figure 4.6 ORF8 shares interactors with DMV components allowing for secretion of DMV components in complex with ORF8*ancestral*

Figure 4.7 Model of SARS-CoV-2 DMV Formation and the role of ORF8

Figure 5.1 The life cycle of Zika virus adapted from Van Leur et al, 2021

Figure 5.2 Roles of E2 conjugating enzyme Ube2g2

Figure 5.3 Virus production restricted upon Ube2g2 knock-out

Figure 5.4 Catalytic activity of Ube2g2 is required for viral production

Figure 5.5 Zika viral entry unaffected by Ube2g2-deficiency

Figure 5.6 Ube2g2-deficiency impairs viral replication

Figure 5.7 Replication complex formation impaired upon Ube2g2-deficiency

Figure 5.8 Ube2g2 deficiency affects membrane rearrangements required for replication and assembly site formation

Figure 5.9 Increased XBP1 levels upon Ube2g2-deficiency

Figure 5.10 Ube2g2-dependent selective ER stress protein turnover

Figure 5.11 Sec62-Chmp4-dependent ER-phagy induced upon Ube2g2-deficiency is responsible for viral restriction

Figure 5.12 NS2b-NS3 induces Ube2g2-dependent ER stress chaperone degradation

Figure 5.13 Ube2g2 is instrumental for viral assembly and release

Figure 5.14 ZIKV-induced lipophagy is dependent on Ube2g2

Figure 5.15 Ube2g2 relocalizes to lipid droplets upon ZIKV-infection to induce lipophagy

Figure 5.16 Working model for Ube2g2's dual activity in ZIKV-infection

Figure 6.1 Proposed model for the secretion pathways of SARS-CoV-2 ORF8

Supplementary Figure 2.1 IFNγ-stimulation restricts ORF8 secretion in 293T cells

Supplementary Figure 2.2 Characteristics of A549-ORF8variant single clones

Supplementary Figure 2.3 Organelle identification for TEM quantification

Supplementary Figure 2.4 Cell-cell communication during infection affects ORF8's role in immune-modulation

Supplementary Figure 2.5 Thapsigargin treatment leads to intracellular ORF8 accumulation across variants, except ΔSP-ORF8

Supplementary Figure 3.1 ORF8 is rapidly secreted as tetramer and detected by autoradiogram in [35S]-pulse-chase assay and mass spectrometry

Supplementary Figure 3.2 Visualization of PCA loadings and analysis

Supplementary Figure 3.3 Volcano plots of intracellular interactomes of ORF8 variants in comparison to Empty-Ctrl A549 cells

Supplementary Figure 3.4 Volcano plots of the intracellular interactome of ORF8*gamma* in comparison to Empty-Ctrl, ΔSP and ORF8*ancestral* A549 cells

Supplementary Figure 3.5 Volcano plots of extracellular interactomes of ORF8 variants in comparison to Empty-Ctrl A549 cells

Supplementary Figure 3.6 Volcano plots of extracellular interactomes of ORF8 variants in comparison to ΔSP-ORF8 A549 cells

Supplementary Figure 3.7 Extracellular interactomes of ORF8*ancestral* and ORF8*ancestral*-C20S show an enrichment for extracellular vesicle trafficking, mucus-secretion and immune response markers

Supplementary Figure 3.8 Extracellular interactomes of ORF8*ancestral*-C20S-N78D and ORF8*gamma* show an enrichment for extracellular vesicle trafficking, mucus-secretion and immune response markers

Supplementary Figure 3.9 Extracellular interactors of ORF8 involved in the immune response

Supplementary Figure 4.1 Inducibility optimization of stably transduced TetOne-constructs

Supplementary Figure 4.2 ORF8 interferes in lipid metabolism

Supplementary Figure 4.3 ORF8 deletion does not significantly interfere with SARS-CoV2 viral production

Supplementary Figure 4.4 SARS-CoV2 DMVs are increasingly engulfed and have less DMV-DMV contact in absence of ORF8

List of Tables

Table 2.1 Plasmids

Table 2.2 Oligonucleotides

Table 2.3 Cell lines used in this chapter

Table 2.4 Antibodies & Fluorescent Ligands

Table 3.1 Cell lines used in this chapter

Table 3.2 Antibodies & Dyes

Table 3.3 STRING-pathway enrichment of the ORF8*gamma* extra- and intracellular interactome

Table 4.1 Cell lines used in this chapter

Table 4.2 Plasmids

Table 4.3 Oligonucleotides

Table 4.4 Antibodies & Dyes

Table 4.5 Known interactors of viral DMV components, their function and ORF8 interaction

Table 5.1 Cell lines used in this chapter

Table 5.2 Oligonucleotides

Table 5.3 Antibodies & Dyes

Supplementary Table 3.1 Reported interactors of SARS-CoV2 ORF8

Supplementary Table 3.2 Reactome and KEGG pathway enrichment of consensus ORF8 interactome described in Supp.Table 3.1

List of Abbreviations

COVID-19: Coronavirus disease 2019
DENV: Dengue Virus
DMV: Double membrane vesicle
ER: Endoplasmic Reticulum
ERAD: Endoplasmic Reticulum–Associated protein Degradation
HCoV-229E: Human Coronavirus 229E
HCoV-OC43: Human Coronavirus OC-43
IF: Immunofluorescence
LD: Lipid Droplet
MS: Mass Spectrometry
Nsp: Non-structural protein
ORF8: Open Reading Frame 8
RO: Replication Organelle
RT-qPCR: Reverse transcription-quantitative polymerase chain reaction
SARS-CoV: Severe acute respiratory syndrome coronavirus
SARS-CoV2: Severe acute respiratory syndrome coronavirus 2
TEM: Transmission Electron Microscopy
UPR: Unfolded Protein Response
Ube2g2: Human Ubiquitin-conjugating Enzyme E2 G2
ZIKV: Zika Virus

Chapter 1 Introduction

1.1 SARS-CoV2

1.1.1. Infection and disease

Severe acute respiratory syndrome coronavirus 2 (SARS-CoV2) is a pathogenic virus that was first detected in early December 2019 and rapidly spread globally, with over 770 million confirmed cases of COVID-19 to date (1-3). This *Betacoronavirus*, belonging to the *Coronaviridae* family of positive-sense RNA viruses, primarily infects nasal and lung epithelial cells, leading to inflammation and alveolar injury. The mechanisms underlying alveolar damage remain poorly characterised, but it is known that the severity of disease in coronavirus infections is largely driven by altered immune responses triggered by specific viral factors. These immune modulations can be recapitulated in infected macrophages, highlighting the importance of understanding the function of viral proteins that interact with the host immune system (4, 5).

The SARS-CoV2 genome encodes 4 structural proteins: Spike (S), Nucleocapsid (Np), Membrane (M) and Envelope (E), 16 non-structural proteins on ORF1ab and 11 accessory proteins (ORF3a, -3c, -3b, 3d/d2, ORF6, ORF7a, -7b, ORF8, ORF9b, -c and ORF10) (**Figure 1.1A**). Several of these proteins have been identified as immune modulators (6-9). While many are evolutionarily conserved, ORF3d and ORF8 are of particular interest, as they show low sequence identity with their SARS-CoV counterparts (32% and 38.9% respectively) and have been implicated as recombination hubs (1, 10). These two accessory proteins were identified as principal serological markers of SARS-CoV-2 infection, with only Np producing a greater antibody response, highlighting their involvement in the immune response (11). Dissecting the involvement of either protein in modulating the immune response and their overall contribution to pathogenesis is therefore an active field of research.

SARS-CoV2 is primarily transmitted through respiratory droplets and aerosols, with an incubation period of 4-5 days before symptom onset (12, 13). While most patients experience mild to moderate respiratory disease characterized by cough, fever, myalgia and headache, a small proportion develop severe illness. Severe disease often results from hypoxaemia due progressive respiratory failure, otherwise referred to as Acute Respiratory Distress Syndrome (ARDS). COVID-19 ARDS is characterized by inflammation, pulmonary vascular leakage and respiration failure, with an estimated 40% mortality rate. These patients present with systemic hyperinflammation marked by elevated serum levels of interleukin-1β (IL-1β), IL-6, IL-8, interferon gamma (IFNγ) and tumor necrosis factor alpha (TNFα), alongside other inflammatory markers, including secreted phospholipase A2 (sPLA2), matrix metalloproteinase-9 (MMP-9), lactate dehydrogenase (LDH) and C-reactive protein (CRP) (14-17).

Severe COVID-19 can also cause extrapulmonary issues, including gastrointestinal symptoms, as well as acute injury to the heart, kidneys, and liver. Additionally, patients may experience cardiac arrhythmias, rhabdomyolysis, coagulopathy, and shock. Although SARS-CoV-2 RNA has been detected at low levels in various organs, the extent to which these symptoms are directly caused by the virus remains largely unclear (18). In the intestine, SARS-CoV-2 has been shown to infect gut epithelial cells. Gastrointestinal symptoms are relatively common, and the presence of infectious viral shedding in faeces suggests that the virus can cause productive infections in the gut (19).

While severe COVID-19 can cause extrapulmonary complications affecting various organs, pulmonary viral replication remains the primary driver of illness. Therefore, this thesis focuses on examining the role of ORF8 specifically in lung and bronchial epithelial cells, as well as in co-cultures with macrophages.

1.1.2. Variants of Concern

Selection pressure on SARS-CoV2 has shaped the circulating SARS-CoV2 population since its emergence in humans. Multiple variants of concern (VOCs) have emerged as a result, such as the Alpha and Omicron variants, which demonstrated increased transmissibility and immune escape, contributing to their enhanced viral fitness (20, 21). Although adaptations are generally attributable to Spike mutations increasing the transmissibility and tropism, several ORFs have also been linked to increased viral fitness, with ORF8 being of particular interest. The strains that have dominated the SARS-CoV2 population with notable ORF8 mutations are described in detail below (**Figure 1.1B**). These include the Alpha strain which quickly dominated in early 2020, the Gamma strain which dominated in South America in 2020 and the XBB1.5 strain, which was one of the main sublineages of Omicron circulating in 2023. Only one naturally occurring ORF8-deletion variant has been reported; Δ382-Singapore, which lacks a proportion of ORF7b and the entire ORF8. The significance of SARS-CoV-2 ORF8 is underscored by the fact that patients infected with this strain experienced milder COVID-19. In a cohort study, patients infected with this variant had a lower incidence of hypoxia and more effective T-cell response (22). Additionally, the variant rapidly disappeared in Singapore, likely due to its reduced viral fitness (23). This highlights an intriguing selective pressure on ORF8, where truncation of ORF8 may be advantageous, but complete deletion hinders viral success. The notable mutations in ORF8 of the VOCs discussed are illustrated in **Figure 1.1C-D**.

1.1.2.1. Ancestral (A)

The ancestral lineage (lineage A) is closely related to the first sequenced strain, Wuhan-Hu-1 (GenBank accession MN908947.3), sampled on December 26th 2019 (24). This strain provides the baseline genome for understanding early virus characteristics and is widely used as the reference genome in SARS-CoV2 research (25). This lineage is considered to reflect the genetic makeup of early SARS-CoV-2 strains. For this thesis, SARS-CoV2

ORF8, S, Np, M and E were generated from cDNA of this first available Wuhan-Hu-1 strain (MN908947.3).

1.1.2.2. Alpha (B.1.1.7)

The Alpha variant (B1.1.7 lineage) emerged in late 2020 as the first VOC, rapidly out-competing the ancestral lineage (26). It was estimated to be 40%-80% more infectious than the ancestral lineage, resulting in high nasopharyngeal viral loads (27). The Alpha variant is typically associated with increased IFN antagonism, showing up to 312-fold greater inhibition of IFN-I compared to the ancestral strain (28).

A defining mutation of the B.1.1.7 lineage is Q27STOP in the ORF8 protein, which introduces an early stop codon in ORF8, resulting in a truncated ORF8 protein (29). Although there have been suggestions that this mutation results in a nonsense protein, the presence of ORF8-specific antibodies in infected-patient serum indicate that the truncated form of ORF8 is indeed produced (30).

The B.1.1.7 variant was shown to produce higher levels of infectious virus in airway, intestinal, and alveolar organoids compared to lineage B (which had comparable IFN resistance as lineage A), with a particular fitness advantage in airway organoids. Although the variant can induce a differential cytokine profile, there is no conclusive evidence of increased hyperinflammation or greater pathogenicity, beyond the observation of prolonged viral shedding (31-33).

1.1.2.3. Gamma (P.1)

The Gamma (P.1) strain emerged in January 2021 in South America and was first described following a SARS-CoV-2 outbreak in Manaus, Brazil, in a population with a high prevalence of previous infections (34). The strain rapidly became responsible for 95% of cases in Brazil and is characterized by several mutations linked to increased viral fitness (35). Moreover, it had acquired a notable mutation in ORF8: E92K. The E92 residue is believed to be part of one of four key salt bridges in ORF8 (R115-E92) that stabilize the ORF8 dimer, which is

held together by a disulfide bond between the C20 residues of each monomer (36). The Gamma strain displayed increased IFN resistance compared to the B lineage exhibiting a 1.9-fold and 4.4-fold increased resistance to IFNβ and IFNλ1 respectively (28).

The Gamma variant was associated with a more severe clinical course compared to the B lineage, with increased mortality and fewer co-morbidities among patients. In Brazil, those hospitalized during the Gamma wave had a higher risk of requiring ICU care and invasive ventilation compared to those hospitalized during the B lineage wave. Notably, the Gamma variant was also more lethal to younger individuals. During this wave, the average age of COVID-19 fatal cases in São Paulo decreased from 69 years before its emergence to 59 years. The average age returned to 71-72 years as the Gamma variant got displaced by the Delta variant (35, 37-40).

1.1.2.4. Omicron (XBB1.5)

The Omicron lineage emerged in late 2021 and is known for its increased transmissibility and potentially reduced disease severity (41, 42). Several sublineages from Omicron BA.2, such as XBB.1.5 which appeared in August 2023, feature an early stop codon in the N-terminal signal peptide of ORF8. The G8 nonsense mutation in ORF8 results in an inability to synthesize full-length ORF8 protein (43). Contrary to the Δ382-Singapore strain, the BA.2-derived strains circulated effectively. However, the prevalence of the G8* mutation has substantially diminished since the rise of other Omicron sublineages derived from BA2.86, specifically JN.1 which arose in late 2023. As of 2024, the G8* mutation prevalence dropped and remains at <5% (44). This suggests that other factors, particularly Spike protein mutations associated with enhanced transmissibility, are currently bigger drivers of viral evolution than ORF8 mutations (45).



Figure 1.1 Sequence analysis of natural SARS-CoV2 variants included in this thesis. Sequences were obtained using the reported accession numbers in (A) of the viruses purchased from BEI resources. Clustal Omega analysis was performed on all five complete genomes using JalView2.11.3.3 A) Genome organization of SARS-CoV2, created using BioRender.com B) Neighbour-Joining (NJ) Phylogenetic tree construction of the complete SARS-CoV2 variant genomes; ORF8*ancestral* (Italy-INMR-NR52284; EPI_ISL_451300); ORF8*alpha* (NR-54000; EPI_ISL_683466); ORF8*gamma* (NR-54982; EPI_ISL_877769); ORF8*XBB1.5* (NR-59104; EPI_ISL_16026423) and Δ382-Singapore (NR-53885; EPI_ISL_414378). C) Alignment of the ORF8 natural variant protein sequences. Red arrows indicate for amino acid changes; G8stop (XBB1.5); Q27stop (Alpha) and E92K (Gamma). Zappo was utilized as colouring scheme. D) DNA sequence alignment of the ORF8 natural variants. Red arrows indicate for point-mutations. Colouring according to nucleotide.

1.1.3. SARS-CoV2 virus life cycle

1.1.3.1. Tropism and entry

At the point of entry SARS-CoV2 typically targets the sustentacular cells in the nasal olfactory mucosa or multiciliated cells in the nasopharynx or trachea (46, 47). The main determinants for this tropism are cell surface expression of transmembrane serine protease 2 (TMPRSS2) and angiotensin-converting enzyme 2 (ACE2+), both essential to allow entry of the virus by SARS-CoV2 Spike-mediated fusion (48). The spike protein consists of two subunits, S1, which binds the host entry receptor ACE2+ and S2 which mediates the membrane fusion (49). The subunits are separated by a furin cleavage site, S1-S2, which is primed in the virus-producing cell. After engaging ACE2+, this allows the S1 subunit to release, and the S2 subunit to be available for activation (50). Activation is mediated by cleavage of the S2' site by TMPRSS2, which allows the spike protein to transition into its post-fusion state, fusing the viral and host lipid bilayers and releasing the viral ribonucleoprotein complex into the cell (51). Entry of SARS-CoV2 is therefore predominantly thought to occur at the cell surface. Alternative entry is possible through the endocytic pathway, where cathepsins can perform the S2' cleavage instead of TMPRSS2. However, studies have shown that this route is not efficiently used for entry in lung epithelial cells (52, 53). Additional entry receptors have also been suggested such as Neuripillin1 (Nrp1) and tyrosine-protein kinase receptor UFO (AXL) (54, 55).

Infection can also occur in the lower respiratory tract, either through inhalation or gradual dissemination along the tracheobronchial tree (56). This can lead to infection of the alveoli, which cause inflammation and limit gas exchange, central features of ARDS and severe COVID-19 (57). In the alveoli, SARS-CoV2 is primarily shown to infect alveolar type 2 cells (AT2), which co-express TMPRSS2 and ACE2+ on their apical surface, whereas alveolar type 1 (AT1) largely lack this expression (48). AT2s are important for pulmonary surfactant secretion to reduce surface tension during respiration. Moreover, AT2 cells are

the progenitor cells of AT1 in the adult lung and thus essential for lung regeneration after damage (58, 59).

1.1.3.2. Translation and replication

After fusion and release of the positive-sense viral genome into the host cell cytoplasm, it can directly initiate translation of ORF1ab through the host translation machinery (**Figure 1.2)**. This produces two polyproteins, pp1a and pp1ab (encoding non-structural proteins 1-16), that encode the replicase and protease proteins required to initiate replication organelle formation at the ER. SARS-CoV2 generates replication organelles as double-membrane vesicles (DMV) from ER tubules, which are extensively described in **Chapter 4**. Within these DMVs, the replication/transcription complex (RTC) assembles to execute transcription and replication shielded from cytoplasmic pattern recognition receptors (PRRs) such as MDA-5 and RIG-I (60-63).

Replication is initiated by the transcription of full-length negative-sense genomic copies, which serve as templates for the generation of new positive-sense genomic RNA. These newly synthesized genomes are translocated to the cytosol through pore-complexes on the DMV. Here, they are either translated by the host translation machinery to produce more RTCs and non-structural proteins (Nsps) or the genomes are packaged into nascent virions (63). Due to transcription regulatory sequences (TRSs) in the viral genome, the RTC executes discontinuous transcription leading to synthesis of nested positive sense subgenomic RNAs (sgRNAs) during replication, which encode accessory and structural proteins (64). These sgRNAs are translated and predicted to produce the accessory proteins; ORF3a,-c,-d/d2, -b, ORF6, ORF7a, -7b, ORF8, ORF9b, -c, and ORF10; and to produce structural proteins, Spike (S), Matrix (M), Envelope (E) and Nucleocapsid (Np). The expression of several of these accessory protein open reading frames (ORFs), such as ORF10 and ORF3d, is however debated and requires further investigation (63, 65, 66).

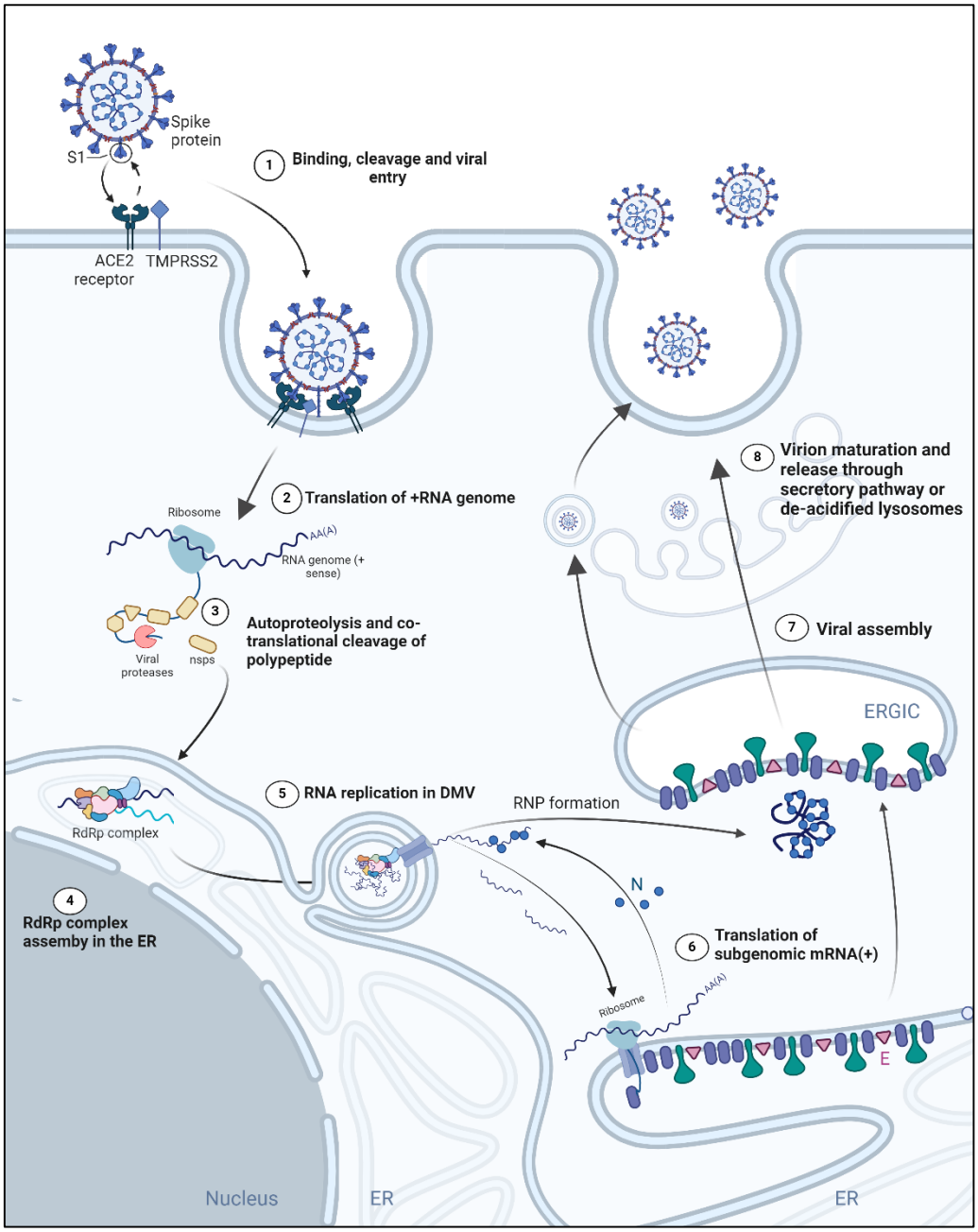


Figure 1.2 The life cycle of SARS-CoV2 virus. SARS-CoV2 infection begins with **1** the binding of the virus to ACE2+ receptors on the host cell, followed by cleavage of the spike protein by TMPRSS2 or, less commonly, cathepsins, facilitating viral entry. Once inside, **2** the positive-sense viral RNA genome is translated by the host machinery to produce polyproteins pp1a and pp1ab. These polypeptides undergo **3** autoproteolysis and co-translational cleavage to generate the replicase and protease proteins needed for replication. Next, **4** the replication/transcription complex (RTC) assembles within double-membrane vesicles (DMVs) derived from ER tubules. The RTC initiates **5** RNA replication to produce new genomic RNA and nested subgenomic RNA (sgRNA) within the DMVs. **6** The sgRNA is translated to produce viral accessory and structural proteins. The structural proteins, along with the viral genome, are then **7** assembled at the endoplasmic-reticulum–Golgi intermediate compartment (ERGIC), where they bud into the ERGIC lumen. Finally, **8** nascent virions mature and are released into the extracellular medium through the secretory pathway or potentially via exosomal pathways. Created using BioRender.com.

1.1.3.3. Viral assembly and release

After translation of the sgRNAs, the structural membrane proteins Spike (S), Matrix (M), Envelope (E) are trafficked to the endoplasmic-reticulum–Golgi intermediate compartment (ERGIC) for assembly. The viral genome complexes with cytosolic Nucleocapsid protein (Np) to form the ribonucleoprotein complex (RNP) and is also delivered to the ERGIC. This complex formation is thought to occur at the DMV pore exits, where Np recognizes an unidentified RNA packaging signal on the +RNA which is absent in sgRNAs (67). The RNP then localizes to the assembly site by Np-M interactions (68).

At the assembly site, M protein dimerization is believed to be crucial for curvature of the ERGIC membrane and its interaction with E protein to be essential for budding of nascent virions into the ERGIC. Expression of SARS-CoV2 M and E are considered the minimum constituents for virus-like particle formation and were found to be essential for localization of Spike and Np to the assembly site (69, 70). Once all four components are concentrated at the ERGIC, assembly occurs by budding into the ERGIC lumen. The nascent virions are primarily trafficked along the secretory pathway to be secreted into the extracellular medium. However, alternative secretion routes have been suggested, with evidence of egress of vesicles containing multiple viruses, indicating possible viral secretion through the exosomal pathway or secretory autophagy. The precise origin of these vesicles remains to be elucidated (67, 71-73).

1.2. SARS-CoV2 ORF8

As mentioned above, there is a particular interest in understanding the functionality of SARS-CoV2 ORF8. Amino acid sequence alignment has shown that ORF8 shares low homology with SARS-CoV (38.9%) and is part of a hypervariable genomic region recognized as a recombination hotspot (1, 74). SARS-CoV2 ORF8 encodes a 121-amino acid protein consisting of a N-terminal ER-signal sequence followed by a predicted Ig-like fold (**Figure 1.3A**) (6). While the Ig-like fold shares similarities with the core fold of ORF7a in both SARS-CoV and -CoV2, ORF8 in SARS-CoV2 possesses two unique dimerization interfaces: a YIDI-motif allowing oligomerization through non-covalent bonds and a Cys20 residue, enabling disulfide bridge formation (75, 76). The Cys20 domain can form mixed disulfide complexes, potentially coordinating ER remodelling (77). The non-covalent dimerization site (YIDI-motif), is located within the uniquely expanded Ig-like core of ORF8 (amino acids 46-83), which also includes a glycosylation site N78, enabling high-mannose N-linked glycosylation of the protein (78) (**Figure 1.3C)**. This unique Ig-like core is predicted to be stabilized by three intramolecular disulfide bonds (C25-C90, C37-C102, C61-C83), whereas four intermolecular salt bridges (D119-R115, R115-**E92**) are suggested to be important for stabilizing the C20-C20 ORF8 dimers (36, 75). The presence of these dimerization sites, glycosylation site, and Ig-like core likely contribute to the extensive interactome observed in proteomics screens. These screens have identified predominantly interactions with factors involved in TGF-β and integrin signalling, as well as glycosylation and ER quality control (79-81).

As mentioned previously, ORF8 antibodies are immunodominant together with ORF3d and nucleocapsid, suggesting that ORF8 is either secreted or presented at the cell membrane aside from ER expression (11). Indeed, ORF8 has been detected at high levels in patient serum, secreted in both glycosylated and non-glycosylated forms, as homodimers, tetramers or higher-order oligomers (78, 82) (**Figure 1.3B**). The unconventionally secreted non-glycosylated homodimeric ORF8 has been linked to

cytokine storm induction (83). However, another study has reported that ORF8 does not possess an unconventional protein secretion signal (UPS). This research demonstrated that it is the glycosylated form of ORF8, rather than the unglycosylated form, that induces the signature pro-inflammatory phenotype associated with severe COVID-19, with robust induction of IL1β, IL-6, and IL-8 in PBMCs (13, 82). These findings highlight significant discrepancies in the current literature regarding ORF8's secretion mechanisms and its role in disease pathology. The contradictory evidence surrounding ORF8 underscores the need for further investigation into its secretion pathways and functional forms. Understanding these aspects is crucial for elucidating ORF8's precise role in SARS-CoV-2 pathogenesis.

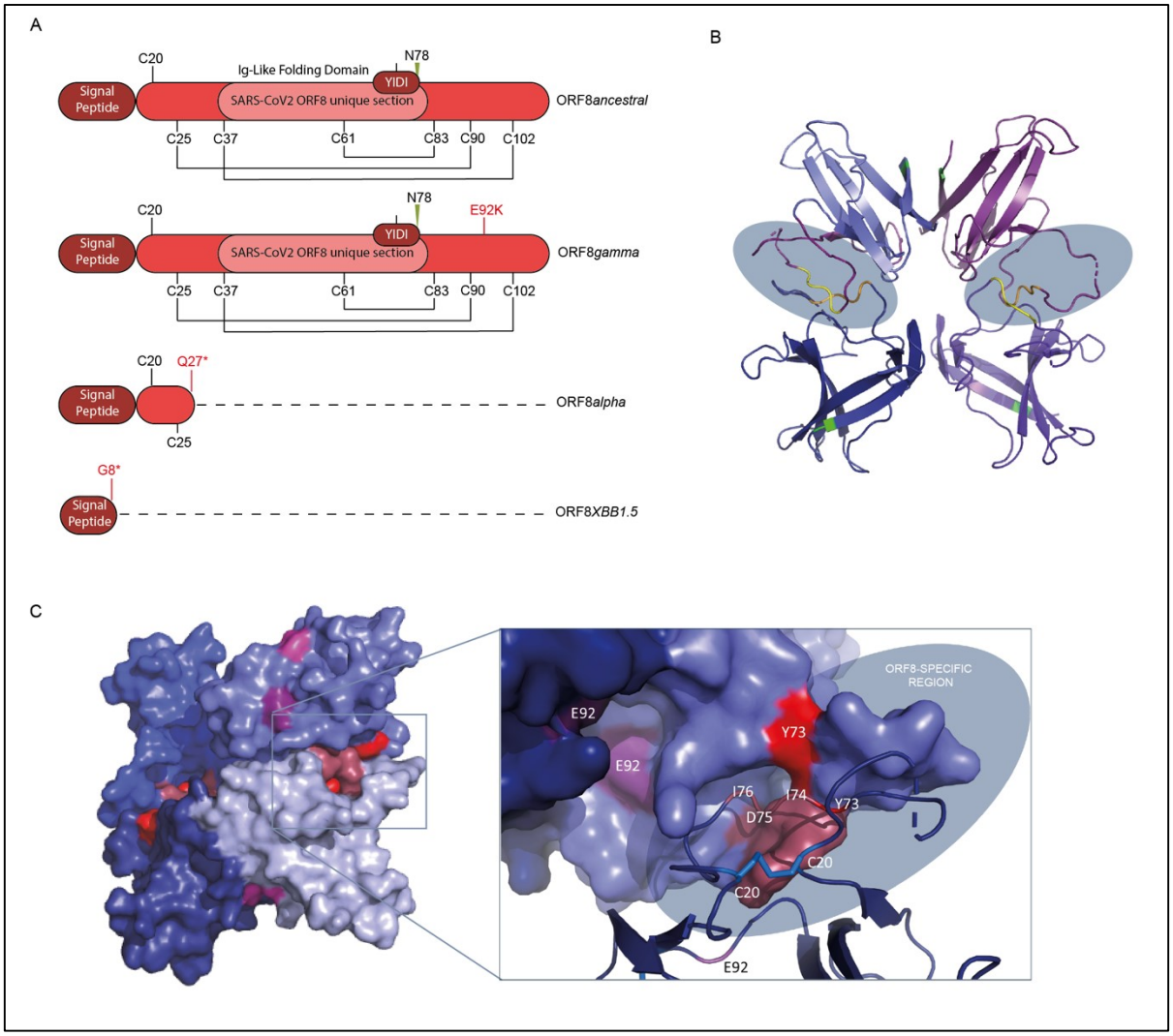


Figure 1.3 Structure of ORF8*ancestral* with indicated multimerization and natural mutation sites. A) Natural variants of ORF8 discussed in this thesis. B) The structure of ORF8 was visualized as a homo-tetramer, showing the Ig-like cores and highlighting the two dimerization interfaces; C20 (green) and the non-covalent YIDI interface (yellow). The

tetramer was generated in Pymol using the structure deposited under PDB ID 7JTL by Flower et al. (75). C) The SARS-CoV2 ORF8 unique section 46-83aa was highlighted; showcasing the natural mutation E92K (purple) of the Gamma strain and the non-covalent dimerization interface; ^{73}YIDI^{76} (Y in Red, IDI in pink).

ORF8 has been implicated in several immune modulatory functions. Firstly, two key components of the innate antiviral response, IFN-I and NFκB signalling, were shown to be inhibited upon ORF8-overexpression in 293T cells (6). Herein, ORF8 was suggested to interfere in IFN-γ signalling by aggregation in lung epithelial cells (76). Impaired IFN-I signalling is one of the key features of early stage severe COVID-19 (84). Moreover, ORF8 was found to interact with the TGFβ receptor (TGFB1 and -2) and suggested to disrupt the TGFβ signalling pathway (79). Interference in this pathway is associated with lung fibrosis and oedema, a common complication of COVID-19 disease (85, 86).

Besides the innate immune interference, ORF8 is thought to disrupt antigen presentation. Effective antigen presentation by HLA class I molecules to CD8+ T-cells is essential for viral elimination and long-term immunological memory. In 293T cells, ORF8-induced downregulation of Major Histocompatibility Complex (MHC) class I was shown to increase resistance to this cytotoxic T-cell killing. In this study, they suggested ORF8 could interfere in MHC-I presentation through autophagy, as a beclin1 knock-out rescued MHC-I expression (87). However, the exact mechanism by which ORF8 can induce autophagy and consequently a loss in the cell surface expression of MHC-I, remains elusive. Furthermore, the specific domains of ORF8 involved in this interaction with autophagy, remain to be determined. Similarly, although the previously discussed non-sense mutation in XBB1.5 ORF8 was shown to impair MHC-I downregulation, the implications of the truncated ORF8 in SARS-CoV2 Alpha or the E92K mutation in SARS-CoV2 Gamma have not been studied yet (43).

1.3. Viral subversion of cellular processes

1.3.1. ER Stress

During positive-sense RNA virus life cycles, ER stress is often induced due to disruptions in ER protein homeostasis. This stress can result from several factors: the exploitation of ER membranes for viral processes, the accumulation of misfolded proteins, disturbances in calcium balance due to viral pore complexes (viroporins), and the disruption or depletion of ER membranes during virion release (88). Such conditions lead to an overwhelmed ER, unable to meet the protein folding demands, resulting in the accumulation of misfolded proteins. This triggers the Unfolded Protein Response (UPR), mediated by three transmembrane proteins: inositol-requiring enzyme 1α (IRE1α), activating transcription factor 6 (ATF6), and PKR-like ER kinase (PERK). Positive-sense RNA viruses such as SARS-CoV-2 and Zika virus (ZIKV), heavily depend on the ER for robust viral RNA and protein synthesis, protein folding and viral assembly. The viruses induce ER remodelling to facilitate replication and assembly, while also shifting translation away from host mRNAs to viral mRNAs. This process floods the ER with viral glycoproteins and excess ER membranes for replication and assembly, collectively contributing to ER stress and UPR activation (89-92).

1.3.2. UPR

UPR is a complex network of intracellular signalling pathways that have evolved to respond to protein misfolding in the ER. As mentioned above, there are three sensors of UPR: ATF6, PERK and IRE1α, that are involved in restoring ER homeostasis by fulfilling three functions: adaptive response, feedback control and cell fate regulation, by inducing the production of oxidoreductases, folding chaperones, and ER-associated degradation (ERAD) components (93). During ER stress, the sensors are activated when their inhibitor, the ER chaperone immunoglobulin binding protein (BiP), encoded by HSPA5, dissociates from them (94). This protein has been detected as a direct interactor of SARS-CoV2 ORF8 and Nsp4, perhaps

further stimulating UPR responses (79, 95, 96). Similarly, ZIKV has been shown to actively suppress BiP transcription and translation in support of tripartite UPR induction (97), indicating the necessity of BiP hijacking to sustain UPR responses for virus production in both SARS-CoV2 and Zika infection.

Following BiP dissociation, IRE1α can dimerize and self-phosphorylate upon detection of misfolded proteins, inducing XBP1 splicing. Spliced XBP1 mRNA encodes the XBP transcription factor which activates UPR genes involved in ERAD, lipid metabolism, and protein folding, as well as induces the production of apoptosis regulator, apoptosis-signaling-kinase 1 (ASK1) (94, 98).

Similarly, PERK oligomerizes and self-phosphorylates in response to the accumulation of misfolded proteins. This results in phosphorylation of eukaryotic initiation factor 2 (eIF2α), which in turn attenuates the general host translation machinery, while stimulating the production of activating transcription factor 4 (ATF4). ATF4 regulates the production of ER-stress-associated pro-apoptotic protein C/EBP homologous protein (CHOP), induces an antioxidant response reducing reactive oxygen species (ROS) levels, and stimulates compensatory autophagy (99, 100).

ATF6, on the other hand, translocates to the Golgi upon ER stress, where it is cleaved. The processed ATF6 isoform then moves directly to the nucleus to activate a different subset of UPR genes. This transcriptional program increases ER capacity and protein folding, and facilitates the removal of misfolded proteins from the ER for degradation by ERAD.

Each pathway plays a distinct role in re-establishing ER homeostasis, but their interactions with viruses are expected to vary based on the virus and time in infection. Viruses, particularly positive-sense RNA viruses, have evolved sophisticated strategies to manipulate these pathways. They exploit the divergence among the UPR pathways to subvert host defenses, prevent apoptosis, and enhance viral replication. In SARS-CoV2 for

example, it was shown that although the IRE1α-pathway was triggered upon infection of induced pluripotent stem cell (iPSC)-derived type II alveolar (iAT2) cells, this did not result in downstream XBP splicing. This suggests that the virus interferes in the downstream signalling of the IRE1α/XBP1 arm of the UPR (90). In contrast, Zika virus appears to utilize XBP1 splicing to facilitate ER redistribution and the formation of replication organelles (101). This suggests that while SARS-CoV-2 and Zika virus both involve ER remodeling, they employ distinct mechanisms to achieve these outcomes (101).

For the PERK pathway, it has been suggested that it is utilized by coronaviruses to favour viral replication. A proteomic study has revealed that viral proteins Nsp4 and Nsp3 may modulate this pathway to reduce host protein synthesis early in infection. This adjustment benefits viral replication while avoiding it inducing apoptotic signalling in later stages of the infection (102).

These examples underscore the complexity of UPR interactions with viral infections. Each UPR arm regulates virus infections differently, with positive-sense RNA viruses developing intricate mechanisms to exploit UPR processes. Particularly noteworthy is the compensatory autophagy, particularly ER-phagy, induced by the PERK-eIF2α-ATF4-CHOP pathway. This process, which helps manage cellular stress, is also strategically hijacked by viruses to enhance their replication and survival and will be discussed in the next section (103, 104).

1.3.3. Autophagy

Building on the understanding of UPR, it is important to note that viruses also exploit autophagy to modulate the immune response. The role of ORF8 in disrupting antigen presentation exemplifies how viruses can manipulate autophagy to downregulate MHC-I expression, highlighting the broader significance of autophagy in viral pathogenesis (87). Autophagy is an evolutionarily conserved self-degradative process critical for maintaining

cellular homeostasis. It removes misfolded or aggregated proteins, eliminates damaged organelles, and degrades pathogens. This process involves the formation of a double membrane-bound vesicle called an autophagosome, which matures and fuses with a lysosome to become a degradative autolysosome. Autophagy plays a vital role in the immune response by capturing and degrading invading pathogens through the lysosomal pathway and by presenting antigens on MHC molecules (105). While autophagy serves as a cellular defense mechanism, growing evidence indicates that viruses have co-evolved with the autophagy machinery, repurposing it to enhance the production of viral progeny. Three major autophagy pathways have been described: chaperone-mediated autophagy, micro-autophagy, and macro-autophagy. Additionally, several specialized selective autophagy pathways exist targeting specific cellular components. These include ER-phagy, in which ER membranes are turned over through autophagy and lipophagy, where lipid droplets are consumed through autolysosomal degradation (105, 106). The following sections will discuss these pathways and their exploitation by viruses in more detail, drawing from a review published by our group on manipulation of selective autophagy by +RNA viruses (106).

1.3.3.1. ER-phagy

ER-phagy (or reticulophagy) refers to the degradation of ER portions within lysosomes or vacuoles. This selective clearance of ER subdomains helps regulate ER size and activity, to re-establish homeostasis after ER stress. ER-phagy relies on the activation of specific ER-phagy receptors, which contain LC3/Atg8-binding motifs in their cytosolic domains to engage with phagophores. Key receptors involved include FAM134B, RTN3, Sec62, p62 and ATL3 (107-110).

As previously discussed, SARS-CoV2 and ZIKV, like many +RNA viruses, induce ER stress. In response to ER-stress, ER-phagy is believed to assist in limiting infection by preventing access to resources from the ER and preventing viral amplification (107). For Zika and Dengue virus, evidence revealed that FAM134B-dependent ER-phagy indeed

serves this function, as siRNA treatment targeting FAM134B leads to increased viral production. However, these flaviviruses have evolved countermeasures: their NS3-encoded protease and NS3-cofactor NS2B can cleave FAM134B, largely circumventing this limitation (111). Similarly, evidence has suggested that SARS-CoV-2 specifically hijacks ER-phagy receptors away from the ER to prevent ER-phagy and thereby facilitating its replication (103). Understanding the precise mechanisms by which viruses subvert ER-phagy to support viral production, could aid in identifying targets for antiviral development.

1.3.3.2. Lipophagy

Lipophagy is the process in which lipid droplets (LDs) are turned-over through autophagy. LDs are endoplasmic reticulum (ER)-related dynamic organelles that store and regulate fatty acids and neutral lipids. The relationship between viruses and lipophagy is complex and suspected to vary depending on the stage of the viral infection. Positive-sense RNA viruses, which replicate at the ER, often induce lipophagy to support their replication. This process provides essential fatty acids for β-oxidation and phospholipids for constructing replication organelles (62, 112, 113). For instance, our lab has demonstrated that the Dengue virus (DENV) NS4A-NS4B complex can trigger lipophagy by hijacking the host protein Aup1 (114). In contrast, SARS-CoV2 ORF3a has been suggested to prevent lipophagy in order to promote viral replication (115).

Beyond their role in neutral lipid storage, lipid droplets are increasingly recognised as critical for innate immune signalling, particularly in the context of inflammation. These organelles contain precursors for various inflammatory lipid mediators, such as prostaglandins and leukotrienes (116). It is hypothesized that SARS-CoV-2 may interfere with LD degradation to modulate the host's inflammatory response. Currently, several aspects of the interaction between viruses and lipid droplets remain poorly understood. Key questions include whether viruses target specific subsets of lipid droplets in lipophagy and how their targeting strategies change throughout different stages of infection. Addressing

these unknowns could provide critical insights into viral manipulation of lipid metabolism and immune responses.

1.4. Aims of the work described in this thesis

As mentioned, SARS-CoV-2 continues to pose a significant threat to global health with already 770 million recorded cases and 7 million recorded deaths to date (3). As new variants continue to arise and cause outbreaks, it is critical to understand the mechanistic underpinnings of pathogenesis and investigate how evolutionary changes impact these mechanisms. Given that ORF8 has been identified as a key recombination hub, it is crucial to explore the functional implications of its mutations. Additionally, understanding the mechanisms by which the virus exploits autophagy pathways to assist in replication and evade immune responses is essential for developing effective therapeutic strategies. This thesis aims to investigate the manipulation of selective autophagy by both SARS-CoV-2 ORF8 and Zika virus, providing insights into broader mechanisms employed by positive-sense RNA viruses.

The aims of this thesis are therefore:

- To investigate how ORF8 modulates the immune response through autophagy and to test whether this modulation differs among natural ORF8 variants (Chapter 2)
- To characterise how ORF8 variants reprogram lung epithelial cells, a primary target of SARS-CoV-2, and identify the secretion routes utilized by ORF8 variants (Chapter 3)
- To investigate the role of ORF8 in the formation of replication organelles (Chapter 4)
- To examine how other positive-sense RNA viruses selectively regulate autophagy to support virus replication and production, using Zika virus as a model system. (Chapter 5)

Chapter 2 Functional characterization of natural variants of SARS-CoV2 ORF8 and their impact on MHC-I expression

2.1. Introduction

As outlined in **Chapter 1**, SARS-CoV-2 accessory protein open reading frame 8 (ORF8) has emerged as a potentially significant contributor to viral pathogenicity of SARS-CoV2 (36, 117). This small, immunoglobulin-like virulence factor plays important but incompletely understood roles during viral infection. Encoded within a genomic locus prone to mutation, ORF8 is known to be secreted, immunodominant, and proposed to interfere with host innate immune responses to enhance viral dissemination and replication (30, 36).

Within the *Coronaviridae* family, the ORF8 gene is unique to the *Sarbecovirus* genus, most of which retain a single continuous ORF8 protein. SARS-CoV2 ORF8 shares only 38.9% sequence homology with SARS-CoV, but 93% with its closest relative bat-CoV RaTG13 (118). This low homology underscores ORF8's rapid evolution and potential importance in viral adaptation.

2.1.1. Structural organization of ORF8

SARS-CoV2 ORF8 is a 121-amino acid protein (~13-14 kDa) that spans positions 27,894–28,259 of the viral genome, preceding the N gene (1, 74). It contains several key features: an N-terminal ER import signal sequence, a free cysteine for homo- and hetero-covalent dimerization (C20), and an Ig-like domain **(Figure 1.3A**). It shares similarities with ORF7a (~45% homology) from both SARS-CoV and SARS-CoV2, but is characterized by SARS-CoV2 ORF8' unique elongated stretch within the Ig-like fold (46-83aa), featuring a 3rd intramolecular disulfide bond resulting in a non-covalent dimerization interface at the YIDI motif (73-76aa) and a N-glycosylation site N78 (74, 119, 120). Through the YIDI-motif and C20 covalent dimerization site, ORF8 is suggested to be able to form functional multimeric assemblies, which were not reported in SARS-CoV. The oligomers are potentially stabilized by four intermolecular salt bridges (D119-R115, R115-**E92**). The protein's flexibility,

particularly in the β4-β5 loop region (46-83aa), is likely crucial for oligomer formation and stabilization of the tetrameric form of ORF8 through the YIDI motifs (78, 119). **Figure 1.3B** depicts a tetrameric model generated using the crystal structure reported by Flower et al. (119). Given that the glycosylation site is near the non-covalent dimerization site it could be affected by oligomerization. It is essential to determine whether higher-order oligomers can still undergo glycosylation and how this, along with oligomerization, impacts ORF8's functionality and role in pathogenesis. Moreover, understanding how natural mutations alter the forms of ORF8 that are expressed and secreted could provide insights into its contribution to pathogenesis of the associated SARS-CoV2 variants.

2.1.2. Immune interference by ORF8

ORF8 has been proposed to influence SARS-CoV-2 pathogenesis by modulating the host immune response through both secreted and intracellular mechanisms. One of the earliest studies on SARS-CoV-2 ORF8 demonstrated its ability to induce MHC-I downregulation via autophagy (87). In this study the authors show that not only Bafilomycin A1 treatment, but also Beclin1 knock-out, an essential protein for autophagy initiation, could rescue cell surface levels of MHC-I, suggesting a direct link between ORF8, autophagy, and MHC-I expression. Among the other immune modulatory functions reported, ORF8 has been shown to mimic Interleukin 17A (IL17A), allowing it to efficiently induce IL17A receptor A/C, to activate NF_KB- signalling and trigger a robust inflammatory response in blood monocytes (121-123). In contrast, intracellular ORF8 has been suggested to form aggregates that inhibit the Interferon (IFN) signalling pathway. This was observed in A549 cells transfected with ORF8-eGFP, where the formation of these aggregates appeared to enable evasion of host immunity, potentially enhancing viral fitness and virulence (124). ORF8 has also been implicated in facilitating viral mRNA transcription and propagation, although the exact mechanisms remain to be elucidated (125). It is important to note that many of these findings were initially obtained using transfection set-ups, which may not fully represent the protein's behaviour during live virus infection. To address this limitation, studies using live

recombinant SARS-CoV-2 viruses have been conducted. One such study comparing wildtype- and ΔORF8-recombinant SARS-CoV2 (Ancestral lineage) infection in lung organoids, revealed a dynamic immunomodulatory role for ORF8 during infection. The protein exhibited an immune antagonistic function early in infection, but supported pro-inflammatory cytokine production at later time-points (117). This suggests that ORF8 has an immunomodulatory role which is complex and time-dependent during the course of infection. However, the precise mechanisms underlying these effects, and how they might be influenced by natural mutations in ORF8, remain unclear and warrant further investigation.

This chapter therefore focuses on investigating the functional differences among natural variants of SARS-CoV-2 ORF8: the ancestral Wuhan-Hu-1, Alpha and Gamma variants. We hypothesize that ORF8*alpha* and -*gamma* exhibit altered functionality compared to the ancestral form: ORF8*alpha*, due to truncation which disrupts the Ig-like fold but retains the free cysteine for dimerization, and ORF8*gamma*, due to the E92K mutation that may destabilize dimeric/oligomeric forms by disrupting an intramolecular salt bridge. To further elucidate ORF8's structure-function relationship, we created additional structural variants to examine how glycosylation and oligomerization status may contribute to its activity. The chapter investigates ORF8's impact on three key cellular processes: MHC-I expression, autophagy, and intracellular membrane reorganization. To evaluate how these functions affect the virus life cycle in an ORF8-dependent manner, we employed Wuhan-Hu-1-based recombinant SARS-CoV2 viruses, including both the wildtype (rSARS-CoV2) and an ORF8-deleted variant (ΔORF8-rSARS-CoV2).

2.2. Methods

2.1.1. Plasmid construction

The codon-optimized pLVX-ORF8*ancestral*-strepII construct, kindly provided by the Krogan Lab (UCSF), was used as template to generate the ORF8 variants (126). The other SARS-CoV2 constructs (**Table 2.1**) were generated from codon-optimized Wuhan-Hu-1 cDNA (Based on GenBank accession MN908947.3), kindly provided by Chris Mok (Hong Kong University). The *alpha* (Q27*), *gamma* (E92K), C20S, C20S-N78D specific mutations were introduced using Q5® mutagenesis (New England Biolabs, MA, USA) using the primers mentioned in **Table 2.2**. The ΔSP variant was generated by standard directional cloning using BamHI and EcoRI, deleting aa0-18.

Table 2.1 Plasmids

Plasmid	Description
pLVX-ORF8*ancestral*-2xstrepII	pLVX-EF1alpha-SARS-CoV-2-orf8-2xStrep-IRES-Puro was a gift from Nevan Krogan (Addgene plasmid # 141390 ; http://n2t.net/addgene:141390 ; RRID:Addgene_141390)
pLVX-ORF8*ancestral*-C20S 2xstrepII	Lentiviral construct expressing ORF8*ancestral*; introduction of C20S mutation using Q5® mutagenesis
pLVX-ORF8*ancestral*-C20S-N78D 2xstrepII	Lentiviral construct expressing ORF8*ancestral*; introduction of C20S and N78D mutations using Q5® mutagenesis
pLVX-Emptry-Ctrl-2xstrepII	Lentiviral control plasmid; subcloned *in-house*
pLVX-ORF8*alpha*-2xstrepII	Lentiviral construct expressing ORF8*ancestral*; introduction of Q27STOP using Q5® mutagenesis
pLVX-ORF8*gamma*-2xstrepII	Lentiviral construct expressing ORF8*gamma*; introduction of E92K using Q5® mutagenesis
pLVX-eGFP	Control lentiviral construct to determine MOI
pcDNA3.1-SARS-CoV2-Spike-*ancestral*	Mammalian expression plasmid expressing SARS-CoV2 Spike, subcloned from Wuhan-Hu-1 cDNA (GenBank accession MN908947.3)
pcDNA3.1-SARS-CoV2-Nucleocapsid-*ancestral*	Mammalian expression plasmid expressing SARS-CoV2 Nucleocapsid, subcloned from Wuhan-Hu-1 cDNA (GenBank accession MN908947.3)
pIRES-SARS-CoV2-M-E-*ancestral*	Mammalian expression plasmid expressing SARS-CoV2 Matrix and Envelope protein, subcloned from Wuhan-Hu-1 cDNA (GenBank accession MN908947.3)
pCI-ORF8*ancestral*-6xHis	In-house generated mammalian expression plasmid expressing ORF8*ancestral* with a 'C-terminal 6xHis-tag for protein production
pCI-ORF8*gamma*-6xHis	In-house generated mammalian expression plasmid expressing ORF8*gamma* with a 'C-terminal 6xHis-tag for protein production
pTetOne-ORF8*ancestral*-HiBiT	In-house generated Doxycyline-inducible mammalian expression plasmid expressing ORF8*ancestral* with a 'C-terminal HiBiT epitope-tag.
pTetOne-HLA-A1-HiBiT	In-house generated Doxycyline-inducible mammalian expression plasmid expressing HLA-A1 with a 'C-terminal HiBiT epitope-tag.
pTetOne-HiBit-Halo-hLC3	Subcloned from Autophagy LC3 HiBiT Reporter Vector purchased from Promega, UK (GA255A)

psPAX2	psPAX2 was a gift from Didier Trono (Addgene plasmid # 12260 ; http://n2t.net/addgene:12260 ; RRID:Addgene_12260)
pMD2.G	pMD2.G was a gift from Didier Trono (Addgene plasmid # 12259 ; http://n2t.net/addgene:12259 ; RRID:Addgene_12259)

Table 2.2 Oligonucleotides

Purpose	Target	Sequence
RT-qPCR Primers	GAPDH	**FP**: 5'-GGAGCGAGATCCCTCCAAAAT-3' **RP**: 5'-GGCTGTTGTCATACTTCTCATGG-3'
	SARS-CoV2 ORF8*ancestral*	**FP**: 5'-TCTCGTGTTCTTGGGCATTATC-3' **RP**: 5'-GCAAGGATCATCGACGACATAA-3'
	SARS-CoV2 Nucleocapsid	**FP:** 5'-TTACAAACATTGGCCGCAAA-3' **RP** 5'-GCGCGACATTCCGAAGAA-3'
	Sarbecovirus E protein	**FP**: 5'-ATATTGCAGCAGTACGCACACA-3' **RP**: 5'-ACAGGTACGTTAATAGTTAATAGCGT-3'
	VACV C11	**FP**: 5'-AAACACACACTGAGAAACAGCATAAA-3' **RP**: 5'-ACTATCGGCGAATGATCTGATTA-3'
	WPRE	**FP**: 5'-CTTCTGCTACGTCCCTTCGG-3' **RP**: 5'-AAGGGAGATCCGACTCGTCT-3'
	HiBit-Halo-Tag	**FP:** 5'-GGCGGCTGTTCAAGAAGATTAG-3' **RP:** 5'-GGACCAACATCGACGTAGTGC-3'
	HSPA5	**FP**: 5'-TAGTCGGAGGGTGCAGGATA-3' **RP**: 5'-CGCTCTGATGCCGATTTTGG-3'
	Total XBP1	**FP**: 5'- TGAAAAACAGAGTAGCAGCTCAGA−3' **RP**: 5'-CTGGGTCCAAGTTGTCCAGAAT-3'
	Spliced XBP1	**FP**: 5'-TGCTGAGTCCGCAGCAGGTG-3' **RP**: 5'-GCTGGCAGGCTCTGGGGAAG-3'
	TNFalpha	**FP**: 5'-CCCCAGGGACCTCTCTCTAA-3' **RP**: 5'-GCTTGAGGGTTTGCTACAACA-3'
	IFNbeta	**FP**: 5'-TAGCACTGGCTGGAATGAG-3' **RP**: '5-GTTTCGGAGGTAACCTGTAAG-3'
	ISG56	**FP**: 5'-TACAGCAACCATGAGTACAA-3' **RP**: 5'-TCAGGTGTTTCACATAGGC-3'
	ISG54	**FP**: 5'-CTGCAACCATGAGTGAGAA-3' **RP**: 5'-CCTTTGAGGTGCTTTAGATAG-3'
	B2M	**FP**: 5'-GGTTTCATCCATCCGACATTGAAG-3' **RP**: 5'-TAGAAAGACCAGTCCTTGCTGAAG-3'
	HLA-B	**FP**: 5'-CTACCCTGCGGAGATCA-3' **RP**: 5'-ACAGCCAGGCCAGCAACA-3'
	Pan-HLA-I	**FP**: 5'-GCCTACGACGGCAAGGATTA-3' **RP**: 5'- TATCTGCGGAGCCACTCCA-3'
	TLR7	**FP**: 5'-TTGGCACCTCTCATGCTCTG-3' **RP**: 5'-GTGTCCACATTGGAAACACCATT-3'
	IRF7	**FP**: 5'-TGGTCCTGGTGAAGCTGGAA-3' **RP**: 5'-GATGTCGTCATAGAGGCTGTTGG-3'
	JUP	**FP**: 5'-CCCATACTCAGTAGCCACGAT-3' **RP**: 5'-GGTGTATGTCTGCTGCCACT-3'
	CD71/Transferrin Receptor	**FP**: 5'-GCGTCGGGATATCGGGTG-3' **RP**: 5'-GCAGGATGAAGGGAGGACAC-3'
Cloning primers	ORF8-6xHis	**FP**: 5'-TAGGGCTAGCATGAAGTTTCTCGTGTTCTT-3' **RP:** 5'-GGATGAATTCTTAGTGGTGATGGTGATGAT GGAGTATAAAGTCAAGGACCACCC-3'
	ORF8-C20S (Q5)	**FP**: 5'-CATCAAGAATCCTCTTTGCAGTCTTGTAC-3' **RP**: 5'-AAAAGCCGCGACTGTGGT-3'
	ORF8-N78D (Q5)	**FP**: 5'-TGACATCGGTGATTATACTGTC-3' **RP**: 5'-ATGTATTGAATCGGACTTTTG-3'
	ORF8-ΔSP	**FP**: 5'-GAATTCGCCGCCACCATG-3'

		RP: 5'-GGATGGATCCTTACTTTTCAAACTGCG-3'
	ORF8-E92K (Q5)	**FP**: 5'-CAACTGCCAAAAACCCAAACT-3' **RP**: 5'- ATCGTAAAGGGGGAACAAC-3'
	ORF8-Q27Stop (Q5)	**FP**: 5'-GTCTTGTACATAACATCAACCTTATG-3' **RP**: 5'-TGCAAAGAGCATTCTTGATG-3'
	HiBit-Halo-hLC3	**FP**: 5'- TAGGGAATTCCGCCATGGTGAGCGG-3' **RP**: 5'- TAGGGGATCCTCACACTGACAATTTCATCCCG-3'
	HiBiT-ORF8	**FP**: 5'- TAGGGAATTCGCCGCCACCATGAAG-3' **RP**: 5'- TAGGGGATCCTTAGCTAATCTTCTTGAACAGCC GCCAG-3'
	HiBiT-HLA-A-A1	**FP**: 5'- TAGGGAATTCGCCACCATGGCCGTC-3' **RP1**: 5'- TAGGCTGTTCAAGAAGATTAGCTAACAC TTTACAAGCTGTGAGAGAC-3' **RP2:** 5'- TAGGGGATCCGGAGGCTCGTGAGCGGCTGGCG GTAGGCTGTTCAAGAAGATTAGCTAAC-3'
	Spike	**FP**: 5'-GGATGCTAGCATGCAGTGCGTAAACCTTA-3' **RP**: 5'-TAGGGCGGCCGCTTATGTGTAATGTAATTTG-3'
	Nucleocapsid	**FP**: 5'-GGATGCTAGCATGTCTGATAATGGACCC-3' **RP**: 5'-TAGGGCGGCCGCTTAGGCCTGAGTTGAGTC-3'
	Matrix	**FP**: 5'-GGATGCTAGCATGGCAGATTCCAACG-3' **RP**: 5'-TAGGGAATTCTTACTGTACAAGCAAAGCAA-3'
	Envelope	**FP**: 5'-GATTGTCGACATGTACTCATTCGTTTCGGA-3' **RP**: 5'-TAGGGCGGCCGCTTAGACCAGAAG-3'

2.2.2. Cell culture

For this chapter, the adenocarcinomic human alveolar basal epithelial cell line A549 and human bronchial submucosal glandular cell line, Calu-3 were utilized as model systems. Lenti-X™ 293T cells were used to propagate lentiviruses for transduction into A549 cells. Calu-3 cells were utilized to propagate SARS-CoV2 viruses and the African green monkey epithelial cell line, Vero E6, was used to titrate the viruses. **Table 2.3** describes all the cell lines utilized and generated *in-house* through lentiviral transduction. A549 and Lenti-X™ 293T cells were maintained in cDMEM (10%FBS), and VeroE6 cells in 1%FBS-DMEM at 37 °C, 5% CO_2. Calu-3 cells were maintained in cEMEM (+ 10% FBS, 1% NEAA, 1% Sodium pyruvate, 1% L-Glutamine) at 37 °C, 5% CO_2. The human leukemic monocytic cell line, Thp1, was employed to explore the innate immune response to ORF8. These cells were maintained in cRPMI (10% FBS, 1% Sodium pyruvate (1mM), 1% HEPES (10mM)).

Stable cell line generation

To generate stable cell lines, LentiX (TakaraBio, Japan) cells were transfected using Lipofectamine3000 (Thermo Fisher, USA) with psPAX.2 and pMD2.G alongside the target protein in a pLVX-backbone (**Table 2.1**). 48-72 hours post transfection the virus was

harvested from the cells by spinning down at 400 g for 5 min to remove cellular debris and passing the virus through a low-protein binding 0.45µM-filter. The virus titre was quantified utilizing a pLVX-eGFP-control virus. Depending on the backbone used, selection was performed using Zeocin®, Blasticidin® and Puromycin for 3-4 consecutive passages and until a control cell line had been completely killed for at least 2 passages. Afterwards the cells were single cell sorted using FACS to obtain single clones. The single clones were selected based on relative expression as measured by western blot and by RT-qPCR (probes: WPRE or insert specific).

Table 2.3 Cell lines used in this chapter

Cell line	Description
Lenti-X™ 293T	Human embryonic kidney cells (TakaraBio) transformed with adenovirus type 5 DNA, that also expresses the SV40 large T antigen. Utilized for lentiviral production.
Calu-3	Human bronchial submucosal glandular cell line (ATCC)
Thp1	Human leukemic monocytic cell line
A549	Adenocarcinomic human alveolar basal epithelial cell line (ATCC)
A549 (high expression pool) • ORF8*ancestral*-strepII • ORF8*gamma*-strepII • ORF8*alpha*-strepII	A549 cells stable transduced at high MOI to express SARS-CoV2-ORF8variants. Selection using Puromycin.
A549 (single clone) • ORF8*ancestral*-strepII • ORF8*ancestral*-C20S-strepII • ORF8*ancestral*-C20S-N78D -strepII • ORF8*gamma*-strepII • ORF8*alpha*-strepII • ΔSP-ORF8*ancestral*-strepII • Empty-Ctrl	A549 cells stable transduced and single clone selected to express SARS-CoV2-ORF8variants at comparable levels. Selection using Puromycin.
A549 (pool) • ORF8*ancestral*-strepII-SC-HiBiT-HaloTag®-hLC3 • ORF8*ancestral*-C20S-strepII-SC- HiBiT-HaloTag®-hLC3 • ORF8*ancestral*-C20S-N78D –strepII-SC-HiBiT-HaloTag®-hLC3 • ORF8*gamma*-strepII-SC- HiBiT-HaloTag®-hLC3 • ORF8*alpha*-strepII-SC- HiBiT-HaloTag®-hLC3 • ΔSP-ORF8*ancestral*-strepII-SC- HiBiT-HaloTag®-hLC3 • Empty-ctrl - HiBiT-HaloTag®-hLC3	Single clone A549 cells (SC) stably expressing SARS-CoV2-ORF8variants, stably transduced with Doxycyline-inducible HiBit-HaloTag®-hLC3 to track autophagic flux. The pools were assessed for comparible expression levels prior to usage in assay. Selection using Puromycin (ORF8 construct) and Zeocin® (HiBit-HaloTag®-hLC3).

VeroE6	African Green Monkey kidney epithelial cell line, used for SARS-CoV2 viral production.
293T/A549-HiBit-ORF8*ancestral*	293T/A549 cells stably transduced with Doxycyline-inducible 'C-terminally HiBit-tagged ORF8*ancestral*. Selection using Zeocin®
Calu3/A549/Thp1-HiBit-HLA-A1-Zeocin	Calu-3/A549/Thp1 cells stably transduced with doxycyline-inducible 'C-terminally HiBit-tagged HLA-A1. Selection using Zeocin®.
Calu3- HiBit-HaloTag®-hLC3-Zeocin	Calu-3 cells stably transduced with Doxycyline-inducible HiBit-HaloTag®-hLC3 to track autophagic flux. Selection using Zeocin®.

2.2.3. Mass spectrometry

For the MHC-I interactome studies, duplicate T75 flasks were seeded at 1 million cells per flask. The cells were collected after 72 hours in RIPA-buffer (50mM Tris pH 7.5,150 mM NaCl, 0.1% Sodium dodecyl sulfate (SDS), 0.5% sodium deoxycholate,1% Triton X 100) supplemented with cOmplete™, Mini, EDTA-free Protease Inhibitor Cocktail (PI) (Roche, Switzerland) for co-immunoprecipitation. Pull-downs were performed using α-HC-10 (MUB2037P, NordicMUBio) and Dynabeads™ Protein-G beads according to manufacturer's protocol. Subsequent preparation for M/S was performed by Dr. Tiaan Heunis (Sanyal Lab) using S-trap™ digestion and analysed by Dr. Tiaan Heunis at the Mass Spectrometry facility at the Biochemistry department (University of Oxford). All IPs were scored against control samples using SAINT and outputs were filtered for proteins with a BH-corrected p-value < 0.05. Proteins were ranked based on fold change calculated in SAINT and variant specific presence. The SAINT fold change scores were log2-transformed and visualized using PRISM 9.0. Pathway enrichment was investigated using Cytoscape 3.8.2.

2.2.4. TEM

The A549 single clones expressing our ORF8 variants were collected from a confluent 10-cm dish using trypsinization. The cells were spun down in complete medium for 5 min at

400 x *g* to inactivate and remove trypsin. The pellets were re-suspended in pre-warmed fixative (4%PFA, 2.5%gluteraldehyde in 0.1M PIPES buffer), prior to standard processing at the Dunn School BioImaging facility (University of Oxford). Images were obtained on the JEOL 1400 TEM using the Gatan Rio CMOS detector and manually quantitated for amount of 'early degradative/recycling vesicles' and late degradative 'lysosomal vesicles' per cell.

2.2.5. Virus production

SARS-CoV2 recombinant viruses were kindly provided by Prof. Sola at the CNB-CSIC (Madrid, Spain) (117). Calu-3 cells were utilized to propagate the viruses.

For each virus, Calu-3 cells were grown to 70-80% confluence in a T175 flask prior to infection at multiplicity of infection (MOI): 0.01. Infection was conducted for 2 hours at 37 °C, 5% CO_2 in EMEM (no FBS). Afterwards the medium was exchanged for cEMEM and the cells were grown for another 72 hours. After 72 hours the supernatant was collected and spun down for 5 min at 400 x *g* to remove cellular debris. Afterwards the viruses were 0.45μM low protein binding syringe (Millipore)-filtered to remove mucus. The resulting medium was exchanged three times by 100-kDa Amicon Ultra-15 column (Millipore) filtration with 1xGlutamax(Gibco) OptiMEM. At the end of each centrifugation step, approximately 2 ml was left in the top compartment. After three exchanges, the purified virus was transferred to a new tube and the Amicon Ultra-15 column was washed three times by adding Opti-MEM I (1X) + GlutaMAX (Gibco) to the top compartment, pipetting up and down several times on the filter and adding each wash to the tube containing the purified virus preparation. This step was repeated until the volume in the purified virus stock was equal to the original volume of culture supernatant. Purified virus was stored at −80°C in aliquots.

Titres of the purified virus were determined by standard plaque assay. In brief, virus was 10-fold serially diluted in technical duplicate. To a 24-wells plate; 100 μL of each serial dilution was added per well. Vero E6 cells were collected in 5e5/mL in 1%FBS-DMEM of

which 500 µL was added per well. The virus-cell mixtures were incubated for 2.5 hrs, afterwhich 500 µL of 1.5%CMC overlay was added. After 48 hours, the overlays were removed and the cells were once washed with PBS. Afterwards the plaques were fixed and visualized using Amido Black Stain (2mM Amido Black powder, 0.1M Sodium acetate (trihydrate), 6% glacial acetic acid). The stain was incubated for at least 2 hours prior to washing the plates in MilliQ water and counting the plaque-forming units per dilution.

2.2.6. Virus kinetics

Virus kinetics were studied in a multicycle system using MOI 0.01 and collecting supernatant and cell lysates at the indicated timepoints. Supernatant was collected for assessment of viral production by standard plaque assay as described above and RT-qPCR; respectively giving the plaque forming units/mL (pfu/mL) and the genome copies/mL.

For RT-qPCR, total RNA was extracted from the supernatant using the Qiagen Viral RNA Mini kit (Qiagen, The Netherlands), in which the AVL buffer was supplemented with 1.3% Triton-X-100 to ensure viral inactivation. RT-qPCR was performed by using the Takara One-step SYBR green kit (Takara Bio Inc., Japan) by probing for SARS-CoV2 Nucleocapsid (**Table 2.2**). A standard curve was included to determine the genome copies/mL. The standard curve was generated using 5 dilutions of 10-fold serial diluted RNA from a virus stock with known titre. All samples were measured in technical triplicates. Plaque assay was performed in biological triplicate and technical duplicate. Results are presented as means ± standard deviation (SD), unless stated otherwise.

The cell lysate was collected for RNA extraction and Western Blotting, respectively in Qiagen RLT buffer (Qiagen, The Netherlands) and RIPA buffer (50mM Tris pH 7.5,150 mM NaCl, 0.1% Sodium dodecyl sulfate (SDS), 0.5% sodium deoxycholate,1% Triton X 100) supplemented with cOmplete™, Mini, EDTA-free Protease Inhibitor Cocktail (PI) (Roche, Switzerland). Total intracellular RNA was extracted using the Qiagen RNeasy Mini

Kit (Qiagen, The Netherlands). Three biological replicates were collected for both total intracellular RNA and for Western Blotting.

2.2.7. Western Blotting

Whole cell lysate (WCL) samples collected in RIPA+PI were freeze-thawed three times and spun down at 20.000 × g for 10 min at 4 °C to clear cellular debris. The lysates were measured for total protein concentrations and were prepared in non-reducing NuPAGE LDS or in reducing Laemmli SDS sample buffer (Thermo Fisher, USA), as described in the figure. Subsequently, the samples were heated to 70ºC for 10 min or 95º for 2 minutes respectively, unless otherwise stated. The samples were run on NuPAGE™ 4–12% Bis-Tris gels (Invitrogen, CA, USA) and immunoblotted using the indicated antibodies on 0.45 µm LF PVDF membranes (**Table 2.4**). Visualization was performed using Odyssey® Fluorescent Western Blotting unless otherwise stated.

Table 2.4 Antibodies & Fluorescent Ligands

Antibodies	Mouse α-Beta Actin	MAB8929 (Bio-Techne (R&D Systems), USA)
	Rabbit α-StrepII-tag	ab76949 (Abcam, UK)
	Mouse α-HC-10	MUB2037P (NordicMUbio, The Netherlands)
	Mouse α-MHC-I (W6/32)	311402 (BioLegend, USA) MA119027 (Life Technologies, USA)
	Mouse α-FLAG® (M2)	F3165 (Sigma-Aldrich, USA)
	Rabbit α-LC3b	2775 (Cell Signalling Technology, MA, USA)
	Rabbit α-Calnexin	2433 (Cell Signalling Technology, MA, USA)
	Rabbit α-SARS-CoV2 Spike	40150-R007 (SinoBiological, China) ab272504 (Abcam, UK)
	Brilliant Violet 510(TM) anti-human HLA-A,B,C	311435 (BioLegend, UK)
	Brilliant Violet 605(TM) anti-human HLA-A,B,C	311431 (BioLegend, UK)
	Alexa Fluor(R) 647 anti-human HLA-A,B,C	311416 (BioLegend, UK)
	IRDye® 800CW Donkey anti-Mouse IgG	926-32212 (LI-COR, UK)
	IRDye® 680RD Donkey anti-Mouse IgG	926-68072 (LI-COR, UK)
Ligands	HaloTag TMR Ligand	G8251 (Promega, UK)
	HaloTag Alexa Fluor 488 Ligand	G1001 (Promega, UK)

2.2.8. Flow cytometry

Flow cytometric analysis was performed on A549 cells. A549 cells were collected by subtle trypsinization, washing and EDTA supplementation to FACS-buffer to prevent clumping of cells. The cells were live-dead stained with Zombie-NIR or –B421 for 20 min at RT. Afterwards the cells were spun down for 6 min at 400 x g at 4ºC, supernatant removed and replaced with the indicated cell surface staining cocktail. Cell surface staining was performed for 30 min on ice. Afterwards the cells were washed in FACS buffer and fixed for 30 min with BD Cytofix/Cytoperm solution (4%PFA). The cells were washed with FACS buffer, prior to intracellular staining for 30 min on ice. Compensation was performed using OneComp eBeads Compensation Beads (Life Technologies, USA). Gating was performed by FFC/SSC, Live/dead staining, followed by the target staining e.g. Brilliant Violet 605(TM)$^{+}$ gating for BV605-anti-human HLA-A,B,C (W6/32). Experiments were performed in technical triplicates, unless otherwise stated, and measured on the BD LSRFortessa™ X-20 Cell Analyzer (BD Biosciences, UK). Analysis was performed using FlowJo (BD Biosciences, UK) and Graphpad Prism 9.

2.2.9. Immunofluorescence

Cells were seeded on 24-well glass coverslips. The cells were either transfected and induced as described previously, or infected with rORF8-SARS-CoV2 or ΔORF8-rSARS-CoV2 at MOI 0.5. At indicated time points the cells were fixed with 4% PFA for 15 min for the transfection set-up or 30 min at RT for the *live virus* set-up. The cells were permeabilized using 0.1% Triton X-100 for 10 min and blocked with 10% normal goat serum (NGS) in 0.1% Triton X-100 for 30 min at RT. Cells were then probed with indicated antibodies for 1 hr in 5% NGS in 0.1% Triton-X-100 at RT (**Table 2.4**). Afterwards, if indicated, Nile Red (Abcam) staining was performed according to manufacturer's protocol for 10 min at RT. The coverslips were mounted on glass slides using Fluoroshield DAPI-mounting medium

(Abcam, UK). Images were obtained on the ZEISS Airyscan 880 and analysed using ZEISS ZEN Microscope Software (ZEISS, Germany) and ImageJ (v1.54j) software.

MPL-MIL-Halo assay

Inducible TetOne-HiBiT-HaloTag®-hLC3 cells were live-stained to evaluate autophagic flux. The assay is performed using cells grown to 70-80%-confluency on coverslips and 48 hours' post Doxycyline-induction (250ng/mL). The cells were permeabilized using BD Perm/Wash™ buffer. To stain the autophagosomal and lysosomal compartments, manufacturer's protocol for rapid live cell labelling using HaloTag® Technology (Promega, UK) was followed. The HaloTag TMR Ligand, a membrane-permeable dye (MPL), and the HaloTag Alexa Fluor 488 Ligand (MIL), a membrane-impermeable dye, were used to label autophagophores (MIL^+), nascent autophagosomes (MIL^+MPL^+), and mature autophagosomes and -lysosomes (MIL^-MPL^+). Staining was performed by incubating cells with the ligands diluted at 1:1000 in culture medium for 15 minutes at 37°C with 5% CO2, in the dark. Following staining, cells were fixed with 4% paraformaldehyde (PFA). Afterwards the coverslips were mounted using Fluoroshield DAPI-mounting medium (Abcam, UK) and visualized on the Zeiss Airyscan 880.

2.2.10. Immunoprecipitation

Immunoprecipitation was performed using Dynabeads™ Protein G beads (ThermoFisher, USA) or MagStrep ""type3"" XT beads 5% suspension (IBA Lifesciences, Germany) according to manufacturer's protocol. Dynabeads™ were utilized to precipitate complete, mature MHC-I using α-MHC-I (W6/32) and all, including immature and non-classical, MHC-I using α-MHC-I Heavy Chain (HC-10). MagStrep ""type3"" XT beads were utilized to precipitate the 'C-terminally StrepII-tagged ORF8 variants. For pulse-chase experiments, the antibodies were first mixed with antigen overnight at 4°C, the complexes were then pulled down by the magnetic beads. The precipitates were eluted in Laemlli buffer by

incubating for 5 min at 95 degrees, prior to standard Western blotting and Coomassie Blue staining, unless otherwise stated.

2.2.11. Pulse-Chase Assay

Cells were collected by trypsinization and starved for 30 min in cysteine/methionine-free DMEM. Afterwards the cells were labelled for 10 min at 37ºC with 10 mCi/ml [35S]methionine/cysteine (EXPRE35S35S Protein Labeling Mix, [35S]-, 2mCi (74MBq), 50mM Tricine (pH 7.4), 10mM 2-mercaptoethanol, Revvity,UK) and chased for the indicated time points. At each time point, supernatant aliquots were taken and the reaction was stopped with cold PBS. Subsequently, the cells were lysed in Tris buffer containing TX-100 and pre-cleared agarose beads for 1 hour at 4ºC. Immunoprecipitations were performed with the indicated antibodies for 3 hours at 4ºC with gentle agitation. Sample elution was performed by heating in reducing (Laemlli) or non-reducing sample buffer (LDS) as indicated. The samples were subjected to SDS-PAGE and visualized by autoradiography.

2.2.12. Nano-Glo® HiBiT assay

HiBiT-hLC3 assay

For the HiBiT-HaloTag®-hLC3 autophagic flux assay, stable cell lines were created to express Doxycycline-inducible HiBiT-HaloTag®-hLC3. The TetOne-HiBiT-HaloTag®-hLC3 plasmid was subcloned from the Autophagy LC3 HiBiT Reporter vector of Promega (GA2550) and ligated into TetOne-Zeocin backbone. After Zeocin® selection, single clones were selected with similar relative expression of both the HiBit-Halo-hLC3 construct and ORF8 construct as measured by RT-qpCR probing for ORF8 and HiBit-Halo-hLC3 (**Table 2.2**). Afterwards the selected single clone cells were plated in at least technical quadruplicates on all-white 96-well plates and induced with 250ng/mL doxycycline for 48 hours prior to luciferase read-out. Luciferase activity was read-out utilizing the Nano-Glo®

HiBiT Lytic Detection System and a luminometer. Luciferase activity is a read-out for total abundance of autophagosomal compartments.

HiBiT-ORF8 assay

To assess the secretion dynamics of ORF8 a 'C-terminally HiBiT-tagged ORF8 was generated under a doxycycline-inducible promotor (pTetOne-ORF8-HiBiT-Zeo). Biological duplicate transductions were performed in 293T cells at MOI 1. The cells were selected using Zeocin® for 3 passages. Extracellular and intracellular levels of ORF8 were measured using the Nano-Glo® HiBiT Extracellular and Lytic Detection Systems (Promega, UK). Cells were seeded in three sets of technical quadruplicates. After 24 hours, the cells were stimulated with Doxycyline (250ng/mL). At 32 hours post induction, the cells were either mock or IFNγ-stimulated (100ng/mL). After a 16-hour IFNγ-treatment, one set of quadruplicate technical repeats was washed and used for assessing the intracellular MHC-I levels. For the other sets, the cells were either changed for fresh medium or directly assessed for extracellular detection of ORF8, providing the cell surface and total extracellular amounts of ORF8 respectively. Medium without cells was used as a control for extracellular detection and non-stimulated cells were used as a control for intracellular detection.

2.2.13. Metabolic Glo™ Assays

To assess metabolic changes in the single clone A549 stable cell lines, the bioluminescent Lactate-Glo™, Glutamine/Glutamate-Glo™ assays (Promega, UK) were employed to report on Glycolysis and Glutaminolysis. The preliminary assays were executed with cell culture medium to assess extracellular consumption/secretion of the three metabolites. The assays were executed with 10.000 cells seeded per well. After 24 hours, the medium was changed for fresh medium and the cells were cultured for 6,24 or 48 hours. The cell culture medium was collected and kept at 4ºC until all time points were collected. The supernatants

were 40-fold diluted in PBS, before processing according to manufacturer's protocol in 96-well white-walled cell culture plates and read out using a plate-reader luminometer.

2.2.14. rVaccinia-Wt and -ORF8 A549 infection: Thp1 co-culture

A549 cells were infected with recombinant Lister Vaccinia strains expressing ORF8 (rVACV-ORF8) or wildtype Lister (rVACV-Wt) at MOI 0.5. Both viruses were kindly gifted by Yongxu Lu (127). After 18 hours of infection the cells were changed for fresh medium or co-cultured with uninfected Thp1 cells in fresh medium. After 24 hours, the cells were washed three times with PBS and the remaining adherent cells were collected in 350 µl RLT per <5e6 cells. Extraction was performed using the Qiagen RNeasy Mini kit. RTqPCR was performed using the One Step SYBR PrimeScript RT-PCR Kit (Perfect Real Time) (TakaraBio, Japan) and the primers mentioned in **Table 2.2**.

2.3. Results

2.3.1. Ectopic expression of natural ORF8 variants leads to cell surface MHC-I downregulation

To study the role of ORF8 in viral pathogenesis, we established stable cell lines using the adenocarcinomic human alveolar basal epithelial cell line (A549). These cells were used as model system as they closely resemble alveolar cells, which are primary targets of viral infection. We generated these stable cell lines through lentiviral transduction. In brief, pLVX-lentiviral constructs were generated for natural variants - *ancestral, alpha, gamma* - and structural variants – *ancestral*-C20S, -C20S-N78D and ΔSP-ORF8*ancestral* with a 'C-terminal StrepII-tag (**Figure 2.1A**). Lentiviruses carrying these constructs, along with a control-eGFP lentivirus, were produced in 293T Lenti-X™ cells. The A549 cells were transduced with these lentiviruses at multiplicities of infection (MOI) of 1 and 0.05, and selected using puromycin. Initially, high MOI (MOI 1) was employed for the natural variants, to facilitate the detection of ORF8 expression and assess the MHC-I phenotype. However, for a more accurate comparison of variant dynamics, MOI 0.05 was later used to establish single clones with comparable expression levels across all variants. These cells, due to the nature of ORF8 and low MOI, require IP for intracellular ORF8 detection.

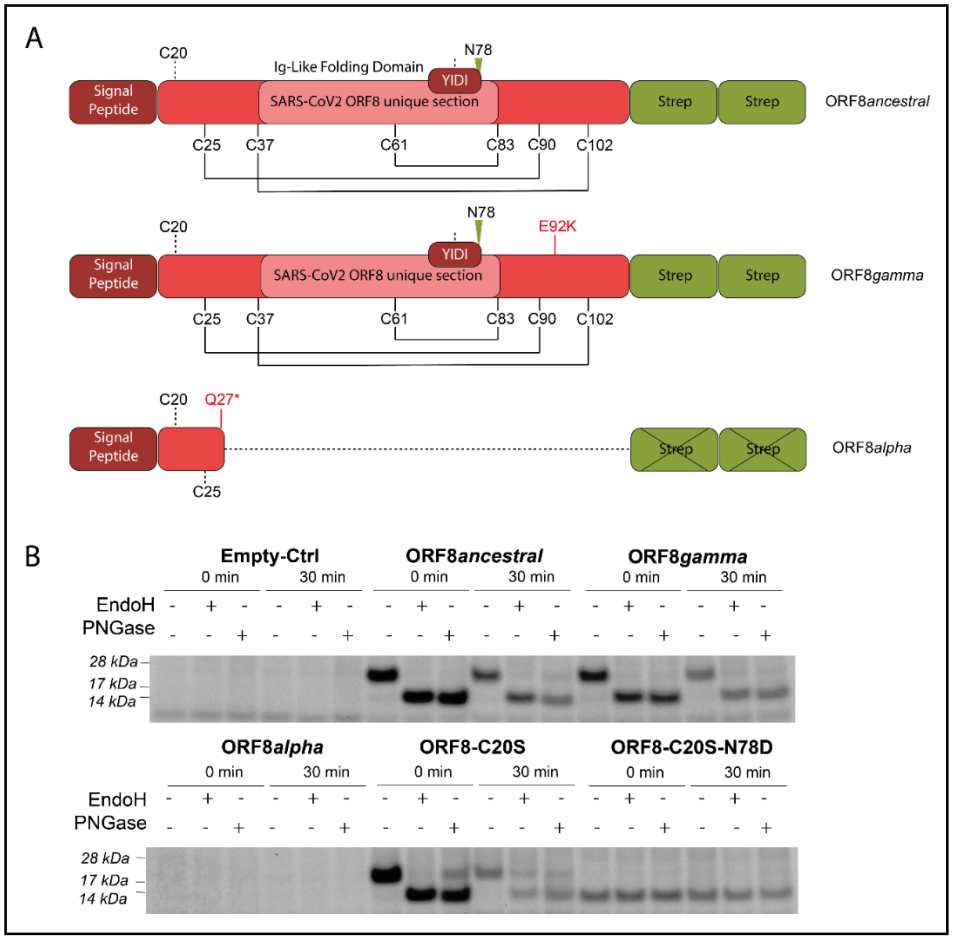


Figure 2.1 A549 stable cell lines were established expressing natural and structural variants of SARS-CoV2 ORF8. A) Model depicting the variants lentivirally introduced into A549 cells, highlighting features of SARS-CoV2 ORF8; the 'N terminal ER signal peptide, the dimerization sites C20 and ^{73}YIDI^{76}, the ORF8 unique section (46-83aa), the intramolecular disulfide bonds, N-glycosylation site and natural mutations introduced. B) Dynamics of de novo synthesized ORF8 in single clone lentivirally transduced variants *ancestral*, -C20S, C20S-N78D, *gamma* and *alpha*, as assessed using [35S]-pulse-chase labelling ± EndoH or PNGase treatment.

In high MOI stable cell lines, we confirmed ORF8*ancestral* and -*gamma* expression intracellularly using α-StrepII antibody (**Figure 2.2A**). As expected, ORF8*alpha* was not detected due to the early stop codon preventing StrepII-tag translation. We could also readily detect ORF8 extracellularly, with both variants exhibiting a similar pattern of secreted ORF8 products; glycosylated and non-glycosylated monomeric ORF8 (~15-17kDa), suspected dimer/trimer ORF8 (~38-40 kDa) and a smear indicating higher order oligomeric forms. These patterns were observed under non-reducing conditions. Under reducing conditions, only monomeric ORF8 was detected, indicating that the smear represents both covalent and non-covalent ORF8 oligomers.

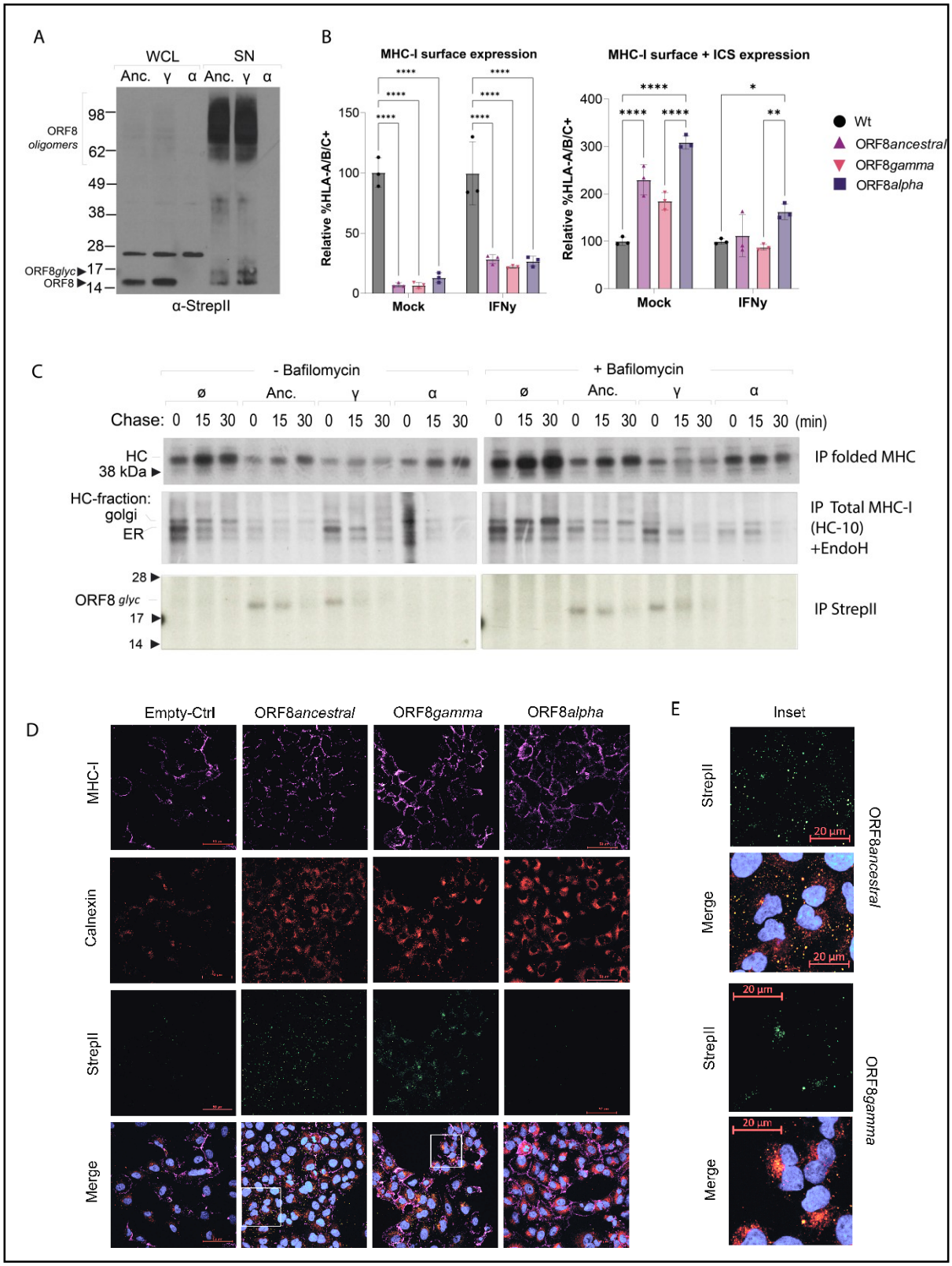


Figure 2.2 Stable overexpression of ORF8 in A549 leads to cell surface MHC-I downregulation. A) ORF8 expression is detected in whole cell lysate and supernatant by resolving by SDS-PAGE and staining for α-StrepII B) FACS analysis of MHC-I cell surface and intracellular (ICS) expression for A549 Wildtype (Wt), A549-ORF8*ancestral*, *-gamma* and *–alpha* using W6/32 staining C) [35S]-pulse-chase assay with 0,15,30 min chase. IPs were performed using W6/32 for folded MHC-I, HC-10 for total MHC-I and MagStrep beads for ORF8. Eluates were prepared under reducing conditions, resolved by SDS-PAGE and visualized using autoradiography. D) Confocal microscopy was performed on the Zeiss Airyscan 880 using the 40x Objective to visualize Calnexin,

MHC-I and StrepII-staining in 0.1%-Triton-X-100 permeabilized stable cell lines. Representative images were shown and their insets highlighting the co-localization of Calnexin and StrepII staining.

ORF8 secretion was further confirmed using a doxycycline-inducible HiBit-ORF8 construct, which demonstrated secretion but no cell surface expression (**Supp. Figure 2.1B**). Notably, IFN-gamma (IFNγ) stimulation significantly reduced ORF8 secretion without affecting intracellular levels. This suggests that during inflammation, ORF8 secretion may be constrained by increased degradation rather than reduced production.

For the natural variant stable cell lines, we assessed whether MHC-I downregulation was indeed observed as previously described for ORF8*ancestral* by Zhang et al. (87). Moreover, we assessed whether this was maintained for the other natural variants. For this purpose, A549 cells transduced and selected for an empty control construct or ORF8*ancestral*, -*gamma* or –*alpha* were seeded for 24 hours and either mock or IFNγ-stimulated (100ng/mL) for 12 hours. Afterwards, the cells were stained with live/dead staining and for HLA-A/B/C. We assessed surface and intracellular MHC-I levels, expressed as a percentage relative to control cells. All ORF8 variants reduced surface MHC-I expression compared to controls, with a slight increase upon IFNγ stimulation, indicating that ORF8 does not fully block MHC-I upregulation. Intracellular MHC-I expression was significantly higher for all variants compared to control, but this accumulation was reduced by IFNγ treatment for all variants except ORF8*alpha*, which maintained significantly increased intracellular MHC-I (**Figure 2.2B**).

These results confirm that ORF8 variants can interfere with cell surface MHC-I expression, maintaining this effect across all natural variants. Increased intracellular MHC-I in mock-treated cells suggests enhanced endocytosis, while reduced accumulation in IFNγ-treated cells may support increased MHC-I recycling or degradation.

2.3.2. Stable cell lines expressing naturally occurring variants of ORF8 reveal differential mechanisms of MHC-I downregulation.

To better investigate the dynamics of MHC-I expression in the presence of natural ORF8 variants, we employed a [35S]-pulse-chase experiment (**Figure 2.2C**). The stable cell lines were pre-treated with 100 ng/mL IFNγ to simulate an immune response and improve MHC-I expression levels on A549 cells. To assess the role of lysosomal degradation in MHC-I downregulation, cells were treated with Bafilomycin A1 (BafA1) for 2 hours (250nM), to block lysosomal acidification. Cells were then starved of cysteine/methionine for 30 minutes, pulsed with [35S]methionine/cysteine for 15 minutes, and chased for 0, 15, and 30 minutes. Lysates were collected to assess MHC-I synthesis and maturation via immunoprecipitation with α-MHC-I (W6/32) and α-HC-10 antibody and Dynabeads™ Protein G, with or without EndoH treatment to determine Golgi entry by complex glycosylation. ORF8 synthesis was detected using a StrepII-antibody.

In untreated cells, ORF8*ancestral* primarily affected MHC-I synthesis, whereas ORF8*gamma* did not affect synthesis but blocked maturation, leaving MHC-I in the EndoH-sensitive form, unlike observed in Empty-control and other variants. ORF8*alpha* showed reduced synthesis with no clear phenotype. MHC-I synthesis and maturation could be partially rescued by Bafilomycin A1 treatment for ORF8*ancestral* and *alpha* but not ORF8*gamma*.

Given that ORF8*gamma* specifically affected MHC-I maturation, we employed confocal microscopy to assess ORF8 localization within the cell. We hypothesized that ORF8*gamma* might form complexes with and retain MHC-I at the ER. In our experimental set-up, cells were pre-treated with 100 ng/mL IFNγ for 12 hours. We then immunostained the cells using StrepII-antibody for ORF8, α-Calnexin for ER and α-HLA-A/B/C-647 for mature MHC-I. Due to previous technical issues with HC-10 staining for total MHC-I, we used mature MHC-I staining instead, which precluded direct assessment of MHC-I retention. No clear

downregulation could be observed in this set-up. However, ORF8*gamma* showed predominantly perinuclear localisation and co-localised with calnexin, suggesting ER retention. In contrast, while ORF8*ancestral* also co-localised with calnexin, it appeared to sequester calnexin into punctate structures. These observations align with previous proteomics studies suggesting direct interactions between ORF8 and calnexin (**Supplementary Table 3.1**) (80, 95, 126).

To investigate which domains are important for MHC-I downregulation, we introduced structural variants of ORF8 into our experimental setup. These variants included ORF8*ancestral*-C20S (covalent dimerization deficient), -C20S-N78D (covalent dimerization and glycosylation deficient) and ΔSP-ORF8 (ER import deficient). We selected single clones based on comparable expression levels of ORF8 based on RT-qPCR (**Supp. Figure 2.2**). For these clones, first the synthesis of ORF8 itself was traced, using [35S]pulse labelling, and chase over 0 and 30 min (**Figure 2.1B**). As observed in our previous MHC-I set-up, proteins trafficking through the secretory pathway gain EndoH resistance at 15-30 min post synthesis (**Figure 2.2C**). Surprisingly, none of the ORF8 variants exhibited EndoH resistance at 30 minutes. However rapid loss of ORF8 was seen for all variants, suggesting that ORF8 secretion might not occur through the secretory pathway, has delayed dynamics or is degraded.

To simulate a pro-inflammatory environment, we assessed the synthesis and maturation dynamics of ORF8 and MHC-I under IFNγ treatment (100 ng/mL, 12 hours), as previously done with the high MOI stable cell lines (**Figure 2.3**). Following IFNγ treatment, cells were exposed to either Bafilomycin A1 (BafA1) to inhibit lysosomal degradation by blocking lysosomal fusion, or Brefeldin A (BrefA) to block the secretory pathway. Our results revealed distinct maturation phenotypes among the ORF8 variants (**Figure 2.3A**). To start, there is an obvious loss of synthesized ORF8*ancestral* over time potentially due to rapid secretion or degradation of ORF8. BafA1 treatment appeared to rescue this secretion or degradation, leading to accumulation of ORF8*ancestral* (**Figure 2.3A**). Similar rescue

effects were observed for ORF8*ancestral*-C20S and -C20S-N78D, although to varying degrees. The C20S-N78D variant showed a complete block in secretion or degradation, while C20S displayed a partial rescue with BafA1 treatment. Interestingly, BrefA treatment partially blocked secretion or degradation for both C20S and C20S-N78D variants. These findings suggest that if secreted not degraded, the glycosylated ORF8 may utilise both the secretory and alternative lysosome-dependent pathways for secretion, while non-glycosylated ORF8 relies primarily on the lysosome-dependent pathway for secretion. It is worth noting that BrefA treatment affected ORF8 synthesis across all variants.

The ORF8*ancestral*-C20S-N78D variant was confirmed to not be glycosylated, as does the ER-signal peptide deficient ORF8 variant (ΔSP). Intriguingly, ΔSP-ORF8*ancestral* levels can, however, be rescued at 20 min chase using BrefA treatment. This suggests that although ΔSP-ORF8*ancestral* is not able to be translocated to the ER, it does rely on BrefA-affected processes for secretion or degradation, for example COPI-vesicles or endocytic recycling mechanisms. Lastly, both BrefA and BafA1 treatments are indicated to be capable of preventing ORF8*gamma* secretion or degradation.

When assessing the turnover of MHC-I, ORF8*ancestral* and –C20S can clearly be rescued over time by BafA1 treatment, where all other variants do not show a similar sensitivity.

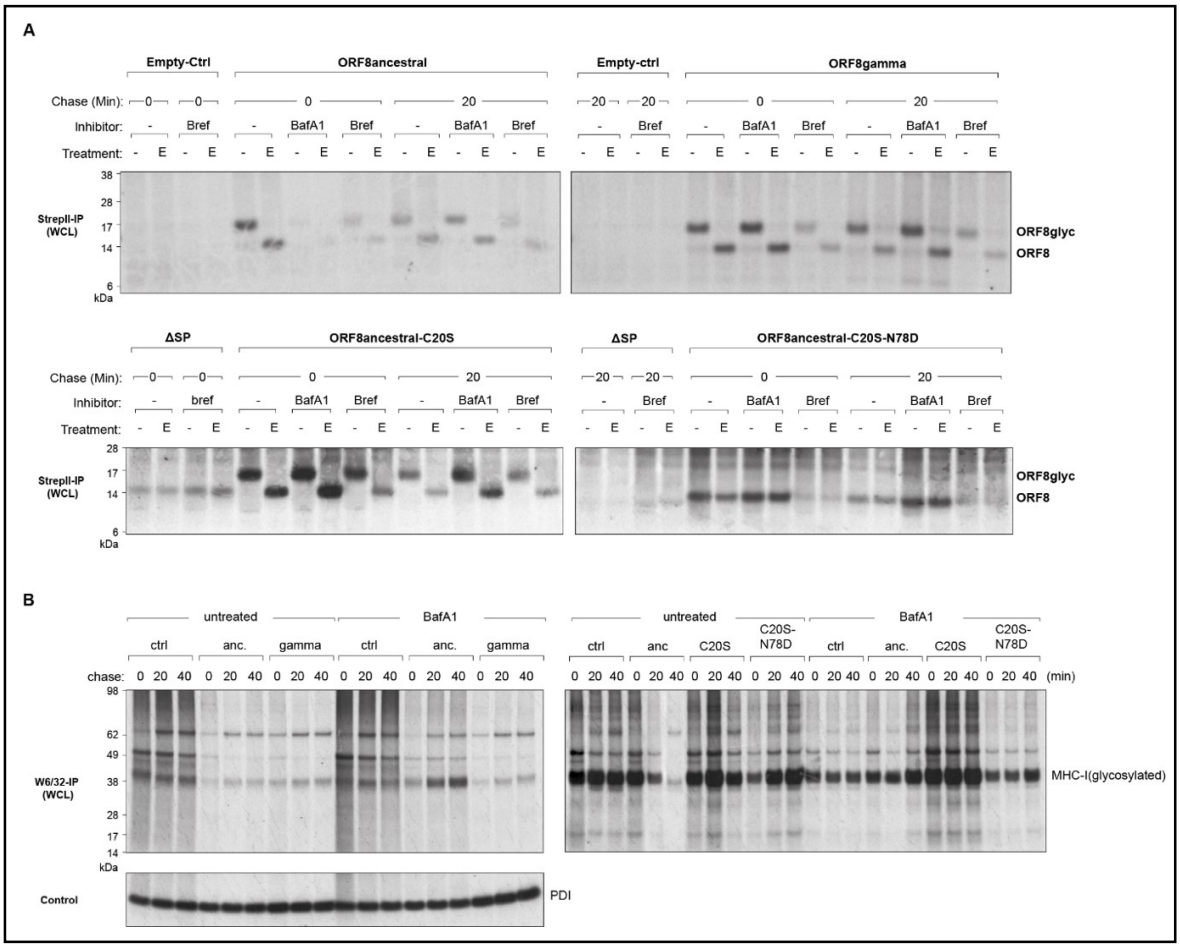


Figure 2.3 ORF8 secretion indicated to rely on lysosomal pathway and secretory pathway, while MHC-I downregulation relies on lysosomal pathway for ORF8*ancestral* and -C20S, but no other variant. A) De novo synthesized ORF8 and B) MHC-I are traced using MagStrep "type3" XT beads and W6/32 antibody conjugated to Dynabeads™ respectively at 0, 20 and 40 min post 15 min pulse with EXPRE35S35S Protein Labeling Mix. Cells were pre-treated for 10 hours with IFNγ (100 ng/mL), followed by a 2-hour treatment with DMSO control, BafilomycinA1 (250nM) of BrefeldinA (3.0 ug/mL) treatment. Representative autoradiograms are shown of three biological repeats for the natural variants, and two biological repeats for the structural variants. ER-resident PDI is utilized as control for protein synthesis.

These pulse-chases have thus revealed the complexity of ORF8 kinetics and its involvement in MHC-I downregulation. One pathway utilized for MHC-I downregulation is the lysosomal pathway, as seen for ORF8*ancestral* and –C20S, and previously suggested by Zhang et al (87). We find evidence that this downregulation mechanism does not rely on the covalent dimerization site C20 and is however suggested to rely on the Ig-like domain. Although the Ig-like fold was *in silico* predicted not be important, as disulfide reductions do

not affect HLA-A binding (128). Considering, ORF8*ancestral*-C20S-N78D does not display similar turnover at 40 min past pulse, it does suggest that the folding and glycosylation status could be important. It has been suggested that if acting through direct interaction, the MHC-I epitopes are predicted to be at the conserved positions 39–42, 104–107, and 110–112, located outside of SARS-CoV2 ORF8 unique regions. These epitopes are predicted to allow for preferential dimerization with MHC-I instead of monomeric ORF8 (129). Given our findings, it is important to confirm whether the direct interaction between ORF8 and MHC-I is maintained across the structural and natural variants we studied. Additionally, we need to investigate whether the previously observed downregulation of MHC-I by ORF8*alpha* and ORF8*gamma* occurs through direct interaction or via indirect mechanisms.

2.3.3. MHC-I interactome altered by expression of naturally occurring variants of ORF8

To better understand the mechanisms by which natural ORF8 variants downregulate MHC-I, an MHC-I interactome study was performed. In this experiment, A549 cells were transfected with SARS-CoV2*ancestral*-Spike, -M, -Np and E to simulate viral assembly and stimulated with IFNγ to mimic an immune response. This set-up was chosen to best mimic viral infection in a BSL2 set-up. Simultaneously, ORF8*variants* were introduced by transfection, to assess the role of ORF8 in the MHC-I life cycle. The complete MHC-I interactome, including mature, immature, classical, and non-classical MHC-I, was analysed by immunoprecipitating MHC-I heavy chains using an HLA Class I Heavy Chain antibody (Nordic MuBio). The results presented in **Figure 2.4** reveal that ORF8 expression induces an enrichment of pathways associated with the immune responses and adherens junctions. Moreover, intracellular interactors were augmented for the ORF8*gamma* and *alpha* variant. A specific enrichment of ribosomal subunits was found, indicative of a potential halt of MHC-I at the translocon. Moreover, specific subsets of MHC-I were found to be enriched, particularly non-classical HFE/HLA-H was found for ORF8*gamma*. This is noteworthy, as

HFE is crucial for maintaining iron homeostasis in the cell. Disruptions in HFE function can lead to iron overload, which may exacerbate conditions associated with ferroptosis. The role of iron overload and the consequential oxidative stress in SARS-CoV2 infection is an active area of research. Studies have already demonstrated that serum iron and ferritin levels can predict COVID-19-related hospitalization, severity, and mortality (130). Additionally, HFE has also been identified in literature as a direct interactor of both Nsp4 (constituent component for SARS-CoV2 replication organelle formation) and ORF8 (79, 131). Further investigation into the role of the HFE-ORF8 interaction in SARS-CoV-2 pathogenesis, could yield valuable insights.

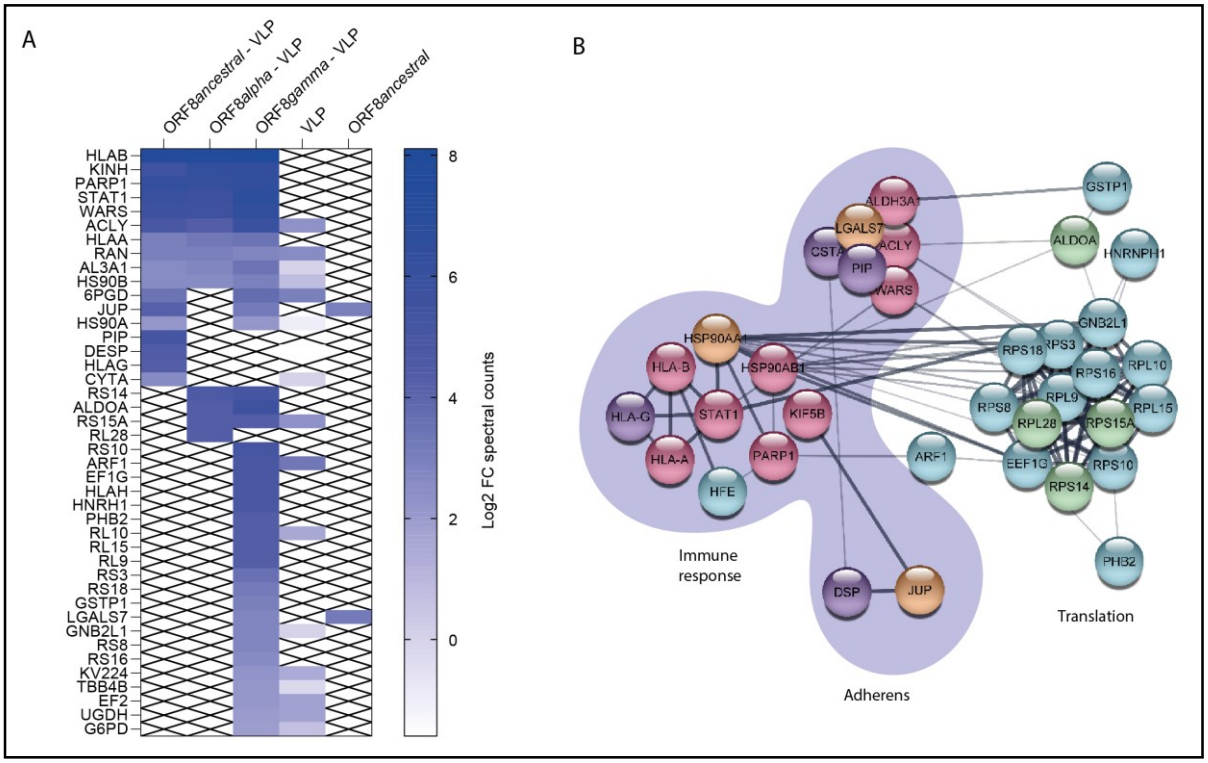


Figure 2.4 Differential interactor enrichment of MHC-I heavy chain during ORF8-transfections in A549 cells. A) Preliminary analysis of HLA-I Heavy-chain (HC) interactor enrichment of A549 cells transfected with SARS-CoV2 viral-like particle (VLP) components (S,Np,M,E) and/or variants of SARS-CoV2 ORF8(*ancestral*, *alpha* and *gamma*). Biological duplicate pull-downs were performed using α-HC-10 (MUB2037P, NordicMUBio), Dynabeads™ Protein-G beads and subsequent preparation for M/S using S-trap™ digestion. All IPs were scored against control samples using SAINT. Digestion and SAINT analysis were executed by Dr Tiaan Heunis (132). The heatmap contains proteins enriched in each IP versus control, using spectral count data. SAINT outputs were filtered for proteins with a BH-corrected p-value < 0.05. Proteins were ranked based on fold change calculated in SAINT and variant specific presence. The SAINT fold change scores were log2-transformed and visualized using PRISM 9.0. B) String visualization of ORF8-variant specific enrichment (excluded proteins <2 FC difference with VLP) using Cytoscape 3.8.2 (https://string-db.org/). Node colors for variant enrichment: Pink = Enriched for all variants; Purple = ORF8*ancestral* enriched; Orange = *ancestral*- and *gamma*-enriched; Blue = *gamma*-enriched; Green = *gamma* and *alpha*-enriched. Enrichment data was grouped based on GO cellular component or process;

Extracellular space/vesicle highlighted in purple (FDR: 2E-11); with subset for immune response (FDR:2E-3) and adherens (FDR:1E-4); and intracellular enrichment for translation (FDR: 2E-12).

2.3.4. ORF8 variants differentially regulate autophagosomal compartments.

Given that the pulse-chase data suggested that ORF8*ancestral* expression impacts lysosomal degradation, we sought to investigate whether this effect is specifically attributable to autophagosomal degradation, as proposed by Zhang et al (87). To study manipulation of autophagy by our ORF8 variants of interest, a doxycycline-inducible tandem-luminescence-fluorescent autophagic flux reporter (HiBit-Halo-hLC3) was introduced into our single clone A549 cells. This construct was stably transduced at MOI 0.1, selected using the Zeocin®-selection marker and assessed for comparable levels of HiBit-Halo-hLC3 introduction by RT-qPCR (**Figure 2.5B**). This system was employed to allow for quantitation of total autophagy compartment abundance by luminescence, as well as visualization of autophagic flux utilizing membrane permeable (MPL) and impermeable HaloTag (MIL) ligands as described by Puri et al. (**Figure 2.5A**) (133). Luminescence read-outs confirmed that ORF8*ancestral* limits autophagosomal compartment abundance, an effect which is reversed in the dimerization-deficient structural variant (**Figure 2.5C**). Moreover, the natural variants ORF8*gamma* and ORF8*alpha* both significantly increase autophagosomal compartment abundance. These findings suggest that ORF8 expression may induce autophagy, with ORF8*ancestral* potentially stimulating autophagic flux or secretory autophagy in a C20-dependent manner.

To further investigate the impact on autophagic flux, light microscopy was employed to visualize subsets of autophagosomal compartments using HaloTag® technology (**Figure 2.5D**). Consistent with the HiBiT-assay results, ORF8*alpha* and -*gamma* showed the highest abundance or higher intensity of both MPL+ and MIL+ vesicles. Intriguingly, both ORF8*ancestral* and -C20S, displayed a near complete loss of early, MIP^+ autophagosomal compartments. The absence of a corresponding loss in MPL^+ signal suggests that ORF8 can stimulate autophagophore maturation in a C20-independent manner, while limiting total

abundance of autophagosomes in a C20-dependent manner. This implies that the observed MPL$^+$ vesicles for ORF8*ancestral* are predominantly autolysosomes, which would explain the loss of HiBiT signal. To prove this observation, use of inhibitors such as BafA1, Chloroquine, or knock-down of autolysosomal fusion tethering components such as VAMP8, STX17, SNAP29 will be essential.

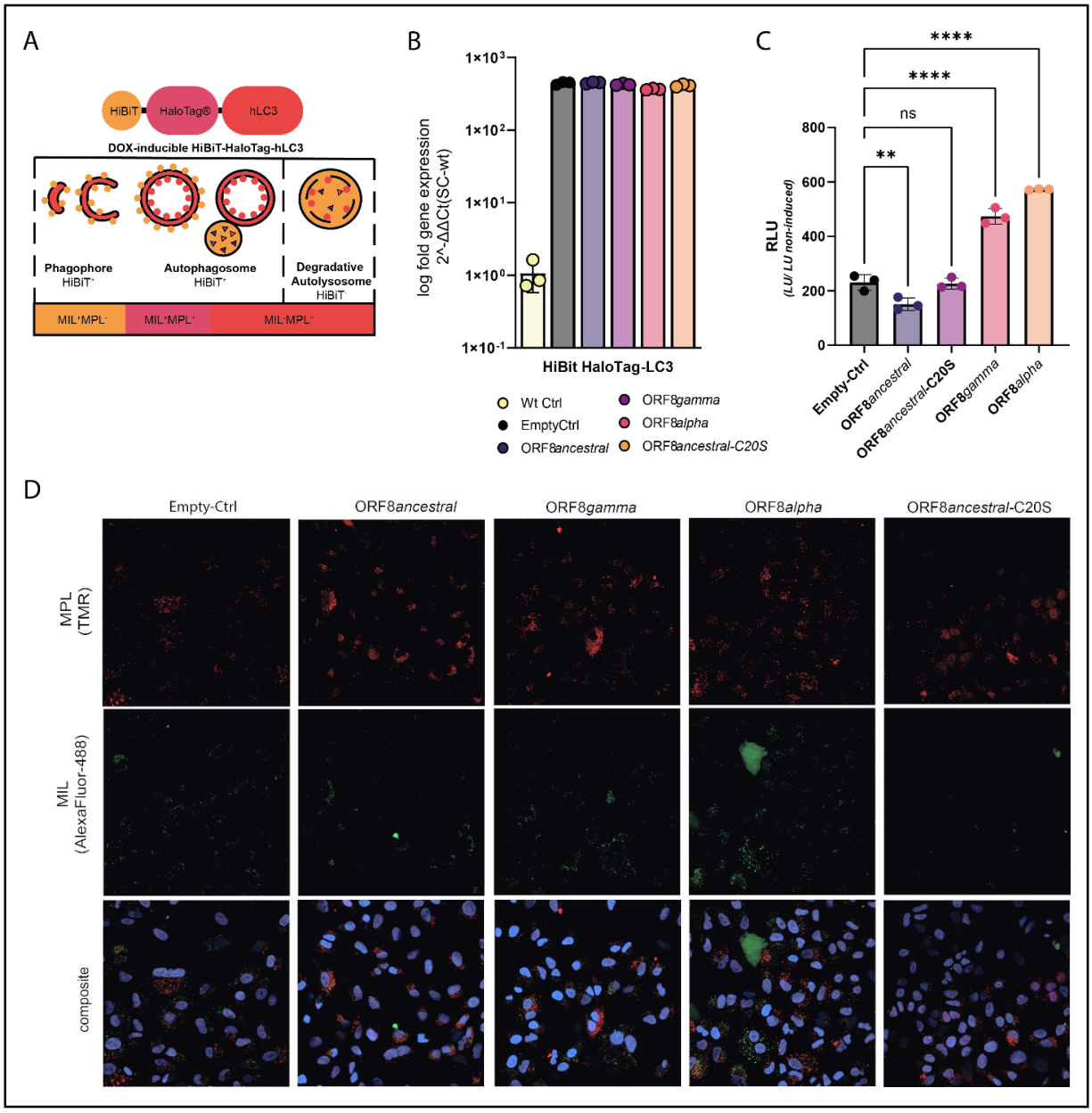


Figure 2.5 ORF8variants interfere in autophagosomal compartment abundance. A) Model depicting the DOX-inducible autophagic flux reporter introduced in the A549-ORF8variant single clones. B) Comparable introduction levels were assured as measured by RTqPCR probing for HiBiT-HaloTag®. C) Three biological replicates with four technical replicates each, were used to determine autophagosomal compartment abundance during homeostasis by means of relative luciferase activity. Relative luciferase activity depicts the luciferase activity in DOX-induced versus non-induced condition. Statistical significance was determined using Dunnett's multiple comparisons test to compare each ORF8-variant cell line to the control (A549 Empty-Ctrl). Significant differences are

denoted as follows: *p < 0.05, **p < 0.01, ***p < 0.001, ****p < 0.0001. D) Autophagix flux was visualized using the membrane permeable HaloTag® TMR Ligand, and the membrane-impermeable HaloTag Alexa Fluor 488 Ligand (MIL). Representative images were shown that were obtained using a 40x objective on the Zeiss Airyscan 880. The images were thresholded using Zen Blue software (V3.3.89).

Transmission Electron Microscopy (TEM) images corroborate the accumulation of mature autophagosomal structures in cells expressing ORF8*gamma* and -*alpha* **(Figure 2.6)**. Single clone A549 stable cell lines were cultured for 48 hours in cDMEM until 90% confluency was reached, prior to collection for TEM analysis. The cells were collected as cell pellets and fixed for 1 hour at RT in 4% formaldehyde, 2.5% glutaraldehyde 0.1 M PIPES buffer (pH7.2) before standard TEM preparation was performed at the Dunn School BioImaging facility (University of Oxford). Manual quantitation of lipid droplets, early degradative vesicles and late degradative/lysosomal vesicles was performed on 40 cells per condition. Categorization and identification was performed as indicated in **Supplementary Figure 2.3** wherein vesicles of endosomal, multivesicular or autophagosomal origin are characterized as 'early degradative vesicles' and (endo/auto)-lysosomes, lamellar bodies and degradative vacuoles are marked as 'lysosomal vesicles'. The images show that ORF8*ancestral* has a rather similar morphology to empty control-transduced cells (Empty-Ctrl), except that it induces visually larger early degradative vesicles. In contrast both ORF8*alpha* and ORF8*gamma* show a significant accumulation of lysosomal vesicles and loss of early degradative vesicles. Interestingly, ORF8*alpha* and ORF8*gamma*-expressing cells induce accumulation of distinct types of vesicles. While ORF8*alpha* induces predominantly traditional auto/endolysosomal vesicles, ORF8*gamma* accumulates specialized lysosomal vesicles resembling (multi)lamellar bodies. In alveolar cells, lamellar body production can be increased under oxidative stress or in a pro-inflammatory response (134). Lamellar bodies are specialized secretory lysosomes found particularly in type II alveolar cells, that are highly enriched in phospholipids. Previous studies have suggested that LBs originate from MVBs and rely on autophagy for maturation. They are crucial for surfactant release into the amniotic fluid in the lungs (134-137). The

potential use of lamellar bodies as a vehicle for ORF8*gamma* secretion and the implications of increased lamellar body production for viral pathogenesis remain open questions that warrant further investigation.

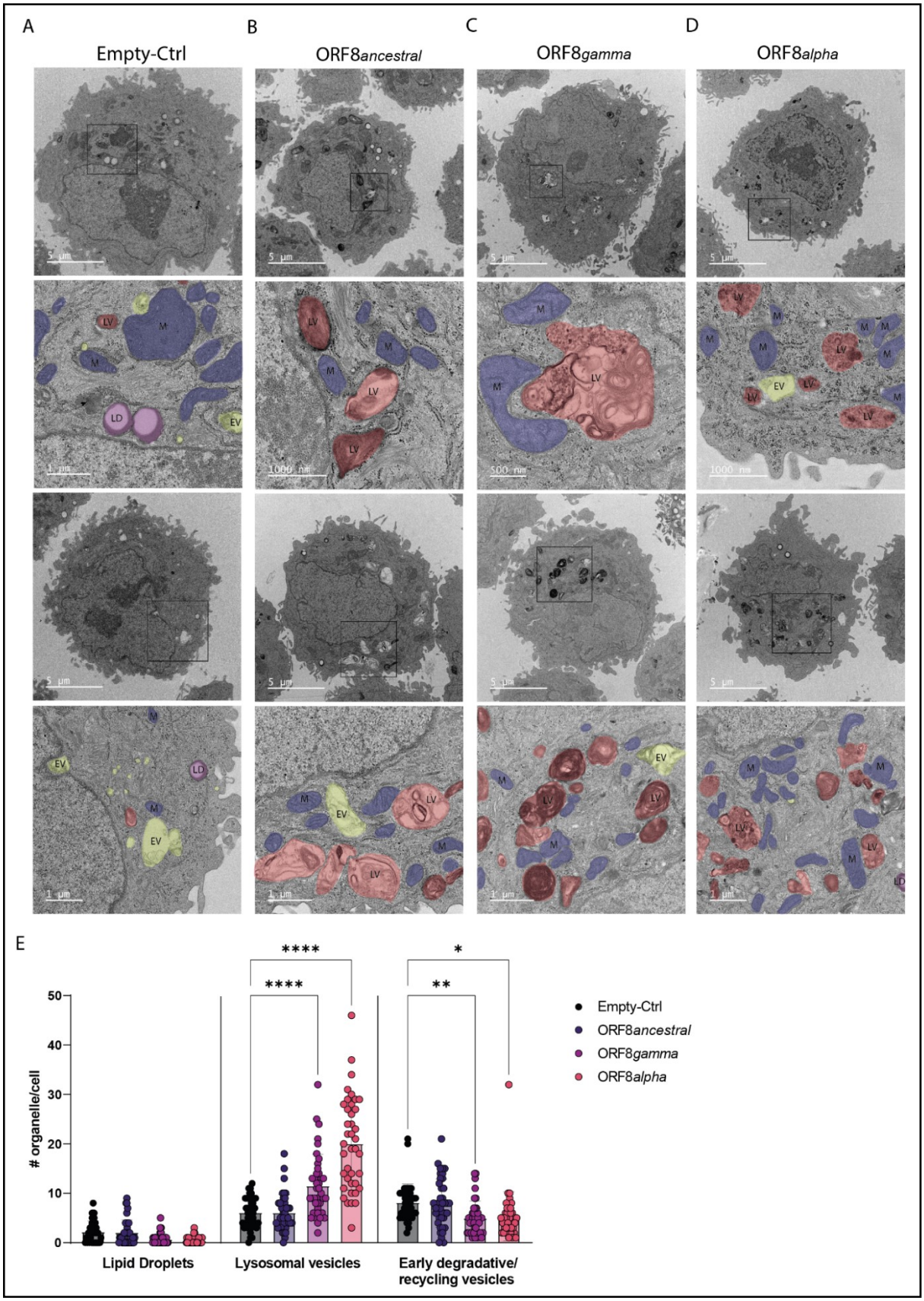


Figure 2.6 Natural variants of ORF8 increase the abundance of lysosomal vesicles in A549 cells in homeostasis. A549 cells stably expressing A) an empty control construct (Empty-Ctrl); B) ORF8*ancestral*; C) ORF8*gamma*; D) ORF8*alpha* were collected as cell pellet and fixed for 1 hour at RT in 4% formaldehyde, 2.5% glutaraldehyde 0.1 M PIPES buffer (pH7.2) before standard TEM preparation was performed by embedding in resin and post-staining on 200 mesh Cu grids using

Reynold's lead citrate. The TEM images were obtained on the JEOL 1400 TEM. E) Quantification was performed by counting Lipid Droplets (LD; purple), Lysosomal vesicles (LV; red; (Endo-, Auto-)lysosomes; lamellar bodies and degradative vacuoles) and early lysosomal/recycling vesicles (EV; yellow; endosomes; MVBs, amphisomes) per cell, for 40 cells per condition. Statistical significance was assessed using Dunnett's multiple comparisons test to compare each ORF8-variant cell line to the control (A549 Empty-Ctrl). Error bars represent standard error of the mean (SEM) calculated from 40 images of individual cells. Significant differences are denoted as follows: *p < 0.05, **p < 0.01, ***p < 0.001, ****p < 0.0001.

Similar to the natural variants, the structural variants C20S and C20S-N78D were visualized using TEM and compared to ORF8*ancestral* (**Figure 2.7A-B**). The TEM results support that autophagosomal maturation is stimulated by ORF8*ancestral* in a C20-independent manner, with a small loss in early degradative/recycling vesicles for both ORF8*ancestral*-C20S and C20S-N78D. Moreover, it suggests that lysosomal degradation or secretion could rely on ORF8 glycosylation status as C20S-N78D leads to an accumulation of degradative vesicles similar to ORF8*alpha* (**Figure 2.7C**).

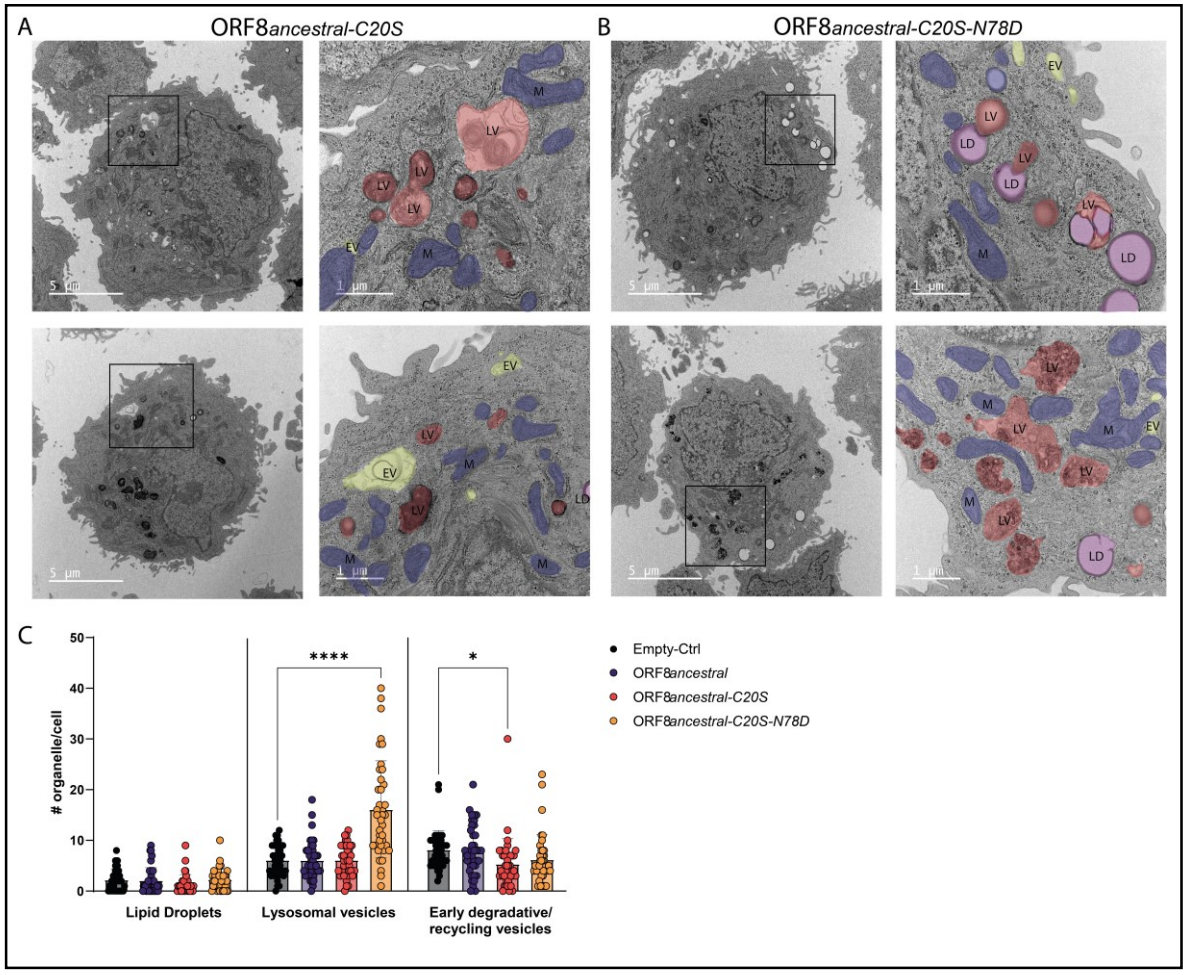


Figure 2.7 Structural variants of ORF8 suggest that unconventional lysosome-dependent secretion might be induced in glycosylation-dependent manner. A549 cells stably expressing A) ORF8ancestral-C20S; or B) ORF8ancestral-C20S-N78D were collected as cell pellet and fixed for 1 hour at RT in 4% formaldehyde, 2.5% glutaraldehyde 0.1 M PIPES buffer (pH7.2) before standard TEM preparation was performed by embedding in resin and post-staining on 200 mesh Cu grids using Reynold's lead citrate. The TEM images were obtained on the JEOL 1400 TEM. C) Quantification was performed by counting Lipid Droplets (LD; purple), (LV; red; (Endo-, Auto-)lysosome; lamellar bodies and degradative vacuoles) and early lysosomal/recycling vesicles (EV; yellow; endosomes; MVBs, amphisomes) per cell (more representative images; **Supp. Figure 2.3**), for 40 cells per condition. Statistical significance was determined using Dunnett's multiple comparisons test to compare each ORF8-variant cell line to the control (A549 Empty-Ctrl). Error bars represent standard error of the mean (SEM) calculated from 40 images of individual cells. Significant differences are denoted as follows: *p < 0.05, **p < 0.01, ***p < 0.001, ****p < 0.0001.

2.3.5. Deletion of ORF8 does not restrict primary infection in bronchial epithelial cells.

As previously discussed in the introduction, it is crucial to confirm our observations in *live virus* infections, as single viral protein expression set-ups do not reflect the cellular re-organization occurring in infection. To confirm the results observed in the stable transduction set-up, rSARS-CoV-2-WT and rSARS-CoV-2-Δ8 recombinant viruses were kindly provided by Dr. Sola at CNB-CSIC (117). In BSL3, the recombinant viruses were propagated in the Calu-3 bronchial epithelial cell line, which is readily susceptible to infection, and titrated using standard plaque assay with the VeroE6 African Green Monkey cell line. With these viruses, we first confirmed whether viral production is affected by ORF8 deletion. Although there was no significant difference observed in viral production, ΔORF8-SARS-CoV2 displayed a delayed production in comparison to rORF8, a phenotype previously observed in infection of organoid-derived cells (**Figure 2.8**) (117). Viral titres were marginally lower at 24 and 48 hours post infection. Given that these small titre differences match the extracellular genome copy differences, no maturation deficiency is expected (**Supp. Figure 4.3**). To assess potential effects on viral replication, we measured intracellular viral gene copies (Nucleocapsid and ORF8). The ΔORF8 virus was confirmed to lack ORF8. Moreover, the Nucleocapsid RNA levels, measured using GAPDH as a control, did not significantly differ between ΔORF8 and rORF8-SARS-CoV2 at 24 and 48 hours post-infection, but were consistent with the titre differences observed extracellularly.

This suggests that the non-significant viral production defect or delay occurs at the stage of viral replication or earlier.

However, as suggested in the referenced paper, ORF8 is not expected to predominantly exert its function in the primary infected cell on viral production, but instead to support pathogenesis by means of immune modulation (117). By RT-qPCR, we assessed mRNA levels of some key immune markers, of which ISG56, IFNβ, HLA-I and B2M are shown in **Figure 2.8C**. A pro-inflammatory response was induced as expected in infected-Calu-3 cells, using ISG56 and IFNβ as read-outs, with a small non-significant delay in induction observed for the ΔORF8-infected cells. A similar reduction was observed for MHC-I upregulation by means of pan-HLA-I and B2M mRNA levels. It would be interesting to see if a longer time-course would similarly show an increase in pro-inflammatory cytokine production for ΔORF8-infected cells as observed in this study by Bello-Perez et al, that reported that ORF8 contributed to promote early and time-limited IFN and pro-inflammatory responses (117). Moreover, it would be interesting to introduce immune cells into this system, to address how ORF8 influences cell-cell communication. Our previous observations indicate that stable cell lines co-cultured with Thp1 cells show an enhanced pro-inflammatory response when expressing ORF8 (**Supp. Figure 2.4**).

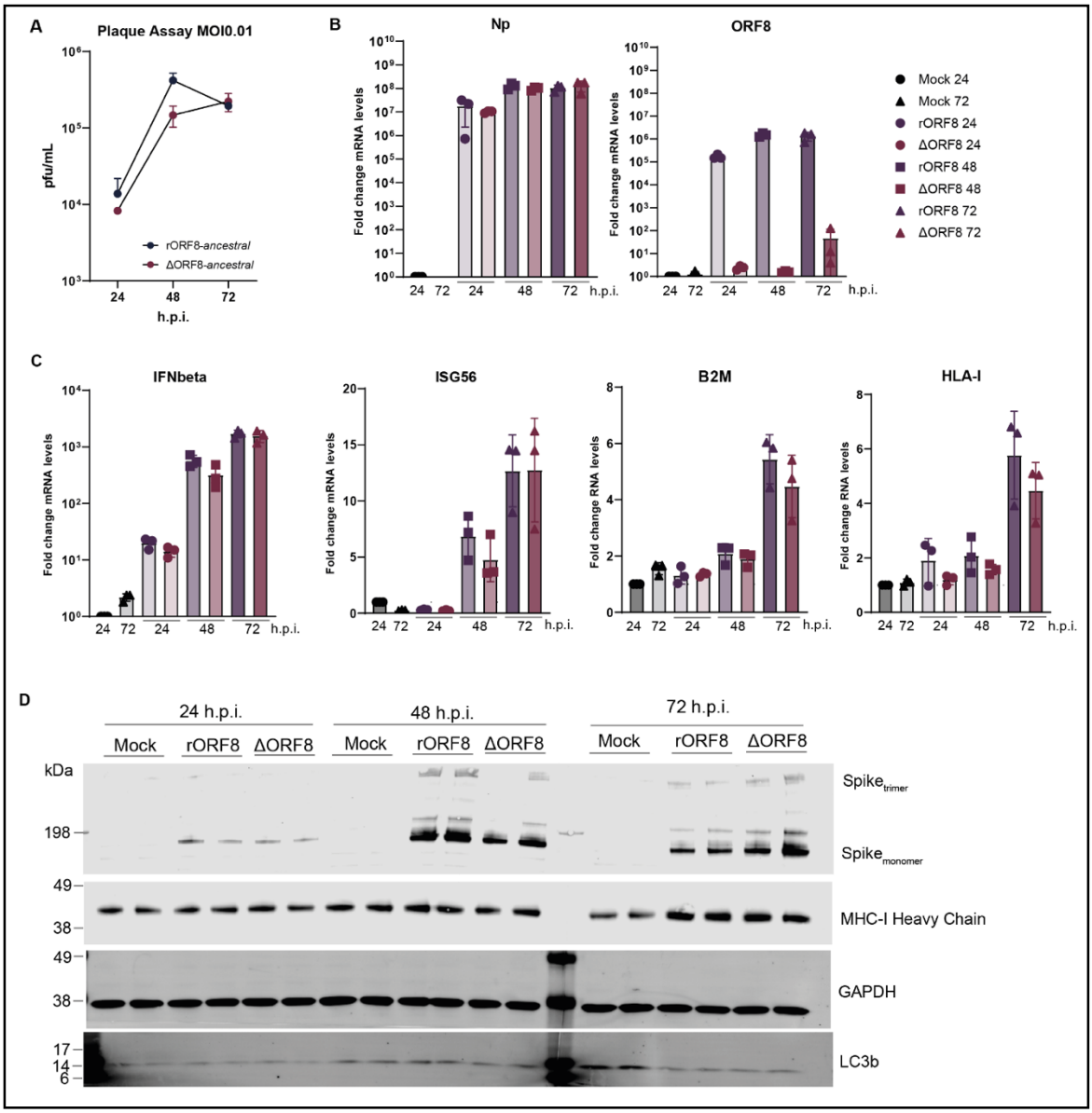


Figure 2.8 ORF8 deletion does not significantly compromise virus production nor immune signalling in Calu-3-infection. Calu-3 cells were infected at MOI 0.01 with rORF8 and ΔORF8-SARS-CoV2 recombinant viruses and were collected at 24,48 and 72 hours post infection. A) Supernatant was titrated using standard plaque assay and reported as plaque forming units (PFU)/mL. Plaque Assay was executed in biological triplicates, measured in technical duplicates. B) intracellular viral gene copies were measured for Nucleocapsid and ORF8 as relative fold change in comparison to Mock control at 24 hours post infection (h.p.i.). C) Transcript levels of several immune markers; interferon beta (IFN-β), IFN-stimulated gene 56 (ISG56), Beta-2 Microglobulin (B2M) and pan-HLA-I were measured and reported as relative fold change in comparison to Mock control at 24 h.p.i. . D) Lysates were resolved by SDS-PAGE and stained for Spike, MHC-I heavy Chain, GAPDH and LC3b. The immunoblots were visualized using IRDyes® on Odyssey® CLx (LI-COR, UK).

2.4. Discussion

In this chapter, we have successfully established stable expression of ORF8 structural and natural variants in lung epithelial cells and demonstrated that these variants lead to rapid secretion of ORF8, and ability to downregulate cell surface MHC-I when overexpressed.

Counterintuitively, in our stable A549 single clones, we observe that ORF8 (*ancestral*, C20S, *gamma*, and ΔSP variants) cell surface MHC-I expression is upregulated in comparison to empty-control transduced cells under homeostatic conditions (**Supp.Figure 2.2C**). Previously, we have also observed, consistent with the findings by Zhang et al., that transfection of ORF8 led to MHC-I downregulation (data not shown) (87). Additionally, while transfection conditions generally enhance immune responses, we have observed that transduction significantly dampens them, as demonstrated by reduced mRNA levels of HLA-B and ISG54 in empty-control transduced cells vs. wild-type cells (data not shown). This suggests that the model system chosen may significantly influence the observed phenotype.

Given that MHC-I downregulation is observed with high intracellular levels of ORF8, while MHC-I stimulation happens when most ORF8 is secreted and intracellular levels are low, we hypothesize that cell surface MHC-I modulation is influenced by both intra- and extracellular ORF8, and could depend on their relative ratio. It will therefore be important to measure intra- and extracellular levels of ORF8 during different phases of infection to understand ORF8 kinetics during *live virus* infection. However, this will heavily rely on improvements in ORF8 antibody quality.

Regarding ORF8 secretion, our pulse-chase experiments with 35S suggested that de novo synthesized ORF8 does not follow the traditional secretory pathway, as indicated by its sustained EndoH sensitivity up to 30 minutes' chase. This suggests that ORF8 may use alternative secretion routes or is delayed in the classical secretion route. Notably, ORF8*ancestral*, and -C20S and C20S-N78D and MHC-I expression for *ancestral* and –

C20S-cells, could be rescued by inhibition of lysosomal degradation using BafA1. Confirming the observation from Zhang et al., that ORF8*ancestral* utilizes lysosomal degradation for MHC-I downregulation (87). However, Brefeldin A treatment also partially rescued ORF8 levels, suggesting multiple routes are used for secretion.

Intriguingly, ORF8*gamma* is not sensitive to BafA1 treatment and appears to interfere instead at the ER quality control stage, as MHC-I remains EndoH-sensitive. The ΔSP-ORF8 variant was detected in the non-glycosylated form similar to C20S-N78D, confirming that it is not targeted to the ER. As, Thapsigargin treatment also did not lead to expected retention of the protein, as seen for all other variants, indicative of all other variants entering the ER (**Supp. Figure 2.5**).

The incomplete rescue of ORF8 by BafA1 treatment may be attributed to partial secretion through the secretory pathway, but could also be linked to secretion of these acidification-blocked vesicles. When blocking lysosomal fusion using BafA1 treatment, lamellar body secretion and secretory ER-phagy have been shown to be stimulated (138, 139). The observed increase in multilamellar body formation in ORF8*gamma* expressing cells suggests that these pathways might be at play. Thapsigargin, an ER Ca2+ releaser and ER-stress inducer, has previously been shown to reduce BafA1-induced secretion and as mentioned before, we did observe increased monomeric ORF8 detection intracellularly for all variants upon Thapsigargin treatment (138). However, Thapsigargin induces UPR and could lead to general ER-retention. To further investigate these potential secretion routes, additional studies are needed, such as knocking down key factors like ABCA3, which is involved in lamellar body formation, to assess its impact on ORF8 secretion (134).

TEM observations revealed that while ORF8*gamma* increased specialized lysosomal vesicle formation, ORF8*alpha* and ORF8*ancestral*-C20S-N78D displayed similar morphologies, with a clear increase in traditional autolysosomal vesicles. This suggests that C20-mediated ORF8 dimers might trigger degradation pathways if N-glycosylation is impaired.

The minimal impact of ORF8 deletion in *live virus* infections compared to its effects in stable expression, might be due to redundancy within SARS-CoV-2. The virus encodes several redundant immunomodulatory proteins with overlapping functions. For instance, proteins like ORF6, ORF7a, M, and E are all implicated to interfere in MHC-I cell surface expression, while ORF3a affects autophagy (140, 141). Previous studies have shown that ORF3a knockdown was necessary to reveal ORF8's role in preventing ER-phagy (103).

Therefore, similar to A549 cells, we have generated Calu-3 cells that express our ORF8 variants. We aim to challenge these cells with ΔORF8-SARS-CoV2, to assess the impact of the natural ORF8 variants on the virus life cycle and immune response and help avoid the confounding effects of other mutations present in these SARS-CoV-2 strains.

In this chapter, we have elucidated the complexity of ORF8's interference with the immune response and revealed that natural ORF8 variants have distinct mechanisms for MHC-I downregulation. As new variants emerge and cause outbreaks, understanding these mechanisms is crucial for developing effective therapeutics, especially given ORF8's association with severe COVID-19 symptoms like cytokine storms. Investigating how different ORF8 variants utilize various secretion routes and their impact on the immune response, will be key to fully understanding ORF8's role in pathogenesis. Thus, this chapter highlights the intricate function of ORF8 and underscores the importance of further research in this area.

Chapter 3 How SARS-CoV2 ORF8 reprograms lung epithelial cells

3.1. Introduction

While much of the research on ORF8 has focused on its impact on the immune response, emerging evidence suggests that ORF8 plays a broader role in cellular reorganization to support virus production. Proteomics studies have indicated that ORF8, along with the Membrane (M) protein and Nsp7, exhibits the highest number of connections in human protein networks, indicative of a multifaceted role for ORF8 (142).

Based on these studies, several groups have validated certain hits. For example p62 the protein encoded by SQSTM1, was found to interact with ORF8 and suggested to modulate ER dynamics by hijacking ER-phagy receptors FAM134B and Atlastin3 (ATL3) (103). Similarly, ER-oxidoreductases hits were validated, suggesting a role in modulating ER dynamics via UPR pathways and inducing convoluted membrane formation (77). This phenotype is reminiscent of rearrangements induced by many positive-sense RNA viruses to generate customised platforms co-opted for replication and assembly. These findings therefore have led to the hypothesis that ORF8 may play a pivotal role in organising replication organelles, which will be further investigated in **Chapter 4**.

Despite anecdotal reports on SARS-CoV2 ORF8's ability to reorganize intracellular membranes, the underpinnings of ORF8-triggered membrane remodelling and their relevance to the virus life cycle are largely undefined. Moreover, the impact of the natural variants of ORF8 on membrane reorganization has yet to be described. With the ongoing emergence of new variants and ORF8 acting as a recombination hub, understanding how sequence variations in ORF8 affect these host interactions and viral fitness is crucial. This chapter therefore investigates the interactomes of various ORF8 variants, including natural forms *(ancestral* Wuhan-Hu-1, *alpha*, and g*amma*) and structural variants (ΔSP-ORF8*ancestra*l, ORF8*ancestral*-C20S, and C20S-N78D).

Moreover, as ORF8 is a secreted protein, we also investigate the extracellular interactome. As discussed previously, the evidence regarding ORF8's secreted forms and their role in disease is contested, with some studies linking non-glycosylated ORF8 to cytokine storms, while others suggest that the glycosylated homodimeric forms induce severe COVID-19-related inflammation (78, 82, 83). Another study suggests that high-order ORF8 oligomers are most likely to drive the inflammatory response (129). These conflicting findings highlight the need for further research into ORF8's secretion pathways and its precise role in SARS-CoV-2 pathogenesis.

We demonstrate that all ORF8 variants under study are secreted from cells. Through analyses of both extracellular and intracellular interactome, we elucidate the secretion routes used by these variants. By analyzing pathway enrichments and identifying unique interacting partners in both the intra- and extracellular milieu, we indicate potential protein targets and inhibitors to validate ORF8 dynamics. We correlate these findings to changes in intracellular membrane reorganization discussed in **Chapter 2**. Additionally, our interactome data provide insights into how different ORF8 variants might differentially modulate immune responses, contributing to our understanding of variant-specific effects on host-pathogen interactions.

3.2. Methods

3.1.1. Cell culture

For this chapter, the single clones of A549 stably expressing ORF8variants – *ancestral*, ΔSP-*ancestral*, *ancestral*-C20S, -C20S-N78D and *gamma*, *alpha* – and empty control, were used that were generated in **Chapter 2**. Please refer to section **2.2.2. Cell culture** and **Table 2.3**.

3.1.2. Secreted ORF8 enrichment

To assess whether ORF8 is predominantly secreted in vesicles, aggregates or as soluble protein, A549 stable cell lines expressing variants of ORF8 were seeded in a T75 to reach confluency in 2 days. After culturing the cell for 2 days at 37 °C, 5% CO_2 in 10%FBS-DMEM, supernatant was collected. The supernatant was cleared from cellular debris by centrifugation at 400 x *g* for 5 min and filtered using a Amicon15® Ultra Centrifugal Filter, 100 kDa MWCO (Millipore, USA) for 30 min at 4700 rpm using a table-top centrifuge at 4ºC. Both the flow through and concentrate were collected and pre-cleared with M2-beads for 1 hr at RT. The pre-cleared supernatants were added to MagStrep "type3" XT beads for O/N incubation at 4ºC. Samples were washed in buffer W (0.1 M Tris-Cl, 0.15 M NaCl, 1 mM EDTA, pH 7.5) and eluted in 1x Laemlli buffer and boiling at 70 degrees for 10 min. The eluted proteins were resolved on SDS-PAGE and stained with Coomassie or stained using StrepII-tag antibody (ab76949; Abcam, UK) and IRDye® 680RD Donkey anti-Rabbit IgG (LI-COR, UK). The immunoblot was visualized using Odyssey® CLx (LI-COR; UK).

3.1.3. Co-IP

To precipitate ORF8-StrepII-variant interactors, co-immunoprecipitation (Co-IP) was performed using MagStrep "type3" XT beads (IBA Lifesciences, Germany) following the manufacturer's protocol. After culturing cells in a T75 flask for 2 days until reaching 90% confluency, both the supernatant and cells were collected for Co-IP. Cells were lysed in 1 mL RIPA buffer (1% Triton X-100, 50 mM Tris-HCl, pH 7.4, 150 mM NaCl, 1 mM EDTA, 0.5% sodium deoxycholate), with added cOmplete™, Mini, EDTA-free Protease Inhibitor

Cocktail (Roche, Switzerland). For intracellular IP, 500 µL of lysate (±2e6 cells) was used. For extracellular IP, the supernatant (10mL) was spun down to remove cellular debris, was Amicon15-100kDa-filtered and the 200 µL-concentrate was used for IP. Antigen-bead binding was performed overnight with 60 µL of 5% bead suspension per sample. Following overnight binding, beads were washed three times with buffer W (0.1 M Tris-Cl, 0.15 M NaCl, 1 mM EDTA, pH 7.5). The samples were then split, with one half reserved for western blot quality control (QC) and the other half (30 µL of 5% bead suspension) used for mass spectrometry. The mass spectrometry samples were frozen dry at -80°C after removing the supernatant.

QC was performed by resolving the eluted proteins by SDS-PAGE and staining using Coomassie and staining using StrepII-tag antibody (ab76949; Abcam, UK) and IRDye® 680RD Donkey anti-Rabbit IgG (LI-COR, UK) (**Table 3.2.**) The immunoblot was visualized using Odyssey® CLx (LI-COR; UK).

Table 3.2 Antibodies & Dyes

Antibodies	Mouse α-Beta Actin	MAB8929 (Bio-Techne (R&D Systems), USA)
	Rabbit α-StrepII-tag	ab76949 (Abcam, UK)
	Mouse α-FLAG® (M2)	F3165 (Sigma-Aldrich, USA)
	IRDye® 800CW Donkey anti-Mouse IgG	926-32212 (LI-COR, UK)
	IRDye® 680RD Donkey anti-Mouse IgG	926-68072 (LI-COR, UK)

3.1.4. Mass spectrometry

For each ORF8 variant, biological triplicates of co-immunoprecipitation (Co-IP) experiments were performed for both extracellular and intracellular ORF8. The antigen-bead complexes were processed at the Target Discovery Institute, University of Oxford, for mass spectrometry analysis. Briefly, the immunoprecipitated samples were on-bead digested using the SMART Digest Kit Trypsin (Thermo Fisher, USA). The resulting tryptic peptides

were desalted and analyzed using the Evosep-TimsTOF Pro with the 30-second Evosep method. The mass spectrometer was operated in data-independent acquisition (DIA) mode.

The raw data were analysed using DIA-NN in library-free mode, against the UniProt human proteome database, including common contaminants and the StrepII-tagged ORF8*ancestral* protein. Retention time-dependent cross-run normalization was applied. To ensure accuracy, protein intensity data were filtered to exclude contaminants. The dataset was then divided into intracellular and extracellular IPs. Proteins were filtered to retain only those identified in all three replicates of at least one experimental group.

Protein intensities were log2-transformed to achieve a symmetrical distribution. Missing values were imputed with random values drawn from a downshifted normal distribution, with values removed if the protein was not identified in all three replicates. Proteins not detected in the control group were classified as ‘unique’ hits. All other proteins were evaluated for significant fold changes. Significant proteins were identified using a Student’s t-test with multiple testing correction, applying a false discovery rate (FDR) threshold of 5% ($q < 0.05$). Proteins exhibiting a fold change greater than 2 (intracellular) or 1.5 (extracellular) and a p-value less than 0.05 were considered significantly enriched.

3.3. Results

3.3.1. ORF8 variants are rapidly secreted in vesicles as glycosylated oligomerized proteins

As mentioned in the central introduction, SARS-CoV2 encodes a classical ER-signal peptide to enter the secretory pathway. In **Chapter 2** we observed that ORF8*ancestral* and *gamma* indeed are rapidly secreted. Using single clone A549 stable cell lines expressing ORF8*ancestral,* -C20S, -C20S-N78D*,* ORF8*gamma*, -*alpha* and ΔSP-ORF8, we assessed whether secretion was also observed for the remaining variants. Moreover, we aimed to address whether ORF8 was secreted as a small soluble protein or was secreted as aggregate or within vesicles. Using Amicon15® Ultra Centrifugal Filter with a 100kDa cut-off, we assessed whether secreted ORF8 would be in the soluble or >100kDa fraction. MagStrep "type3" XT beads were used to precipitate ORF8 from Amicon flow-through (FT) and concentrate (>100kDa fraction). **Figure 3.1A** demonstrates, using ORF8*gamma* and -*ancestral* as examples, that ORF8 is predominantly found in the >100kDa fraction. **Figure 3.1C** shows StrepII-tag mediated IP for all ORF8 variants, confirming that all variants are secreted, except the signal-peptide deficient variant. Moreover, barely any signal can be seen intracellularly, supporting the observation in **Chapter 2** that ORF8 is rapidly secreted, limiting intracellular detection. For secreted ORF8*ancestral*-C20-N78D, we again observe that ORF8 is not capable of being glycosylated. Moreover, the double banding pattern suggests that ORF8 is post-translationally modified or has incomplete cleavage of the ER-signal peptide.

The ORF8 protein was predominantly secreted as glycosylated monomers, with higher order oligomers appearing to be non-glycosylated. Surprisingly, C20S and C20S-N78D mutations did not compromise ORF8 secretion and oligomerization. The C20S-N78D variant showed it was preferentially secreted in oligomeric form, with lower detection levels of the monomeric form in comparison to the other variants. This suggests that oligomerization is C20- and glycosylation-independent and perhaps YIDI-motif dependent.

In this set-up, reducing but incomplete denaturing conditions (70ºC,10 min) were utilized, suggesting that oligomerization occurs by highly stable non-covalent binding, as the C20S-mutated ORF8 variant is still capable of high-order oligomerization. Whether oligomerization instead could rely on the ^{73}YIDI^{76}-motif or more broadly on the specific Ig-like folding, should be confirmed by mutating the ^{73}YIDI^{76}-motif.

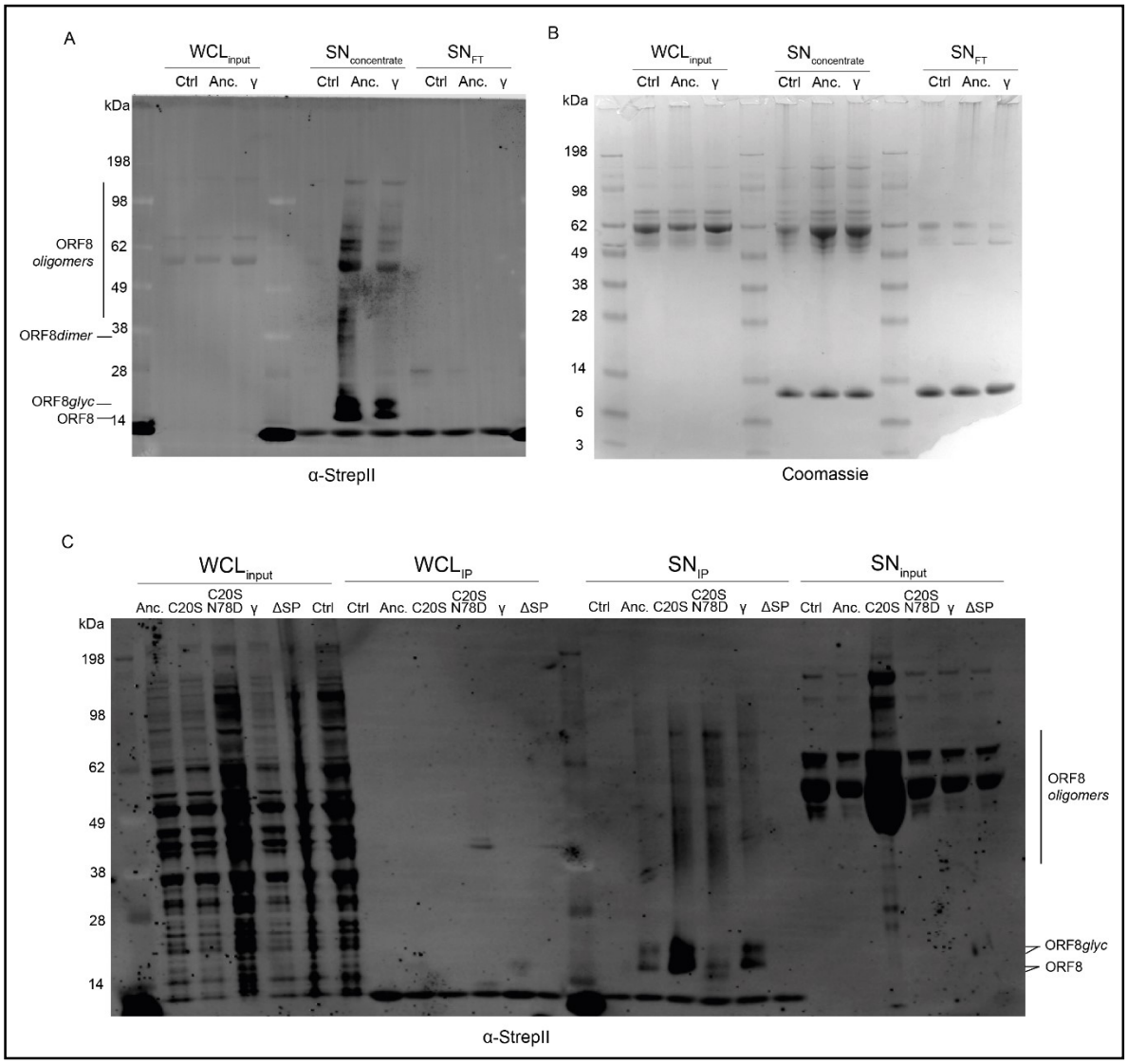


Figure 3.1 ORF8 variants are predominantly secreted in vesicles. A549 stable cell lines expressing ORF8 variants: ORF8*ancestral* (Anc.); -*ancestral*-C20S (C20S); -*ancestral*-C20S-N78D (C20S-N78D); -*gamma* (γ) or ΔSP-ORF8*ancestral (*ΔSP) or empty control (Ctrl) were cultured for 2 days until 90% confluency was reached. Cells were collected in RIPA buffer and supernatant was cleared from cellular debris before both were supplemented with protease inhibitors. Supernatant was filtered using the Amicon15® Ultra Centrifugal Filter. A-B) The supernatant of empty ctrl, ORF8*ancestral* and ORF8*gamma* were subjected to Amicon15®-100kDa filtration. The flow-through (SN_{FT}) and concentrate ($SN_{concentrate}$) from the Amicon15 filter were incubated with MagStrep "type3" XT beads O/N. The antigen-bead complexes were eluted using Laemlli buffer and heated to 70 degrees for 10 min. The eluted proteins and whole-lysate input (WCL_{input}) were resolved by SDS-PAGE and stained using A) StrepII-tag antibody (ab76949; Abcam, UK) and IRDye® 680RD Donkey anti-Rabbit IgG (LI-COR, UK) for visualization of Odyssey® CLx and B) Coomassie. C) Cell lysate

and supernatant of all stable cell line variants were subjected to Co-IP using MagStrep "type3" XT beads. The supernatant was concentrated using Amicon15®-100kDa filtration. The eluted proteins and whole-lysate (WCL_{input}) and supernatant concentrate (SN_{input}) input were resolved by SDS-PAGE and stained using StrepII-tag antibody (ab76949; Abcam, UK) and IRDye® 680RD Donkey anti-Rabbit IgG (LI-COR, UK) for visualization of Odyssey® CLx.

Compared to the intracellular ORF8 pulse-chase results from **Chapter 2**, It is important to note that the extracellular IP results shown in **Figure 3.1** represent steady state levels of ORF8, whereas the pulse chase exclusively demonstrated the intracellular dynamics of de novo synthesized ORF8. To address this distinction, we investigated the secretion patterns of the newly synthesised pool of ORF8. **Supplementary Figure 3.1A** illustrates the secretion of newly synthesised ORF8 using supernatants from the [35S]-pulse-chase assay. This figure reveals rapid secretion of tetramers (~53kDa) for de novo synthesized ORF8, which can be detected for *ancestral*, *gamma* and *ancestral*-C20S, but not -C20S-N78D. Intriguingly, PNGase treatment in this set-up does not result in a lower molecular weight band, suggesting that tetrameric ORF8 does not display glycosylation, but does rely on N78 for tetramerization. This discrepancy between forms of ORF8 released after de novo synthesis and those found in the supernatant, suggests that ORF8 may have the capacity to be re-adsorbed and released in different forms, making the interactions of ORF8 complex and dynamic.

3.3.2. ORF8 variants rewire the cell

Considering these complex dynamics of ORF8, an ORF8 interactome study was set-up to aid in identifying the specific secretory routes utilized by ORF8 variants. Three biological replicates of A549 stable cell lines expressing the ORF8 variants were collected to perform StrepII-tag-driven IP on, for both whole cell lysate and concentrated supernatant. **Figure 3.1** shows a representative blot. The antigen-bead complexes were subsequently processed at the Target Discovery Institute (University of Oxford), for mass spectrometry analysis using the Evosep-TimsTOF Pro with the 30-second Evosep method. Briefly, the immunoprecipitated samples were on-bead digested using the SMART Digest Kit Trypsin (Thermo Fisher, USA) and analyzed using the Evosep-TimsTOF Pro, that was operated in

data-independent acquisition (DIA) mode. The raw data were analysed using DIA-NN in library-free mode, were normalized and filtered from common contaminants. Proteins were filtered to retain only those identified in all three replicates of at least one experimental group and were log2-transformed to achieve a symmetrical distribution. Missing values were imputed with random values drawn from a downshifted normal distribution, with values removed if the protein was not identified in all three replicates. After filtering, 2,765 proteins were identified for the intracellular-IP samples and 1,081 proteins were identified from the extracellular-IP samples. Principal Component Analysis (PCA) was performed (**Supp. Figure 3.2**) and volcano plots were generated (**Supp. Figure 3.3-3.6**) using Perseus software (v2.1). The PCA plots reveal that there is relatively high variability between replicates, which is not uncommon for IP samples. However, the volcano plots reveal that there are still many significant and unique hits; a total of 596 unique interactors intracellularly and 73 extracellularly. Proteins not detected in the control group were classified as 'unique' hits. Significant proteins were identified using a Student's t-test with multiple testing correction, applying a false discovery rate (FDR) threshold of 5% ($q < 0.05$). Proteins exhibiting a fold change greater than 2 for intracellular interactors and 1.5 for extracellular interactors and that have a p-value less than 0.05, were considered significantly enriched.

To understand how ORF8 modulates the cells and is secreted, we opted to assess the extracellular interactors first. Considering ORF8 was indicated to be recycled alongside being de novo synthesized and secreted, the intracellular interactome is complex. Therefore, the proteins identified as 'unique' in the extracellular interactomes were first matched to their log2 intensity data intracellularly and visualized in heatmaps in **Figure 3.2**. Moreover, all significant or unique extracellular interactions of ORF8 were visualized by categorizing them by cellular component and marking them by enriched Kyoto Encyclopedia of Genes and Genomes (KEGG) pathways, presence of an Ig-like fold and/or involvement in lipid metabolism (**Supp. Figure 3.7-3.8**). Herein a clear enrichment for

proteins involved in extracellular vesicle trafficking, mucus secretion and immune response markers could be seen. Moreover, many cell surface and endosomal recycling markers are found. These hits again indicate, that ORF8 potentially can be recycled and secreted by binding certain cell surface receptors.

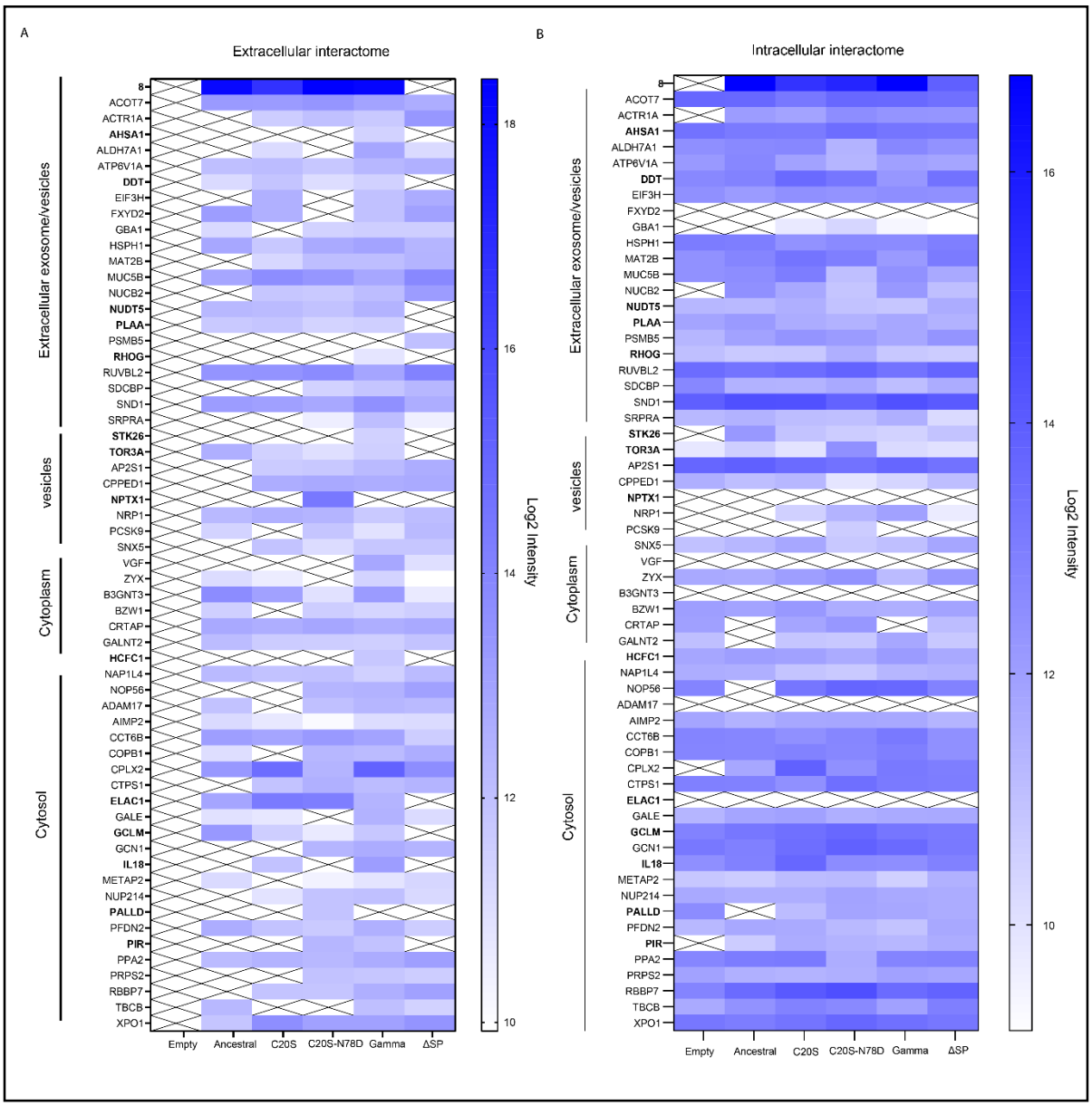


Figure 3.2 Protein hits identified as unique interactor for extracellular ORF8 matched to intracellular log2 intensity data. The heatmaps indicate the interactors of ORF8 that are unique (not present in control replicates) in the intracellular extracellular interactome and are identified in both environments. The heatmaps indicate the mean log2 intensity of three biological replicates. In bold are interactors that are not found in the extracellular ΔSP-ORF8-IP. Proteins are categorized by their subcellular localization as identified using string.db (v12).

Considering extracellular detection of ΔSP-ORF8 was not seen (**Supp. Figure 3.1B**), the hits shared with ΔSP-ORF8 could potentially be false discoveries. Hence a specific focus was put on the protein hits which were not present in the extracellular ΔSP-ORF8 interactome (in bold in **Figure 3.2**). From the protein hits (11) that remained, some notable markers were IL-18, DDT, AHSA-1 and NPTX1. AHSA1 for ORF8*gamma* and NPTX1 for ORF8*ancestral*-C20S-N78D, because they could indicate for the secretion route utilized, as these proteins are involved in exosomal release (through Heat shock protein HSP 90-alpha) and synaptic vesicle release respectively (143, 144). Whereas, Interleukin-18 (IL-18) and D-Dopachrome Tautomerase (DDT), a functional homologue of Macrophage Migration Inhibitory Factor (MIF; also identified for ORF8*gamma*), have pro-inflammatory roles. When DTT is released, it can bind CD74 on DC cells and macrophages and G-protein-coupled receptors CXCR4 and CXCR2 on leukocytes and can have anti-apoptotic effects on lung epithelial cells. And most importantly increased detection of this protein in PBMCs from COVID-19 patients, has been shown to be correlated with severity of disease and non-survival (145-147). Similar to DTT, serum IL-18 levels reflect severity of disease and is normally only secreted in response to inflammasome activation (148, 149). Equally, the specific identification of Phospholipase A-2-activating protein (PLAA) as an interactor, may be linked to the observed elevated levels of secreted phospholipase A2 (sPLA2) in severe COVID-19, of which the plasma levels have been suggested to serve as a predictor of mortality (14, 15). It will be key to confirm these direct interactions and to assess whether ORF8 expression alone or in the context of recombinant virus infections directly increases their extracellular levels. This could provide a link between reduced severity of disease observed for SARS-CoV2 strains that have lost ORF8 expression (Δ382-Singapore variant and Omicron BA.2 sublineage) (22, 41).

3.3.3. ORF8 displays complex relationship with the immune response

Analysing the intracellular interactions proved challenging due to the approximately 600 unique hits across different variants. To navigate this complexity we compared our results

with four published ORF8 interactome studies (79, 80, 95, 126). While many hits were not shared between these four interactomes, 129 protein interactions were reported in at least two independent studies, as summarized in **Supplementary Table 3.1**. A network was generated using Cytoscape (v3.10.2) with a PPI enrichment of 1.0E-16. This network revealed significant enrichments in several reactome pathways, including antigen presentation (Folding, assembly and peptide loading of class I MHC), UPR (ATF6 and IRE1α chaperone genes), asparagine N-linked glycosylation and KEGG pathway 'Protein processing in endoplasmic reticulum'. All significant reactome pathway and KEGG pathways enrichments are summarized in **Supplementary Table 3.2**. The proteins identified as interactors in our studies are highlighted in bold. This summary shows that AHSA1, and NPTX-1 have been previously reported, rendering them promising targets for follow-up studies using bi-directional immuno-precipitation.

Given that the literature-based proteomic screens focused on intracellular ORF8, extracellular interactions with ORF8 such as IL-18 and DDT might be underrepresented in these screens. These hits remain interesting for further investigation to understand ORF8's contribution to the immune response. Moreover, the additional enriched immune markers identified in our extracellular interactome, although represented in ΔSP-ORF8; CXCL-5, TGF-beta 2, VGF, C1QTNF3, CD44 and ICOSL6 warrant further investigation, as they are significantly enriched in comparison to ΔSP-ORF8 (**Supp. Figure 3.5-3.9**). Of particular interest is the specific significant enrichment of cell surface marker IL6ST for ORF8*ancestral* and HAS1 for ORF8*gamma*. In contrast, ADAM17/10/15, Transferrin receptor protein 1 and Neuripillin1/2 are shared across variants. This pattern suggests that signalling and potential up-take mechanisms may differ among ORF8 variants, potentially utilising both shared and variant-specific routes.

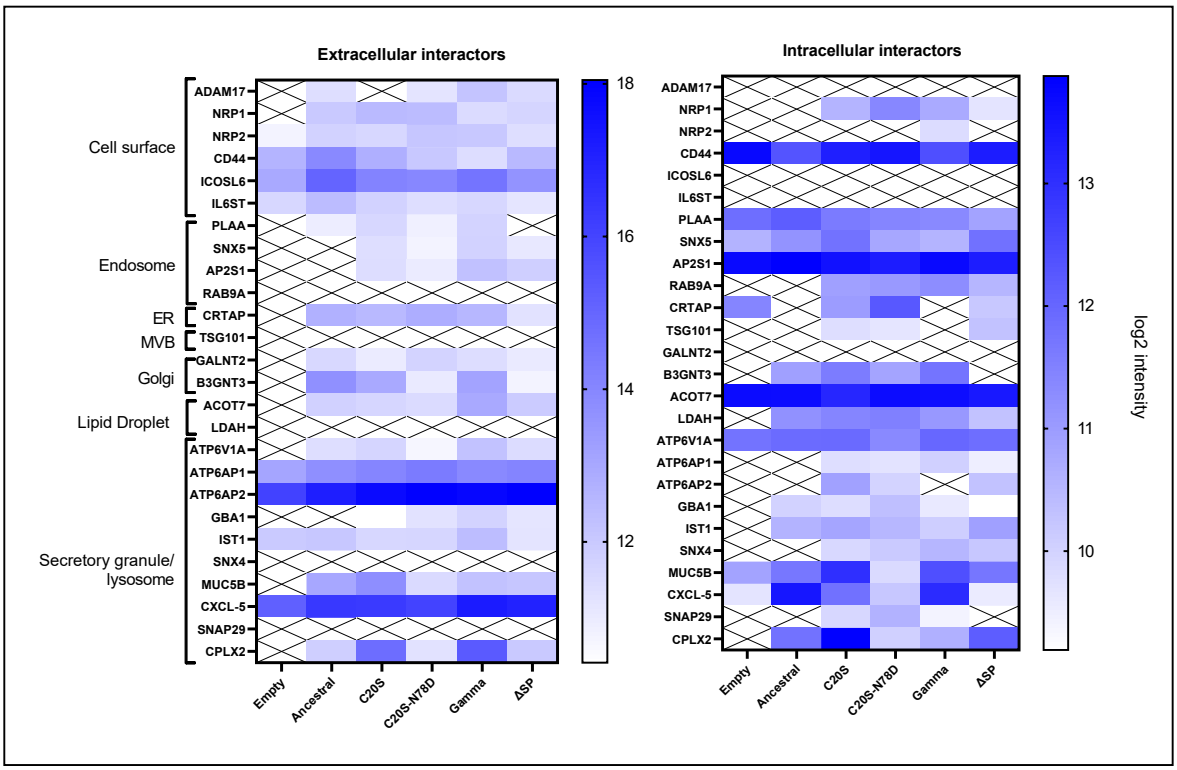


Figure 3.3 Unique or significantly enriched interactors of ORF8 involved in secretion. The heatmaps indicate the interactors of ORF8 that are either unique (not present in control replicates) or exhibit significant fold changes in the intracellular (>2-fold) or extracellular (>1.5-fold) interactome that are identified in both environments and involved in secretion processes. The heatmaps indicate the mean log2 intensity of three biological replicates per ORF8 variant. Subcellular localization was annotated using String.db (v12).

To elucidate potential ORF8 secretion mechanisms, a heatmap was generated for the significant or unique interactors identified that are associated with secretion (**Figure 3.3**). This secretion heatmap and the extracellular interactomes highlight enrichments of endosomal markers such as SNX5, PCSK9, AP2S1 and PLAA. These findings further support the hypothesis that secreted ORF8 could be recycled, explaining the differing ORF8 secretion patterns between newly synthesized ORF8 and steady state ORF8 (**Figure 3.1 and Supp. Figure 3.1A**). Moreover, this heatmap reveals specific protein interactors of ORF8 that are lost for ORF8*ancestral* intracellularly but are identified extracellularly, potentially indicating C20-dependent secretion. These include ATP6AP1/2, NRP1, CD44, CRTAP. Moreover, ORF8*ancestral* shows a specific loss of intracellular interactions with RAB9a, SNAP29 and SNX4. Interestingly, these hits are associated with suggested

secretion routes of Interleukin 1 beta (150). One particular route of IL1B secretion that could support ORF8 release is amphisomal secretion. Amphisomes are products of autophagosome maturation which are at the intersection of the autophagy and endo-lysosomal pathways (151). This could explain the enrichment of endolysosomal recycling markers such as SNX4, GBA1, ATP6AP1/2, RAB9a and SNAP29 and the C20-dependent increased secretion of mature autophagosomes for ORF8*ancestral* in **Chapter 2**.

Given that many of these interactors are not exclusive to a single pathway, it will be important to investigate this route along with other unconventional release pathways, such as exosomal and lysosomal secretion, to determine their involvement in ORF8 secretion. Further studies should aim to distinguish between these potential secretion mechanisms and their relative contributions to ORF8 release.

3.3.4. ORF8*gamma* undergoes defective maturation and unconventional secretion via lamellar bodies

Mass spectrometry confirmed our observations from **Chapter 2** that ORF8*gamma* behaves significantly differently from ORF8*ancestral*. The interactome of ORF8*gamma* shows dramatic changes both intracellularly and extracellularly (**Figure 3.4**). We previously postulated that the E92K mutation could cause a folding deficiency, as it was predicted to be involved in a salt-bridge formation that was important for stabilization of ORF8 dimers (36, 75). This could make homo-dimerization unfavourable or result in an improperly folded protein, potentially causing it to accumulate in the ER. This could stall other processes and induce ER stress. This hypothesis is supported by the enrichment of ORF8*gamma* interactors in chaperonin-mediated unfolded protein folding (FDR: 1.81E-05; p-value: 2.51E-08) or protein translation (FDR: 0.0031; p-value:7.33E-07) (**Table 3.3**). However, we have found that ORF8*gamma* is still capable of being glycosylated and secreted (**Figure 3.1, Supp.Figure 3.1B**) with unique and significant hits of ORF8*gamma* relating to extracellular exosomes (FDR: 4.61E-12; p-value: 5.42E-15). Intriguingly, ORF8*gamma* has an increase in mitochondrial interactors (FDR:1.88E-09: 4.33E-06) and is enriched for the

GO Process “Response to oxygen-containing compound” (FDR: 0.041, p-value: 1.50E-04). These findings suggest that cells expressing ORF8gamma likely experience oxidative stress.

Table 3.3 STRING-pathway enrichment of the ORF8*gamma* extra- and intracellular interactome

Interactome	category	description	FDR value	p-value	genes
Intracellular	UniProt Keywords	Acetylation	4.30E-09	6.36E-12	ATP5D|GOLT1B|NR3C1|AKR7A2|MPDU1|SLC12A2|LIG1|CPT1A|NDUFA9|SOD1|PSMA5|EIF2D|ARL6IP5|PHIP|PDXK|ALDH5A1|SFXN1|H1FX|IDH2|CYB5A|ERGIC3|ZC3HC1|ASCC3|CMPK1|RPRD1B|NOL10|TRIP12|PPP1CB|RPL31|CPS1|STMN1|H2AFY|UQCRB|RPL27|RER1|HYOU1|PSMB3
Intracellular	COMPARTMENTS	Mitochondrion	4.33E-06	1.88E-09	MRPS34|ATP5D|NR3C1|MTFR1|CPT1A|NDUFA9|SOD1|MTERF3|NDUFS4|TMEM70|ALDH5A1|SFXN1|RHOT2|IDH2|CYB5A|MRPL24|RPL23L|CPS1|UQCRB|MRPS21
Intracellular	GO Process	Translation	0.0031	7.33E-07	MRPS34|DRG2|EIF2D|RPL36AL|MRPL24|RPL23L|RPL31|RPL37A|MRPS21|RPL27
Intracellular	GO Component	Extracellular exosome	0.0184	2.80E-04	AKR7A2|SLC12A2|BLVRB|SOD1|PSMA5|PDXK|IDH2|CMPK1|SH3BGRL|TXNDC5|PPP1CB|RPL31|STMN1|RPL37A|H2AFY|RPL27|HYOU1|PSMB3
Extracellular	GO Component	Extracellular exosome	4.61E-12	5.42E-15	MIF|AHSA1|KRT9|NARS|LTBP2|PRDX5|ATP6V1A|CCT6A|OLA1|AKR1B1|FXYD2|CCT3|ALDH1A1|GBA|MAT2B|SRPR|RHOG|SND1|TOR3A|GSTO1|ACTR1A|ACOT7|SHBG|AKR1C3|G6PD|MST4|CCT4|MVP|PLAA|DDT|ALDH7A1|NUDT5|EIF3H|NUCB2|MUC5B|RUVBL2
Extracellular	Reactome Pathways	Association of TriC/CCT with target proteins during biosynthesis	1.81E-05	2.51E-08	CCT6A|CCT3|GBA|CCT6B|NOP56|CCT4
Extracellular	COMPARTMENTS	Vesicle	0.0161	4.89E-05	MIF|VGF|COPB1|NRP1|PRDX5|ATP6V1A|OLA1|AKR1B1|ALDH1A1|PCSK9|GBA|RHOG|SNX5|SHBG|AKR1C2|CPPED1|G6PD|MST4|MVP|PLAA|COPZ1

Extracellular	GO Function	Oxidoreductase activity	0.0119	3.67E-05	TXNL1|PRDX5|AKR1B1|ALDH1A1|CYB5B|AKR1B10|GSTO1|PIR|AKR1C3|AKR1C2|G6PD|ALDH7A1
Extracellular	GO Process	Response to oxygen-containing compound	0.041	1.50E-04	VGF|PRDX5|ATP6V1A|IL18|AKR1B1|CXCL5|PCSK9|ADAM17|GBA|AKR1B10|GCLM|AKR1C3|AKR1C2|G6PD|MST4|PLAA|RUVBL2

Building on our observations from **Chapter 2** that ORF8*gamma* expression induces the accumulation of the specialized secretory lysosomal vesicle, the lamellar body (LB), we aimed to investigate this particular organelle in our interactomes. Although lamellar bodies are poorly described in literature, several studies have reported on their contents (134, 135, 152). Based on these studies, the ORF8-interactomes were assessed for significant enrichment or unique interaction with proteins associated with lamellar bodies. As expected, ORF8*gamma* was particularly associated with proteins important in lamellar body formation. Significant intracellular interactors included Pom121, SOD1, SH3BGRL, STMN1, SLC12A2 (**Figure 3.4**). These protein interactors are detected intracellularly not extracellularly, which fits with their expected localization to the outer limiting membrane of the LB (134).

We previously observed that ORF8*gamma* expressing cells actively secrete glutamine and glutamate (**Supp. Figure 2.2**). It would be valuable to investigate whether this occurs in a LB-dependent manner or in response to ORF8*gamma* induced-oxidative stress. Notably, elevated extracellular levels of glutamate have previously been linked to ARDS (153).

Moreover, we identified unique interactors for ORF8gamma, both intra- and extracellularly, that are linked to ER-resident acetylation. Extracellularly, 47 out of 113 interactors relate to acetylation, as determined using the String.db database (FDR: 7.24e-13). Acetylation, a post-translational modification, can alter the enzymatic activity of both host and viral

proteins, often by directly acetylating lysine residues. The addition of a lysine at position 92 in SARS-CoV-2 ORF8 (E92K) might facilitate acetylation or interaction with Nε-lysine acetyl CoA transferases. ER-resident acetylation has been reported to regulate proteostasis and reticulophagy. Acetylated ATG9 promotes autophagy, while unmodified ATG9 can induce reticulophagy (154). We hypothesize that ORF8*gamma* may induce reticulophagy by hijacking Nε-lysine acetyl CoA transferases. Future research should investigate ER acetylation activity and the status of proteins like ATG9 in the context of ORF8*gamma* expression.

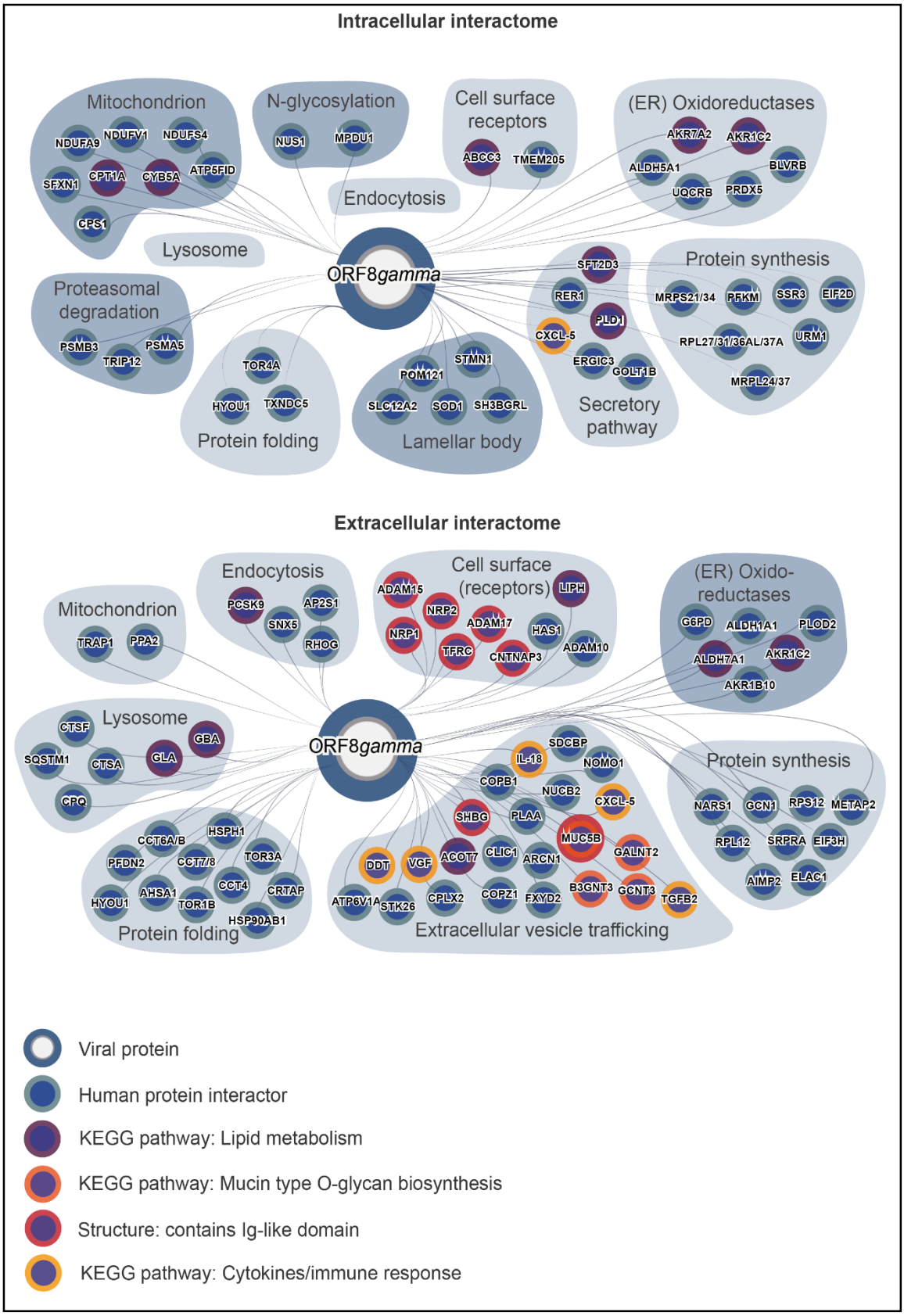


Figure 3.4 The intra- and extracellular interactome of SARS-CoV2-ORF8*gamma* shows increased association with markers of acetylation, oxidoreductases and lamellar body markers. Protein intensities were log2-transformed and analysed in Perseus (v2.1). Uniquely identified protein interactors (not present in all three control replicates) and significantly enriched interactors were included in the visualization. KEGG pathways and subcellular localization were assigned using String.db (v12). Proteins reported to contain an Ig-like domain were highlighted.

3.4. Discussion

In this chapter, we have shown that all variants except ΔSP-ORF8 rapidly get secreted from the cell. Moreover, specific forms of ORF8 have different secretion dynamics. The 35S-Pulse Chase revealed that the early release of ORF8 is predominantly comprised of tetrameric ORF8 (<30 min chase), whereas in steady state, monomeric, di/trimeric and oligomeric ORF8 are detected. Monomeric ORF8 is herein 'N-linked glycosylated.

Our interactome study suggests that secreted ORF8 can bind cell-surface receptors including Neuropilin 1 and Transferrin Receptor 1 for potential re-adsorption and recycling. To confirm the recycling of ORF8 (and MHC-I for ORF8*ancestral*), we will use various inhibitors to target different endocytic pathways. Specifically, genistein, Pitstop2™, and chlorpromazine will be employed to investigate Caveolin-dependent and Clathrin-mediated endocytosis independently, while Dynasore will be used to block both pathways simultaneously. Alternative routes that could be pertinent to investigate, are the CLIC/GEEC pathway for lipid-anchored protein uptake, considering the lamellar body hypothesis and ORF8 interactors such as GPI-anchored CD44 (**Figure 3.3, Supp.Figure 3.9**), or phagocytosis in the context of immune cells.

We did not detect ΔSP-ORF8 extracellularly by Western blot or mass spectrometry, unlike Lin et al. (83). This group, however, reported significantly impaired secretion, which may explain why we were unable to clearly detect it as ORF8 detection is also limited by unique peptides. This could mean that the hits found in the ΔSP-ORF8 extracellular interactome could be valid. Another explanation could be that ΔSP-ORF8 is excluded by Amicon15-100kDa filtration. The structural variants will therefore, similar to ORF8*ancestral* and *gamma* be assessed for >100kDa or soluble release.

Exploring the role of recycled versus newly synthesized ORF8 in the immune response could yield valuable insights. Our western blot and pulse-chase analyses suggest that different forms of ORF8 are released at distinct stages of expression. Given the substantial overlap between the intracellular interactomes of ΔSP-ORF8 and ORF8*ancestral* and numerous cytosolic interactors, we hypothesize that re-adsorbed ORF8 might be able to enter the cytosol. The ΔSP-ORF8 variant could in that case assist in differentiating between interactors associated with re-adsorbed ORF8 and those linked to de novo synthesized ORF8. This differentiation is particularly relevant in light of conflicting reports regarding whether glycosylated or non-glycosylated ORF8 or oligomers are contributing to cytokine storm induction (78, 83, 129).

Regarding de novo synthesized ORF8, a unique interactor, RER1, was identified in all variants except ΔSP-ORF8. Although not directly linked to secretion, RER1's role in retrieving proteins from the cis-Golgi or ERGIC to the ER for quality control may explain the delayed or blocked N-linked glycosylation seen in **Chapter 2** (155). This is consistent with the observation of significant enrichment of the Reactome pathway for 'Golgi-to-ER retrograde transport' in our literature consensus interactome (**Supp. Table 3.2**). Investigating whether ER retrograde transport of ORF8 causes delayed glycosylation or Golgi-independent secretion, could assist in resolving another conflict regarding the unconventional secretion of ORF8 without an associated unconventional secretion signal (82, 83).

For secretion of de novo synthesized ORF8, a couple of unconventional routes will be investigated, such as the previously discussed SNAP29-dependent amphisomal-release pathway which could be utilized in a C20-dependent manner. Moreover, we will investigate VAMP7-dependent secretory ER-phagy (SERP), which is involved in the secretion of ER-phagy receptors ATL3 and RTN4—both identified as interactors of ORF8 (103, 156, 157). Another potential secretion route for ORF8, could be through secretory granules, which

typically release mucus and other lung defense factors. Notably, ORF8 interacts with proteins commonly secreted via these granules, such as MUC5b, PLAA and CXCL-5 (158-160). We aim to validate these interactors and target these pathways using siRNA strategies.

Although we thus have found that intracellular ORF8 expression has the capacity to massively rewire the cell, it is predominantly the secreted ORF8 products, which we think drive the altered immune response. This is supported by a previous publication indicating that ORF8 acts as a 'virokine', a viral protein with cytokine-like activity. It was observed in *live virus* infections, that ORF8 alters the innate immune response differently after multiple cycles of infection in mice, suggesting that it acts differently when cell-to-cell communication and immune cell recruitment has kicked off (117). Where early in infection a mild downregulation was observed for MX1, IFN-β, and ISG15, after multiple cycles of infection these mRNA levels were significantly upregulated in comparison to ΔORF8-infection. This is supported by our preliminary observation in a Thp1 co-culture experiment with rVaccinia-ORF8 or rVaccinia-infected A549 cells (**Supp. Figure 2.4**). Here, we observed that infected lung epithelial cells co-cultured with Thp1, significantly induced their innate immune response in presence of ORF8, with significant increases in ISG56, TLR7 and HLA-B mRNA levels. Perhaps this could be explained by the significant enrichment of proteins involved in leukocyte adhesion, interacting with ORF8; IL18, IL6ST, CD44 (GO Process: Positive regulation of leukocyte cell-cell adhesion; FDR: 0.0065; p-value: 3.8E-6). This would support that this response was driven by secreted ORF8.

In the case of ORF8*gamma* it is indicated that the diverging cellular rewiring and the consequential immune response, might not be directly orchestrated by secreted ORF8 itself, but rather by oxidative stress.

Overall, the interactomes have given indications for the pathways utilized by ORF8 for secretion and how it modulates the cell and immune response. The enrichments and IPs indicate for 2 stages of ORF8 secretion 1) de novo synthesized ORF8 that is secreted following ER-localization; 2) secreted ORF8 that binds the cell surface and can be recycled and secreted through several potential pathways. Identifying the precise mechanisms and domains of ORF8 responsible for these processes is crucial for understanding its role in pathogenesis and exploring potential therapeutic strategies.

Chapter 4 The role of SARS-CoV2 ORF8 in DMV formation

4.1. Introduction

SARS-CoV-2, like other positive-sense RNA viruses, employs sophisticated mechanisms to evade host immune detection during replication. A key strategy is the formation of double-membrane vesicles (DMVs), which serve as replication organelles and shield viral RNA intermediates from recognition by innate immune sensors such as RIG-I-like receptors (61). SARS-CoV2 DMV formation has been suggested to predominantly be orchestrated by 3 non-structural viral proteins; Nsp3, Nsp4 and Nsp6 (161, 162). However, in this chapter the contribution of ORF8 to DMV biogenesis will be studied.

4.1.1. SARS-CoV2 DMV biogenesis

Previous studies have demonstrated that transfection of SARS-CoV2 Nsp3 and Nsp4 alone is sufficient to induce biogenesis of double-membrane vesicles (62, 161, 163). Nsp3 (1945 aa, ~200 kDa), the largest of the three ER-transmembrane Nsps, contains two conserved transmembrane (TM) domains that anchor it to the ER. It has a single luminal loop with both its N-terminus and C-terminus facing the cytosol (161). The protein has multiple domains including the papain-like protease (PLpro), ubiquitin-like domain 1 (Ubl1) and macrodomains I-III (Mac1-3) (164). The PLpro domain not only supports replication-transcription complex (RTC) formation by cleaving the polyprotein during synthesis, but also modulates the immune response by its de-ubiquitinating and de-ISGylating activities (5).

Nsp4 (~44 kDa), a tetraspanning membrane protein interacts with Nsp3 via its first luminal loop with the TM domains of Nsp3. This leads to their oligomerization to form pore complexes (161, 165), which are essential for recruitment of specific host and viral proteins as well as lipids in support of viral replication (60, 161). Additionally, Nsp4 is thought to be essential in anchoring the RTC to the DMV (60). Together, Nsp3 and Nsp4 form the pore complex spanning the double-membrane, a prerequisite for DMV formation (161).

The hexaspanning viral membrane protein Nsp6 (~34 kDa), on the other hand, plays a key role in efficient ER-zippering and positioning of DMV clusters in the perinuclear region (162). Nsp6 is important not only for ER-membrane zippering but also for LD recruitment to the DMVs, facilitating lipid re-modelling and fueling replication (162, 166). Nsp6 achieves the zippering action by homo-oligomerization through its 'C-terminal amphipathic helix, thereby constricting the ER-lumen. The resulting zippered ER-connectors allow for lipid influx but restrict entry of bulky luminal ER-anchored membrane proteins. This restriction is believed to be essential for maintaining the specialized composition of the DMVs necessary for viral replication (60, 162). Additionally, Nsp6 can assist in tethering DMVs to LDs through the Rab18-DFCP1 complex (162).

How the biogenesis of DMVs exactly takes place is poorly understood but is proposed to occur though 3 possible routes; 1) through establishing a reticulovesicular network of convoluted membranes (CMs) and DMVs by bending of ER tubules; or 2) by closure of autophagosomal membranes with lipid channel interactions with the ER; or 3) through exvagination of single-membrane EDEMsomes from ER tubules that fold on themselves to form DMVs (61, 62). These DMVs have an average diameter of 338nm with a luminal space of 18 nm (80,000-90,000nm^2) (167). As described above, Nsp4 can span this luminal space and form a pore complex with Nsp3 with a 2-3nm diameter, allowing for communication between the interior and the surrounding cytosol or other DMVs (161). The DMVs can be found isolated or in contact with the ER through Nsp6-zippered ER connectors (162). The DMVs commonly cluster together and may fuse with one another to form vesicle packets. The clustering and fusion are thought to facilitate the efficient exchange of factors needed for viral replication (60, 168).

4.1.2. DMV formation and the ER stress response

SARS-CoV-2 infection induces significant ER stress due to extensive ER remodelling and the burden of viral protein production. This triggers the unfolded protein response (UPR),

primarily through the IRE1α pathway (89, 169), leading to the upregulation of various ER stress proteins such as FAM134B, RTN3, and BiP. Many of these proteins have been identified as dependency factors in +RNA viral infection, as they contribute to the necessary ER remodelling (103, 170, 171). However, one of the pathways induced during ER-stress recovery is ER-phagy. ER-phagy is the process in which autophagosomal membranes are recruited to the ER to engulf and turnover ER membranes. This presents a potential challenge for virus replication, as it could lead to the degradation of replication complexes, a phenotype seen in **Chapter 5**. RNA viruses are thus expected to employ strategies to evade or disrupt ER-phagy. However, the detailed sequence of events by which +RNA viruses induce UPR, promote ER expansion while preventing ER-turnover and apoptosis, to reorganize the ER for viral production, is poorly described.

4.1.3. ER-phagy & DMV formation: a complex relationship

Considering that DMV formation is postulated to occur in autophagosomal-derived membranes budding from the ER, this led to the hypothesis that DMV formation may depend on ER-phagy dysfunction (62). This dysfunction has previously been linked to SARS-CoV2 ORF8 (103).

Tan et al. demonstrated that ORF8 forms complexes with p62 to sequester ER-phagy receptors ATL3 and FAM134B into p62 condensates (103). It was found that FAM134B can preferentially bind ORF8 over LC3 and be recruited to p62/ORF8 condensates, allowing for increased viral replication. The relationship between SARS-CoV-2 and ER-phagy is however complex. For instance, other studies have shown that ORF3a induces FAM134B-dependent reticulophagy (172).

Another ER-phagy pathway previously linked to SARS-CoV2 replication involves Reticulon 3 (RTN3) and Reticulon 4 (RTN4) (157, 170). These proteins located on the outer layer of the ER membrane, contain a conserved reticulon homology domain (RHD) that allows them to induce curvature in ER tubules. RTN3 is an ER stress protein that can

actively recruit autophagosomal membranes to the ER via its LC3-interacting region (173). RTN3 typically recruits autophagosomal membranes to degrade ER tubules in a FAM134B-independent fashion. Previous studies have shown that RTN3 and RTN4 are specifically recruited by Nsp3 and Nsp4. In the absence of RTN3 or RTN4, replication is impaired, and dsRNA and DMV formation are compromised, whilst the ER remains intact (157, 170). This suggests that RTN3 and RTN4 interaction is instrumental for DMV curvature.

Given these complexities, it is important to investigate ER-phagy dysfunction in *live virus* infection set-ups, to understand the overall contribution of ORF8. This study aims to address this by employing recombinant SARS-CoV2*ancestral* (rSARS-CoV2) and ΔORF8-SARS-CoV2*ancestral* viruses, allowing for direct comparison of virus-triggered phenotypes with and without ORF8. Building on the findings of **Chapter 2 and 3**, which demonstrated that the ORF8 variants differentially impact autophagosomal compartments and the ER, this chapter will further explore the relationship between ER-reprogramming and DMV formation. We have focused on the role of SARS-CoV-2 ORF8 variants in this process, hypothesizing that the increased formation of degradative vesicles and disordered ER associated with ORF8*gamma* expression could lead to reduced DMV formation. It is important to note that the results discussed in this chapter are preliminary and include several areas that end with proposed models for future investigation.

4.2. Methods

4.2.1. Cell lines

For this chapter, the human cervical cancer (HeLa) cell line and human bronchial submucosal glandular (Calu-3) cell line were utilized as model systems. Calu-3 cells were utilized to propagate SARS-CoV2 viruses and the African green monkey epithelial cell line, Vero E6, was used to titrate the viruses. Lenti-X™ 293T cells were used to propagate lenti- and retroviruses. **Table 4.1** describes all the cell lines utilized and generated *in-house* through lenti- or retroviral transduction.

HeLa cells were maintained in DMEM supplemented with 10%TetFBS to prevent leaky expression of the introduced constructs. Calu-3 cells were maintained in cEMEM (10 % FBS, 1% NEAA, 1% Sodium pyruvate, 1% L-Glutamine). VeroE6 cells were kept in 1%FBS-DMEM for titration of viruses. Lenti-X™ 293T were maintained in cDMEM (10%FBS).

Inducible cell lines were treated with 250 ng/mL doxycycline (TakaraBio, Japan) 24-72 hours prior to read-out. This optimal induction range was determined using stably transduced inducible pTetOne-eGFP cells (**Supp. Figure 4.1)**.

Table 4.1 Cell lines used in this chapter

Cell line	Description
Lenti-X™ 293T	Human embryonic kidney cells (TakaraBio) transformed with adenovirus type 5 DNA, that also expresses the SV40 large T antigen. Utilized for lentiviral production.
Calu-3	Human bronchial submucosal glandular cell line (ATCC)
HeLa	Human cervical cancer cell line (ATCC)
Hela-$_{min}$DMV$_{-Nsp3}$ (NSP4)	HeLa cells stable transduced and single clone selected to express SARS-CoV2-NSP4-FLAG. NSP4 is introduced under a doxycycline-inducible promoter TRE3GS.
Hela-DMV$_{-Nsp3}$ (NSP4-6)	HeLa cells stable transduced and single clone selected to express SARS-CoV2-NSP4-FLAG and NSP6-3xFLAG. The constructs are introduced under a doxycycline-inducible promoter TRE3GS.
HeLa-SARS-CoV2-DMV-BioID2 (NSP3-4-6)	HeLa cells stable transduced and single clone selected to express SARS-CoV2-Myc-BioID2-NSP3; -NSP4-FLAG and –NSP-6-3xFLAG. NSP4 and NSP6 are introduced under a doxycycline-inducible promoter TRE3GS. NSP3-Myc-BioID2 is constitutively expressed.

HeLa-SARS-CoV2-DMV$_{min}$-BioID2 (NSP3-4)	HeLa cells stable transduced and single clone selected to express SARS-CoV2-Myc-BioID2-NSP3 and -NSP4-FLAG. NSP4 is introduced under a doxycycline inducible promoter TRE3GS. NSP3-Myc-BioID2 is constitutively expressed.
HeLa-SARS-CoV2-NSP3-BioID2	HeLa cells stable transduced and single clone selected to express SARS-CoV2-Myc-BioID2-NSP3.
VeroE6	African Green Monkey kidney epithelial cell line, used for SARS-CoV2 viral production

4.2.2. Virus production

SARS-CoV2 recombinant viruses were kindly provided by Prof. Sola at the CNB-CSIC (Madrid, Spain)(117). Calu-3 cells were utilized to propagate the viruses.

For each virus, Calu-3 cells were grown to 70-80% confluence in a T175 flask prior to infection at multiplicity of infection (MOI) 0.01. Infection was conducted for 2 hours at 37 °C, 5% CO_2 in EMEM (no FBS). Afterwards the medium was exchanged for cEMEM and the cells were grown for another 72 hours. After 72 hours the supernatant was collected and spun down for 5 min at 400 x *g* to remove cellular debris. Afterwards the viruses were 0.45µM low protein binding syringe (Millipore) filtered to remove mucus. Afterwards the medium was exchanged three times by 100-kDa Amicon Ultra-15 column (Millipore) filtration with 1xGlutamax(Gibco) OptiMEM. At the end of each centrifugation step, approximately 2 mL was left in the top compartment. After three exchanges, the purified virus was transferred to a new tube and the Amicon Ultra-15 column was washed three times by adding Opti-MEM I (1X) + GlutaMAX (Gibco) to the top compartment, pipetting up and down several times on the filter and adding each wash to the tube containing the purified virus preparation. This step was repeated until the volume in the purified virus stock was equal to the original volume of culture supernatant. Purified virus was stored at −80°C in aliquots.

Titres of the purified virus were determined by standard plaque assay. In brief, virus was 10-fold serially diluted in technical duplicate. To a 24-wells plate; 100 µL of each serial dilution was added per well. Vero E6 cells were collected in 5e5/mL in 1%FBS-DMEM of which 500 µL was added per well. The virus-cell mixtures were incubated for 2.5 hrs, afterwhich 500 µL of 1.5%CMC overlay was added. After 48 hours, the overlays were

removed and the cells were once washed with PBS. Afterwards the plaques were fixed and visualized using Amido Black Stain (2mM Amido Black powder, 0.1M Sodium acetate (trihydrate), 6% glacial acetic acid). The stain was incubated for at least 2 hours prior to washing the plates in MilliQ water and counting the plaque-forming units per dilution.

4.2.3. Transfection

Transfection was executed using TransIT-LT1 (Mirius Bio) or Lipofectamine3000 (Thermo Fisher) as transfection reagent. The plasmids used for transfection are described in **Table 4.2**. The inducible NSP4-, NSP6- and empty control plasmids were generated in the pTetOne backbone from TakaraBio using directional cloning with BamHI and AgeI (Nsp6) or AgeI and EcoRI (NSP4) restriction enzymes (New England Biolabs). Please see **Table 4.3. Oligonucleotides** for the primers used. Ligation was performed using DNA Ligation Kit MightyMix (TakaraBio) and plasmids were transformed into One Shot™ Stbl3™ Chemically Competent E. coli (Thermo Fisher). Plasmids were whole-plasmid sequenced prior to transfection.

For production of lenti- and retroviruses, Lenti-X™ 293T cells were transfected using Lipofectamine3000 as described in section **4.2.4 Transduction**.

For the transfection of NSP3 and his-tagged ORF8-variants into HeLa-NSP4-NSP6-cells; Lipofectamine3000 was used according to manufacturer' protocol (1.5 µL Lipofectamine 3000: 1 µL P3000 reagent: 0.5 µg DNA in OptiMEM). Samples were collected at 48 hours post transfection, unless otherwise stated.

Transfection of pLVX-ORF8 variants into the HeLa-DMV-BioID2 cells was performed using TransIT-LT1 to reduce toxicity, as the cells required transfection at 60-70% confluence and to be subjected to doxycycline treatment (250 ng/mL) at 16 hours post transfection. Transfection was executed according to manufacturer' protocol (1.5µL TransIT-LT1 to 0.5 µg DNA in 24-wells plates; or scaled accordingly; prepared in OptiMEM). The cells were collected at 62 hours post transfection for analysis by Immunofluorescence or Transmission Electron Microscopy.

Table 4.2 Plasmids

Plasmid	Description
pTetOne-3xFLAG-NSP6*ancestral*	In-house generated; SARS-CoV2-NSP6*ancestral* 'N-terminally tagged with 3x-FLAG inserted into a pTetOne inducible backbone (TakaraBio) with Blasticidin® resistance
pTetOne-FLAG-NSP4*ancestral*	In-house generated; SARS-CoV2-NSP4*ancestral* 'N-terminally tagged with 1x-FLAG inserted into a pTetOne inducible backbone (TakaraBio) with Zeocin® resistance
pBABE-myc-BioID2-NSP3*ancestral*	Gift from Kyle Roux (Addgene plasmid # 185997 ; http://n2t.net/addgene:185997 ; RRID:Addgene_185997)
pBABE-myc-BirA*-LC3	Gift from Jayantha Debnath
psPAX2	psPAX2 was a gift from Didier Trono (Addgene plasmid # 12260 ; http://n2t.net/addgene:12260 ; RRID:Addgene_12260)
pMD2.G	pMD2.G was a gift from Didier Trono (Addgene plasmid # 12259 ; http://n2t.net/addgene:12259 ; RRID:Addgene_12259)
pCL-10A1	Retroviral packaging plasmid; NBP2-29542 (Novus Biologicals)
pLVX-eGFP	pLVX-EF1alpha-eGFP-2xStrep-IRES-Puro was a gift from Nevan Krogan (Addgene plasmid # 141395 ; http://n2t.net/addgene:141395 ; RRID:Addgene_141395)
pTetOne-empty	In-house generated; Empty control plasmid with Blasticidin® or Zeocin® resistance
pCI-ORF8*ancestral*-6xHis	In-house generated mammalian expression plasmid expressing ORF8*ancestral* with a 'C-terminal 6xHis-tag
pCI-ORF8*gamma*-6xHis	In-house generated mammalian expression plasmid expressing ORF8*gamma* with a 'C-terminal 6xHis-tag
pLVX-ORF8*ancestral*-2xstrepII	pLVX-EF1alpha-SARS-CoV-2-orf8-2xStrep-IRES-Puro was a gift from Nevan Krogan (Addgene plasmid # 141390 ; http://n2t.net/addgene:141390 ; RRID:Addgene_141390)
pLVX-ORF8*alpha*-2xstrepII	Lentiviral construct expressing ORF8*ancestral*; introduction of Q27STOP using Q5® mutagenesis
pLVX-ORF8*gamma*-2xstrepII	Lentiviral construct expressing ORF8*gamma*; introduction of E92K using Q5® mutagenesis

4.2.4. Transduction

Retroviral production

To produce the stable cell lines expressing the myc-BioID2-SARS-CoV2-NSP3 or myc-BirA*-LC3 constructs, retroviruses were produced by transfecting 293T LentiX cells with the retroviral packaging plasmid pCL-10A1 (3µg) and the construct of interest (5 µg). Transfection was performed on 10-cm dishes with 36 µL Lipofectamine™ 3000 and P3000™ reagent (Thermo Fisher, USA), using manufacturer's protocol. After 48 hours, the supernatant was collected, cleared from cellular debris and 0.45uM syringe filtered.

Retroviruses were not titrated, but transduced at Vvirus/Vtot of 1:40 and selected using the selection marker puromycin, unless alternatively stated. Puromycin selection was

performed side-by-side to a non-transduced control. Single clones were seeded using FACS single cell seeding, after the control had reached 100% cell death and at least 3 rounds of puromycin selection had passed (2->5->2 µg/mL). Single clones were screened for construct expression by RT-qPCR and Western Blotting.

Lentiviral production

Lentiviruses were produced in 293T LentiX cells. Transfection was executed on 10-cm dishes with 36 µL Lipofectamine™ 3000, P3000™ reagent and 1µg VSV-G (pMD2.G); 2µg Gag-pol (psPAX2); 3µg target plasmid, using manufacturer's protocol. After 48 hours the supernatant was collected, cleared from cellular debris and 0.45uM syringe filtered.

A pLVX-eGFP plasmid was utilized to estimate MOIs. For all produced viruses, the titre was estimated by measuring WPRE copy numbers by RTqPCR. Using transduction efficiency estimates of pLVX-eGFP on the target cell lines, the MOI was extrapolated. To ensure single introduction of the construct, MOI 0.025 was used to transduce the DMV constructs into Hela wildtype cells. After 2-6 hours of virus addition to the target cell in OptiMEM, the medium was supplemented with 8 ug/mL polybrene to increase transduction efficiency. After 24 hours, OptiMEM was exchanged for cDMEM (10%FBS). Selection was initiated after another 24 hours. For Zeocin® selection, the cells were selected with 200ng/mL Zeocin®, which was added in cold medium and incubated for 1 hr at RT prior to incubation 37 °C, 5% CO_2. For Blasticidin® selection, 2.5 µg/mL Blasticidin® was used. Using a non-transduced HeLa cell line, selection efficiency was monitored. After the control reached 100% cell death at least 1 passage prior, single cell seeding was performed using FACS. Single clones were screened for construct expression by RT-qPCR and Western Blotting.

4.2.5. RT-qPCR

To measure RNA levels, RNA was extracted using the Qiagen Viral RNA Mini kit for extracellular viral genome quantification and the Qiagen RNeasy Mini kit for quantifying intracellular RNA levels. In *live virus* set-ups, the infectious supernatant (SN) was inactivated for 10 minutes at RT in lysis buffer AVL (560 µL per 140 µL SN) supplemented with 1.3% Triton X-100 to ensure viral inactivation. For intracellular RNA extraction, RLT buffer alone could ensure complete viral inactivation. All cell pellets were lysed using 350 µl RLT per <5e6 cells. Extraction was executed according manufacturer's protocol.

The extracted RNA was subjected to RT-qPCR using the One Step SYBR PrimeScript RT-PCR Kit (Perfect Real Time) (TakaraBio, Japan) and the primers mentioned in **Table 4.3**. All primers were designed and validated in-house, except for the SARS-CoV2 Sarbeco E protein primers, which were taken from WHO recommendations (174).

Table 4.3 Oligonucleotides

Purpose	Target	Sequence
RT-qPCR Primers	GAPDH	**FP**: 5'-GGAGCGAGATCCCTCCAAAAT-3' **RP**: 5'-GGCTGTTGTCATACTTCTCATGG-3'
	SARS-CoV2 NSP3*ancestral*	**FP**: 5'- TCTGTGACCGTGAAGAACGG-3' **RP**: 5'- GGTTCACGAAGTGGCTCAGA-3'
	SARS-CoV2 NSP4*ancestral*	**FP**: 5'-ATCGAGTACACCGACTTCGC-3' **RP**: 5'-GGGATTCGTAAGCCACGCTA-3'
	SARS-CoV2 NSP6*ancestral*	**FP**: 5'-TGAAGCACAAGCACGCTTTC-3' **RP**: 5'-CATGATGCGCATGACCCAAG-3'
	SARS-CoV2 ORF8*ancestral*	**FP**: 5'-TCTCGTGTTCTTGGGCATTATC-3' **RP**: 5'-GCAAGGATCATCGACGACATAA-3'
	SARS-CoV2 Nucleocapsid	**FP: '**5-TTACAAACATTGGCCGCAAA-3' **RP** 5'-GCGCGACATTCCGAAGAA-3**'**
	BioID2	**FP**: 5'-TGAAGGAGTGGAACGTGAGC-3' **RP**: 5'-GGTTCTCGAACTCCTTGGGG-3'
	WPRE	**FP**: 5'-CTTCTGCTACGTCCCTTCGG-3' **RP**: 5'-AAGGGAGATCCGACTCGTCT-3'
	Sarbecovirus E protein	**FP**: 5'-ATATTGCAGCAGTACGCACACA-3' **RP**: 5'-ACAGGTACGTTAATAGTTAATAGCGT-3'
Cloning primers	EcoRI-N-FLAG-**NSP4**-AgeI-insert	**FP**: 5'-AAAAGGGAATTCATGGACTACAAAG ACGATGACGACA-3' **RP**: 5'-AAAAGGACCGGTCTACTGCAGCACG GCGCTGGTGATAGA-3'
	AgeI-N-FLAG-**NSP6**-BamHI-insert	**FP**: 5'-AAAAGGACCGGTATGGACTACAAAG ACGATGACGACA

		RP: 5'- AAAAGGGGATCCCTACTGCACGGTG GCCACCTTGATGCA

4.2.6. Western Blotting

To visualize and quantify protein levels, whole cell lysates (WCL) were collected in RIPA-buffer (1% (v/v) Triton X-100, 50 mM Tris-HCl, pH=7.4, 150 mM NaCl, 1 mM EDTA, 0.5% (w/v) sodium deoxycholate) or for *live virus* collection, in RIPA lysis buffer modified with 5mM DTT and 0.1% Sodium dodecyl sulfate (SDS) and EDTA removed. The lysis buffers were supplemented with cOmplete™, Mini, EDTA-free Protease Inhibitor Cocktail (Roche, Switzerland). Infectious supernatant was collected by inactivation in 1% FA for 30 minutes.

The WCL samples were freeze-thawed three times and spun down at 20.000 × g for 10 min at 4 °C to clear cellular debris. The lysates were measured for total protein concentrations and the lysate and supernatant samples were prepared accordingly in non-reducing NuPAGE LDS or in reducing Laemmli SDS sample buffer (Thermo Fisher, USA). Subsequently, the samples were heated to 70ºC for 10 min or 95ºC for 2 minutes respectively, if denaturing conditions were required. The samples were run on NuPAGE™ 4–12% Bis-Tris gels (Invitrogen, CA, USA) and immunoblotted using the indicated antibodies on 0.45 µm LF PVDF membranes (**Table 6.4**). Visualization was performed using Odyssey® Fluorescent Western Blotting, unless otherwise stated.

Immunoprecipitation was conducted using MagStrep ""type3"" XT beads 5% suspension to precipitate interactors of ORF8-StrepII-variants according to manufacturer's protocol. The precipitates were eluted in Laemmli buffer by incubating for 5 min at 95 degrees, prior to standard Western blotting and Coomassie Blue staining.

Table 4.4 Antibodies & Dyes

Antibodies	Mouse α-Beta Actin	MAB8929 (Bio-Techne (R&D Systems), USA)
	Rabbit α-LC3b	2775 (Cell Signalling Technology, MA, USA)
	Rabbit α-Calnexin	2433 (Cell Signalling Technology, MA, USA)
	Rabbit α-SQSTM1/p62	5114 (Cell Signalling Technology, MA, USA)
	Rabbit α-Bip/Grp78	11587-1-AP (Proteintech, USA)

	Rabbit α-Reticulon-3	A302-860A (Thermo Fisher, USA)
	Rabbit α-Reticulon-4	10950-1-AP (Proteintech, USA)
	Rabbit α-Perilipin3	ab47638 (Abcam, UK)
	Mouse α-LAMP2	NBP2-22217 (Novus Biologicals, USA)
	Mouse α-FLAG® (M2)	F3165 (Sigma-Aldrich, USA)
	Rabbit α-StrepII-tag	ab76949 (Abcam, UK)
	Mouse α-BioID2	ab232733 (Abcam, UK)
	Mouse α-Myc-tag	2276 Cell Signalling Technology, MA, USA)
	Mouse α-dsRNA (rJ2)	MABE1134-100UL (Sigma Aldrich, USA)
	Goat α -mouse Alexafluor®488	A-11001 (Abcam, UK)
	Goat α-mouse Alexafluor®647	A-21235 (Abcam, UK)
	Goat α-rabbit Alexafluor®555	A-21428 (Abcam, UK)
	IRDye® 800CW Donkey anti-Mouse IgG	926-32212 (LI-COR, UK)
	IRDye® 800CW Donkey anti-Rabbit IgG	926-32213 (LI-COR, UK)
	IRDye® 680RD Donkey anti-Mouse IgG	926-68072 (LI-COR, UK)
	IRDye® 680RD Donkey anti-Rabbit IgG	926-68073 (LI-COR, UK)
Dyes	Nile Red	N1442 (Thermo Fisher, USA)

4.2.7. Immunofluorescence

Cells were seeded on 24-well glass coverslips. The cells were either transfected and induced as described previously, or infected with rORF8-SARS-CoV2 or ΔORF8-rSARS-CoV2 at MOI 0.5. At indicated timepoints, the cells were fixed with 4% PFA for 15 min for the transfection set-up or 30 min at RT for the *live virus* set-up. The cells were permeabilized using 0.1% Triton X-100 for 10 min and blocked with 10% normal goat serum (NGS) in 0.1% Triton X-100 for 30 min at RT. Cells were then probed with indicated antibodies for 1 hr in 5% NGS in 0.1% Triton-X-100 at RT (**Table 5.3**). Afterwards, if indicated, Nile Red (Abcam) staining was performed according to manufacturer's protocol for 10 min at RT. The coverslips were mounted on glass slides using Fluoroshield DAPI-mounting medium (Abcam, UK). Images were obtained on the ZEISS Airyscan 880 and analysed using ZEISS ZEN Microscope Software (ZEISS, Germany) and ImageJ (v1.54j) software.

4.2.8. Transmission Electron Microscopy

For Transmission Electron microscopy, *live virus*-infected Calu3 cells were prepared using standard TEM protocol, but preceded by a 1-hour fixation using 4%PFA, 2.5%gluteraldehyde in 0.1M PIPES buffer at RT, prior to removal from the BSL3. Proof-of-inactivation was completed for this fixation method and approved to fulfill BSL3 safety regulations.

Calu-3 cells were seeded 48 hours prior to infection. Cells were washed and infected at MOI 0.5 with rORF8-SARS-CoV2*ancestral*, ΔORF8-SARS-CoV2*ancestral* or mock for 24 hours. After 24 hours the cells were visualized by brightfield microscopy, washed and collected by trypsinization. The cells were spun down in complete medium for 5 min at 400 x *g* to inactivate and remove trypsin. The pellets were resuspended in pre-warmed fixative (4%PFA, 2.5%gluteraldehyde in 0.1M PIPES buffer) and incubated for 1hr at RT, followed by 24 hours at 4 degrees, prior to standard processing at the Dunn School BioImaging facility (University of Oxford). Images were obtained on the JEOL 1400 TEM using the Gatan Rio CMOS detector and manually quantitated for amount of double-membrane vesicles and degradative vesicles per cell.

4.3. Results

4.3.1. SARS-CoV2 ORF8 facilitates DMV formation

To investigate the role of ORF8 in SARS-CoV-2 DMV formation, a cell-based model system was developed. HeLa cells were engineered to express the key non-structural proteins involved in DMV formation: Nsp3, Nsp4, and Nsp6 (**Figure 4.1A-B)**. These cells were created through sequential stable transduction to express doxycycline-inducible 'N-terminally FLAG-tagged ancestral NSP4 and NSP6 (**Figure 4.2A-B)**.

To study the effect of ORF8 variants on DMV-formation, Hela-DMV$_{\text{-Nsp3}}$ (Nsp4,6)-cells were used. Single clones were established and transfected with 'C-terminally FLAG-tagged Nsp3 and the 'C-terminally His-tagged ORF8 variants (*ancestral* and *gamma)* using Lipofectamine3000. After 42 hours of induction with 250 ng/mL doxycycline and 50 hours post transfection, the cells were fixed and analysed by immunofluorescence. The cells were stained for Nsp3,4,6 using anti-FLAG(M2) antibodies, and the ER using anti-Calnexin antibodies (**Figure 4.1C)**. Due to ORF8's secretory nature, intracellular staining with anti-His antibodies was unsuccessful without blocking secretion. Confocal microscopy revealed that Nsp3 localizes to the cytoplasm when expressed by itself (DMV no DOX), whereas it co-localizes with Nsp4 and 6 to perinuclear larger structures, indicative of DMVs, upon Doxycycline induction. Moreover, a clear difference in DMV formation can be observed in the presence of ORF8*ancestral* transfection, in comparison to Nsp3 only or Nsp3 + ORF8*gamma.* Quantification of DMVs (FLAG^{+}) and ER-derived compartments (CNX^{+}) per cell was performed on 30-40 cells per condition, by assigning ROIs for FLAG^{+} cells and calculating the abundance, size and mean intensity of DMVs and ER-derived compartments per cell using the 'analyze particles' feature on ImageJ (Pixel size: 0.1-∞). Our results indicated for increased mean signal intensity of DMVs in the presence of ORF8*ancestral*, significant clustering of ER structures in the presence of ORF8*ancestral* and increased DMV sizes in the presence of ORF8*ancestral* but not the -*gamma* variant (**Figure 4.1D-E)**. While not significant, a trend towards reduced number of DMVs per cell when expressing

ORF8 was observed, which could be a consequence of 'increased size' reflecting DMV clustering. These observations suggest that ORF8ancestral may assist at the ER in DMV growth and/or clustering.

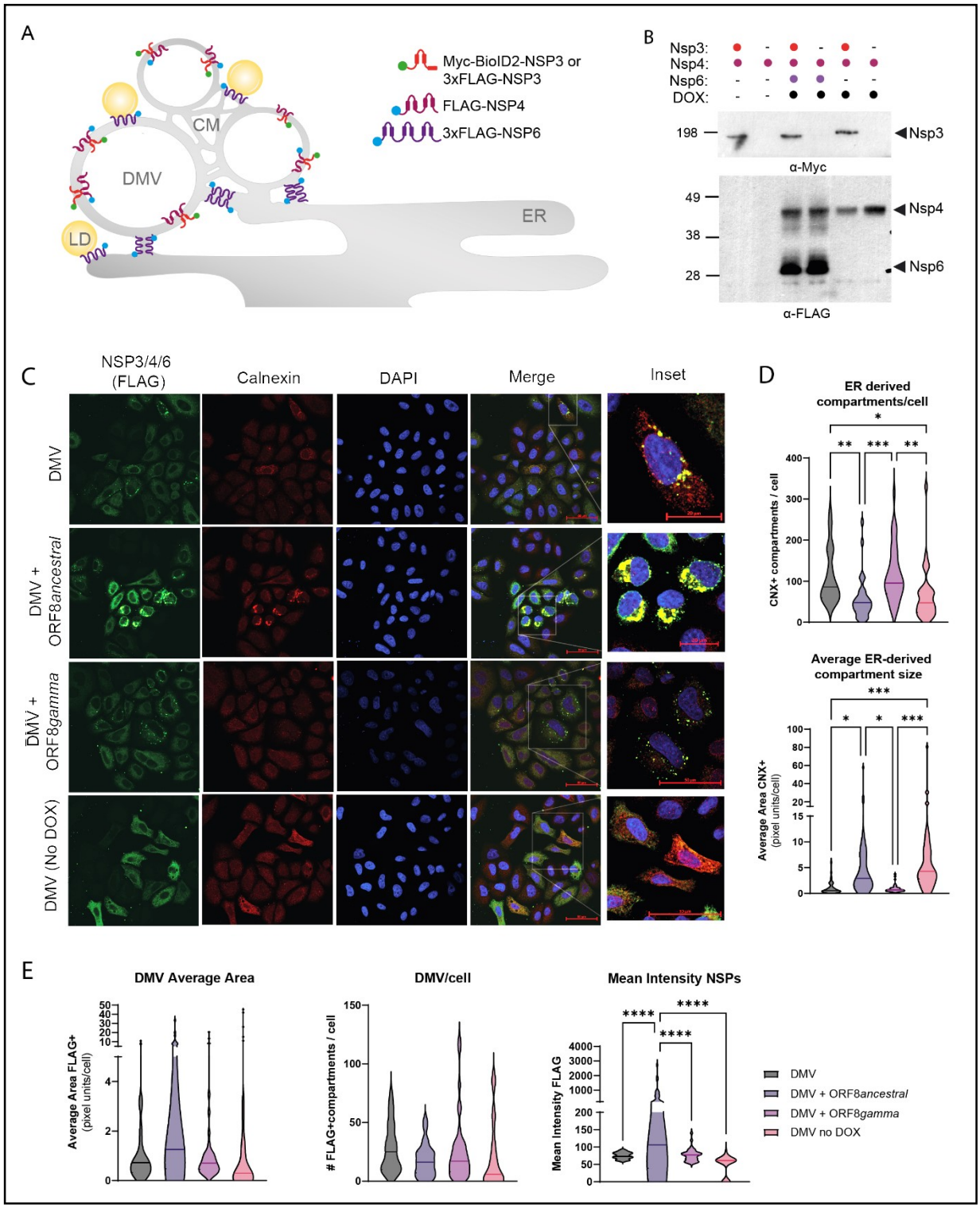


Figure 4.1 SARS-CoV2 DMV formation is impacted by ORF8 variant expression. A) DMV formation model, indicating the constructs used to study DMV formation; 3xFLAG-Nsp3 or MycBioID2-Nsp3, 1xFLAG-Nsp4 and 3xFLAG-Nsp6. B) Expression of the stable constructs in HeLa cells, detected by Western Blotting by staining using α-FLAG and α-Myc. C) HeLa-Nsp4-Nsp6 cells

were transfected with 3xFLAG-NSP3 and the respective 6xhis-ORF8 variant using Lipofectamine3000. The cells were induced with 250 ng/mL Doxycycline (DOX) 8 hours post transfection. After 42 hours the cells were collected and fixed in 4%PFA for Immunofluorescence. Cells were stained for DMVs and ER-derived compartments and the nucleus using anti-FLAG, anti-Calnexin and DAPI respectively. D-E) Quantification of amount of DMVs ($FLAG^+$) and ER-derived compartments (CNX^+) was performed by assigning ROIs for $FLAG^+$ cells (30-40 cells per condition) and calculating the abundance, size and mean intensity of DMVs and ER-derived compartments per cell using the 'analyze particles' feature (Pixel size: 0.1-∞) on ImageJ. Data represents mean ± SD; *P < 0.05; **P < 0.01; ***P < 0.001; ****P <0.0001 (measured by ANOVA followed by Tukey's comparison test.

To improve this experimental set-up and reduce variability associated with transfection efficiency, Nsp3 was stably introduced by retroviral transduction with the constituently-expressing Myc-BioID2-tagged ancestral NSP3 construct (**Figure 4.1A**). Expression levels of all three Nsps were assessed using RT-qPCR using probes targeting BioID2 (Nsp3), NSP4 and NSP6 (**Table 4.3**). Nsp3,-4,-6 introductions were successful for all combinations; Nsp3, Nsp4, Nsp3+4, Nsp4+6; Nsp3+4+6 (**Figure 4.2A**). To study the effect of natural ORF8 variants on DMV biogenesis, the HeLa-SARS-CoV2-DMV-BioID2 (Nsp3-4-6) and HeLa-SARS-CoV2-$_{min}$DMV-BioID2 (Nsp3,4) were utilized. These cells were treated with or without doxycycline to induce Nsp4 and Nsp6 expression. The natural ORF8 variants - ORF8*ancestral*, ORF8*gamma* and ORF8*alpha* were transfected into the DMV-producing cells, using pLVX-ORF8-strepII constructs to allow for detection by StrepII instead of 6xhis and to include ORF8*alpha*. 6 Hours post transfection, Nsp4 and Nsp6 expression was induced using doxycycline treatment (250 ng/mL) and at 48 h.p.t. the cells were collected for analysis by RT-qPCR, Western Blotting, Immunoprecipitation, Immunofluorescence and TEM.

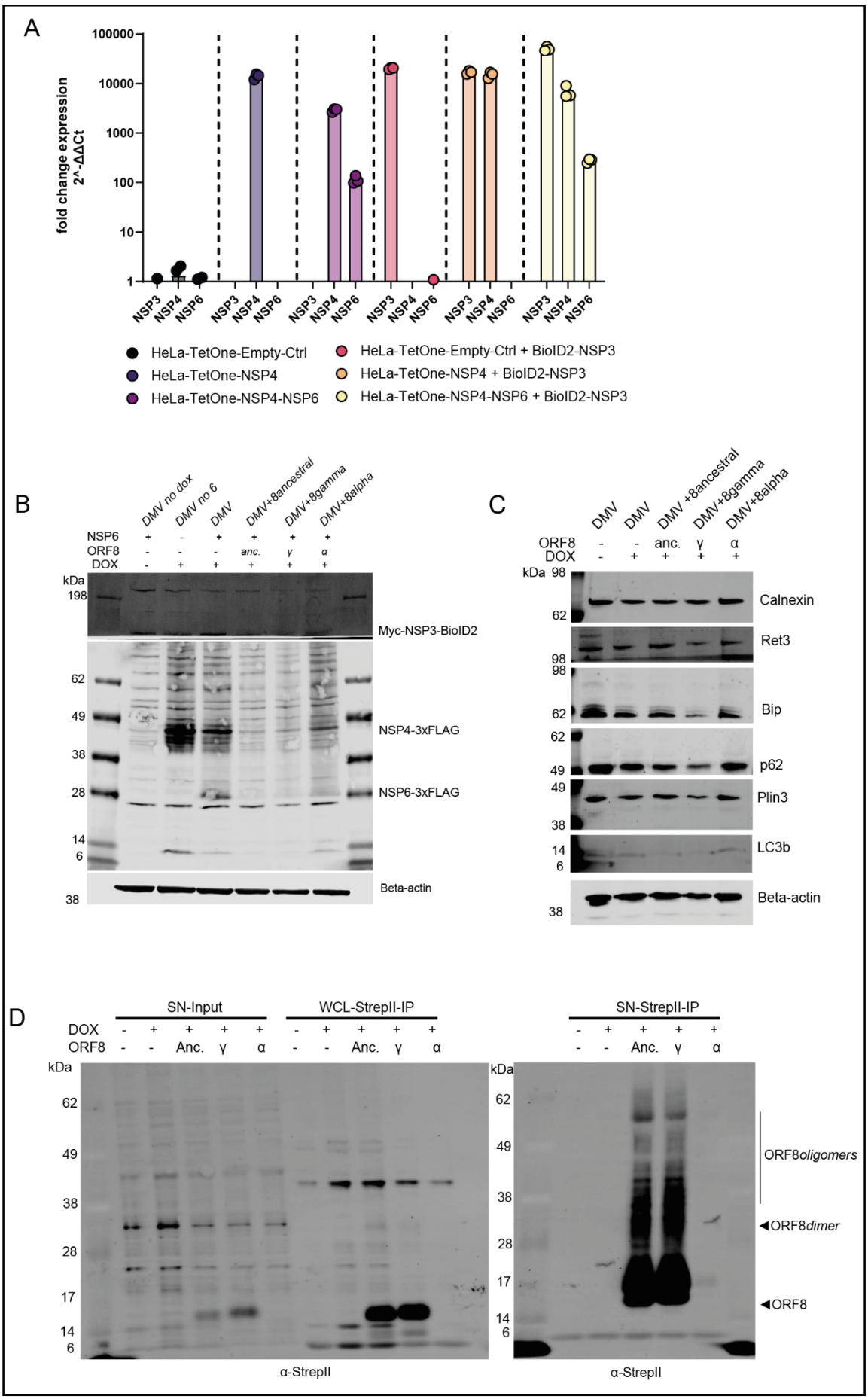

A
fold change expression
2^-ΔΔCt
100000
10000
1000
100
10
1
NSP3
NSP4
NSP6
HeLa-TetOne-Empty-Ctrl
HeLa-TetOne-NSP4
HeLa-TetOne-NSP4-NSP6
HeLa-TetOne-Empty-Ctrl + BioID2-NSP3
HeLa-TetOne-NSP4 + BioID2-NSP3
HeLa-TetOne-NSP4-NSP6 + BioID2-NSP3
B
DMV no dox
DMV no 6
DMV
DMV+8ancestral
DMV+8gamma
DMV+8alpha
NSP6
ORF8
DOX
anc.
γ
α
kDa
198
62
49
38
28
14
6
Myc-NSP3-BioID2
NSP4-3xFLAG
NSP6-3xFLAG
Beta-actin
C
DMV
DMV
DMV +8ancestral
DMV+8gamma
DMV+8alpha
ORF8
DOX
anc.
γ
α
kDa
98
62
49
38
14
6
Calnexin
Ret3
Bip
p62
Plin3
LC3b
Beta-actin
D
SN-Input
WCL-StrepII-IP
SN-StrepII-IP
DOX
ORF8
Anc.
γ
α
kDa
62
49
38
28
17
14
6
ORF8oligomers
◄ORF8dimer
◄ORF8
α-StrepII
α-StrepII

Figure 4.2 ORF8 variant expression impacts DMV component expression. A) Stable transduction of Myc-BioID2-NSP3, 1xFLAG-Nsp4 and 3xFLAG-Nsp6 into HeLa cells was verified by RTqPCR with specific primers directed towards BioID2, Nsp4 and Nsp6 (**Table 4.3**) B-D) HeLa-DMV and HeLa-Nsp4-Nsp3 were transfected with pLVX-ORF8 variants; ORF8*ancestral* (Anc.), ORF8*alpha* (α), ORF8*gamma* (γ) or empty-ctrl using TransIT transfection reagent. After 16 hours the media was changed for 250 ng/mL Doxycycline or control medium. After 48 hours the cells were collected for Western Blotting and Immunoprecipitation by lysing the cells in RIPA-buffer. B) Expression levels of DMV components were determined at 62 h.p.t. by resolving the proteins on SDS-PAGE and staining for Nsp3 using anti-BioID2 and Nsp4 and -6 by anti-FLAG(M2). C) Protein levels of several autophagy, ER stress and lipid markers were assessed; LC3b, p62/SQSTM1, Plin3, BiP and Reticulon-3 (Ret3) were assessed at 62 h.p.t. D) ORF8 transfection efficiency was assessed by immunoprecipitating the lysates and supernatants with anti-StrepII).

Our experiments confirmed that Nsp4 and Nsp6 expression was strictly dependent on doxycycline induction (**Figure 4.1B, 4.2B**). Transfection was confirmed at 48 hours post transfection by intra- and extracellular detection of the ORF8*ancestral* and *gamma* variants by immunoprecipitation using their C' terminal StrepII-tag (*alpha* has a non-functional StrepII-tag due to early stopcodon) (**Figure 4.2D**). At 48 hours post transfection, the cells were stained for DMVs using α-FLAG, α–calnexin (CNX) for the ER and DAPI for nuclear staining. Similar to His-staining, staining for ORF8 by α-StrepII was sub-optimal due to ORF8's secretory nature. Consistent with our previous observations, the network of $FLAG^+$ structures increased when co-expressing ORF8*ancestral* or *alpha* (**Figure 4.3A-B)**. Future studies could benefit from including a dimerization-deficient ORF8 variant for comparison. In contrast, ORF8*gamma* disrupted the organization of these distinct $FLAG^+$ structures, with expression observed throughout the ER and in smaller punctate structures across the cell. This widespread ER-staining could be an indicator for Unfolded Protein Response and ER expansion, processes previously suggested to be induced by ORF8*gamma* in A549 cells in **Chapter 3**.

Intriguingly, Western Blotting revealed that Nsp3, -4 and -6 levels were reduced when co-expressing ORF8*ancestral* or *gamma*. This indicates a potential trade-off between autophagosomal membrane usage for DMV formation and degradative/secretory autophagosomes (**Figure 4.2B**). This is supported by the loss of LC3 signal for both conditions. In contrast ORF8*alpha* expression did not interfere with Nsp4 and Nsp6

expression to the same extent, while allowing for an increase in the FLAG^{+} punctate structures (**Figure 4.2B, 4.3A**).

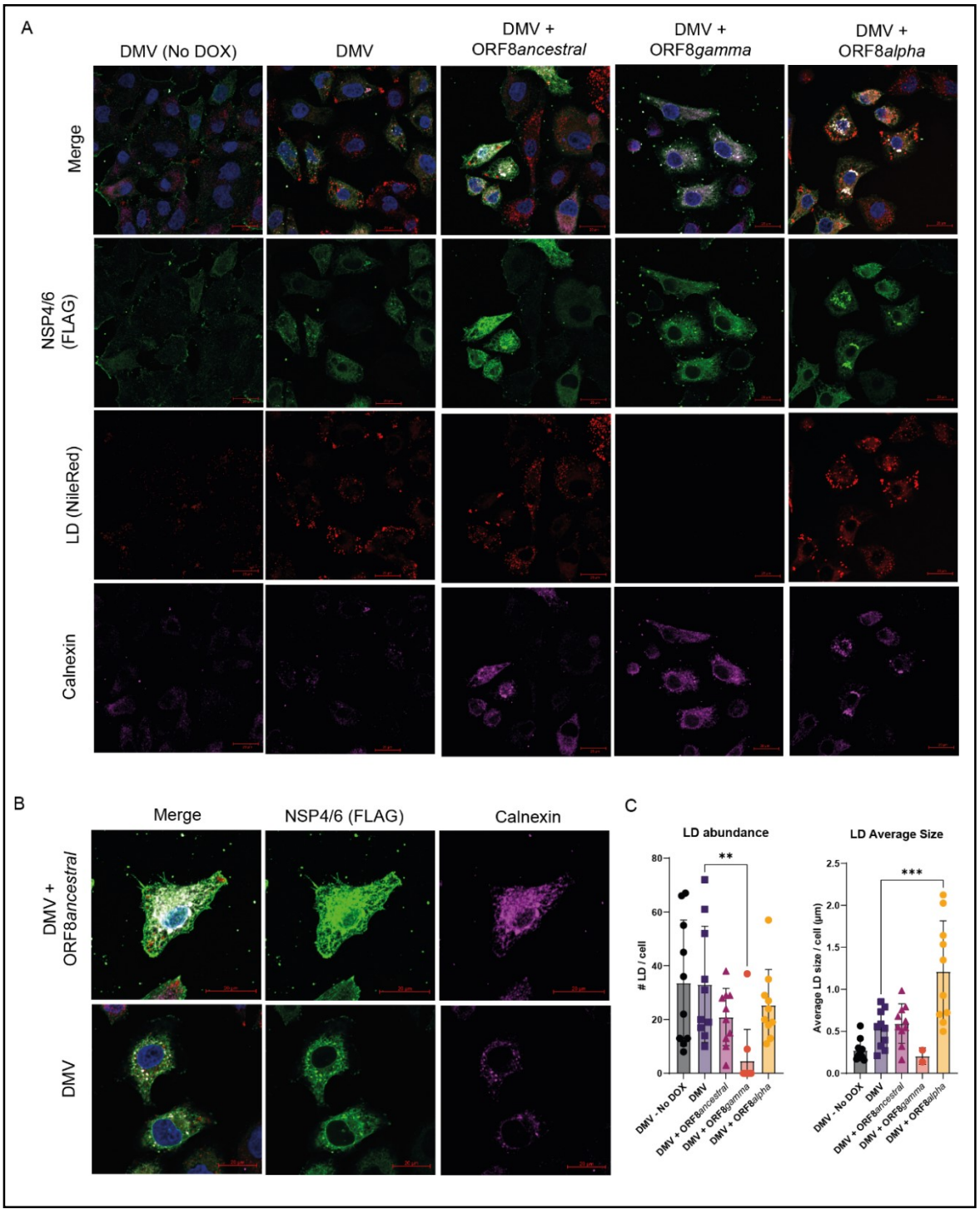


Figure 4.3 DMV formation and LD metabolism affected by ORF8*variant* expression. HeLa-DMV-producing cells were transfected with pLVX-ORF8-StrepII variants; ORF8*ancestral*, ORF8*alpha*, ORF8*gamma* or empty-ctrl using TransIT transfection reagent. After 16 hours the media was changed for 250 ng/mL Doxycycline or control medium. After 48 hours the cells were collected for Immunofluorescence by fixing slides in 4%PFA. A) Cells were stained for DMVs, Calnexin, LDs and the nucleus by using anti-FLAG, -calnexin, Nile Red and DAPI respectively. The slides were visualized on the Zeiss Airyscan 880 using a 40x Objective. B) Representative zoomed in image of DMV network formation in HeLa-DMV cells with and without ORF8*ancestral* expression. C) Quantification of the lipid droplet abundance and average size per cell was performed using ImageJ using the 'analyse particles' plug-in. Quantification was performed by analysing at least 2 images per condition, using ROI manager to selectively investigate cells showcasing calnexin clustering, assumed as 'DMV-producing'; for the non-doxycyline-induced condition any cell was selected. Per

condition, 10 cells were analysed. Statistical significance was determined using Dunnett's multiple comparison test.

Given the importance of lipid droplets (LD) in fueling viral replication and providing lipids for DMV formation, we opted for co-staining with NileRed in this set-up, rather than the suboptimal ORF8 staining (**Figure 4.3A**) (166, 175). Nile Red staining was used to assess LD changes upon ORF8 variant expression. Herein, the read-out was restricted due to the DMV-induction efficiency and the fact that the transfection efficiency of ORF8 could not be validated. Only cells clearly showing ER-reorganization by means of Calnexin clustering, were considered 'DMV-producing' and were included in analysis. This meant that the current preliminary study was limited to 10 cells/condition, limiting statistical testing. Interestingly, ORF8*gamma* transfection does lead to a significant reduction in LDs with a mean of 5 LDs/cell, whereas all other conditions have a mean in the range of 20-35 LDs/cell. This observation marks a significant divergence from ORF8*ancestral* in their contribution to DMV formation. In cells expressing ORF8*gamma*, DMVs were not only more widespread and less distinct compartments, but aberrant lipophagy or lipolysis might also be occurring in these cells. One hypothesis is that ORF8*gamma* induces increased ER turnover, necessitating enhanced lipolysis to accommodate this process. In support of this hypothesis, reduced protein levels of Perilipin-3 (PLIN3) and Reticulon-3 (RTN3) were seen specifically in ORF8*gamma*-transfected DMV-producing cells (**Figure 4.2C**). Another interesting observation is, that ORF8*alpha* expression induces a significant increase in lipid droplet size when producing DMVs, with the average size of LDs increasing to 1.2µm (SD:0.6), whereas in homeostasis LDs are observed around 0.3µm (SD:0.1), and this increases to an averaged 0.5µm (SD:0.2) when producing DMV in presence or absence of ORF8*ancestral*.

To further explore how ORF8 variants could influence DMV growth by facilitating lipid availability, we selectively investigated the intracellular ORF8 interactomes of **Chapter 3** for proteins involved in lipid metabolism (**Supp. Figure 4.2**). ORF8 was found to

predominantly interact with ER-resident lipid metabolic proteins; particularly several lipases. This suggests that ORF8 may be involved with processes leading to the production of free cholesterol and free fatty acids. The presence of key lipases like LIPE (hormone-sensitive lipase) and LYPL1 (lysophospholipase 1), along with phospholipase D1 (PLD1), indicate for a potential role for ORF8 in lipid mobilization and remodelling. This aligns with the hypothesis that ORF8 could be involved in facilitating lipid availability necessary for DMV growth.

In conclusion, the three natural variants of SARS-CoV-2 ORF8 are indicated to have distinct effects on DMV formation. Both ORF8*ancestral* and ORF8*alpha* variants are associated with enhanced DMV network formation and increased DMV growth. In contrast, ORF8*gamma* expression appears to inhibit DMV formation. Specifically, ORF8*ancestral* promotes the expansion of the DMV network, while ORF8*alpha* induces a more pronounced condensation of FLAG+ structures into punctate forms. However, since validating ORF8 transfection efficiency is challenging in these cells due to the nature of ORF8, further investigation using recombinant viruses was essential to understand the precise role of ORF8 in DMV formation.

4.3.2. DMV growth is restricted in absence of ORF8 in *live virus* infection

To confirm that ORF8 contributes to DMV growth and network establishment, rORF8-SARS-CoV2 and ΔORF8-SARS-CoV2 infections were conducted. In this set-up, Calu-3 cells were infected at MOI 0.5 and collected after 24 hours in 4%PFA for immunofluorescence and in 4%PFA, 2.5%gluteraldehyde in 0.1M PIPES buffer for TEM. For confocal microscopy, the cells were stained with anti-LC3 to visualize autophagosomal compartments and anti-dsRNA (J2 clone) to identify replication sites (**Figure 4.4A**). Counterintuitively, a significant increase in replication sites and their cluster sizes was observed in absence of ORF8 (**Figure 4.4D-E)**. However, this comes at the cost of

increased co-localization of autophagosomal compartments with these replication sites, indicative of increased DMV turnover through autophagy (**Figure 4.4B-C**).

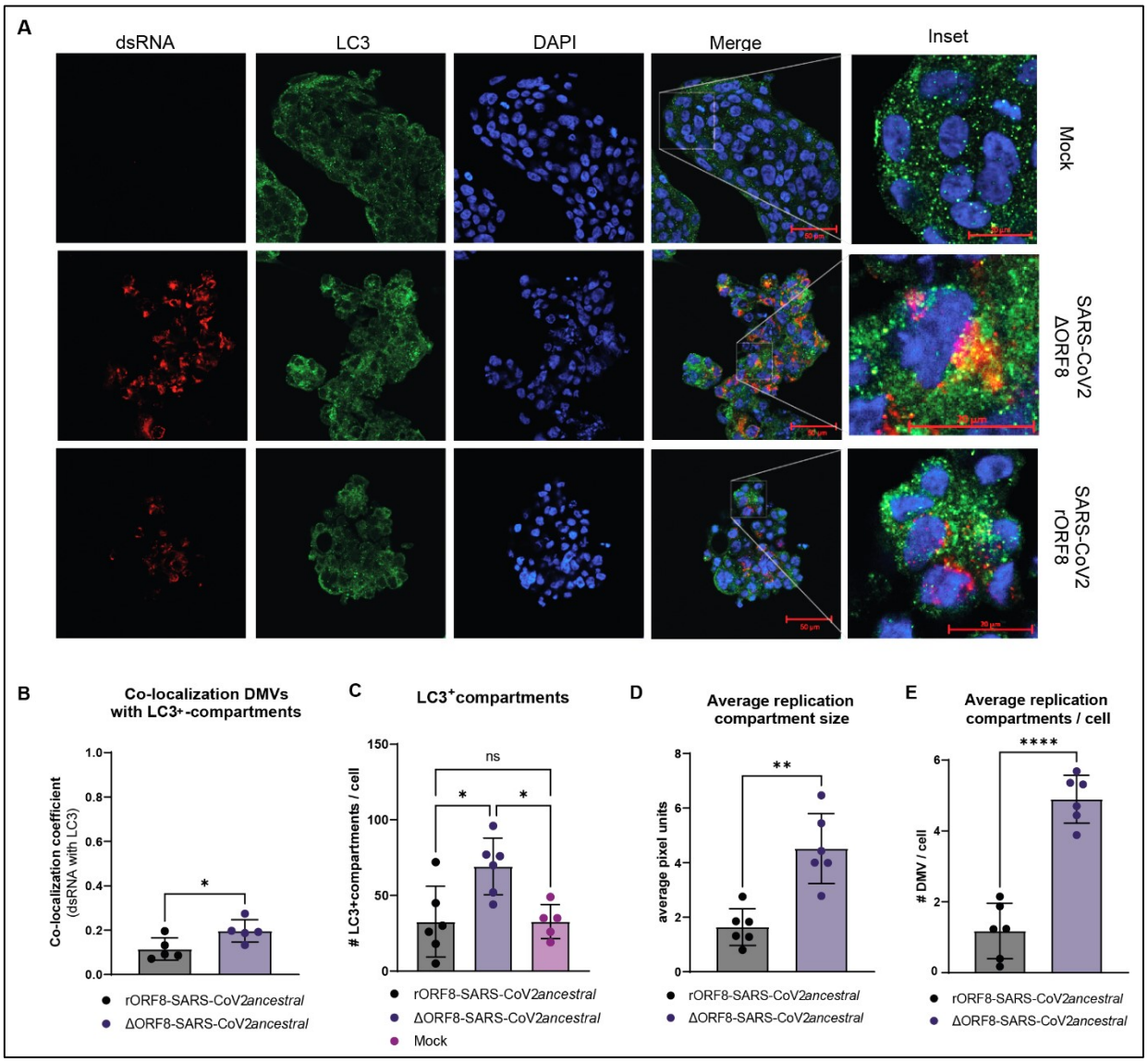


Figure 4.4 DMV formation in overdrive in absence of SARS-CoV2 ORF8. Calu-3 cells were infected at MOI 0.5 with rORF8 or ΔORF8-SARS-CoV2*ancestral* and fixed at 24 hours post infection. A) Cells were stained for replication- and macro-autophagosomal compartments using antibodies directed to dsRNA(red) and LC3(green) respectively. A) Cells were visualized using the Zeiss Airyscan 880 with the 40x objective. B) Co-localization of replication organelles (dsRNA$^+$) with macro-autophagosomal compartments (LC3$^+$) was quantified using JaCoP on ImageJ 1.54f. The co-localization coefficient was determined using 5 images per condition with ±25 dsRNA$^+$ cells per image and statistical significance was determined using standard student T test. C) LC3$^+$-compartments were quantified using ImageJ using the 'analyse particles' plug-in. Quantification was performed by analysing 6 images (±25 cells per image) per condition and statistical significance was determined using Tukey's multiple comparison test. D-E) The amount and average size of the replication compartments was quantified using the 'analyse particles' plug-in using the DAPI staining to determine the amount of cells and dsRNA signal for the amount and size of replication compartment by means of area. Statistical significance was tested using standard student T test.

Transmission electron microscopy (TEM) analysis confirmed and expanded upon the observations we made through confocal microscopy (**Figure 4.5**). TEM visualization of Calu-3 cells, a bronchial glandular cell line, revealed significant morphological changes upon SARS-CoV2 infection in the presence or absence of ORF8. Classical DMVs were observed in both rORF8-SARS-CoV-2 and ΔORF8-SARS-CoV-2 infections. The DMVs displayed typical double membranes with filamentous structures in the lumen, likely corresponding to viral dsRNA. Tight membrane–membrane contact was observed, with multiple DMVs clustering together, as previously described by Klein et al (167) (**Supp. Figure 4.3**). Interestingly, the size of the DMVs is significantly reduced in absence of ORF8. The average size of SARS-CoV2 DMVs is estimated around 80,000-90,000 nm^2, which is observed for rORF8-SARS-CoV2 (median 81377nm^2; 95% CI: 75552 - 88000) (**Figure 4.5B**) (167). In contrast, the average DMV size is reduced to 52441 nm^2 (95% CI: 46000 – 54000) in the absence of ORF8. Moreover, DMVs are increasingly found engulfed by degradative vesicles in ΔORF8 infection (**Figure 4.5A;** Zoom-in second representative cell; not marked in blue to allow for better visualization of the degradative vesicles containing DMVs). This results in the amount of DMVs per cell, excluding DMVs within degradative vesicles, being significantly lower in comparison to rSARS-CoV2 (**Figure 4.5B**). Additionally, this infection leads to other significant morphological changes. The cells displayed increasingly dilated ER (yellow), elongated/fused mitochondria or swollen mitochondria, vacuoles, membrane blebbing and degradative vesicles (blue) (**Figure 4.5 and Supplementary Figure 4.4**). These results indicate that deletion of ORF8 might compromise SARS-CoV2's ability to regulate ER-stress and prevent necroptosis, leading to increased DMV turnover. This could explain why the increase in DMV formation in ΔORF8-rSARS-CoV2 infection observed using confocal microscopy, does not correlate with increased viral production (**Supp. Figure 4.2**). Similarly, it could be hypothesized that the reduced DMV size could hinder viral replication and thus viral production.

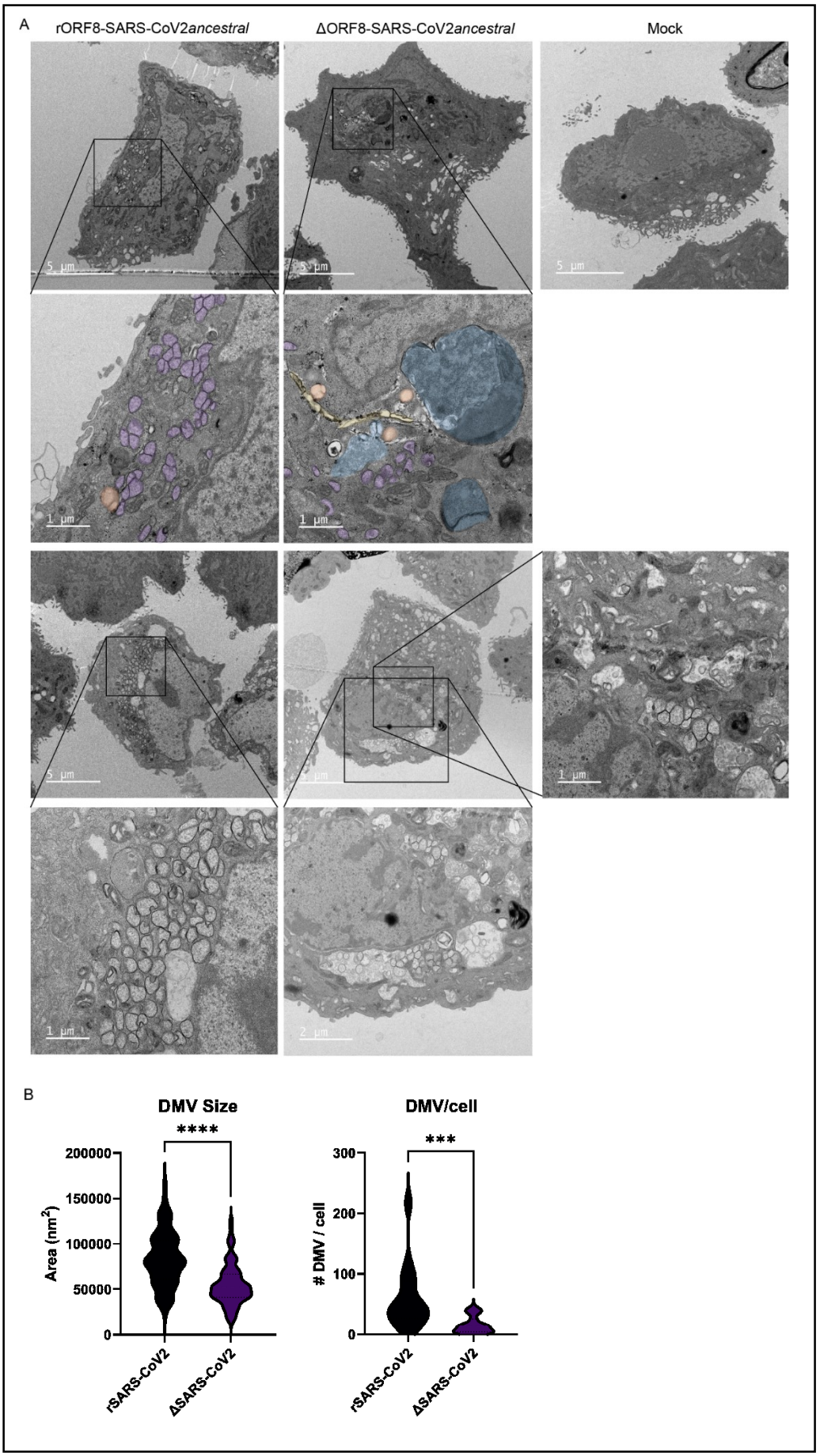

A
rORF8-SARS-CoV2ancestral
ΔORF8-SARS-CoV2ancestral
Mock
5 µm
1 µm
2 µm
B
DMV Size
****
Area (nm²)
200000
150000
100000
50000
0
rSARS-CoV2
ΔSARS-CoV2
DMV/cell
***
DMV / cell
300
200
100
0
rSARS-CoV2
ΔSARS-CoV2

Figure 4.5 SARS-CoV2 DMVs are significantly reduced in size in absence of ORF8. Calu-3 cells were infected at MOI 0.5 with rORF8-SARS-CoV2*ancestral* or ΔORF8-SARS-CoV2*ancestral*. After 24 hours, the cells were fixed in 4%PFA, 2.5%gluteraldehyde in 0.1M PIPES buffer and processed by the Dunn School BioImaging facility (University of Oxford). Images were obtained on the JEOL 1400 TEM using the Gatan Rio CMOS detector. A) Representative images of mock-, rORF8-SARS-CoV2*ancestral*- (rSARS-CoV2) or ΔORF8-SARS-CoV2*ancestral*-infected (ΔSARS-CoV2) cells are shown, highlighting DMVs (purple). These DMVs are commonly found within degradative vesicles in the case of ΔORF8-SARS-CoV2*ancestral*-infection (**Supp. Fig. 4.4**). Some key features such as Lipid droplets (yellow) and degradative vesicles (blue), dilated ER (yellow) are highlighted in the upper representative cells, but left out in the bottom cells. B) Quantitation of the area per DMV was performed on 5-10 different cells per condition, for a total of 100 DMVs per condition. The amount of DMVs/cell, excluding DMVs within degradative vesicles, was quantified for 15 different cells/condition. Statistical significance was assessed using an unpaired Student's t-test followed by a two-tailed Mann-Whitney U test. *P<0.05, **P < 0.01; ***P < 0.001; ****P < 0.0001 (compared to rORF8-SARS-CoV2*ancestral*).

4.3.3. DMV components share interactions with ORF8

To elucidate how ORF8 influences DMV growth and reticulovesicular network establishment, we compared known interactors of Nsp3, Nsp4, Nsp6 with the ORF8-interactome from **Chapter 3**. A comprehensive literature search was conducted to identify validated interactors of SARS-CoV2 Nsp3, Nsp4, Nsp6. The identified interactors were cross-referenced with the ORF8 intracellular interactome data. The proteins that were represented in the ORF8 intracellular interactome are described in **Table 4.5**. The table details the function of each protein and their specific viral partner within the DMV. The table also describes whether a ‘unique’ or significantly changed interaction for ORF8 variants was observed. ‘Unique’ reports protein hits that are absent in all three empty control replicates. Significantly changed interactions are reported when they are larger than 2-fold and p<0.05, unless otherwise stated. The interactions are also represented as heatmap in **Figure 4.6A**. Although no direct interaction with Nsp3,4,6 was reported for BAG3 and COPS4, these proteins were included due to their ‘unique’ interaction with ORF8 and their reported general necessity in DMV formation (176).

Table 4.5 Known interactors of viral DMV components, their function and ORF8 interaction.

Protein	Function	ORF8 interaction	DMV interaction
ARF4	ADP-ribosylation factor 4, involved in vesicle trafficking; suggested by a previous study of our lab to be involved in alternative viral secretion through secretory autophagy (177)	No significant change	Nsp4 (95)
AUP1	Ancient ubiquitous protein 1, involved in the ubiquitin-proteasome system. Shown in our lab to assist in flaviviral lipophagy induction (114, 178).	No significant change	Nsp4, nsp6(179)
ATP5MG	Mitochondrial membrane F-type ATP synthase	No significant change	Nsp6 (126, 180)
ATP6AP1	Vacuolar-type proton ATPase subunit S1; required for luminal acidification of secretory vesicles	Unique hit in intracellular ORF8interactome; all variants except *ancestral*	Nsp6 (79, 126, 180-183); prevents lysosomal acidification
BAG2	Co-chaperone for HSP70 and HSC70 chaperone proteins. Assist in proteasomal degradation of misfolded proteins	No significant change	Nsp4, Nsp6 (96)
BAG3	Co-chaperone for HSP70 and HSC70 chaperone proteins. Component of chaperone-mediated autophagy	Unique hit in ORF8-interactome; all variants	Suggested to be important in β-coronaviral DMV formation and replication (176)
COPS4	COP9 signalosome complex subunit 4; The COP9 signalosome complex (CSN) can regulate autophasome maturation and the ubiquitin-proteasome system	Unique hit in intracellular ORF8interactome; all variants except *ancestral* and *gamma*	SARS-CoV2 Replicon (176)
FXR1	Fragile X mental retardation syndrome-related protein 1, involved in stress granule formation	No significant change	Nsp3 (184-186)
FXR2	Fragile X mental retardation syndrome-related protein 2, involved in stress granule formation	No significant change in interaction between empty-ctrl vs ORF8variants, but Interaction lost for ORF8*gamma*	Nsp3 (184-186)
HSD17B12	Very-long-chain 3-oxoacyl-CoA reductase, involved in long-chain fatty acid elongation in the ER	No significant change, but previously identified as ORF8 interactor in literature (95, 126)	Nsp3 (186)
HSPA5	Endoplasmic reticulum chaperone BiP; plays a key role in protein folding and quality control, part of ER-stress sensor	No significant change, but previously identified as ORF8 interactor in literature (80, 95, 126)	Nsp4 (79, 96)

NOP2	M5C RNA methyltransferase,	Significant increase in interaction for *Anc.; -C20S; -C20S-N78D* and *gamma*	Nsp3-4 (186)
PLAA	Phospholipase A-2-activating protein, involved in synaptic vesicle recycling and macroautophagy	No significant change intracellularly, however found as unique interactor for extracellular ER-signal peptide-sufficient ORF8	Nsp4+6 (183)
RABL3	Atypical small GTPase, Rab-like protein 3, involved in vesicle trafficking	Unique hit in intracellular ORF8interactome; all variants except *ancestral*	Nsp6 (79, 95, 187)
REEP5	Receptor expression-enhancing protein 5. ER-tubule localized protein, forms a complex with **TRAM1**	No significant change	Nsp3 (183)
RTN4	Reticulon-4; together with RTN3 establishes and stabilizes ER tubules	Significant loss in intracellular interaction ORF8*ancestral*-C20S and C20S-N78D	Nsp3-4 (157)
TMEM33	Regulator of the tubular ER network. Can suppress **RTN3/4**-induced biogenesis of ER tubules. Positively regulates unfolded protein response.	No significant change, but previously identified as ORF8 interactor in literature (95, 126)	Nsp3,4 (96, 186)
TMEM41B	Transmembrane protein 41B. Integral ER protein that regulates LD and autophagosome formation with **VMP1**	Loss of intracellular detection for ORF8*ancestral*	Nsp3-4 (188)
TMEM106B	Lysosomal transmembrane protein 106B	Significant but <2-fold change for ORF8*ancestral* and –C20S (1.7)	Nsp3 (183)
TRAM1	Translocating chain-associated membrane protein 1; forms a complex with **REEP5**, essential for translocation of secretory proteins across the ER membrane	No significant change	Nsp3 (183)
VAPB	Vesicle-associated membrane protein-associated protein B; part of the endoplasmic reticulum unfolded protein response (UPR)	Unique hit in intracellular ORF8interactome for C20S, C20S-N78D and ΔSP	Nsp4,6 (179)
VMP1	Vacuole membrane protein 1. Integral ER protein that regulates LD and autophagosome formation with **TMEM41B**	Unique hit in intracellular ORF8interactome for all variants except *ancestral*	Nsp3-4 (179, 188)
ZC3HAV1/ ZAP/PARP13	Zinc finger CCCH-type antiviral protein 1, can bind viral RNA	No significant change	Nsp3(186)

As mentioned in the introduction, the formation of DMVs is generally thought to involve autophagosomal processes. The observation that ΔORF8-SARS-CoV2 displays reduced DMV size and less extensive reticulovesicular network suggests that ORF8 may play a role in autophagophore growth from the ER. However, the specific autophagosomal biogenesis mechanism utilized by these viruses is poorly described. Analysis of shared interactors between DMV components and ORF8 provides insight into potential mechanism of ORF8's influence on DMV formation. As highlighted in **Figure 4.6A**, there is an enrichment for the ER-tubule resident VMP1 lipid scramblase for all variants except ORF8*ancestral*. The scramblases TMEM41B and VMP1 have previously been confirmed as host dependency factors in SARS-CoV2 infection (188, 189), and have been linked to ER-derived autophagophore formation by interacting with the lipid channel ATG2, allowing for phopholipid influx into the phagophores (190). After channelling the lipids through the ATG2 channel, transbilayer transfer is believed to be executed by ATG9 to allow for phagophore growth. ATG9a has indeed been linked to DMVs before as an interactor of Nsp3 and Nsp6, but wasn't identified as an interactor of ORF8 in our study (183). After the phagophore bends through an undescribed route, Vps37a, Tsg101 and Chmp4b are recruited to close the double-membrane vesicle (190). Many of the proteins involved in this process are shared with ORF8, with Chmp4b and Tsg101 also found as unique intracellular interactors for ORF8variants in our interactome studies from **Chapter 3**, making this a plausible route through which ORF8 could influence DMV formation. Particularly as TMEM41B, VAPB and VMP1 dictate lipid availability and influx into the phagophore, ORF8 could potentially stimulate DMV growth through this route.

Given the role of ORF8 in autophagic flux, it is also possible that ORF8 could facilitate DMV formation by allowing a block in ER-phagic degradation, particularly blocking the turnover of ER tubules. Notably, the vacuolar-type proton ATPase ATP6AP1 is found as an interactor for both ORF8 and Nsp6 (**Figure 4.6A)**. ATP6AP1 was previously shown to be essential for the life cycle of SARS-CoV2 and has been directly linked to the prevention of autolysosomal acidification and accumulation of non-digestive

autophagosomes (180, 191, 192). An observation we see solely for ORF8variants ORF8*gamma* and –*alpha* (**Figure 4.4**), whereas we suggest that ORF8*ancestral* induces secretion of these non-digestive autophagosomes. This is supported by the detection of Nsp6 and low levels of Nsp4 in complex with ORF8*ancestral* in the supernatant from lung epithelial cells **(Figure 4.6B)**. Similarly, RTN4 which is suggested as an essential host component of DMVs, was found in complex with ORF8 extracellularly (157, 170). The shared interaction of Rab3L, a rab-like protein involved in vesicle trafficking, of Nsp6 and variants of ORF8, but not *ancestral*, could potentially be the link for alternative trafficking of these non-digestive autophagosomes (79).

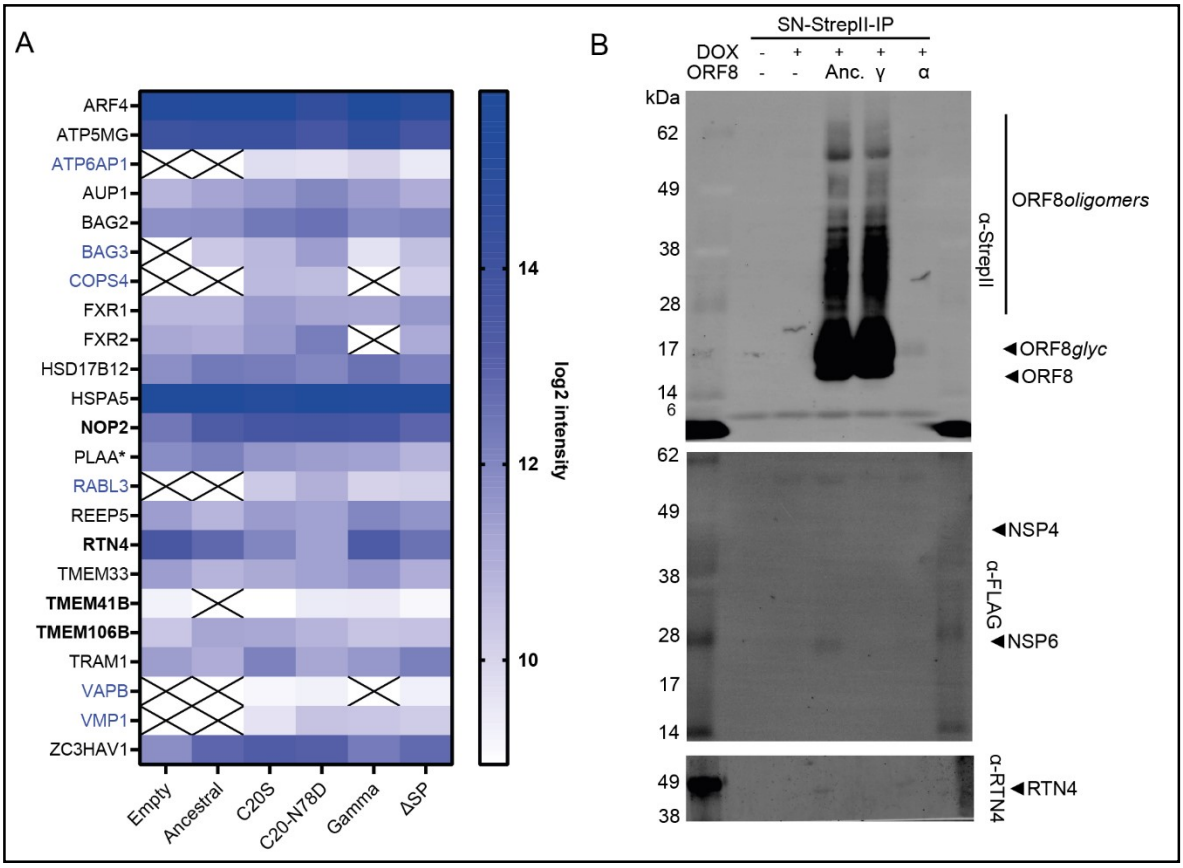


Figure 4.6 ORF8 shares interactors with DMV components allowing for secretion of DMV components in complex with ORF8*ancestral*. A) The log2 intensity of reported SARS-CoV2 DMV interactors is shown using the intensities recorded in ORF8 interactome studies from **Chapter 3**. In bold are DMV components which have a significant phenotype in the ORF8 interactome studies. Blue writing highlights hits that are found as unique interactors of ORF8. The asterix indicates proteins that are found as unique extracellular interactors for ORF8. Significance is determined at log2 FC > 1 or < 1 and $p < 0.05$; 'unique' indicates absence in any of the three empty control replicates. Statistical analysis was performed using Student's T-test in Perseus (v2.1.0.0). B) HeLa-DMV-cells were transfected with pLVX-ORF8*ancestral/gamma/alpha*-strepII using TransIT transfection reagent. After 16 hours the media was changed for 250 ng/mL Doxycycline or control medium. The cells were lysed using RIPA-buffer. ORF8 transfection efficiency was assessed by immunoprecipitating the lysates and supernatants using MagStrep 'Type3' Strep-Tactin Beads,

resolving by SDS-PAGE and staining using anti-StrepII. Interactors were confirmed by staining using anti-FLAG(M2) and anti-Reticulon-4 (RTN4).

4.4. Discussion

It is widely accepted that Nsp3 and Nsp4 are the minimum constituents for DMV-formation, with Nsp6 enhancing this process by means of Lipid Droplet recruitment and membrane zippering (161, 162). However, the contribution of other non-structural proteins to DMV-formation is poorly described. In this chapter, we provide useful insights in how ORF8 contributes to DMV formation. Expanding on previous research that suggested SARS-CoV-2 ORF8 could support DMV formation by subverting ER-phagy by forming p62-ORF8 condensates trapping ER-phagy receptors FAM134B and ATL3 (103). Our findings reveal a more complex role of ORF8 in DMV establishment, indicating that it prevents 1) extensive DMV turnover and 2) assists in DMV formation, growth and reticulovesicular network establishment.

We developed an inducible SARS-CoV2 DMV-producing cell line by sequentially introducing Nsp4, Nsp6 and Nsp3. This system allows for the study of SARS-CoV2 double-membrane vesicle kinetics outside of the Biosafety level 3 containment. The cells were generated with various combinations of these proteins to examine their individual contributions to ER remodelling and DMV establishment. Protein expression was confirmed by RT-qPCR and Western blotting, while DMVs were verified by immunofluorescence, revealing FLAG+ reticulovesicular networks and punctate structures.

When introducing natural variants of ORF8 into the inducible DMV set-up by transfection, both as pCI-6xhis- or pLVX-StrepII-tagged constructs, we observed that ORF8*gamma* was unable to establish typical DMV networks. Whereas, ORF8*ancestral* and ORF8*alpha* were able to orchestrate more extensive reticulovesicular networks than empty-ctrl. This suggests ORF8 most likely functions by mixed disulfide bond interactions in the ER, which would be in line with a paper suggesting that mixed disulfide bonds with ER oxidoreductases are important for ORF8-induced ER stress induction and remodelling (77). We will include our pLVX-ΔSP-ORF8*ancestral* and ORF8*ancestral*-C20S mutants in future set-ups to confirm the necessity of these domains.

Although we thus observed a clear phenotypic change, quantification of the DMVs itself was not possible, as the extensive networks complicated the read-out. For future set-ups it should be considered to have an alternative tag for Nsp6 or to optimize visualization of the DMVs using the tags of Nsp3, Myc and BioID2, instead of FLAG. Similarly, we are not able to validate the efficiency of ORF8 transfection in these cells. Therefore, with Calu-3 cells stably expressing ORF8 variants and recombinant viruses in place, the better approach could be to visualize DMVs by TEM and IF in a *live virus* ΔORF8-rSARS-CoV2 set-up. This would most importantly be more physiologically relevant than our HeLa set-up. In this set-up we could introduce our Myc-BioID2-Nsp3 (or -Nsp6) to enable the verification of identified interactors and their localization to DMVs and ER connectors using close-proximity biotinylation or simple IP. Nevertheless, our DMV set-up remains a valuable and straightforward system for validating host proteins and pathways involved in DMV formation and an improvement to the previous studies using transfection set-ups.

By comparing our interactome data from **Chapter 3** with known DMV interactors, we identified the VMP1-TMEM41b-dependent pathway as a key candidate for DMV formation, with clear stages at which ORF8 could assist (193). **Figure 4.7** depicts our hypothesized model. To address whether this pathway is involved and whether the scramblases-, Tsg101- and Chmp4b-interactions of ORF8 are essential for efficient lipid influx to the DMV, multiple steps will have to be confirmed. The identified shared interactors: VMP1, VAPB, RTN4 should be validated and investigated for their direct contribution to ORF8 function and DMV formation by either siRNA treatment or CRISPR-Cas9 knock-out. It is postulated that DMV growth will be blunted in KD of TMEM41B and VMP1 as both scramblases have already been shown to be essential for viral production (188, 189).

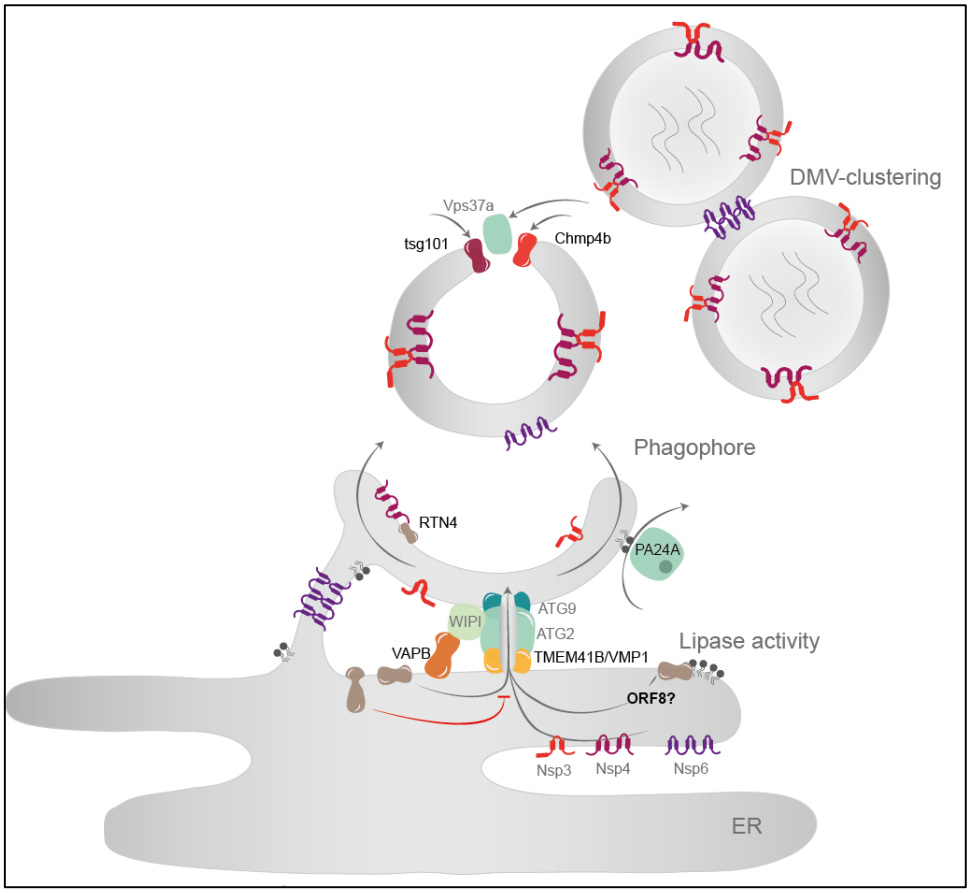


Figure 4.7 Model of SARS-CoV-2 DMV formation and the role of ORF8. This model illustrates the formation of double-membrane vesicles (DMVs) in SARS-CoV-2-infected cells and the supporting role of the viral ORF8 protein. The model is based on prior research detailing VMP1-TMEM41b-dependent phagophore formation (193). According to the model, the phagophore, which serves as a membrane platform for DMV formation, originates from the endoplasmic reticulum (ER). This process involves Nsp6 connectors and an ATG2-dependent lipid channel, facilitating lipid influx necessary for phagophore growth. Nsp3, Nsp4, and Nsp6 are recruited to the phagophore, although the exact mechanisms of this recruitment are not yet fully understood. Within the phagophore, Nsp3 and Nsp4 form a pore, while Nsp6 contributes to DMV tethering. The closure of the phagophore is proposed to be mediated by a tethering complex that includes ESCRT machinery components such as Tsg101, Chmp4b, and Vps37a. Proteins highlighted in bold in the model are identified as interactors of ORF8 in our study, suggesting potential stages where ORF8 may play a supportive role. Additionally, ORF8's interactions with lipase activity proteins, such as LYPL1 and PLD1, might influence DMV growth.

Intriguingly, our *live virus* infection studies initially seemed to contradict our stable expression results, indicating for increased DMV formation by the observation of increased dsRNA staining in ΔORF8-SARS-CoV2 infection. However, TEM revealed that these DMVs were in fact engulfed en masse in large autophagosomes/vacuoles. When excluding these engulved DMVs from quantification, the amount of DMVs per cell and their size (~64% of the expected DMV size) were significantly reduced in absence of ORF8. Similarly, the

general morphological changes in these cells indicated that deletion of ORF8 might reduce SARS-CoV2's ability to control of ER-stress and prevent necroptosis, leading to increased DMV turnover. Curiously, the dsRNA staining does suggest that the RTC was actively replicating and that the dsRNA wasn't degraded in these autophagosomes/vacuoles. Moreover, the observed significant but minimal co-localization of LC3 suggests the possibility of LC3-independent formation of autophagosomes or vacuoles. The expectation is however, that the engulvement of these DMVs does prevent the nascent RNA from efficiently exiting and trafficking for assembly, considering no increase in viral production was seen. These vesicles thus warrant further investigation, as does the potential necroptosis phenotype. This could be investigated by assessing inflammasome activation, Mixed Lineage Kinase Domain-Like Protein (MLKL) phosphorylation and caspase cleavage status.

To conclude, this chapter suggests a multifaceted role of ORF8 in DMV formation, revealing that while Nsp3 and Nsp4 are essential for DMV formation and Nsp6 aids through ER-zippering and lipid recruitment, ORF8 prevents excessive DMV turnover and supports DMV growth and network establishment (**Figure 4.7**). ORF8*gamma* fails to support DMV formation due to increased ER turnover, while ORF8*ancestral* and ORF8*alpha* allow for improved DMV formation. In support, deletion of ORF8 in SARS-CoV-2-infected cells was shown to disrupt viral control over autophagy and ER remodelling, leading to DMV-turnover and stunted DMV growth. Future research should focus on confirming the role of specific shared interactors and investigating therapeutic targets related to ORF8's mechanisms. These insights enhance our understanding of DMV formation and may inform novel therapeutic strategies for COVID-19.

Chapter 5 +RNA virus replication organelle formation requires intricate balance in selective autophagy

5.1. Introduction

Positive-sense RNA viruses require extensive ER-remodelling for their propagation. These viruses have therefore established intricate host modulation strategies to support replication organelle (RO) formation. In this chapter, we will be discussing a host dependency factor, Ube2g2, which we have found to be a key player in the establishment of replication compartments of human coronaviruses (hCoVs) and flaviviruses. This chapter will describe the results published in 2023 in *Nature Communications* under the title “Viral subversion of selective autophagy is critical for biogenesis of virus replication organelles” (178). Similar to the viral factor, SARS-CoV2 ORF8, the host ubiquitin-ligating enzyme Ube2g2 is able to modulate autophagy. Ube2g2 is shown to have dual proviral activity upon flaviviral infection, acting in conjunction with Aup1 to induce lipophagy, and to assist in prevention of Sec62-dependent ER-phagy by degrading ER-stress chaperones (178).

This chapter describes a role for Ube2g2 in hCoV, Zika (ZIKV) and Dengue virus (DENV) infection, with the mechanism of Ube2g2’s proviral activity being described using Zika virus (ZIKV) infection. Zika-virus is a member of the arthropod-borne *Flaviviridae* family, which comprises of other significiant human pathogens such as Dengue virus (DENV), Yellow Fever virus (YFV) and Japanese Encephalitis virus (JEV). These viruses, similar to SARS-CoV2, are human pathogens posing an imminent threat to global health, due to increased human-vector contact and lack of effective FDA-approved antivirals (194). Especially, as the *Aedes* mosquitoes, the primary vectors for both Dengue and Zika viruses, are rapidly expanding their geographical range as a result of climate change, exacerbating the risk of outbreaks (195). For instance, dengue alone is responsible for around 100 million clinically diagnosed cases each year (196). Despite the severe health impact of these infections, there are no approved antiviral treatments for flaviviruses to date, and the effectiveness of existing vaccines, particularly for DENV, remains uncertain. Elucidation of the host cellular

pathways utilized in the viral life cycle for viral success could drive development of therapeutics (194).

To identify dependencies on host cellular pathways, it is key to understand the virus life cycle. The life cycle of Zika virus can roughly be divided into 3 stages; 1) binding and entry; 2) translation and replication; 3) assembly and release, and can be seen in **Figure 5.1** which is adapted from van Leur et al. (194). For binding and entry, Zika virus attaches to the cell surface and subsequently is internalized through receptor-mediated endocytosis. The specific entry receptor for individual members of the *Flaviviridae* family are yet to be identified. However, several attachment factors have been identified such as C-type lectins, dendritic cell-specific intracellular adhesion molecule-3-grabbing non-integrin (DC-SIGN) (197). During endocytosis the virions are exposed to an acidic environment within the endosomal compartments, triggering viral uncoating. This enables the fusion of the viral envelope with the endosomal membrane, to deliver the viral RNA to the cytosol (197, 198). As Zika virus, like all flaviviruses, is a positive strand RNA (+RNA) virus, the 11kb-genome can directly be translated by the host translational machinery. The resulting polyprotein is cleaved by host and viral proteases to generate 3 structural (C, PrM, E) and 7 non-structural proteins (NS1, NS2A, NS2B, NS3, NS4A, NS4B, NS5). The three structural proteins are utilized to assemble nascent +RNA into infectious progeny. Whereas, the non-structural proteins are key to subvert the immune response and orchestrate rearrangements of the intracellular membranes. In concert with host proteins, convoluted membranes and invaginations will be formed in the ER, referred to as the replication organelles (RO), where replication takes place and vesicle packets (VP) in which virions are assembled (199, 200). In the RO, the +RNA is used as a template by NS5 to generate an intermediate negative-sense RNA. This intermediate is then utilized to produce progeny +RNA, which in turn can be utilized for incorporation into nascent virions or can be translated into viral proteins. For production of nascent virions, the +RNA is transported along the rough ER in close proximity to the RO, to the assembly site, the VPs. Here it will be assembled together with

the structural proteins (C, PrM, E). Capsid will be transported to VPs using lipid droplets and can encapsidate the +RNA to form nucleocapsid (201). Whereas PrM and E are recruited to VPs as heterodimers facing the ER lumen. Once PrME trimerizes on the ER, Nucleocapsid can bud into the ER forming the immature virion. Specifically the formation of RO and VPs is tightly orchestrated by the virus, as the RO and VPs are often found juxtaposed to eachother to enable direct encapsulation of the newly synthesized RNA (199, 200, 202, 203).

The ER-internalized immature virions accumulate in ER cisternae and are suggested to be predominantly released through the secretory pathway. During this transport through the trans-golgi network, the virus undergoes maturation. The PrM-E complexes transition into dimers, allowing for furin cleavage of PrM. In this process the virion becomes infectious by the release of the Pr peptide. Increasingly more evidence is found for viral release not solely relying on the secretory pathway. As an alternative exit route for flaviviruses, secretory autophagy is suggested (177, 204). This mechanism is still poorly understood, but could lead to membrane-enclosed viral release, which has implications for pathogenesis.

As DENV and ZIKV require massive reorganizations of ER to form the RO and VPs, interference in these processes might pose therapeutic opportunities (62, 200). Membrane re-organizations are typically driven through changes in post-translational modifications (PTM), such as ubiquitination, that target cellular components for proteasomal or autophagosomal degradation. Therefore, in a previous study from our group, a ubiquitination screen was performed aiming to identify any infection-specific ubiquitination changes (114). Ubiquitination consists of three steps. Firstly, an E1 protein activates a ubiquitin in an ATP-dependent manner. Next, the activated ubiquitin (Ub) is conjugated to an ubiquitin conjugase, E2 protein, through a thioester-link, forming the Ub-E2 complex. Finally, an E3 ubiquitin ligase catalysing the Ub/Ubl transfer onto a lysine residue of the intended substrate, for example a misfolded cytosolic protein, and allowing for mono- or

poly-ubiquitination of the substrate. Dependent on the type of ubiquitin-linkage of the substrate, the fate or function of the substrate is decided. Typically, K48-linkage is associated with proteasomal degradation and K63-linkage with signalling functions, for example.

For this ubiquitination screen, an HA-tagged hydrolysis-resistant ubiquitin probe (HA-UbL73P∗) was utilized to prevent this final step of poly-ubiquitination and be able to screen all mono-ubiquitinated proteins. This probe was delivered to the cytosol prior to infection using perfringolysin O. The cells were challenged with Dengue Serotype 2 (DENV) virus and ubiquitinated proteins were purified by immunoprecipitation using the HA-tag. Upon mass spectrometry analysis of the precipitated proteins, differential ubiquitination profiles were found. As expected many proteins were found specifically ubiquitinated upon infection. Intriguingly, two proteins, Ancient ubiquitous protein 1 (Aup1) and Ubiquitin-conjugating enzyme E2 G2 (Ube2g2) were specifically found to be unconjugated upon infection, where they are predominantly found in mono-ubiquitinated form in homeostasis. It was therefore hypothesized that both proteins serve a proviral role in unconjugated state.

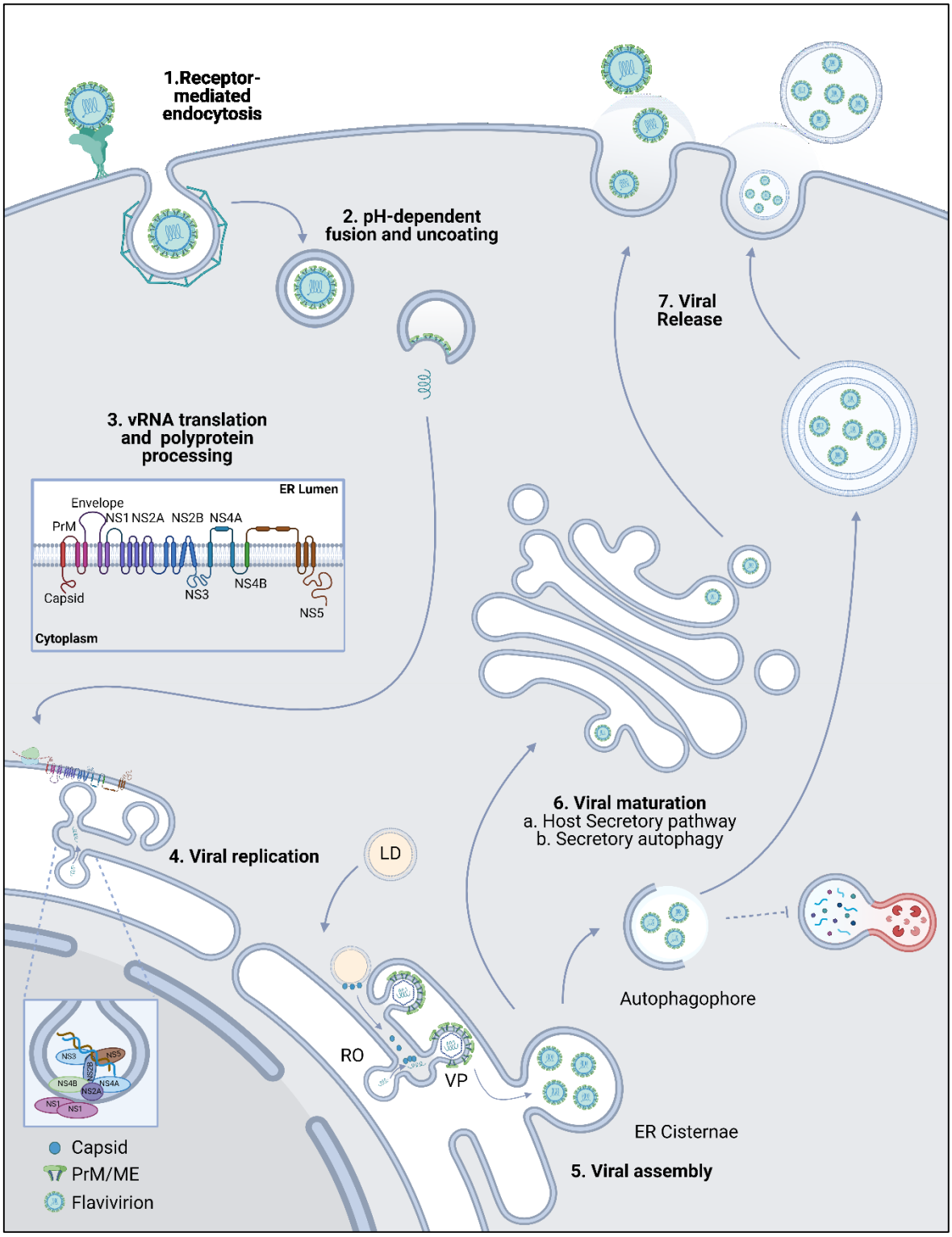


Figure 5.1 The life cycle of Zika virus adapted from Van Leur et al, 2021 (194). Zika virus infection start with the **1.** Internalization of the virion by attachment and receptor-mediated endocytosis. **2.** Under the mildly acidic environment of the endosome, the viral membrane fuses with the endosomal membrane. The virion uncoats and nucleocapsid is released into the cytoplasm. **3.** In the cytoplasm, vRNA can be directly translated by the host translational machinery. The generated polyprotein is inserted into the ER membrane and subsequently cleaved by host and viral proteins to generate 3 structural proteins and 7 non-structural proteins. **4.** These non-structural proteins form the viral replication complex. After initial viral replication, these viral proteins assist in generating Replication Organelles (RO) and vesicle packets (VP) on the ER to shield the virus from immune

sensors in the cytoplasm. In the RO, +ssRNA is generated and transported to another invagination in close-proximity on the ER, the assembly site, the VP. **5.** For virion assembly, structural proteins Pre-M (PrM), Envelope (E) and Capsid (C) protein have to be recruited to these VPs with +ssRNA. For encapsidation of the +ssRNA, capsid protein accumulates and complexes on lipid droplets (LD). When these LDs are recruited to the VPs, capsid can encapsidate +ssRNA and form nucleocapsid. Simultaneously, heterodimers of prM and E are recruited to the VP and trimerize. This allows the VP to bud into the ER, forming an immature virion. **6.** Virions accumulate in ER cisternae before transport through the GBF1-dependent host secretory pathway or through secretory autophagy, during which the virion matures through furin cleavage (205, 206). **7.** Nascent virions can be released as free virions or when transported through secretory autophagy, in membrane enclosed forms derived from autophagosomes. This allows for quasispecies release in a host-derived lipid bilayer (206). Created using BioRender.com.

Aup1 is a type-III membrane protein with dual localization at Lipid Droplets (LDs) and the ER (207). The protein exists predominantly in the mono-ubiquitinated form (114). Aup1 has three identified domains; a ubiquitin binding domain (CUE domain), a Ube2g2 binding domain (G2BR domain) and an acyltransferase domain (207). Particularly, the acyltransferase domain is known to be regulated by ubiquitination and is solely active when the protein is unmodified. Through this acyltransferase activity of Aup1, DENV NS4A was found to be able to recruit autophagosomes to LDs for consumption of the LDs, a process called lipophagy. Viral-induced Aup1-dependent lipophagy was found to be key for efficient viral assembly and egress in DENV infection (114).

In this chapter, the role of its co-factor, Ube2g2 is investigated. Ube2g2 is a soluble E2 protein involved in the Endoplasmic Reticulum–Associated protein Degradation (ERAD) pathway (**Figure 5.2**). ERAD is the process in which misfolded proteins get retro translocated to the cytosol and signalled for proteasomal degradation through ubiquitination. The E2 protein has several identified domains; the RING-binding domain, the G2BR-interacting region and the active cysteine C89, through which it can link an activated ubiquitin. Confirmed E3 partners of Ube2g2 include Hrd1 and autocrine motility factor receptor (AMFR); Hrd1 interacts through the RING-binding domain, while AMFR competitively binds to both the G2BR and RING domains, facilitating the poly-ubiquitination of the substrates (208-210).

For this chapter, it was hypothesized that, as a co-factor of Aup1, Ube2g2 is similarly essential for viral-induced lipophagy as Aup1, but it might also play an extended role in ER stress recovery as one of the key E2 proteins in ERAD. This chapter describes work published in *Nature Communications*: "Viral subversion of selective autophagy is critical for biogenesis of virus replication organelles" (178). The study identifies Ube2g2 as a host dependency factor supporting ZIKV infection through its dual role in (i) triggering lipophagy in conjunction with Aup1 and (ii) restricting ER-phagy upon Xbp1-IRE1α triggered ER expansion by degrading ER chaperones such as Calreticulin (Calr), Sel1L, and Herpud1.

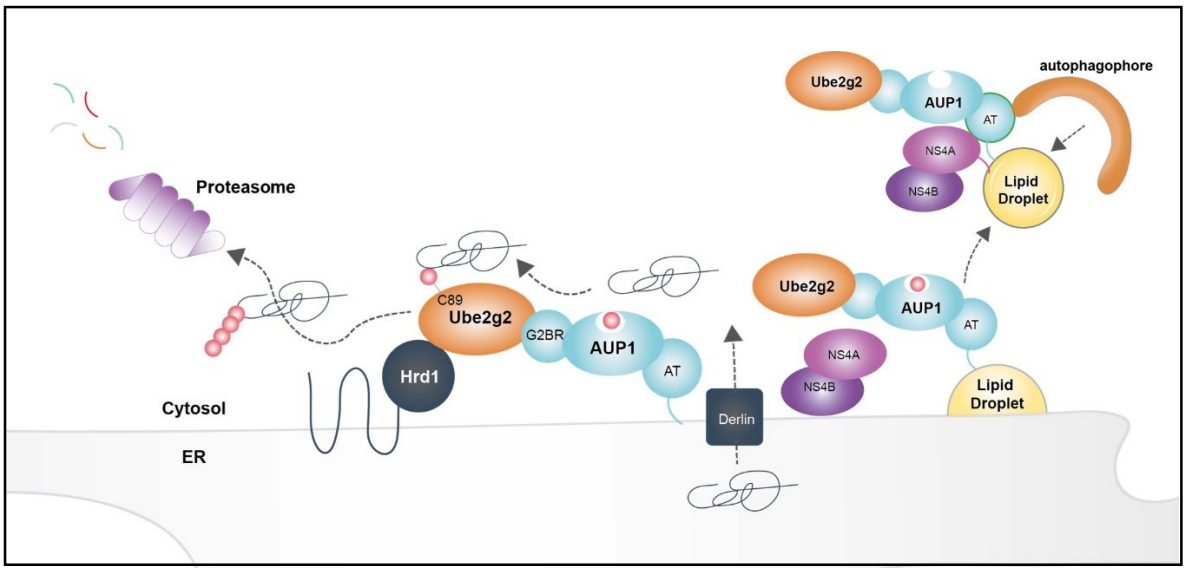


Figure 5.2 Roles of E2 conjugating enzyme Ube2g2. Ubeg2 is part of the ERAD pathway and has previously been confirmed to act in complex with Aup1, a host dependency factor for DENV-induced lipophagy (114, 211). Ube2g2 includes a G2BR-interacting region and a RING-binding domain, with Aup1 interacting through the G2BR-binding domain (211). Confirmed E3 partners of Ube2g2 are Hrd1 and AMFR; Hrd1 interacts via the RING-binding domain, while AMFR can bind competitively through both the G2BR and RING domains (209, 212). For simplicity, the figure depicts only Hrd1-dependent ERAD, in which soluble misfolded proteins are exported to the cytoplasm through Derlin. Ube2g2 then transfers E1-activated ubiquitin (red) via its active cysteine residue, C89, to these proteins (213). In partnership with its cognate E3s, the targeted misfolded proteins will be K48-polyubiquitinated for proteasomal degradation. When Ube2g2 interacts with Aup1, the protein can also be transported as complex to lipid droplets (LDs). On LDs it has been shown that upon DENV-infection it can interact with the NS4A-NS4B complex to prevent ubiquitination and activate the acyltransferase activity of Aup1, leading to autophagophore recruitment to the LD. Subsequently the LDs are hydrolysed through lipophagy. In absence of the Ube2g2-Aup1 complex DENV-induced lipophagy is blocked (114).

5.2. Methods

5.2.1. Cell lines

For this chapter, Human cervical cancer cell line HeLa and Hela-Difluo™ hLC3 cells were utilized as model systems. Knock-out of Ube2g2 was generated using sgRNA sequences described in **Table 5.1** and reconstituted using lentiviral transduction. The in-house generated HeLa-ZIKV-PrME virus like particle (VLP) producing cell line was depleted of Ube2g2 using the siRNA sequences described in **Table 5.2**. African green monkey epithelial cell line, Vero E6, or human diploid MRC5 cell line were utilized to titrate viruses. All cells were maintained in DMEM supplemented with 10%FBS and 1% penicillin and streptomycin and grown at 37ºC, 5%CO_2, unless stated differently. *Aedes albopictus* mosquito clone C6/36 cell line was used to propagate flaviviruses (cultured at 28ºC, 5%CO_2 in 10%FBS-EMEM).

Knock-out of Ube2g2 was established using CRISPR/Cas9. Potential Ube2g2-targeting sgRNA sequences were discovered using previously published protocols. The sgRNAs were designed to target 242-261 bp of Ube2g2 and cloned into the CRISPR/Cas9 vector pX459. The pX459-sgRNA clone was transfected into HeLa cells using FuGENE HD Transfection reagent (Promega, USA). The clones were subsequently selected using puromycin (1.5 to 3 µg/ml in 3 days), single cell diluted and verified by immunoblotting for Ube2g2 deletion.

Reconstitution of Ube2g2 was established by subcloning the lentiviral pcHMWS-IRES-hygromycin backbone to carry Ube2g2 or the site-directed mutated C89K-Ube2g2 cDNA. These constructs were co-transfected with pHKIP115 (HIVgag-pol) and pHKIP131 (VSV-G) into 293T cells using PEI as transfection reagent. After 48 hours the lentiviruses were collected and stably transduced into the knock-out cell lines. These cells were subjected to hygromycin selection (500 µg/mL), single clone selected and verified for reconstitution by immunoblotting for Ube2g2. HeLa Ube2g2-eGFP-Aup1-mCherry cells were similarly

generated by a two-step selection procedure with pseudoviruses generated with the lentiviral pcHMWS-IRES to carry Ube2g2-eGFP and Aup1-mCherry respectively.

Table 5.1 Cell lines used in this chapter

Cell line	Description
293T	Human embryonic kidney cell line (ATCC)
C6/36	*Aedes albopictus* Mosquito cell line (ATCC)
HeLa	Human cervical cancer cell line (ATCC)
HeLa Ube2g2$^{-/-}$	HeLa Ube2g2 knockout cell line (In-house generated)
HeLa rUbe2g2(±FLAG)	HeLa Ube2g2-/- reconstituted with Ube2g2 ± c-terminally flanked FLAG-tag (In-house generated)
HeLa rUbe2g2-C89K (±FLAG)	HeLa Ube2g2-/- reconstituted with catalytically inactive Ube2g2 (C89K) ± c-terminally flanked with a FLAG-tag (In-house generated)
HeLa ZIKV-PrME	HeLa stably expressing ZIKV PrME virus like particles (In-house generated)
HeLa-Difluo™-hLC3	Human cervical cancer cell line stably expressing the RFP::GFP::LC3 fusion protein (Invivogen)
HeLa-Difluo™-hLC3 Ube2g2$^{-/-}$	HeLa-Difluo™-hLC3 Ube2g2 knockout cell line
Huh7	Human hepatoma cell line (ATCC)
MRC5	Human diploid cells (Prof. Mok, HKU-Pasteur Research Pole)
Vero	Monkey kidney epithelial cell line (ATCC)

5.2.2. Virus infections

ZIKV MR766 and NC-14-5132 and DENV2 (16681) were propagated in the C6/36 cell line and titrated using plaque assay in Vero E6 cells by challenging with 10-fold serial dilutions of infectious supernatants for 60 min at 37°C. Cells were subsequently incubated in a semi-solid overlay of methyl-cellulose-based medium (MEM 2.85g, 1.2% (w/v) Methyl Cellulose,1% 1 M HEPES, 1.5% 0.2 M Glutamine, 3% (v/v) 7% NaHCo3, 10% FBS). The virus titre was determined after 6 days of incubation using crystal violet (0.1% (w/v) crystal violet, 20% EtOH, 80% dH2O) to visualize the plaques.

HCoV-229E and OC43 were kindly gifted by Dr Chris Mok. Standard TCID50 assay in MRC5 cells was utilized to determine viral titres. Cells were seeded in 96-well plates and incubated at 37 °C, 5% CO2 until 80–90% confluent and challenged with half-log serial dilutions of virus for 3–4 days. Afterwards, the cells were inspected for cytopathic effects to

calculate the TCID50/mL. Similarly, Influenza A strain A/WSN/33(H1N1) was propagated in MDCK cells supplemented with 0.3% bovine serum albumin (BSA) (Sigma-Aldrich) in the presence of 1 µg/mL tosylphenylalanyl chloromethyl ketone (TPCK)-treated trypsin (Thermo Scientific) and subjected to standard TCID50 testing to determine the viral titre.

5.2.3. Virus kinetics

HeLa wt, Ube2g2$^{-/-}$, rUbe2g2^{WT} and rUbe2g2^{C89K} cells were plated in 12-well plates. Infection was conducted at MOI 2, unless otherwise stated. At the indicated time points, supernatants and lysates were collected. Quantification of viral production was performed by plaque assay and RT-qPCR.

The supernatants were 10-fold serially diluted to quantify viral production by means of plaque forming units/mL (pfu/mL), indicative of infectious particles per mL. The serially diluted samples were added to a Vero cell monolayer and adsorbed for 60 min at 37 °C, 5% CO_2. The cells were washed with PBS and overlaid with methyl cellulose-based medium (10%FBS). After 6 days of incubation at 37 °C, 5% CO_2, the cells monolayers were fixed and stained using crystal violet. The resulting pfu/mL were represented as means ± standard deviation (SD), unless stated otherwise.

The supernatants were simultaneously used to assess extracellular viral RNA levels, by extracting total RNA using the Takara viral extraction kit (Takara Bio Inc., Japan). RT-qPCR was performed by using the Takara One-step SYBR green kit (Takara Bio Inc., Japan) by probing for ZIKV E **(Table 5.2)**. A standard curve was included to determine the pfu/mL. The standard curve was generated using 7 dilutions of 10-fold serial diluted RNA from a virus stock with known titre. Hereby, the recorded Ct value could be translated to estimated pfu/mL values. All samples were measured in technical triplicates. Results obtained from RTqPCR were presented as means ± standard deviation (SD), unless stated otherwise.

The cell lysates were collected in RIPA-buffer (1% (v/v) Triton X-100, 50 mM Tris-HCl, pH=7.4, 150 mM NaCl, 1 mM EDTA, 0.5% (w/v) sodium deoxycholate) to assess viral protein production by Western blotting.

For coronaviruses HCoV-229E and OC43, wildtype and Ube2g2$^{-/-}$ were seeded in 24-wells plated and infected at MOI 0.1. Supernatants were collected at 24 h.p.i. and viral production was quantified by standard TCID50 as described above.

Table 5.2 Oligonucleotides

Purpose	Target	Sequence
RT-qPCR Primers	ZIKV envelope	**FP**: 5'-TTGGGTTGTGTACGGAACCTG-3' **RP**: 5'-GTGCTTTGTGTATTCTCTTGA-3'
	GAPDH	**FP:** 5'-GGAGCGAGATCCCTCCAAAAT-3' **RP:** 5'-GGCTGTTGTCATACTTCTCATGG-3'
	Spliced Xbp1 (set 1)	**FP**: 5'-TGC TGA GTC CGC AGC AGG TG-3' **RP**: 5'-GCT GGC AGG CTC TGG GGA AG-3'
	Spliced Xbp1 (set 2)	**FP**: 5'-GCT GAG TCC GCA GCA GGT-3' **RP**: 5'-CTG GGT CCA AGT TGT CCA GAA T-3'
	Total Xbp1	**FP**: 5'- TGA AAA ACA GAG TAG CAG CTC AGA−3' **RP**: 5'-CTG GGT CCA AGT TGT CCA GAA T-3'
Cloning primers	rUbe2g2	**FP** (no-FLAG): 5'-ATATGGATCCGCCACC ATGGCGGGGACCGCGCTCAAG-3' **RP:** 5'-CACGCTCGAGTCACAGTCCCAGAGACTTCT GGACGATC-3'
sgRNA	ube2g2_A1_s	CACCG-GTTGGGATGAAACATCTCAC
	ube2g2_A1_a	AAACGTGAGATGTTTCATCCCAACC
siRNA	siRNA-CHMP4	L-018075-01-0020 (SMARTpool; Horizon, UK)
	siRNA-Sec62	L-010218-01-0020 (SMARTpool; Horizon, UK)
	siRNA-Ube2g2	L-009095-00-0020; L-009095-00-0020 (SMARTpool; Horizon, UK)
	siRNA-NT	A-001206 (SMARTpool; Horizon, UK)

5.2.4. Western Blotting

To visualize protein levels by immunoblotting, lysates collected in RIPA-buffer (1% (v/v) Triton X-100, 50 mM Tris-HCl, pH=7.4, 150 mM NaCl, 1 mM EDTA, 0.5% (w/v) sodium deoxycholate) were freeze thawed three times and spun down at 18,624 × g at 4 °C to clear

cellular debris. The lysates and supernatants were measured for total protein concentrations and the samples were prepared accordingly in NuPAGE LDS sample buffer. Subsequently the samples were run on NuPAGE™ 4–12% Bis-Tris gels (Invitrogen, CA, USA) and immunoblotted using the indicated antibodies (**Table 5.3)**.

Table 5.3 Antibodies & Dyes

Antibodies	Rabbit α-Aup1	Ab101984 (Abcam, UK)
	Rabbit α-Ube2g2	Ab174296 (Abcam, UK)
	Rabbit α-Hrd1	LS-C668919 (LSBio, WA, USA)
	Rabbit α-Herpud1	Ab150424 (Abcam, UK)
	Rabbit α-Hsp70	10995-1-AP (Proteintech, USA)
	Rabbit α-Fam134b	61011 (Cell Signalling Technology, MA, USA)
	Rabbit α-Gp78	ab101284 (Abcam, UK)
	Rabbit α-Bip	C50B12 (Cell Signalling Technology, MA, USA)
	Rabbit α-LC3b	2775 (Cell Signalling Technology, MA, USA)
	Mouse α-Ubiquitin	Ab7780 (Abcam, UK)
	Mouse α-GAPDH	#2118 (Cell Signalling Technology, USA)
	Mouse α-4G2	In house made
	Rabbit α-Capsid	GTX133317 (GeneTex, USA)
	Rabbit α-prM	GTX133305 (GeneTex, USA)
	Rabbit α-NS1	GTX133307 (GeneTex, USA)
	Rabbit α-NS2B	GTX133308 (GeneTex, USA)
	Rabbit α-NS3	GTX133309 (GeneTex, USA)
	Rabbit α-NS4A	GTX133704 (GeneTex, USA)
	Rabbit α-NS4B	GTX133311 (GeneTex, USA)
	Rabbit α-NS5	GTX638132 (GeneTex, USA)
	Goat α-Rabbit Texas Red®	Ab6719 (Abcam, UK)
	Goat α -mouse Alexafluor®488	Ab150117 (Abcam, UK)
	Goat α-rabbit Alexafluor®488	Ab150077 (Abcam, UK)
	Goat α-mouse Alexafluor®647	Ab150119 (Abcam, UK)
	Goat α-rabbit HRP	7074 (Cell Signalling Technology, USA)
	Goat α-mouse HRP	Ab97040 (Abcam, UK)
Dyes	CytoPainter ER Staining Kit – Green Fluorescence Hoechst 33342 Nuclear Stain (included in the ER staining kit)	Ab139481 (Abcam, UK)
	Nile Red	N1442 (Thermo Fisher, USA)
	Octadecyl rhodamine B (R18)	O246 (Thermo Fisher, USA)
	BODIPY™ 493/503	D3922 (Thermo Fisher, USA)
	BODIPY® 558/568 C12	D3835 (Thermo Fisher, USA)

5.2.5. R18 fusion assay

Pre-labelling of Zika virus with octadecyl rhodamine B Chloride (R18) was executed by incubating MR766 virus or control medium with 1:1000 2x R18 dye (Thermo Fisher, USA) for 1 hour on ice. Subsequently, the residual dye was cleared by ultracentrifugation at 28000 rpm for 1 hour with a 25% sucrose cushion. The labelled virus or control media were carefully re-suspended on ice for 1 hour.

The labelled virus and control medium were incubated at MOI100. This MOI is based on the titre determined prior to labelling. Viral attachment was synchronized by incubating for 1 hour at 4°C, before incubating for 1 hour at 37°C. The cells were washed, trypsinized and fixed in 4%PFA after 1 hour to proceed with analysis using flow cytometry (Attune NxT, Invitrogen). The gating strategy composed of gating on SSC, FSC followed by measurement on the YL1 Emission filter (585/16nm) for read-out of the R18 signal. The %-$R18^{+}$ -population in $Ube2g2^{-/-}$ and wildtype HeLa cells was analysed using FlowJo (OSX64-10.5.3.). To confirm the flow cytometric results, viral internalization was visualized using confocal microscopy. For this set-up, the wildtype and $Ube2g2^{-/-}$ cells were infected at MOI400 for 1 h at 4 °C and fixed after 2.5-hour incubation at 37 °C post infection. The fixed cells were stained with Hoechst staining (Thermo Fisher) for 15 min at 37 °C and observed under the LSM confocal microscope.

5.2.6. Luciferase-based replicon assay

Dr. Chengfeng Qin (Beijing Institute of Microbiology and Epidemiology) kindly provided the luciferase reporter replicon plasmid utilized in this assay. The ZIKV Renilla Luciferase replicon was transcribed using the Ribomax T7 RNA polymerase kit (Promega, USA) and purified using Takara MiniBEST Universal RNA extraction kit (Takara Bio Inc., Japan). The purified replicon was transfected into wildtype and $Ube2g2^{-/-}$ HeLa cells using Lipofectamine 3000 (Thermo Fisher, USA). These cells were seeded 24 hours prior to transfection in 24-wells plates and washed with PBS before transfection. Lysates were collected at the indicated timepoints in lysis buffer prepared as described for the Renilla Luciferase Assay

system (Promega, USA). The luciferase expression was measured in quadruplicate for each condition.

5.2.7. Pulse Chase assay

Cells were collected at indicated timepoints post infection, were trypsinized and starved for 30 min in cysteine/methionine-free DMEM. Afterwards the cells were labelled for 10 min at 37ºC with 10 mCi/ml [^{35}S]methionine/cysteine (EXPRE^{35}S^{35}S Protein Labeling Mix, [35S]-, 2mCi (74MBq), 50mM Tricine (pH 7.4), 10mM 2-mercaptoethanol, Revvity,UK) and chased for the indicated time points. At each time point, supernatant aliquots were taken, the reaction was stopped with cold PBS. Subsequently, the cells were lysed in Tris buffer containing TX-100 and pre-cleared agarose beads for 1 hour at 4ºC. Immunoprecipitations were performed with the indicated antibodies for 3 hours at 4ºC with gentle agitation. Sample elution was performed by heating in reducing (Laemmli) or non-reducing sample buffer (LDS) as indicated. The samples were subjected to SDS-PAGE and visualized by autoradiography.

5.2.8. Immunofluorescence

Cells were seeded on 24-well glass coverslips and infected with ZIKV at MOI 5. At indicated timepoints the cells were fixed with 4% PFA for 30 min at RT. The cells were permeabilized using 0.1% Triton X-100 for 5 min and blocked with 5% normal goat serum in 0.1% Triton X-100 for 1 h at RT. Cells were then probed with indicated antibodies for 1 hr at RT. Nuclei were stained with either DAPI or Hoechst stain (**Table 5.3)**. The coverslips were mounted on glass slides and visualised using Carl Zeiss LSM confocal microscope. Images were analysed using ZEISS ZEN Microscope Software (ZEISS, Germany).

5.2.9. TEM

Transmission Electron Microscopic (TEM) pictures were prepared and obtained by the Electron Microscope Unit (Department of Pathology, HKU). HeLa wildtype and Hela Ube2g2$^{-/-}$ cells were seeded at a cell density of 1.5 x 10^6 in 10-cm dishes and infected with ZIKV at MOI 5. After 1-hour incubation at 37°C, the cells were washed and incubated in full

DMEM medium (10% FBS) for 24 or 72 hours. At each timepoint the cells were collected by gently scraping cells of the dishes and fixing in 1:10 v/v of 2.5% glutaraldehyde in 0.1M sodium cacodulate-HCl (pH7.4) overnight at 4°C. As controls, two samples were collected at 24 hours that were subjected to control media rather than ZIKV.

5.2.10. VLP release assay

To assess maturation and release of Zika viral particles, the in-house generated HeLa-ZIKV-PrME cell line was used. In the knock-down set-up, 2e6 cells were seeded in duplicate on 10-cm dishes. The cells were transfected 24 hours post seeding with either DsiRNA targeting Ube2g2 or scrambled non-targeting DsiRNA (TriFECTAa® RNAi Kit, Integrated DNA Technologies, USA). DharmaFECT™ (Horizon Discovery, UK) was used as per manufacturer's protocol to conduct these transfections. At 24 and 48 hours post transfection, complete medium containing FBS was changed to OptiMEM for an additional 24 hours, to allow for VLP accumulation in the supernatant. At 48 and 72 hours post transfection, the supernatant and cell lysates were collected. The supernatant was Amicon® Ultra-15 filtered at 4 °C at 4000 × g for 50 min. The lysates were collected in 500 µL RIPA-buffer (% (v/v) Triton X-100, 50 mM Tris-HCl, pH=7.4, 150 mM NaCl, 1 mM EDTA, 0.5% (w/v) sodium deoxycholate). Cellular debris was removed by freeze-thawing the samples three times and spinning down at 18,624 x *g* at 4 °C for 15 min. The protein concentrations of the lysates were measured on Nanodrop™ (Thermo Fisher, MA, USA) and used for preparation of the cell lysate and supernatant samples for immunoblotting. Western blot quantifications were performed using ImageJ.

5.2.11. Lipid Droplet quantification

For quantification of lipid droplets (LDs) two approaches were used, flow cytometry and confocal microscopy. Wildtype and Ube2g2$^{-/-}$ cells were infected with ZIKV at MOI 5 and were fixed at the indicated time points using 4% PFA for 30 minutes at RT.

For quantitation using flow cytometry, intracellular LDs were stained 30 min prior to fixation by incubating the cells with BODIPY™ 493/503. Analysis was performed on the

Attune NxT acoustic focusing cytometer (Thermo Fisher, USA) using the %-BODIPY+ population and mean fluorescence intensity in comparison to unstained controls as read-out.

For imaging, the fixed cells were stained using Nile Red dye (Thermo Fisher, USA) for 10 min at RT. The average positive NileRed area per cell was calculated using the “analyse particles” macro in ImageJ. The quantification was performed using three independent experiments with a sample size of >500 cells for each condition.

5.2.12. Fluorescent free fatty acid labelling

HeLa-rUbe2g2-eGFP cells were seeded and starved by culturing them in HBSS medium for 1 hour, prior to incubating them 12 and 16 hours with 1 µM BODIPY® 558/568 C12 (Thermo Fisher, USA). Afterwards the cells were washed three times in PBS and subjected to virus infection. After 1 hour of viral absorption, the cells were chased in HBSS medium for another 24 hours. Subsequently the cells were fixed with 4%PFA and probed with anti-ZIKV capsid antibody for visualizing by confocal microscopy.

5.2.13. Statistics

Data are presented as mean values ± SD (standard deviation) or SEM (standard error of mean), calculated using Microsoft Excel 2016/version 16.36 and GraphPad Prism version 9.3.1. The threshold for statistical significance was set at P value < 0.05. P value significance intervals (*) are provided within each figure legend, together with the statistical test performed for each experiment.

Statistical significance was calculated in GraphPad Prism using one-way ANOVA followed by post hoc test for comparisons or unpaired Student’s t test. N values are indicated within figure legends and refer to biological replicates. Derived statistics correspond to analysis of averaged values across biological replicates.

Sample sizes were determined based on the numbers required to achieve statistical significance using indicated statistics, but with a minimum of 3 independently performed experiments to ensure data reproducibility. No data was excluded from the analyses.

5.3. Results

5.3.1. Ube2g2-deficiency restricts viral production of +RNA viruses

As an E2-conjugating enzyme, Ube2g2 has several distinct binding domains for E1 (G2BR) and RING E3-ligases (G2BR and RING-binding domain), alongside an active-site cysteine essential for Ub/Ubl exchange (C89) (211-213) (**Figure 5.3A)**. To study the functional impact of Ube2g2 on virus infection, CRISPR/Cas9 editing was employed to generate Ube2g2$^{-/-}$ HeLa cells. Several single clones were verified for knock-out by western blotting. Multiple clones displayed a similar phenotype, however to simplify the set-up, clone I was chosen for all future experiments (**Figure 5.3B)**. In this background, Ube2g2 was reconstituted using lentiviral stable transduction. Using site-directed mutagenesis a catalytically inactive form of Ube2g2 (C89K) was generated to investigate the necessity of the catalytic activity in viral infection. Both the reconstituted wildtype (rUbeg2^{WT}) and catalytically inactive (rUbe2g2^{C89K}) were expressed to similar levels (**Figure 5.4A**). As expected the rUbeg2^{WT} was ubiquitin modified, whereas rUbe2g2^{C89K} remained unmodified. Similarly, total cellular ubiquitination profiles were significantly reduced for the reconsituted catalytically inactive Ube2g2 in comparison to reconstituted wildtype (**Figure 5.4F**).

Wildtype and Ube2g2$^{-/-}$ cells were infected with DENV2 and New Caledonian Zika virus and viral titres were determined by plaque assay and RT-qPCR at 24 and 48 hours post infection (**Figure 5.3C,D**). Ube2g2 deficiency significantly reduced viral production. Herein, confounding effects of cellular toxicity of the Ube2g2 knock-out were excluded, as cell viability is not significantly affected (**Figure 5.4C**). Next, the question was whether this viral production deficiency is restricted to flaviviruses or is generally applicable to +RNA viruses. For this purpose, the cells were subjected to human coronavirus (HCoV-229E and OC43) and influenza virus infection (H1N1) and assessed for viral production. A similar restriction in viral production was observed in human coronavirus infections (replicates at the ER), but not for influenza infection (replicates in the nucleus) (**Figure 5.3E,F)**.

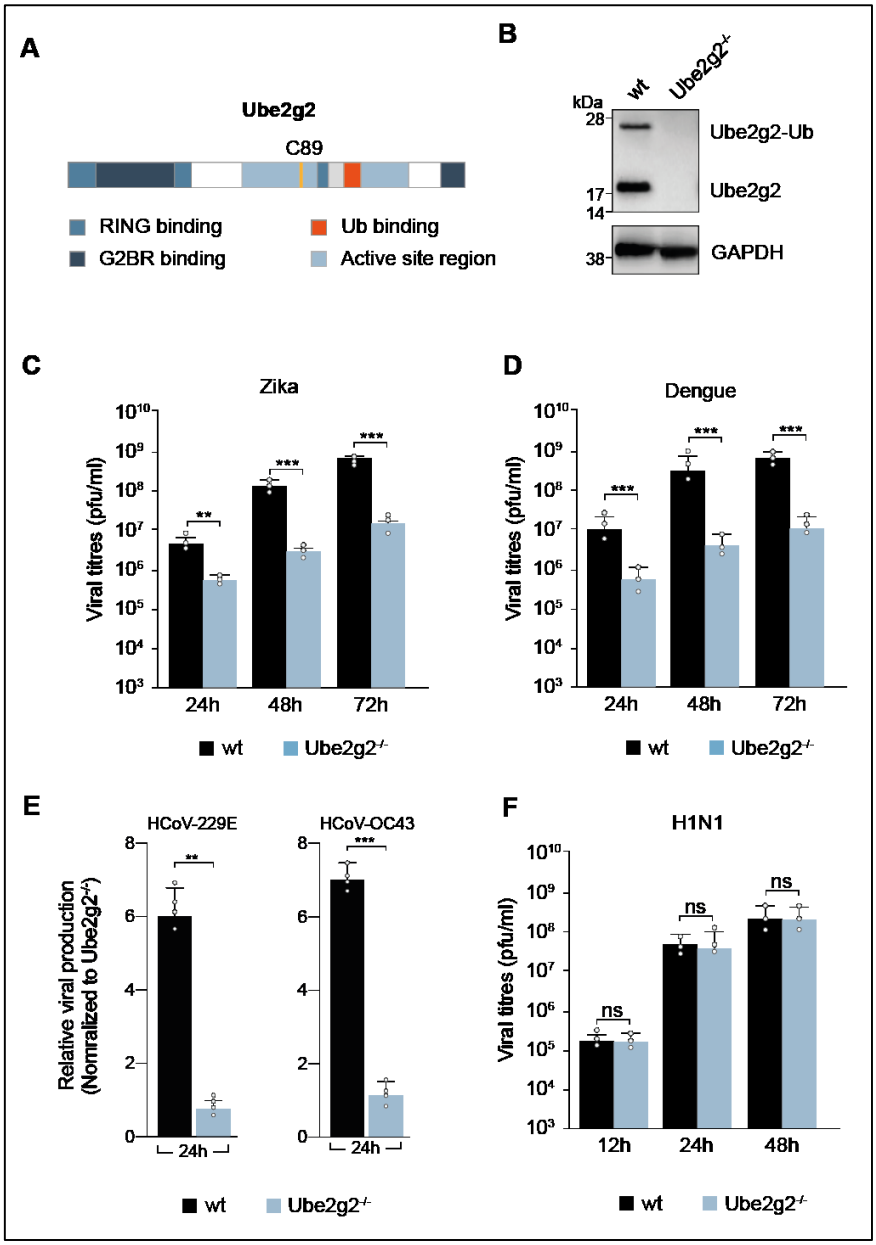


Figure 5.3 Virus production restricted upon Ube2g2 knock-out. A) Schematic of the domains in Ube2g2. The catalytic cysteine C89 is mutated to lysine in this study. Aup1 interacts with the G2BR domain and the cognate E3 through the RING±G2BR-domain. B) Single clones of Ube2g2$^{-/-}$ HeLa cells were generated using CRISPR/Cas9 and lysates of knock-out and wildtype cells were generated and resolved by gel electrophoresis to determine expression of Ube2g2 by immunoblotting. Wild-type and Ube2g2$^{-/-}$ cells were challenged with C) ZIKV and D) DENV2 at MOI5. Extracellular virus production was determined at the indicated time points using plaque assay. Error bars represent mean ± SD, n = 3 biologically independent experiments. **P < 0.01; ***P < 0.001 (compared with wild-type by ANOVA followed by one-sided Dunnett's test) E) Wild-type and Ube2g2$^{-/-}$ cells were infected with human coronaviruses HCoV-229E and HCoV-OC43 at MOI 0.1. Extracellular virus production was determined at 24 hours post infection using qPCR with probes for nucleocapsid. Error bars represent mean ± SD, n = 4 biologically independent experiments. **P < 0.01; ***P < 0.001 (derived using unpaired Student's t test). F) Wild-type and Ube2g2$^{-/-}$ cells were infected with H1N1pdm strain at MOI 0.1. Viral production was measured by plaque assay. Data are presented as mean ± SD, n=3 biological replicates. Statistical significance derived using ANOVA followed by one-sided Dunnett's test.

The rUbe2g2^{WT} and rUbe2g2^{C89K} HeLa cells were included in the set-up, to assess the necessity of the catalytic activity of Ube2g2 for its proviral role. The virus production could be rescued by reconstituting the wildtype but not the catalytically inactive form of Ube2g2 (**Figure 5.4D**). This phenomenon was confirmed to not be a cell type specific effect as hepatocytes showed similar restriction in viral production (**Figure 5.4E**).

In a previous study from our group, the cognate partner of Ube2g2, Aup1 was found to be instrumental for virus-triggered lipophagy induction in support of viral production (114). As Aup1 has previously been shown to interact directly with Ube2g2 through its G2BR domain, it was tested whether this interaction is maintained in viral infection and whether Aup1 levels are affected by Ube2g2 knock-out (114, 211). Aup1 protein levels were maintained upon Ube2g2 knock-out in both homeostasis and infection (**Figure 5.4B**). By immunoprecipitation of endogenous Ube2g2 in mock- and Zika-infected cells using Protein G-beads, the interaction with Aup1 was studied by blotting for Aup1. As anticipated, Ube2g2 interaction with Aup1 is maintained during the course of infection (**Figure 5.4G**). During infection, Ube2g2 is therefore expected to be able to act through the Aup1-Ube2g2 complex and could be necessary to support this Aup1-dependent virus-triggered lipophagy observed in DENV infection. Moreover, as the catalytic activity of Ube2g2 is required, its role in ERAD is suspected to contribute to the +RNA viral lifecycle.

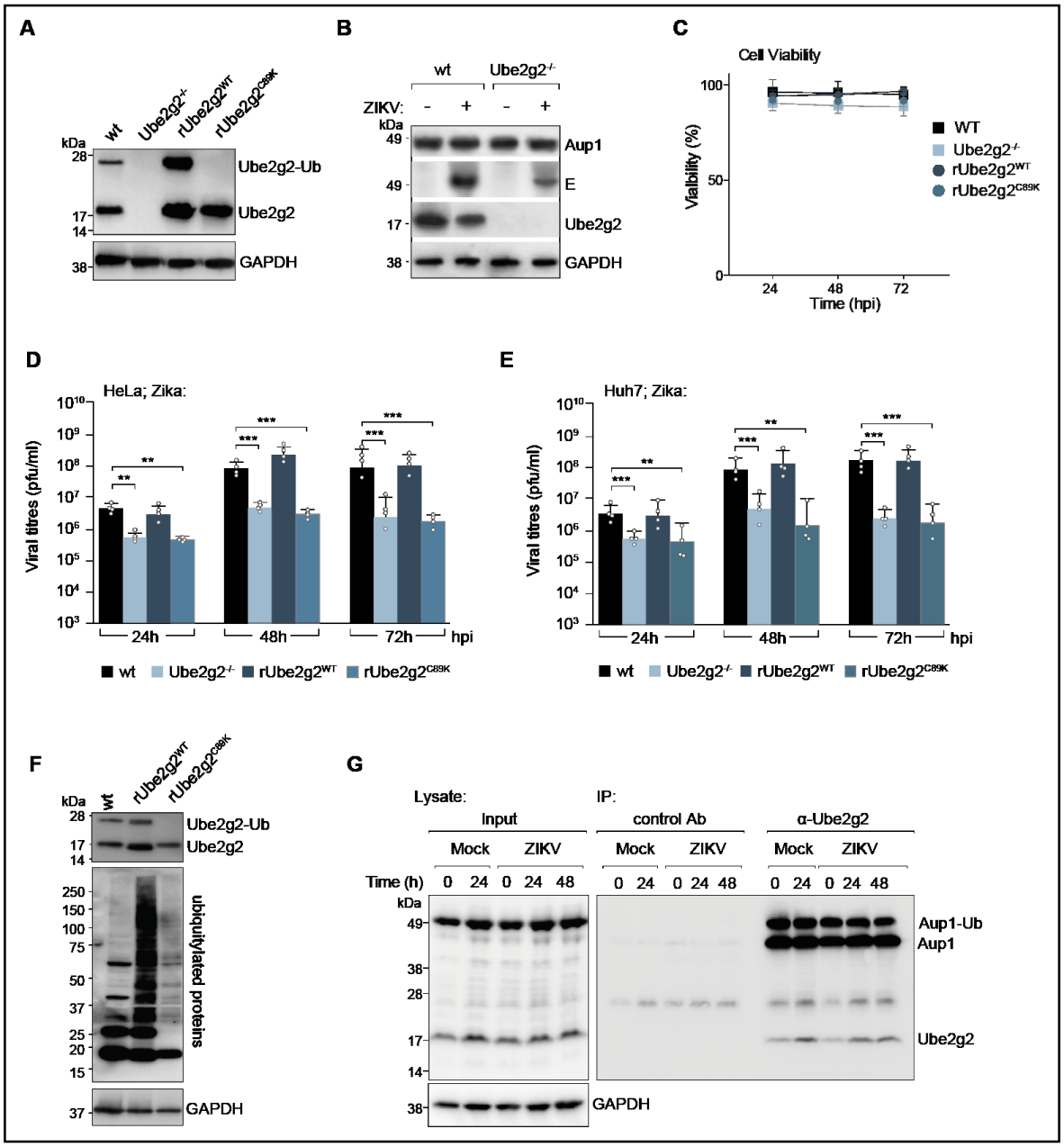


Figure 5.4 Catalytic activity of Ube2g2 is required for viral production. A) wild-type (rUbe2g2^{WT}) and C89K (rUbe2g2^{C89K}) mutant variants of Ube2g2 were reconstituted into the deletion background; Ube2g2$^{-/-}$ single clone I. Expression levels of Ube2g2 were determined in lysates resolved by gel electrophoresis and immunoblotted for Ube2g2. B) Lysates from mock or Zika-infected wild-type and Ube2g2$^{-/-}$ cells (48 hpi) were immunoblotted for viral E-protein along with Aup1 and Ube2g2. C) Cell viability of wildtype (WT), Ube2g2$^{-/-}$, rUbe2g2^{WT} and rUbe2g2^{C89K} cells was measured using MTT assay as per the manufacturer's protocol. Error bars represent mean ± SD from three independent experiments. D) HeLa and E) Huh7 Wild-type, Ube2g2$^{-/-}$, rUbe2g2^{WT} and rUbe2g2^{C89K} cells were challenged with Zika virus at MOI 5. Infectious virus production was measured using plaque assay. Data is presented as mean ± SD, n=4 biological replicates. **P < 0.01; ***P < 0.001 (compared with wild-type by ANOVA followed by one-sided Dunnett's test). F) Cellular ubiquitination profiles were measured in lysates from wildtype, rUbe2g2^{WT} and rUbe2g2^{C89K} cells using immunoblotting. F) Endogenous Ube2g2 was immunoprecipitated from mock and Zika virus-infected HeLa cells at indicated time intervals and was probed for Aup1.

5.3.2. Ube2g2 is required for efficient viral replication

To study at which stage of the virus life cycle Ube2g2 was required, the life cycle was roughly divided in three different steps 1) viral entry and fusion; 2) translation and replication; 3) assembly, maturation and release. To exclude a role of Ube2g2 in viral entry, an octadecyl rhodamine B (R18) fusion assay was employed. R18 is a self-quenching dye at high concentrations, but is released upon dilution (Excitation/Emission: 556/578 nm). This dye allows for evaluation of viral entry and fusion of R18-labelled *live virus* with host endosomal membranes (**Figure 5.5A**). For this set-up, Zika virus was pre-labelled with R18 and purified using ultracentrifugation prior to incubation on wildtype and Ube2g2$^{-/-}$ cells for 48 hours. Viral internalization was quantified by flow cytometry and visualized by confocal imaging. Red punctate structures indicate fusion of internalized virus particles with the endosomal membranes and where visible in both ZIKV-infected wildtype and Ube2g2$^{-/-}$ cells (**Figure 5.5B**). There was no clear difference observed in amount of punctae per cell between wildtype and Ube2g2$^{-/-}$ cells. Similarly, using flow cytometry, the percentage of R18+ population was found to be ~40% for both wildtype and Ube2g2$^{-/-}$ cells, with no significant difference between the two cell lines (**Figure 5.5C**). These results indicate that Ube2g2 has no influence on viral entry.

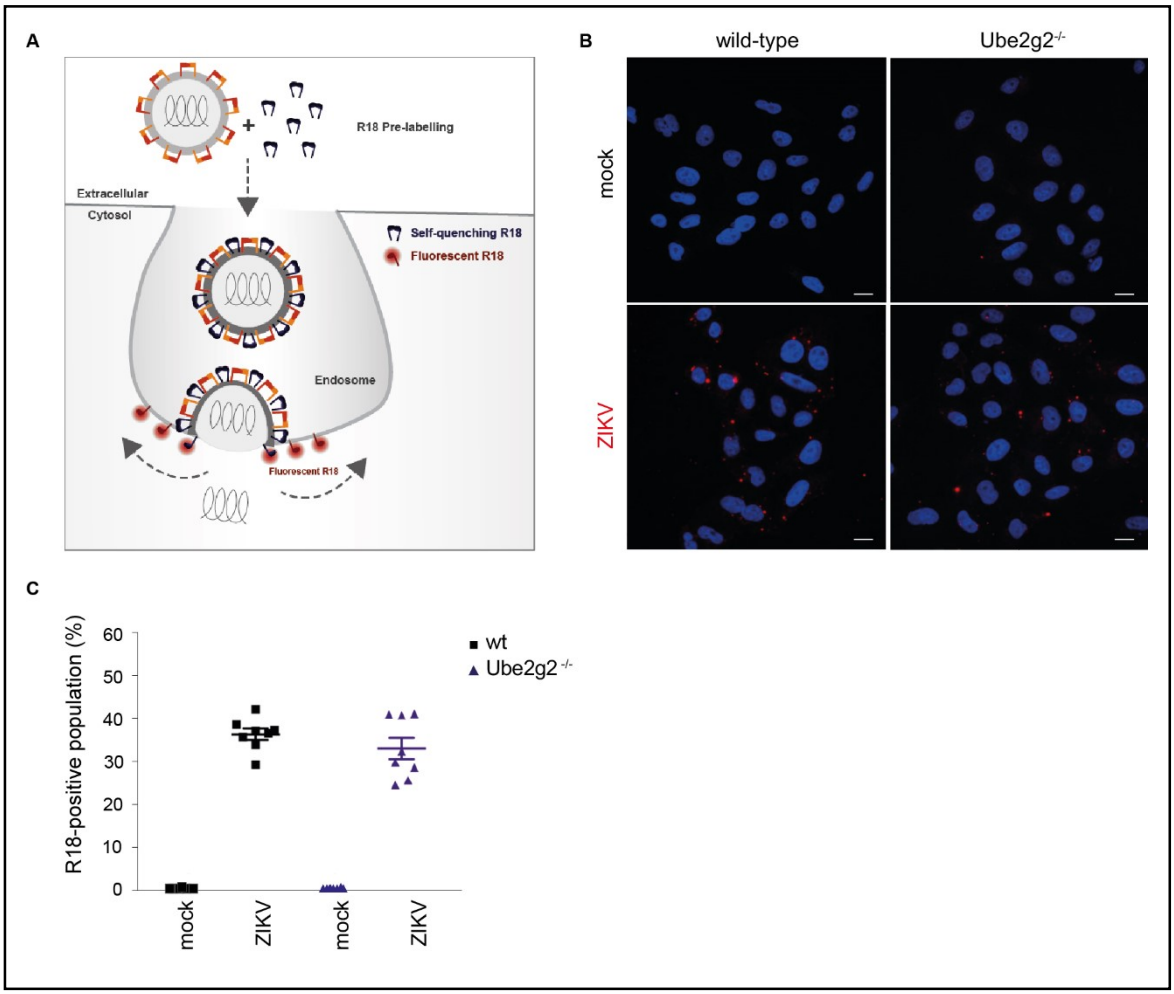


Figure 5.5 Zika viral entry unaffected by Ube2g2-deficiency. A) Schematic of the R18 fusion assay. B+C) Wild-type and Ube2g2$^{-/-}$ cells were infected with either R18 labelled ZIKV at MOI 400 or pre-labelled control medium for 1 hr at 4ºC degrees, followed by 2.5 hrs at 37ºC,5%C0$_2$. B) For immunofluorescent imaging, the cells were 4%PFA fixed, Hoechst stained and visualised by confocal microscopy. Hoechst staining indicates nuclei; red puncta structures indicate fused R18-labelled virus. C) Quantitation of viral entry was performed by measuring the R18+ positive population using flow cytometry at 2.5 hours post infection. Error bars represent mean ± SD, n = 3 biologically independent samples.

To study the role of Ube2g2 in translation and replication, a luciferase-based replicon assay was employed. This Zika replicon is a self-replicative viral RNA which expresses all viral non-structural genes, but has the structural genes replaced with a Renilla luciferase reporter (**Figure 5.6A**), allowing to read out viral replication by measuring luciferase intensity. This system allows for decoupling viral replication from confounding factors in the viral lifecycle such a viral entry. The Zika replicon was transfected into wildtype and Ube2g2$^{-/-}$ cells and every two hours cells were lysed and the luciferase activity was measured to

allow for assessment of both the translation (0-6 h.p.t.) and replication phase (6 h.p.t onwards). During translation, comparable levels of luciferase activity were found for both cell lines (**Figure 5.6B**). However, when the replication phase was initiated, the luciferase activity of wildtype cells luciferase increased exponentially, but the knock-out cells significantly remained lower in intensity. When including the reconstituted wildtype and catalytically inactive Ube2g2 cells, this defect in replication was confirmed to require the catalytic activity. A cumulative effect on replication could be observed at later time points (24 and 48 hours post transfection) (**Figure 5.6C,D**). To confirm Ube2g2 is required for efficient viral replication, intracellular Zika RNA production was measured by RT-qPCR for infected wildtype Ube2g2$^{-/-}$ cells (**Figure 7.6E**). The results are presented as the fold change of intracellular viral RNA between wildtype and Ube2g2$^{-/-}$ cells (2^-ΔΔCt (WT/Ube2g2$^{-/-}$)). These data confirm the viral genome replication is significantly lowered in Ube2g2-deficient cells in comparison to wildtype cells.

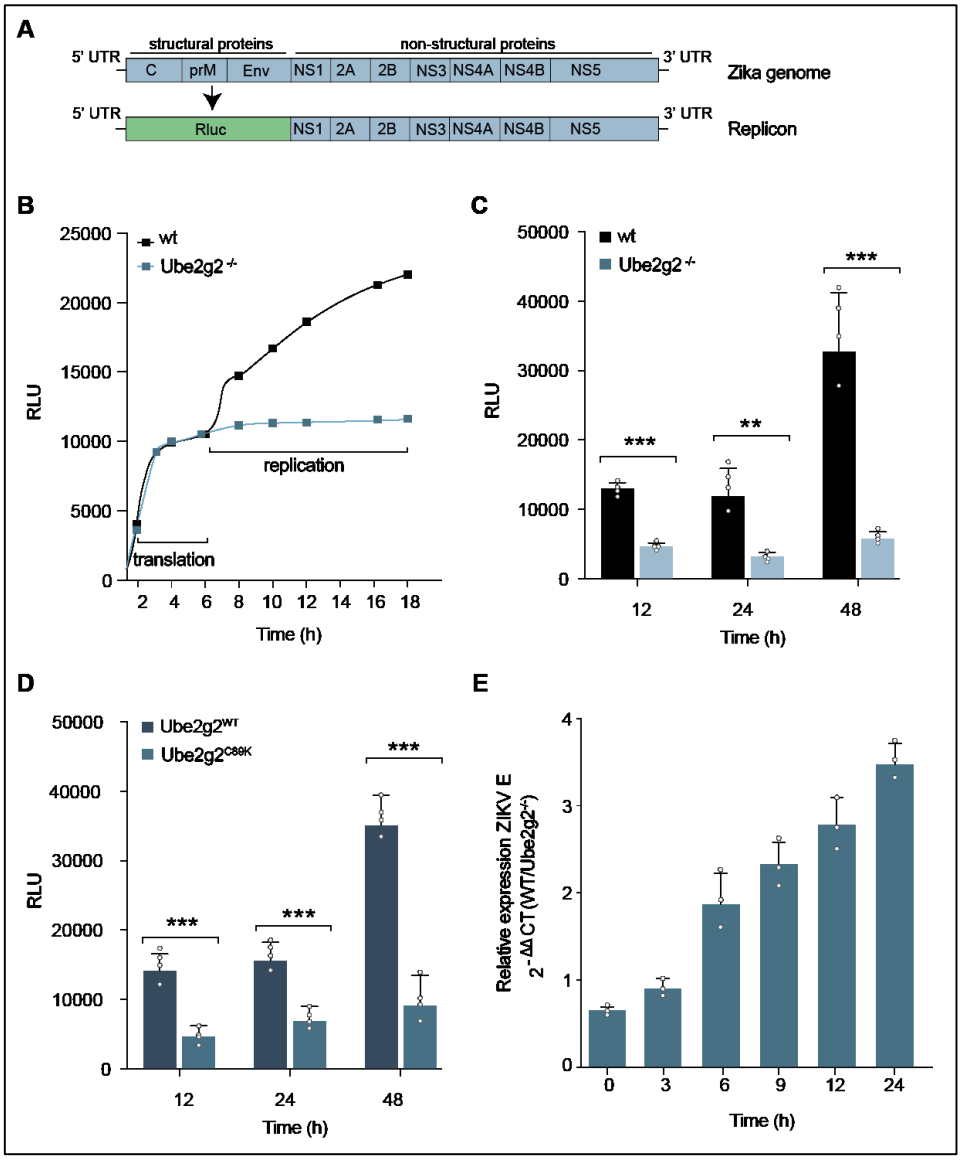


Figure 5.6 Ube2g2-deficiency impairs viral replication. A) Schematic representation of the Zika virus replicon in which the structural genes are substituted by a *renilla* luciferase reporter. B-D) Luminescence read-out at indicated time points post transfection of transiently ZIKV replicon RNA-transfected wildtype and Ube2g2$^{-/-}$ cells to measure (B) translation (0-6h.p.t.) and (B-D) replication in wild-type, Ube2g2$^{-/-}$, Ube2g2^{WT} and Ube2g2^{C89K} cells (6-48 h.p.t.); Luciferase activity is shown as relative luminescence units (RLU). **P < 0.01; ***P < 0.001 (compared with wild-type by ANOVA followed by one-sided Dunnett's test). E) Wild-type and Ube2g2$^{-/-}$ cells were infected with ZIKV at MOI 5. The total RNA was extracted at the indicated time points, and viral production was measured by qPCR. Internal GAPDH control was used to calculate ΔCt values. Relative intracellular ZIKV E transcript levels were presented as $2^{-\Delta\Delta Ct}$ (Wild-type vs Ube2g2$^{-/-}$). Data is presented as mean ± SD, n=3 biological replicates.

5.3.3. Viral replication organelle formation impaired in absence of Ube2g2

To understand the replication defect observed in Ube2g2$^{-/-}$ cells, it was assessed how replication organelle formation is affected by the deficiency. Replication organelle formation

is orchestrated by the Zika virus non-structural proteins, that act together as the replication complex to remodel the ER and make membrane invaginations for replication (194). To assess if the replication complex is affected by Ube2g2 deficiency, the viral protein production levels were assessed in infected wildtype and Ube2g2$^{-/-}$ cells at 24 and 48 hours post infection. The non-structural proteins were significantly attenuated at both timepoints, whereas the structural proteins are only significantly reduced at multicycle replication (**Figure 5.7A**), indicating for a specific effect on the replication complex. This early loss in expression of non-structural proteins such as NS5 and NS4A-NS4B, indicates for either synthesis or turnover being affected. This leads to defective replication, which in return results in a cumulative defect in viral protein production highlighted by the structural proteins being affected at later time points.

To study whether Ube2g2-deficiency in fact leads to defective synthesis versus increased degradation of these non-structural proteins, a [35S]-pulse-chase assay was utilized to measure the fate of newly synthesized proteins (**Figure 5.7B**). Zika-infected wildtype, Ube2g2$^{-/-}$, rUbe2g2 and rUbe2g2^{C89K} cells (12 h, 24 h and 48 h post infection) were starved and pulse labelled with [35S]cysteine/methionine before being chased in cold media for the indicated time intervals. At each time point, viral proteins were immunoprecipiated, ran on SDS-PAGE gel and detected by autoradiogram. In addition, viral particle release was measured in the supernatant. As observed in **Figure 5.4D**, virus production from Ube2g2-deficient and -catalytically inactive cells was indicated to be significantly lower compared to Ube2g2-proficient cells, as seen by reduced amounts of secreted M and E protein (**Figure 5.7F**). Interestingly, the pulse-chase results show that the viral proteins are similarly synthesized intracellularly, with only a minor delay for Ube2g2-deficient cells, as can be seen for structural protein E and PrM (**Figure 5.7C-E**). But synthesis of the non-structural proteins was rapidly followed by their degradation in absence of catalytically active Ube2g2. These results indicate that stable replication complex formation is impaired in absence of catalytically active Ube2g2. This likely results

from impaired ER membrane remodelling required for efficient replication organelle formation. Intriguingly, although synthesis of structural proteins was not dramatically affected by Ube2g2 deficiency, classical oligomerization was not observed, indicative of also an assembly defect.

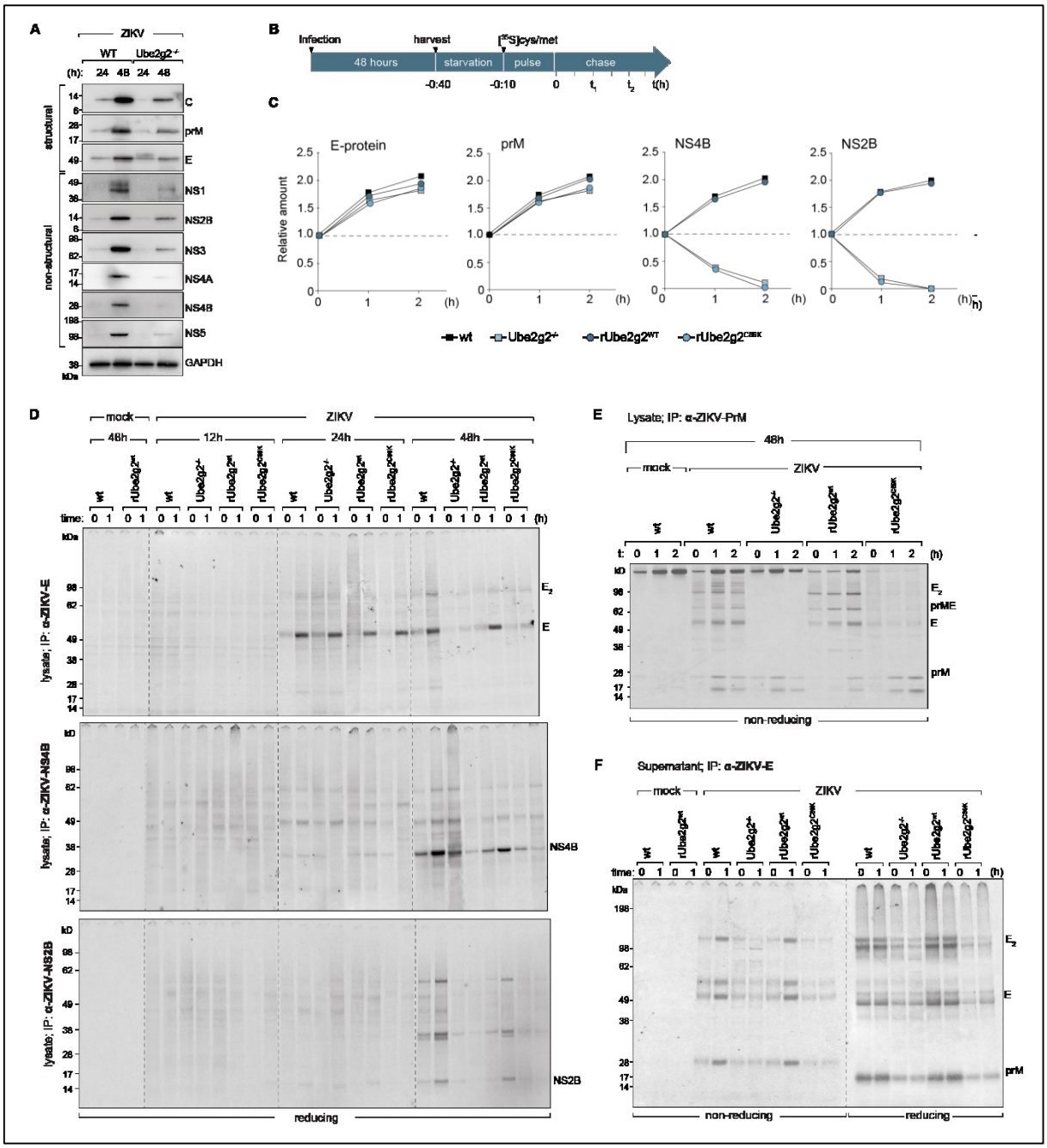


Figure 5.7 Replication complex formation impaired upon Ube2g2-deficiency. A) Wildtype and Ube2g2$^{-/-}$ cells were infected with ZIKV at MOI 2. Expression levels of non-structural and structural proteins were analysed using Western Blotting. Data is representative of four biological independent samples. B) Schematic of the pulse-chase assay. Cells were harvested at 12, 24 and 48 hours post infection, starved from cysteine/methionine for 30 min and pulsed with 20µCi of [35S]cysteine/methionine for 10 min, followed by chase in cold media for the indicated time points.

Supernatants and cell pellets were collected and immunoprecipitated for each time point. C) Quantitation of indicated viral proteins from pulse-chase assays. Values are representative of at least four independent biological experiments. D) Lysates from indicated cells were subjected to immunoprecipitation on anti-E, anti-NS4B and anti-NS2B for autoradiography. E) Viral prM was immunoprecipitated from radiolabelled cells under non-reducing conditions and detected by autoradiography. F) Released virus particles were immunoprecipitated from supernatants (48 h post infection) using anti-ZIKV-E antibodies, subjected to non-reducing versus reducing (+βME) conditions, resolved by gel electrophoresis and detected by autoradiography. All images are representative of at least 3 independent biological replicates.

To confirm the defect in replication complex and organelle formation, transmission electron microscopy and immunofluorescence were used to visualize these structures in wildtype and Ube2g2-deficient cells 24 hours post ZIKV infection. By immunofluorescence it was seen that ZIKV-infected wildtype cells displayed typical perinuclear distribution of both double-stranded RNA (dsRNA) and viral E-protein (**Figure 5.8A**). Herein, E-protein indicates viral assembly sites and dsRNA, as intermediate of virus RNA replication, the replication organelles. Whilst dsRNA and E-protein largely co-localised in wildtype cells, the Ube2g2$^{-/-}$ cells displayed reduced and more dispersed distribution of E-protein and dsRNA, confirming defective membrane rearrangements were at play (**Figure 5.8B**). Similarly, by TEM analysis of wildtype and Ube2g2$^{-/-}$ cells, it was revealed that viral progeny production was significantly attenuated in the Ube2g2$^{-/-}$ cells (**Figure 5.8C-H**). Moreover, viral replication sites (RO) and assembly sites (vesicle packets (VP)) could be clearly observed in wildtype but not knock-out cells. Where in wildtype cells ER sheets were substantially dilated and had large amounts of virus-induced invaginations (RO and VP); the typical condensed convoluted membranes and replication organelles were not observed in Ube2g2$^{-/-}$ cells. Instead, more ER whorls and lysosomes were present in the Ube2g2$^{-/-}$ cells. Collectively, these results support that defective membrane rearrangements underpin the block in effective replication organelle formation.

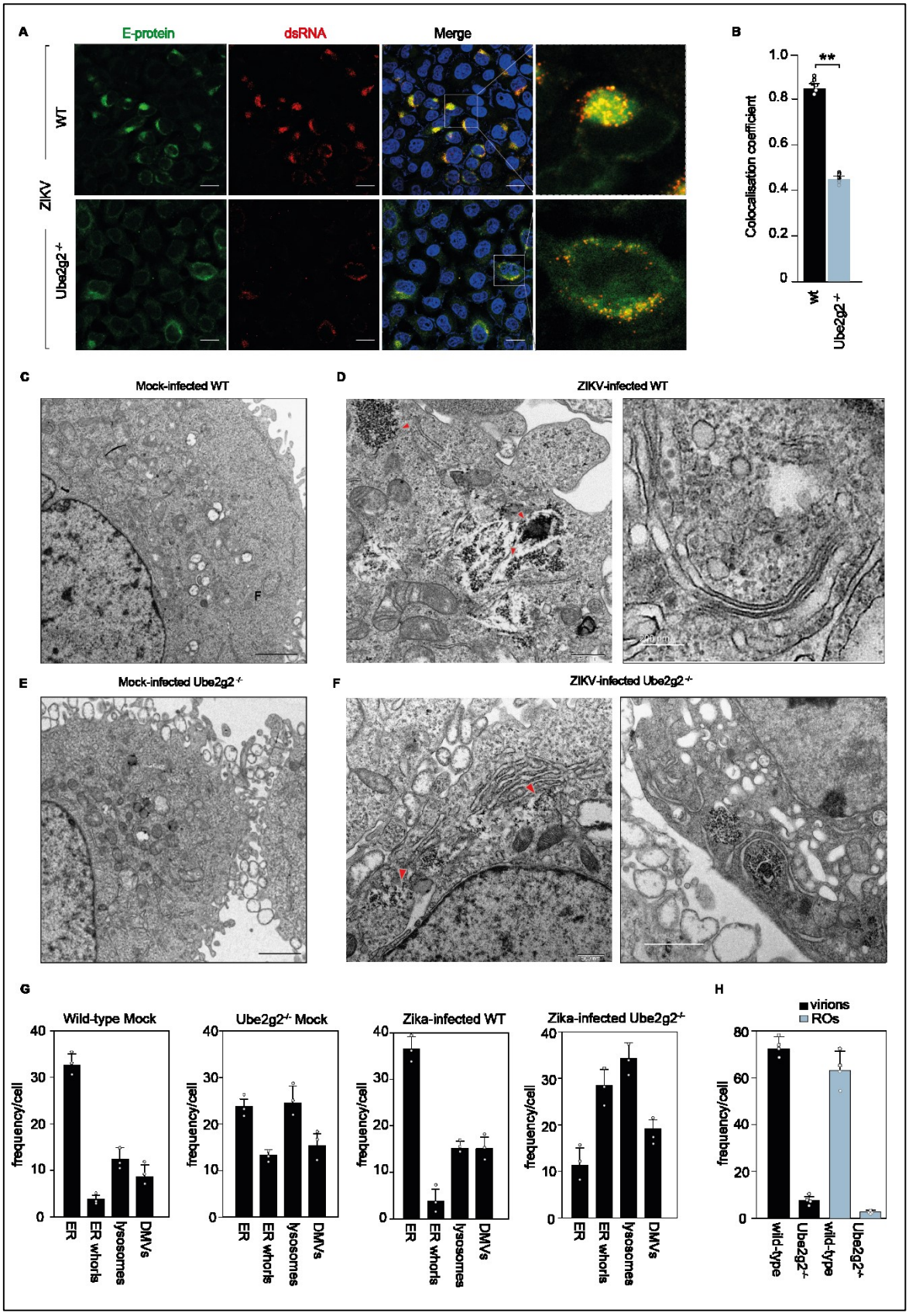


Figure 5.8 Ube2g2 deficiency affects membrane rearrangements required for replication and assembly site formation. A) Wild-type and Ube2g2$^{-/-}$ cells were infected with Zika at MOI 5. Cells were fixed at 24hpi and probed with anti-ZIKV envelope E-protein (488) and anti-double stranded (ds) RNA (555). Nuclei were visualised by Hoechst staining; Scale bar = 10 µM. B) Pearson's

correlation coefficient was measured to determine co-localisation of dsRNA and ZIKV E. Error bars represent mean ± SD, $n = 6$ biologically independent samples; $^{**}P < 0.01$; $^{***}P < 0.001$ (compared with wild-type by ANOVA followed by one-sided Dunnett's test). C-F) TEM sections of mock and Zika-infected wild-type and Ube2g2$^{-/-}$ cells. The frequency of indicated organelles was determined per cell for >20 images. G. Quantitation of the frequency of indicated organelles per cell in wild-type and Ube2g2$^{-/-}$ cells. Error bars represent mean ± SD, n=3 biological replicates. H) Quantitation of the frequency of intact virions (red arrows) per cell in wild-type and Ube2g2$^{-/-}$ cells. Error bars represent mean ± SD, n=4 biological replicates.

5.3.4. Ube2g2-deficiency induces Sec62-dependent ER-phagy in ZIKV-infection

Establishment of the ER membrane rearrangements for efficient viral production, requires a sequence of events. ER expansion by UPR induction while countering ER-phagy are key to allow for these rearrangements (214). To verify UPR induction, XBP1 splicing was measured in virus-infected wildtype and Ube2g2-deficient cells. Spliced XBP1 was detected by RT-qPCR as fold change compared to mock-infected wildtype cells (**Figure 5.9A)**. Although both wildtype and Ube2g2$^{-/-}$ induced increased XBP1 splicing upon infection, basal levels of spliced XBP1 where already increased in Ube2g2$^{-/-}$ cells, indicative of elevated ER stress in the knock-out cells (**Figure 5.9B**). To evaluate ER-expansion in response to UPR induction, one of the key viral strategies to allow for ER-expansion was studied; cleavage of the ER-phagy receptor FAM134B to prevent FAM134B-dependent ER-phagy upon UPR induction (215). Zika virus has previously been shown to employ its main protease NS3 to cleave ER-phagy receptor FAM134B (111). As anticipated, FAM134B cleavage is observed following ZIKV-infection and is unaltered in presence or absence of Ube2g2 (**Figure 5.10A)**. However, the abundance of FAM134B was found to decrease over the course of infection in Ube2g2-deficient cells, indicative of ER-phagy induction in absence of Ube2g2.

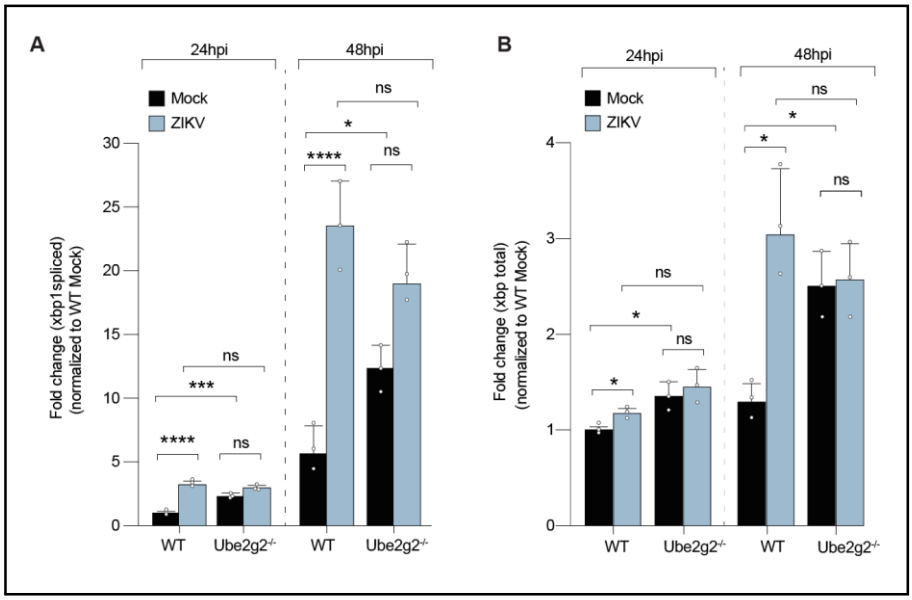


Figure 5.9 Increased XBP1 levels upon Ube2g2-deficiency. A,B) Wild-type and Ube2g2$^{-/-}$ cells were mock or virus-infected at MOI 2 for indicated time points. At each time point, Xbp1 splicing was measured by RT-qPCR using probes for spliced XBP1 and total XBP1. Data are presented as mean ± SD, *n* = 3 biologically independent samples; *P < 0.05; ***P < 0.001; ****P < 0.0001 (derived from unpaired Student's t test for within group comparisons).

To study this potential selective ER-phagy induction further and address ER stress recovery, the fate of a number of ER-phagy receptors and ER stress chaperones were traced using the pulse chase assay described previously (**Figure 5.10C,D)**. ER stress recovery after ER expansion, typically occurs through selective degradation of specific chaperones, particularly ER stress chaperones such as Herp/Herpud1, Sel1L, Hsp70 or by induction of ER-phagy (216). Infected wildtype and Ube2g2$^{-/-}$ cells were pulsed with [35S]cysteine/methionine and chased for 45 minutes. Interestingly, rapid degradation of ER stress chaperones Herpud1, Sel1L and calreticulin was seen in infected wildtype cells, whilst this was blocked in knock-out or catalytically dead Ube2g2 cells (**Figure 7.10B**). Even an increase in expression of these ER stress chaperones was observed over time in Ube2g2-deficient cells. ER-phagy receptors including Rtn3, Fam134a and Fam134c remained unaffected (**Figure 5.10C)**. Whereas ATL3, another ER-phagy receptor accumulates in infection in wildtype cells, but is specifically degraded in the Ube2g2$^{-/-}$ and rUbe2g2^{C89K} cells, a receptor previously shown to be important for viral assembly, maturation and release (204). Moreover, another ER-phagy receptor, Sec62 is specifically

induced in Ube2g2$^{-/-}$ and Ube2g2^{C89K} cells. Summarizing, Ube2g2-deficiency is suggested to stabilise stress response chaperones and increase Sec62 expression. This could indicate for Sec62-dependent ER-phagy. Sec62-dependent ER-phagy is one of the critical pathways in ER recovery in which the ER is rapidly turned over (217, 218). Increased ER-phagy induction in Ube2g2$^{-/-}$ cells was suggested by TEM, as seen by an increased abundance of lysosomes at the ER, where the ER showcased altered morphology (**Figure 5.7F**). This ER-turnover was indeed suggested to be Sec62-dependent as ZIKV-infected wildtype and Ube2g2$^{-/-}$ cells were stained for Sec62 and the lysosomal marker, Lamp1 protein, and showed co-localization for the Ube2g2$^{-/-}$ cells (**Figure 5.11A**).

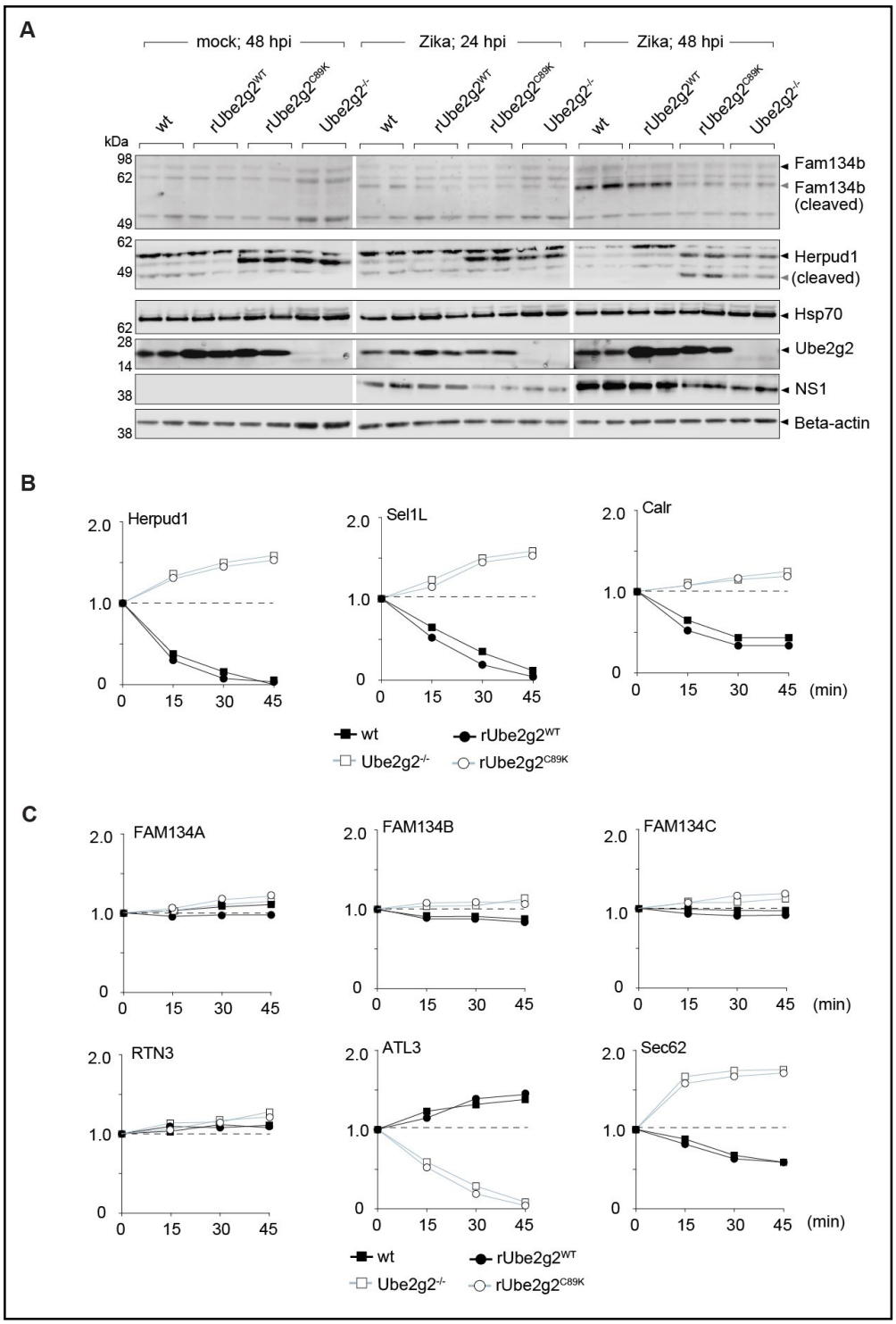


Figure 5.10 Ube2g2-dependent selective ER stress protein turnover. A) Expression of FAM134B, Herpud1 and Hsp70 was measured by immunoblotting in wild-type, Ube2g2$^{-/-}$, rUbe2g2^{WT} and rUbe2g2^{C89K} cells at indicated timepoints post infection with ZIKV MOI 2. B,C) Novel synthesis and turnover of the B) ER stress chaperones and C) ER-phagy receptor proteins indicated, were quantitated using pulse chase in [35S]cysteine/methionine labelled cells at 48 hours post infection with ZIKV MOI 2.

To confirm Sec62-mediated ER-phagy is responsible for viral restriction, wild-type, Ube2g2$^{-/-}$, rUbe2g2^{WT} and rUbe2g2^{C89K} cells were depleted from Sec62. Moreover, as this

ER-phagy pathway was described to be Chmp4-dependent, usage of this pathway was confirmed by separately depleting Chmp4 (**Figure 5.11B**) (108, 217). Both the Chmp4-depleted and Sec62-depleted cells were supplemented with free fatty acids prior to Zika virus challenge, to circumvent any effects from lipophagy defects in the Ube2g2 deficient cell lines, a pathway postulated to involve Ube2g2 which is discussed in the next section. Interestingly, both Sec62- and Chmp4-depletion in Ube2g2$^{-/-}$ and Ube2g2^{C89K} cells can rescue viral production (**Figure 5.11C**). This data highlights that Ube2g2 allows for fine-tuning of ER stress recovery in ZIKV infection and prevents replication complex degradation by selectively inhibiting Sec62-dependent ER-phagy.

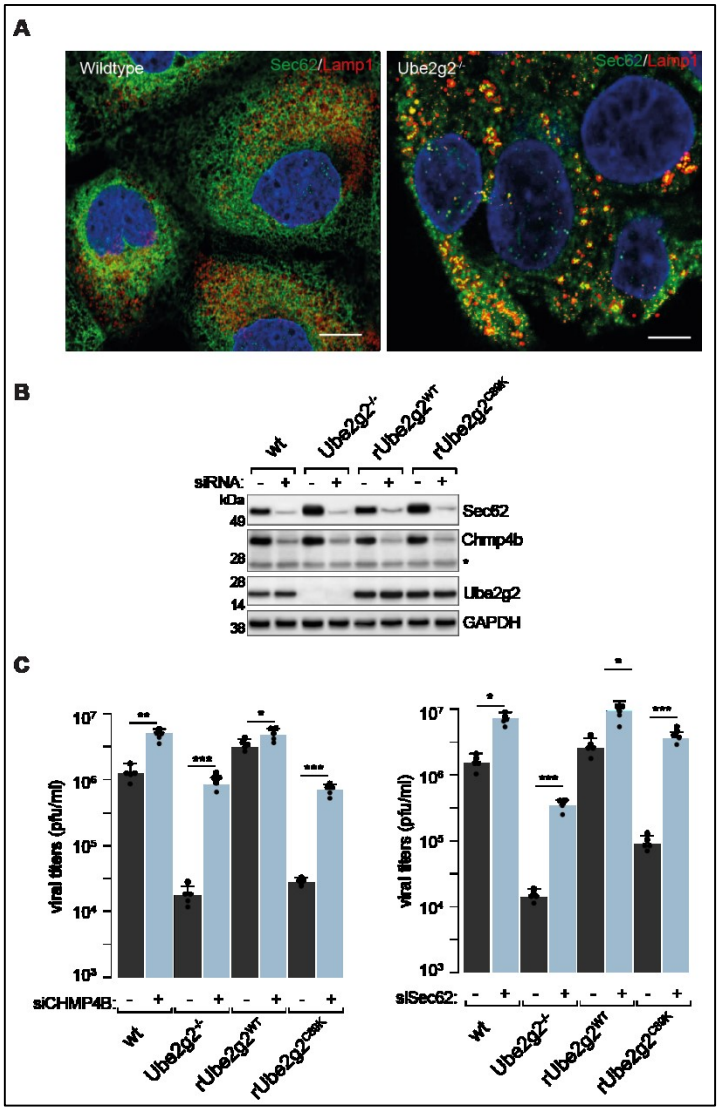


Figure 5.11 Sec62-Chmp4-dependent ER-phagy induced upon Ube2g2-deficiency is responsible for viral restriction. A) Sec62 and Lamp1 were visualised as measure of ER-phagy in wild-type and Ube2g2$^{-/-}$ cells at 48 h.p.i. with ZIKV MOI 2, using Carl Zeiss LSM 780/980 confocal

microscope (Scale bars=10μm). B) Immunoblots were performed with lysates from indicated cells (wild-type, Ube2g2$^{-/-}$, rUbe2g2^{WT}, rUbe2g2^{C89K}) expressing non-targeting siRNA as control or against Chmp4 or Sec62. GAPDH was measured as loading control. C) Viral titres were measured in the cells described in B) that were grown in media supplemented with 10 mM FFA conjugated to BSA and subjected to ZIKV at MOI 2 for 48 hours. Viral titres were determined using standard plaque assays. Data represent mean ± SD n = 5 biologically independent samples; *P < 0.05; **P < 0.01; ***P < 0.001; ****P <0.0001 (compared with wild-type by ANOVA followed by one-sided Dunnett's test).

5.3.5. NS3-induced cleavage of ER-chaperones requires Ube2g2 to prevent ER-phagy

As FAM134B is cleaved by NS3 at the reticulon homology domain (HRD) shared by other ER-phagy receptors such as Reticulon 3, it was hypothesized that perhaps the rapid Ube2g2-dependent degradation of the ER-stress chaperones Herpud1, Calreticulin, Sel1L was driven by the viral protease as well (111). To determine whether the viral protease is responsible for this degradation, Zika NS2B-NS3 was transfected into in wild-type, Ube2g2$^{-/-}$, rUbe2g2^{WT} and rUbe2g2^{C89K} cells (**Figure 5.12A**). The rapid turnover of these stress response proteins was recapitulated in the wildtype and rUbe2g2 when expressing NS2B-NS3 (**Figure 5.12B**). Moreover, the turnover was blocked in Ube2g2$^{-/-}$ and rUbe2g2^{C89K} cells, confirming that NS3-dependent degradation of the ER stress response proteins relies on Ube2g2-dependent ubiquitination. Collectively, this data highlights that selective inhibition of ER-phagy is critical to biogenesis of viral replication organelles.

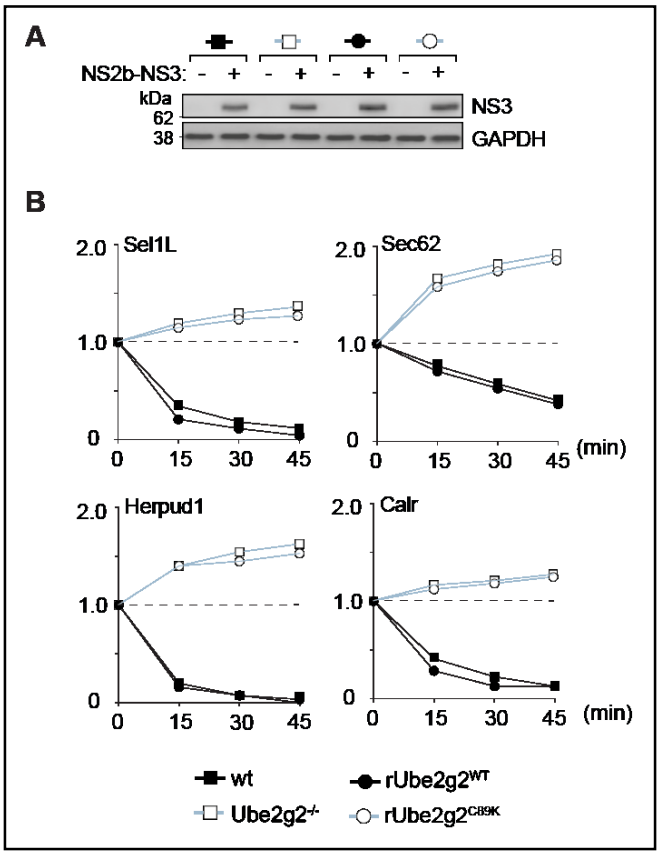


Figure 5.12 NS2b-NS3 induces Ube2g2-dependent ER stress chaperone degradation. Zika NS2b-NS3 or empty-vector was transfected into wild-type, Ube2g2$^{-/-}$, rUbe2g2^{WT}, rUbe2g2^{C89K} cells. A) Lysates were collected at 24 h.p.t. and NS3 Expression was detected using immunoblotting. B) Turnover of indicated ER proteins was quantitated by pulse chase in [35S]cysteine/methionine labelled cells as described previously.

5.3.6. Ube2g2-deficiency restricts viral release

Lastly, it was assessed whether Ube2g2 plays a role in viral assembly, maturation and release. To specifically address assembly and secretion of virus particles, a ZIKV-PrME-virus like particle (VLP) system was utilized. These cells constitutively express the viral structural proteins PrM and E, but not the capsid, to specifically study viral release in absence of viral entry and replication (**Figure 5.13A**). These HeLa ZIKV-VLP cells were transfected with Dicer-substrate small interfering RNAs (DsiRNAs) targeting Ube2g2 or a non-targeting control and assessed for intra- and extracellular VLP production, by collecting supernatant and cell lysates. Compared to HeLa ZIKV-VLP cells transfected with non-targeting siRNA, Ube2g2-targeting siRNA resulted in a dramatic reduction of released mature form VLPs but not intracellular VLPs (**Figure 5.13B,C**). This phenomenon was not

ZIKV-VLP specific, as release of an unrelated protein, Vesicular Stomatitis Virus Glycoprotein (VSV-G), was also affected by the Ube2g2 depletion (**Figure 5.13D,E)**. VSV-G was transfected into wildtype and Ube2g2$^{-/-}$ cells and assessed for turnover and secretion using [35S]-pulse-chase. The cells were pulsed with [35S]cysteine/methionine for 10 min and chased for indicated time intervals afterwhich VSV-G was immunoprecipitated. The precipitates were subjected to EndoH treatment to assess glycosylation status as measure for ER-to-Golgi transport. VSV-G transport was quantified as the amount of EndoH resistant form as fraction of total VSV-G. Similar to VLP-production, VSV-G transport was found to be impaired in Ube2g2-deficient cells. Additionally, the ER-resident pool is actively degraded over time, in support of observed increased ER-phagy in Ube2g2-deficiency. Collectively, this data suggests that Ube2g2 facilitates efficient viral release.

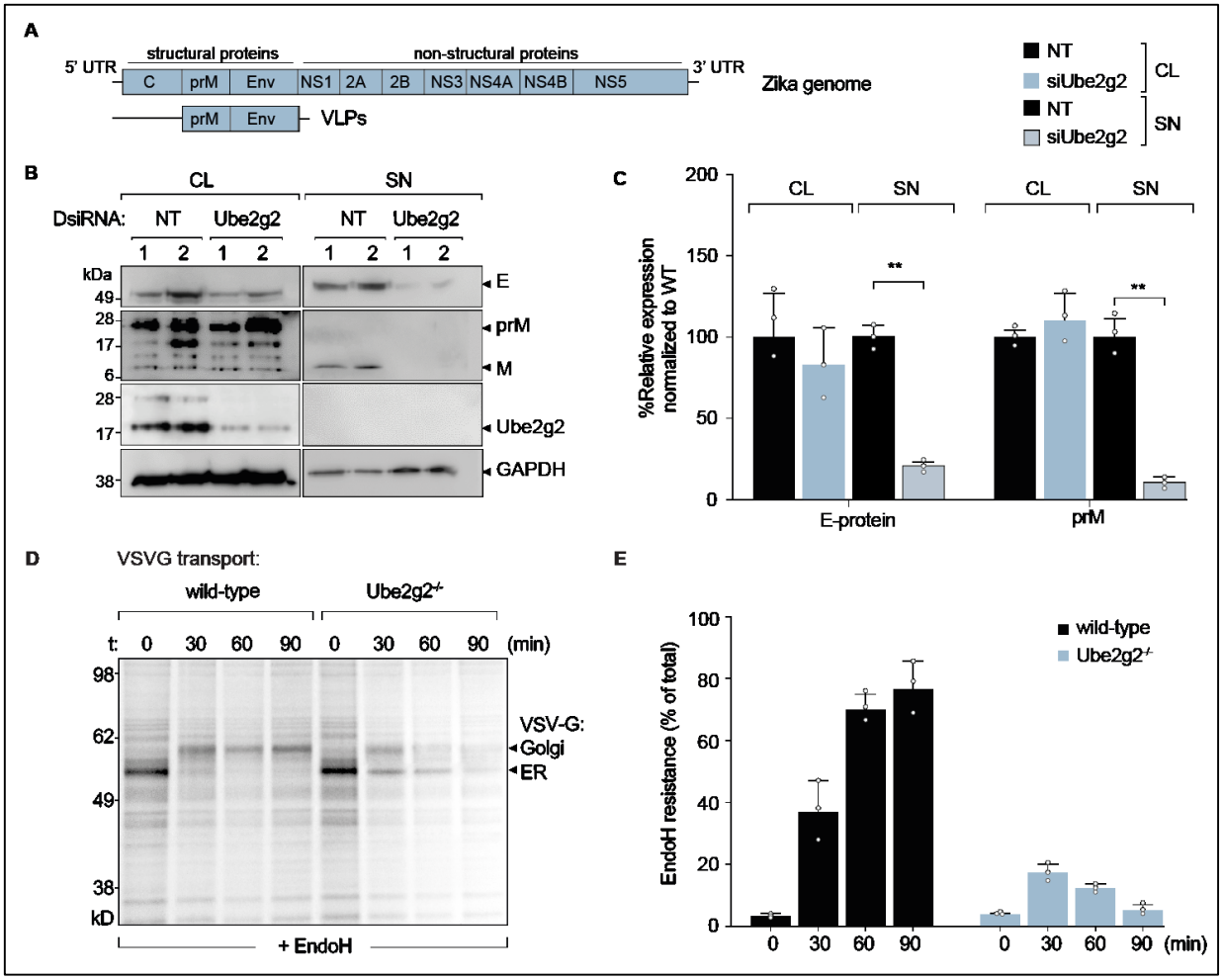


Figure 5.13 Ube2g2 is instrumental for viral assembly and release. A) Schematic of the virus-like-particle (VLP) construct stably transduced in HeLa cells. B) The constitutively VLP-secreting

HeLa-ZIKV-VLP cell line was subjected to Ube2g2 or non-targeting (NT) siRNA. Lysates (CL) and supernatants (SN) from cells were collected and immunoblotted for ZIKV viral PrM and E proteins. C) Quantification of viral PrM and E protein levels in cell lysate and supernatant of NT-siRNA-treated or Ube2g2-depleted cells. The protein levels are normalized to NT-siRNA-treated cells (WT). Error bars represent mean ± SD, $n = 3$ biologically independent samples; $^{**}P < 0.01$; $^{***}P < 0.001$ (compared with wild-type by ANOVA followed by one-sided Dunnett's test). D) Wild-type and Ube2g2$^{-/-}$ cells were transfected with vesicular stomatitis virus glycoprotein using Lipofectamine3000. The cells were pulsed with [35S]cysteine/methionine at 24 h.p.t. and chased in cold media for indicated time intervals. VSV-G was immunoprecipitated at each time point and treated with EndoH at 37 °C for 1 h, resolved by SDS-PAGE and detected by autoradiography. The image is representative of 3 independent experiments. E) Quantitation of EndoH-resistant forms of VSVG was determined from densitometric analyses of autoradiograms. Data is presented as mean ± SD, n = 3 biologically independent samples.

5.3.7. ZIKV-induced lipophagy depends on Ube2g2 and is required for efficient viral release

To address how Ube2g2 is involved in viral release, it was hypothesized that lipophagy could play a role. This form of selective autophagy of lipid droplets is thought to be a consistent feature for membrane remodelling during flavivirus infections and suggested to be critical for assembly and secretion of progeny virions (106, 114, 194, 206). Previous work from the group has shown that Ube2g2's co-factor, Aup1 was instrumental for DENV-triggered lipophagy (114). It was therefore hypothesized that Ube2g2 could be instrumental for ZIKV-induced lipophagy and subsequently virus assembly/secretion. As lipid droplet turnover has previously been shown to contribute to secretion of heavy cargo through the secretory pathway, this could also explain the VSV-G trafficking defect observed in Ube2g2 deficiency (219).

To assess lipophagy induction, lipid droplet abundance was assessed in both the VLP set-up as well as *live virus* infection. The HeLa-ZIKV-VLPs cells were transfected with siRNA targeting Ube2g2 or control siRNA and stained using NileRed and α-ZIKV-E protein. The lipid droplet abundance was quantified using %Nile Red positive area per cell. Lipid droplet abundance was clearly decreased in wildtype VLP-secreting cells but was inhibited in Ube2g2 deficient cells, indicative of defective lipophagy (**Figure 7.14A,B**). In line with these findings, a similar phenotype was found in ZIKV-infected wildtype and Ube2g2$^{-/-}$ cells, with a significant loss in lipid droplets at 48 and 72 h.p.i. in wildtype cells. Whereas Ube2g2$^{-/-}$ cells do not show LD hydrolysis, but rather an accumulation of LDs (**Figure 5.14C,D**).

To confirm that lipid droplet abundance is decreased due to autophagosomal consumption of lipid droplets, immunofluorescent images were obtained in ZIKV-infected cells. Using cells expressing eGFP-Ube2g2, Ube2g2 can be seen localizing to lipid droplets by either pulsing with a fluorescent fatty acid reporter (Bodipy 558/568 C12) (**Figure 5.15A**) or staining with Nile Red to visualize lipid droplets (**Figure 5.15C**). Moreover, co-localization with lysosomal marker Lamp1 can be seen, indicative of lipophagy being at play (**Figure 7.15E**). This becomes particularly apparent by employing the lysosomal inhibitor Bafilomycin A1 to block autophagic flux. Supporting that Ube2g2 facilitates lipophagy as part of the Aup1-Ube2g2 complex.

Finally, it was assessed whether virus production could be rescued by exogenously supplying free fatty acids to bypass impaired lipophagy in Ube2g2$^{-/-}$ cells. While virus production could be rescued in Aup1-deficient cells, it could not in Ube2g2-deficient cells (**Figure 5.14E)**. This further supports Ube2g2 having an additional function in the virus lifecycle, whereas Aup1 is acting solely in support of the infection in the Ube2g2-Aup1-complex facilitating lipophagy.

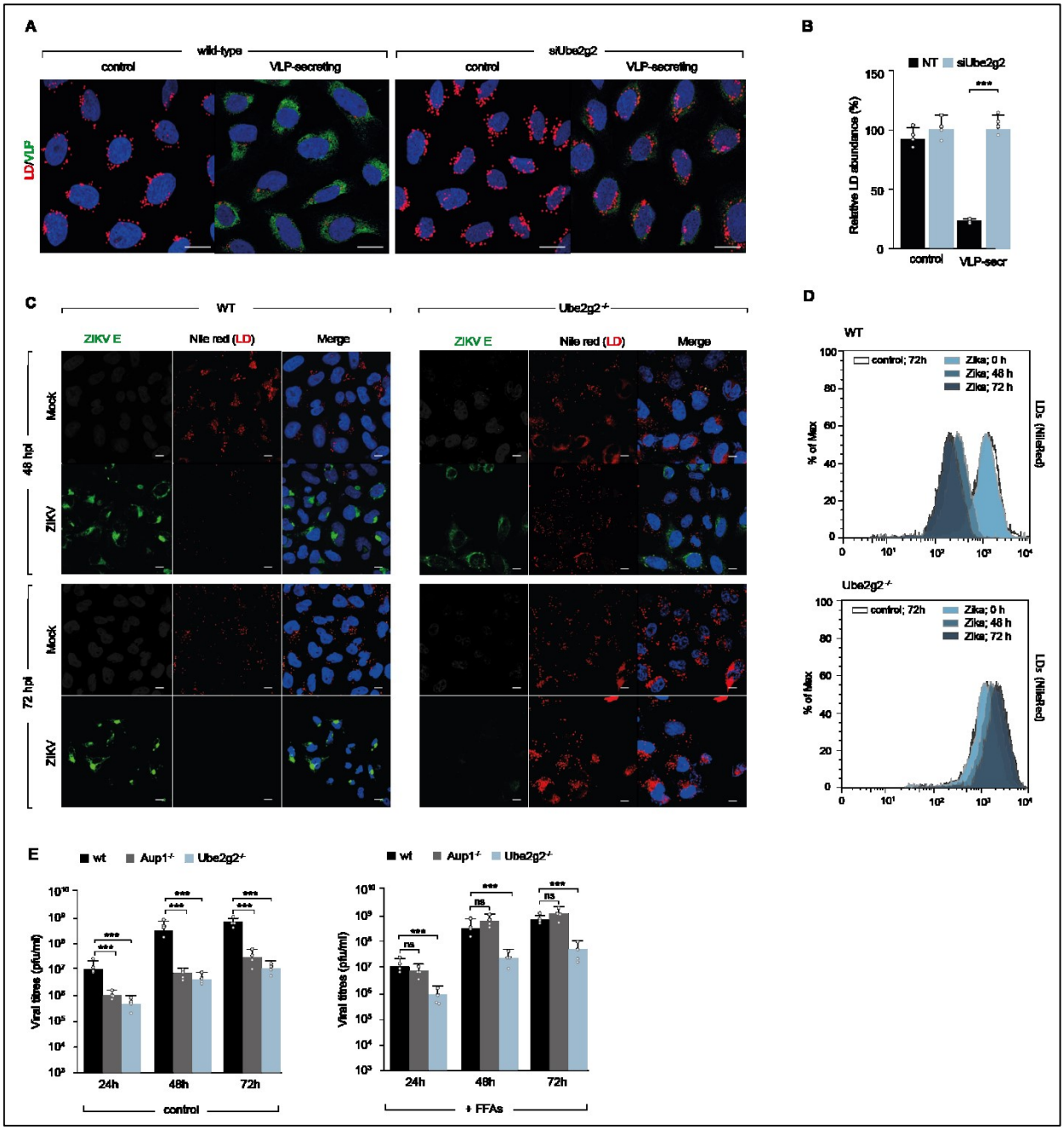


Figure 5.14 ZIKV-induced lipophagy is dependent on Ube2g2. A) VLP-secreting cells were treated with non-targeting and Ube2g2-targeting siRNA followed by Nile red staining for lipid droplets and anti-ZIKV-E staining for VLPs. B) Abundance of lipid droplets was quantified by Nile red positive area over 500 cells. Error bars represent mean ± SD of relative LD abundance as % of control cells. n = 4 biologically independent samples. **P < 0.01; ***P < 0.001 (compared with wild-type by ANOVA followed by one-sided Dunnett's test). C) Wild-type and Ube2g2$^{-/-}$ cells were infected with ZIKV at MOI 5. Cells were fixed at 48hpi and 72hpi and visualized using anti-ZIKV-E staining (488) and Nile red dye. Nuclei were stained with Hoechst. (Scale bars = 5 µm). D) LDs in mock and Zika-infected wild-type and Ube2g2$^{-/-}$ cells were quantitated by flow cytometry at 48 h and 72 h post infection. E) Wild-type, Aup1$^{-/-}$ and Ube2g2$^{-/-}$ cells were mock or virus-infected and grown in medium supplemented with -/+ FFAs (10 mM) conjugated to BSA for indicated time points. Viral titres were measured using plaque assay. Data are presented as mean ± SD, n = 4 biologically independent samples; ***P < 0.001 (compared with wild-type by ANOVA followed by one-sided Dunnett's test).

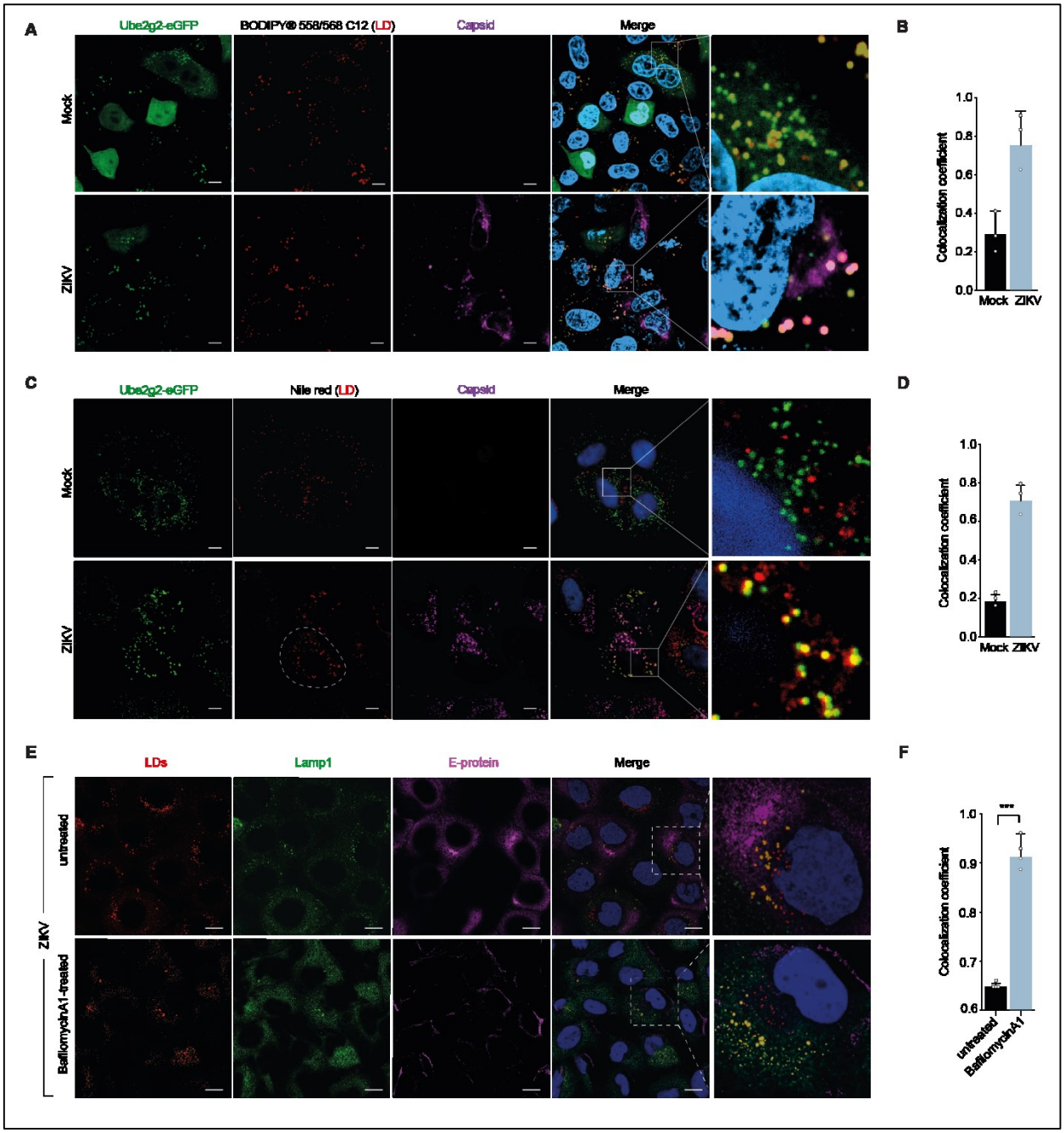


Figure 5.15 Ube2g2 relocalizes to lipid droplets upon ZIKV-infection to induce lipophagy. A-D) Wild-type cells expressing GFP-Ube2g2 were either mock or Zika-infected at MOI 5. Cells were fixed at 24hpi and probed for Ube2g2 and LDs. LDs were stained with either BODIPY-C12 (A,B) or Nile Red dye (C,D). Nuclei were stained with Hoechst; (Scale bars = 5 µm). Co-localisation of Ube2g2 with LDs was measured using Pearson's correlation coefficient. Data is presented as mean ± SD, n = 3 biologically independent samples. E,F) Wild-type cells treated with DMSO only or with Bafilomycin A1 (100 nM in DMSO) were infected with ZIKV (MOI 5, 24 h), fixed with 4% PFA and visualised with Nile Red, anti-Lamp1 and anti-E antibodies. Colocalization of LDs with Lamp1 was determined using Pearson's correlation coefficient (Scale bars=10µm). Data is presented as mean ± SD, n=4 biological replicates. **P < 0.01; ***P < 0.001 (compared with wild-type by ANOVA followed by one-sided Dunnett's test).

5.4. Discussion

It is well established that +RNA viruses require massive rearrangements of the ER to establish replication compartments along ER-derived membranes (89, 199, 200). This process poses a massive burden on the ER to synthesize these new components as well as viral proteins. This commonly results in ER stress in which the unfolded protein response is induced. For both corona- and flaviviral infection, UPR induction is observed (89, 169, 194). In particular the IRE1α pathway is triggered (89, 101). This pathway splices XBP1, which in spliced form can induce synthesis of ER stress chaperones and ERAD components. This allows for ER-expansion but comes at a cost and can induce apoptosis. How +RNA viruses are able to orchestrate UPR induction, followed by ER expansion and ER stress recovery to complete the ER remodelling, without inducing apoptosis is poorly understood. With this chapter, mechanistic insights are provided into how Zika virus is capable of selectively manipulating ERAD components and autophagy to allow for the required ER reorganizations in support of viral production. It is shown that Ube2g2 drives degradation of a subset of ER stress response proteins whilst inducing lipophagy, to allow for efficient establishment of the ER compartments for replication and assembly.

Deficiency of Ube2g2 resulted in a combined defect in lipophagy and ER stress recovery. This ultimately led to the Chmp4-Sec62-dependent ER-phagy induction, whereby the replication complexes get degraded and replication is attenuated. By delineating the specific steps in Zika viral-induced ER reorganization, we determined that Ube2g2 was required for Aup1-Ube2g2-dependent lipophagy as well as for degrading specific chaperones to prevent apoptosis and allow for membrane proliferation. **Figure 5.16** depicts the current understanding of Ube2g2's dual activity in the Zika viral life cycle. By studying the role of Ube2g2 in the viral life cycle, mechanistic insights were obtained into how the specific intermediate steps are performed for efficient biogenesis of viral replication organelles. Moreover, it shows how Zika virus has managed to obtain an intricate balance in inducing selective autophagy pathways to support the viral life cycle.

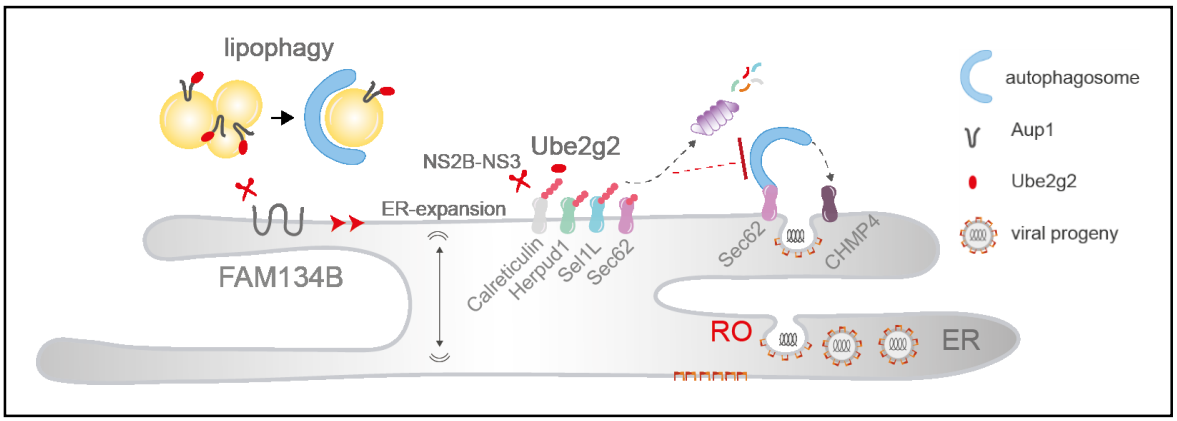


Figure 5.16. Working model for Ube2g2's dual activity in ZIKV-infection. Ube2g2 acts in complex with Aup1 to induce lipophagy in ZIKV infection. Lipophagy provides free fatty acids and energy for viral assembly and release through β-Oxidation. Alongside, Ube2g2 is required to prevent ER-phagy induction by selectively degrading ER stress chaperones cleaved by ZIKV NS3. In absence of catalytically active Ube2g2, ER stress chaperones are stabilized and induce Sec62-Chmp4-dependent ER-phagy by which ZIKV replication complexes are degraded.

Whilst the host dependency factor Ube2g2 is shown to play a key role in +RNA virus infection in this chapter, targeting the enzyme for host-directed antivirals (HDAs) could prove difficult as the human E2 repertoire only comprises of 40 E2 enzymes. As E2 enzymes are involved in many host cellular processes, targeting Ube2g2 could lead to toxicity and adverse effects. It could however be interesting to interfere in a specific interaction or to dysregulate the intricate balance in selective autophagy usage. As an example, we have shown that upon Ube2g2 knock-out, viral-induced lipophagy is inhibited, suggesting that the Aup1-Ube2g2 complex is essential for recruitment of NS4A and the autophagophore. Interfering in this complex or the interaction with NS4A, could be a promising HDA opportunity.

Similarly, dysregulating the balance in selective autophagy more specifically, might be a more promising route to investigate than the general broadly-targeting HDAs such as Chloroquine. This antimalarial drug has been proven efficient in blocking +RNA viral replication by blocking autophagy, however is plagued by reports of adverse effects (220, 221). Rather than generally targeting autophagy, perhaps selectively stimulating Chmp4-Sec62-dependent ER-phagy, could be an interesting avenue to explore.

An easier opportunity could be to shield FAM134B from cleavage by NS3 and thereby prevent ER-expansion required for establishment of RO and VP. This most likely will increase immune sensing and clearance of the virus. Moreover, it could have broad-spectrum applications, as most +RNA viruses rely on ER-expansion for establishment of virus production. For flaviviruses, at least West-Nile Virus (WNV), DENV and ZIKV NS3 have been shown to cleave FAM134B and due to the high conservation of the binding pockets of NS3 among flaviviruses, this is expected to be broader applicable to Yellow Fever Virus (YFV) and Japanese Encephalitis Virus (JEV) (111, 222). Shielding specific targets from NS3 cleavage could be a more suitable approach in comparison to targeting NS3 directly. Most importantly, because viral NS3 could potentially obtain resistance. Another aspect is that certain cleavage products of NS3 have been shown to have antiviral activity. A study by Cao et al. showed that viral production is reduced due to heat shock protein DNAJB6 (Hsp40) interacting with Yellow Fever Virus (YFV) NS3 (223). Maintaining these interactions could be beneficial. Moreover, shielding FAM134B from cleavage could have even more broad-spectrum potential, as SARS-CoV2 has been shown to also have adopted a mechanism to specifically hijack FAM134B to prevent ER-phagy (103).

Alternatively, based on the results obtained in the pulse-chase assay for ER chaperones, it could be interesting to investigate the role of Atlastin-3 (ATL3) further. This protein was found to accumulate during infection, but is selectively degraded upon Ube2g2 knock-out. The accumulation could indicate for a proviral role of this protein in infection. The hypothesis would be that ATL3 could play an instrumental role in stalling ER-phagy and supporting secretory autophagy. Controversially, in SARS-CoV2 infection ATL3 was shown to be selectively targeted to p62 condensates, similar to FAM134B, in support of viral replication (103). Further research into the role of ATL3 in +RNA virus infection is thus required. Considering how divergent the replication strategies of flaviviruses and coronaviruses are, with coronaviruses establishing DMVs instead of ER-invaginations for replication, a different balance in selective autophagy could be required. Subsequently, autophagy cargo receptor proteins usage might be different to fit the replication strategy.

Nevertheless, developing inhibitors or PROTACs (Proteolysis Targeting Chimeras) targeting ATL3 could potentially lead to adverse effects. This concern arises from the fact that hereditary mutations in the ATL3 gene, which render the protein inactive, have been associated with neuropathy (224). This suggests that ATL3 plays an essential role in normal neuronal function. Given this context, it would be interesting to investigate whether ATL3 is being specifically exploited during Zika virus infection. If ATL3 is actively hijacked by Zika virus, this interaction could potentially contribute to the neuronal manifestations observed in Zika virus infections, such as microcephaly and other neurological disorders. Understanding this relationship could provide valuable insights into the pathogenesis of Zika virus and highlight potential therapeutic targets that are safer and more specific. A previous study by Neufeldt et. al. suggested that knock down of ATL3 resulted in reduced Dengue virus (DENV) production by preventing viral release (204). They observed that DENV virions increasingly accumulated in ER cisternae. Additionally, the study demonstrated that ATL3 directly interacts with ADP-ribosylation factor 4 (ARF4), with this interaction increasing upon DENV infection. ARF4 is a factor previously identified in our group as being essential for flaviviral maturation and release (177). Interestingly, Neufeldt et al. particularly suggested that both ARF4 and ATL3 are essential for the alternative secretion of DENV, as VSV-G maturation is unaffected (204). Suggesting that ATL3 could perhaps play an essential role for the switch in ER-phagy to secretory autophagy. In support of this hypothesis, secretory autophagy was previously suggested to be utilized for flaviviral secretion and it is known that ATL3 can be alternatively secreted in a similar fashion (156, 177).

In this chapter the mechanistic underpinnings of the proviral role of Ube2g2 have been established for Zika virus. However, as therapeutic targeting of Ube2g2 itself could proof difficult, it will be essential to assess whether Ube2g2's dual action is conserved among

+RNA viruses, to determine the best target in selective autophagy for potential HDA development.

Chapter 6 Discussion

In this thesis we have established an in vitro system for studying the role of SARS-CoV2 ORF8 variants. Using A549 stable cell lines we investigated the role of ORF8 in pathogenesis and explored the functional implications of natural and structural mutants.

We showed that the ER-signal peptide allows for all variants to be translocated to the ER, whereas the deletion of the ER signal peptide prevented this translocation (**Supp.Fig. 2.5**). Moreover, we confirm that the N78 residue is the only residue responsible for glycosylation of this secretory protein and that the C20-residue is not essential for oligomerization **(Figure 2.1, 3.1**). We demonstrate that all ORF8 variants, except ΔSP-ORF8, can be secreted in vesicles or as aggregates, primarily as monomers, tetramers, or higher-order oligomers. This secretion can occur delayed through the classical secretory pathway or they can be secreted through alternative secretion routes, with tetramers detected as early as 30 minutes after synthesis (**Figure 2.3, Supp.Figure 3.1**). These early-secreted tetramers are not glycosylated, suggesting alternative secretion. Notably, these tetramers are only observed for ORF8*ancestral*, -C20S, and ORF8*gamma*, but not in ORF8-*ancestral*-C20S-N78D, indicating that the N78 residue could be essential for tetramer secretion, but not by means of providing glycosylation. Furthermore, when the N78 residue was mutated to prevent glycosylation, there was a shift towards increased higher-order oligomerization, suggesting that N-glycosylation may limit oligomerization options for ORF8 (**Figure 3.1**). The observation of secreted oligomers not being glycosylated may connect previous studies that separately indicated the importance of secreted oligomeric ORF8 or alternatively secreted non-glycosylated ORF8 in inducing cytokine storm (83, 129).

Aside from the effect of ORF8 mutations on the dynamics of ORF8 itself, we explored the broader functional implications of the mutations within this system. We first addressed the observation of autophagy-dependent cell surface downregulation of MHC-I by Zhang et al. (87). We confirmed that all natural variants are capable of downregulation MHC-I in an

overexpression set up: ORF8*ancestral*, *-gamma* and *–alpha*. Moreover, using pulse-chase we show that autophagic flux inhibition by BafA1 indeed rescues MHC-I expression for ORF8*ancestral* (**Figure 2.3**). Whereas ORF8*gamma* affects MHC-I expression at the ER quality control stage and ORF8*alpha* showcased an intermediate phenotype. In this pulse-chase, we also noticed the limited host protein synthesis for particularly A549 cells expressing ORF8*ancestral*. We believe that this could possibly explain why rSARS-CoV2 doesn't show significantly increased viral production in comparison to rSARS-CoV2-ΔORF8, despite the observed supportive role in DMV formation and growth (**Figure 2.8**, **4.5**). A recent study by Kim et al.; namely suggested that Spike maturation was limited by ORF8 inhibition of host protein synthesis (225).

Although the natural variants are suggested to interfere with antigen presentation through different mechanisms, all three variants were clearly shown to disrupt the autophagy pathway. By TEM and quantitative HiBiT assay, we showed that the autophagosomal compartment was diminished in a C20-dependent manner for ORF8*ancestral*, whereas *-gamma* and *-alpha* accumulated autophagosomal vesicles, particularly lamellar bodies and mature autophagosomes/-lysosomes respectively (**Figure 2.5-2.7**).

Considering that the autophagy pathway was indicated to be essential for DMV formation previously, we investigated in **Chapter 4** whether ORF8 variants could play a role in DMV formation (105, 226). For this purpose, we successfully established a Doxycycline-inducible DMV-producing cell line expressing *ancestral* Nsp3, -4 and -6, improving on the current studies using transfection (**Figure 4.1A-B**). Using this system and using *live virus* infection we showed that ORF8*ancestral* not only prevents ER-phagy, as previously suggested by Tan et al., it also actively supports DMV growth and reticulovesicular network establishment (**Figure 4.1C, 4.3, 4.5**) (103). Moreover, we show that the three natural variants of SARS-CoV-2 ORF8 have distinct effects on DMV formation. Both ORF8*ancestral* and *-alpha* are capable of assisting in DMV growth and reticular vesicular

network establishment. With specifically ORF8*ancestral* promoting the expansion of the DMV network, while ORF8*alpha* induces a more pronounced DMV condensation (**Figure 4.3**). Moreover, we observed that a modest increase in size of LDs accompanies DMV production, which is even more significantly augmented by ORF8*alpha* expression. This could result from ORF8-induced lipid metabolism reprogramming, wherein we see an increase in lipase interactions (**Supp.Figure 4.2**). Perhaps, ORF8 may interact with lipases to block lipolysis. SARS-CoV-2 has been observed to prevent lipolysis early in virus infection, which is believed to be another immune modulation strategy of the virus that prevents the production of inflammatory lipid mediators (116, 227).

With this thesis we show that ORF8*alpha* (B1.1.7.) in contrast to suggestions in literature, is able to exert an immunomodulatory function (10). We show, that ORF8*alpha* expression alone, does not only still allow for cell surface MHC-I downregulation, it also results in significant alterations in the host cell; as observed by the accumulation of degradative vesicles (**Figure 2.2, 2.6**). Moreover, ORF8*alpha* was suggested to alternatively support DMV formation, with an accumulation of larger LDs and larger DMVs (**Figure 4.3**). Whether this results in functional DMVs, or whether similar to ΔORF8-rSARS-CoV2 infection, these 'larger DMVs' by IF indicate engulfed DMVs, remains to be determined. This will be addressed by TEM of the DMV-producing cell lines co-expressing *alpha* or ΔORF8-rSARS-CoV2-infected Calu-3-ORF8*alpha* cells.

It is important to note that these results are still preliminary, especially since ORF8*alpha* expression could not be confirmed at the protein level as the StrepII-tag is non-functional. Direct detection using ORF8-specific antibodies is limited, as most antibodies perform sub-optimally, and those with reported antigen specificity are typically not directed at the 0-26 amino acid region. Furthermore, the expected size of the produced protein (~3 kDa) further hinders efficient detection. The successful introduction of the construct was, however, confirmed by means of mRNA detection (**Supp.figure 2.2A**). To facilitate the study of ORF8*alpha* protein dynamics and interactions, a stable cell line expressing C-

terminally V5-tagged ORF8*alpha* has been generated, and a C-terminal HiBiT-tagged ORF8*alpha* will be developed. The working hypothesis is that the presence of a free cysteine enables covalent dimerization, which plays a central role in ORF8*alpha*'s interactions and host modulation.

As discussed in **Chapters 2-4**, ORF8*gamma* also displays a distinct phenotype compared to ORF8*ancestral*. Unlike other variants, ORF8gamma may not actively reprogram the cell. Instead, the observed phenotype could result from the consequences of ER retention, overwhelming ER quality control, or disruptions in acetylation processes. This is supported by TEM and MS observations, which showed an increase in late degradative vesicles, particularly lamellar bodies, as well as enriched interactions with ribosomal units, mitochondrial proteins, ER-resident proteins, and proteins involved in oxidative stress (**Figure 2.6, 3.4, Table 3.3**).

The hypothesis was that ORF8*gamma* could cause a folding deficiency, and thereby cause these effects, but similar to ORF8*ancestral*, -*gamma* is detected extracellularly as glycosylated monomer and high-order oligomer (**Figure 2.2A, 3.1A,C**). Notably, oxidoreductases and other stress-related proteins were found in complex with ORF8*gamma* extracellularly, suggesting that secretory autophagy or lamellar body secretion, a crucial organelle in the AT2 cells for providing surfactant in the lungs, might be involved (**Figure 3.4**). Particularly, we found evidence for lamellar body secretion by enrichment for lamellar body specific interactors intracellularly such as NPC2 or SLC12A2. The biogenesis of LBs in alveolar cells is still poorly understood, however there have been suggestions that Multi-Vesicular Bodies (MVBs) are the precursor, as they are essential for providing the surfactant proteins. Whereas the route for surfactant phospholipids delivery to LBs is a lot less understood, but is shown to not be MVB- nor Golgi-dependent. Instead it has been suggested to require autophagy or to be directly transported from the ER (136, 228, 229). Particularly these last suggestions, let us speculate that ER-phagosomes could

be a source for LB biogenesis and could provide a mechanism by which ORF8*gamma* can be secreted. Both of which warrant further investigation.

Aside from characterizing the functional implications of ORF8 natural variants, this thesis also presents a hypothesized model for ORF8's role in SARS-CoV-2 DMV formation, addressing the currently poorly understood mechanistic underpinnings of DMV formation (**Figure 4.7**). Utilizing our ORF8-interactome analysis from **Chapter 3**, we identified shared interactors with Nsp3, Nsp4, and Nsp6, as documented in the literature (**Table 4.5**, **Figure 4.6**). One of the key pathways we identified involves the VMP1-TMEM41b-ER-phagophore axis, which could play a crucial role in DMV formation, particularly since VMP1, TMEM41b, and RTN4 have all been shown to be essential host dependency factors (157, 188, 193, 226, 230). We propose that ORF8, by interacting with ER-localized lipases, scramblases, Tsg101 and Chmp4b may support DMV growth by mobilizing lipids and ensure turnover is prevented by recruiting ATP6AP1 to the DMV site. These interactions will be confirmed and these proteins will be investigated for their direct contribution to ORF8 function and DMV formation, by either siRNA treatment or CRISPR-Cas9 knock-out.

Returning to the complex relationship between ER-stress recovery and DMV establishment, this VMP1 pathway is particularly noteworthy. A recent study has shown that knocking out VMP1 strongly activates PERK while suppressing ARF6- and IRE1α-dependent UPR under stress conditions (230). We could speculate that ORF8 and/or Nsp3-4 directly interacting with VMP1 could exert a similar function. It could allow for exploitation of the PERK-dependent UPR arm involved in ER expansion and autophagy, without inducing the other UPR arms, to tailor UPR induction to support DMV formation. This could explain the limited UPR induction observed in SARS-CoV2 infection in comparison to other coronaviruses, with only partial activation of IRE1α and activation of PERK (6, 7). Also explaining why Nsp6 hijacking BiP solely induced PERK activation and not the other arms of UPR (8). This hypothesis should be testing by assessing PERK activation in presence of ORF8 and/or Nsp3/4.

In conclusion, we have shown that ORF8 exerts multiple functions and these can drastically change for natural variants. This thesis highlights the complexity of ORF8's involvement in cellular reprogramming and the importance for investigating the evolution of this protein. Notably, we have shown that the natural variants all maintain the capacity to downregulate MHC-I, but they achieve this through different mechanisms. Only ORF8*ancestral* shows BafA1-dependency, whereas the MHC-I-phenotype for ORF8*alpha* is less pronounced and ORF8*gamma* interferes at the maturation stage. Particularly, we show that all three natural variants modulate autophagy differently, with ORF8*alpha* and ORF8*gamma* leading to accumulation of autolysosomal vesicles and ORF8*ancestral* to their secretion. With particularly the accumulation of the specialized lysosomal vesicle, lamellar bodies, for ORF8*gamma*.

Moreover, this study is the first to explore the extracellular interactome of ORF8. Not only providing interactors that could have implications for ORF8's involvement in the immune response, such as IL-18 and DDT, but also providing leads for secretion routes used (**Supp.Figure 3.9**). Based on the extracellular and intracellular interactomes of ORF8 variants, it was suggested that ORF8*gamma* could utilize LBs as an alternative secretion route, whereas ORF8*ancestral* could be employing secretory ER-phagosomes (**Figure 3.4; 2.5, Supp.Figure 3.7**). A proposed model for the secretion pathways utilized by ORF8 variants can be seen in **Figure 6.1**. These pathways are poorly described and by investigating these pathways through this viral protein, we could assist in elucidating the mechanistic underpinnings of these pathways.

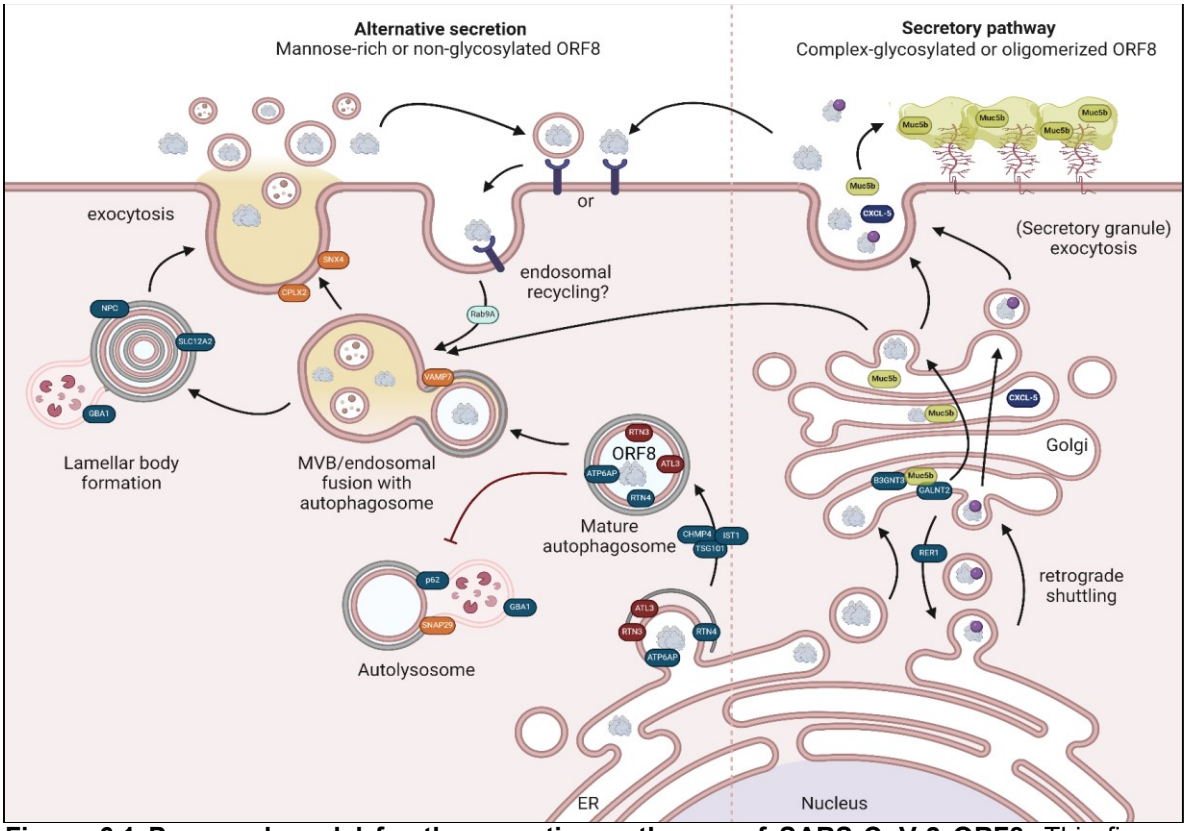


Figure 6.1 Proposed model for the secretion pathways of SARS-CoV-2 ORF8. This figure illustrates the hypothesized secretion routes for SARS-CoV2 ORF8 variants, highlighting unique and significant interactome hits identified in **Chapter 3** that are involved in these pathways. ORF8 is proposed to utilize both conventional and alternative secretion mechanisms, potentially involving amphisomes/multivesicular bodies (MVBs), lamellar bodies, and direct lysosomal secretion. Furthermore, ORF8 may access these alternative pathways through the modulation of ER-phagy processes. Created using BioRender.com.

Additionally, it has been established that serum levels of phospholipase A2, IL-18 and DTT are correlated with severe COVID-19; all proteins, or in the case of phospholipase A2 its activator PLAA, we have identified to be co-secreted as interactor of ORF8 (**Supp.Figure 3.9**). We would like to confirm that ORF8 is responsible for their secretion using our recombinant virus infection set-up, to address whether there is a direct link between ORF8 secretion and development of severe disease.

Finally, in **Chapter 5** we highlight how another +RNA virus, ZIKV, is capable to similarly fine-tune autophagy pathways; by hijacking Ube2g2 to induce lipophagy and prevent ER-phagy early in infection, to establish replication organelles and assembly sites (**Figure 5.16**). In this study, Ube2g2 was also shown to be a host dependency factor in common

coronavirus infection (**Figure 5.3E**). We aim to assess whether SARS-CoV2 similarly relies on Ube2g2 for DMV formation and assembly site establishment. Based on the observation that SARS-CoV2 and Zika replicate at distinct locations in the ER, in DMVs formed from ER-tubules versus RO invaginations in ER-sheets respectively (170, 199, 231), a dissimilar reliance on ER-phagy is expected. This is because ER-phagy receptors also have distinct locations within the ER, with for example FAM134B enriched in ER-sheets. Knock-out of FAM134B was therefore also shown not to affect SARS-CoV2 infection (170). We would expect instead that modulation of ATL3 or RTN3 could be more important for ER expansion in SARS-CoV-2 infections, as they are found on the ER tubules (232). These are modulated in SARS-CoV2 infection, as previously discussed, but this is suggested not to involve Ube2g2 or the ERAD process (103). Moreover, there is currently no evidence for lipophagy induction in SARS-CoV2 infection. Instead, lipid metabolism rewiring by SARS-CoV2 is indicated to prevent lipophagy and induces lipid droplet accumulation (233). This highlights how host cell reprogramming can be virus-specific and emphasizes the value of interactome studies in identifying targeted therapies for specific viruses.

In conclusion, this thesis underscores the intricate fine-tuning mechanisms +RNA viruses have developed for host cellular remodeling. It reveals how these viruses can reshape the endoplasmic reticulum (ER) in diverse ways, alter lipid metabolism, and modify secretory pathways. Although, particularly for the SARS-CoV2 chapters, interactors and associated hijacked pathways still require confirmation, this study offers valuable insights into host dependency factors that may be targeted for antiviral strategies.

Apart from intracellular rewiring, we have also shown using Chapter 3 that ORF8 variants are secreted and can interact with numerous extracellular proteins, many of which are involved in immune signalling.

We therefore believe it is crucial to study how natural variants affect ORF8's functions outside of the cell. This is because ORF8 likely plays a key role in modulating the immune response in the extracellular space, as previous studies have linked particularly extracellular ORF8 to cytokine storm induction (82, 83, 234). We therefore have produced, mammalian-produced purified ORF8-proteins and together with conditioned medium from stable cell lines, recombinant SARS-CoV2-infected cells and rVaccinia infected cells, we will investigate the contribution of secreted ORF8 to pathogenesis. Particularly, our preliminary observation of rVaccinia-infected alveolar cells responding differently to ORF8 expression, when co-cultured with Thp1 cells, indicates for ORF8's involvement in cell-cell communication and subsequent immune signalling (**Supp.Figure 2.4**).

That ORF8 is capable of interfering in cell-cell communication was previously suggested by the observation of ORF8 binding to the cell surface immune marker IL17RA (4). Moreover, we have identified a couple of cell surface receptors ourselves as direct interactors in our extracellular interactome, such as TFRC, CD44, Nrp1 and IL6ST, that warrant validation. It will be assessed whether ORF8 can actively be internalized or whether it is inducing a signalling cascade, by studying several endocytosis routes as mentioned in the discussion in **Chapter 3** by blocking certain signaling cascades or knocking down indicated cell surface interactors of ORF8 such as Nrp1. Based on the observation of secreted ORF8 being released in vesicles containing endosomal and MVB markers, it is suggested that ORF8 could be actively internalized and recycled.

This thesis advances our understanding of ORF8's intricate role in pathogenesis and the precise ways in which +RNA viruses can modulate host cellular processes, particularly focusing on autophagy. It also underscores that while initial proteomic screens and transfection studies have guided SARS-CoV-2 viral protein research, the results from these studies often fail to capture the full functionality of the proteins. Our findings, obtained through VLP and DMV setups, reveal significantly altered interactions, highlighting the

limitations of transfection-based approaches in reflecting the complete biological behaviour of these viral proteins. Additionally, this thesis has shown that a secretory immune-modulatory viral protein like ORF8 can have a multifaceted role in infection, especially when it has broadly-recognized dimerization interfaces. This thesis presents the first extracellular ORF8 interactome, revealing direct interactors that may explain ORF8's role in cytokine storms. Additionally, it offers insights into the vesicular origins and pathways involved in ORF8 secretion, which could hold therapeutic potential.

References

1. Chan JF, Kok KH, Zhu Z, Chu H, To KK, Yuan S, et al. Genomic characterization of the 2019 novel human-pathogenic coronavirus isolated from a patient with atypical pneumonia after visiting Wuhan. Emerging microbes & infections. 2020;9(1):221-36.
2. Zhou P, Yang X-L, Wang X-G, Hu B, Zhang L, Zhang W, et al. A pneumonia outbreak associated with a new coronavirus of probable bat origin. Nature. 2020;579(7798):270-3.
3. WHO COVID-19 Dashboard [Internet]. World Health Organisation. 2020 [cited 30/11/2021]. Available from: https://covid19.who.int/
4. Giamarellos-Bourboulis EJ, Netea MG, Rovina N, Akinosoglou K, Antoniadou A, Antonakos N, et al. Complex Immune Dysregulation in COVID-19 Patients with Severe Respiratory Failure. Cell Host Microbe. 2020;27(6):992-1000.e3.
5. Munnur D, Teo Q, Eggermont D, Lee HHY, Thery F, Ho J, et al. Altered ISGylation drives aberrant macrophage-dependent immune responses during SARS-CoV-2 infection. Nature Immunology. 2021;22(11):1416-27.
6. Li JY, Liao CH, Wang Q, Tan YJ, Luo R, Qiu Y, et al. The ORF6, ORF8 and nucleocapsid proteins of SARS-CoV-2 inhibit type I interferon signaling pathway. Virus Res. 2020;286:198074.
7. Beyer DK, Forero A. Mechanisms of Antiviral Immune Evasion of SARS-CoV-2. J Mol Biol. 2021:167265.
8. Xu D, Biswal M, Neal A, Hai R. Review Devil's tools: SARS-CoV-2 antagonists against innate immunity: Curr Res Virol Sci. 2021 Nov 18:100013. doi: 10.1016/j.crviro.2021.100013.
9. Kasuga Y, Zhu B, Jang K-J, Yoo J-S. Innate immune sensing of coronavirus and viral evasion strategies. Experimental & Molecular Medicine. 2021;53(5):723-36.
10. Wagner C, Kistler KE, Perchetti GA, Baker N, Frisbie LA, Torres LM, et al. Positive selection underlies repeated knockout of ORF8 in SARS-CoV-2 evolution. Nature Communications. 2024;15(1):3207.
11. Hachim A, Kavian N, Cohen CA, Chin AWH, Chu DKW, Mok CKP, et al. ORF8 and ORF3b antibodies are accurate serological markers of early and late SARS-CoV-2 infection. Nature immunology. 2020;21(10):1293-301.
12. Guan WJ, Ni ZY, Hu Y, Liang WH, Ou CQ, He JX, et al. Clinical Characteristics of Coronavirus Disease 2019 in China. N Engl J Med. 2020;382(18):1708-20.
13. Huang C, Wang Y, Li X, Ren L, Zhao J, Hu Y, et al. Clinical features of patients infected with 2019 novel coronavirus in Wuhan, China. Lancet. 2020;395(10223):497-506.
14. Kuypers FA, Rostad CA, Anderson EJ, Chahroudi A, Jaggi P, Wrammert J, et al. Secretory phospholipase A2 in SARS-CoV-2 infection and multisystem inflammatory syndrome in children (MIS-C). Exp Biol Med (Maywood). 2021;246(23):2543-52.
15. Snider JM, You JK, Wang X, Snider AJ, Hallmark B, Zec MM, et al. Group IIA secreted phospholipase A2 is associated with the pathobiology leading to COVID-19 mortality. J Clin Invest. 2021;131(19).
16. Del Valle DM, Kim-Schulze S, Huang H-H, Beckmann ND, Nirenberg S, Wang B, et al. An inflammatory cytokine signature predicts COVID-19 severity and survival. Nature Medicine. 2020;26(10):1636-43.
17. Martinez Mesa A, Cabrera César E, Martín-Montañez E, Sanchez Alvarez E, Lopez PM, Romero-Zerbo Y, et al. Acute Lung Injury Biomarkers in the Prediction of COVID-19 Severity: Total Thiol, Ferritin and Lactate Dehydrogenase. Antioxidants (Basel). 2021;10(8).
18. Berlin DA, Gulick RM, Martinez FJ. Severe Covid-19. N Engl J Med. 2020;383(25):2451-60.
19. Guimarães Sousa S, Kleiton de Sousa A, Maria Carvalho Pereira C, Sofia Miranda Loiola Araújo A, de Aguiar Magalhães D, Vieira de Brito T, et al. SARS-CoV-2

infection causes intestinal cell damage: Role of interferon's imbalance. Cytokine. 2022;152:155826.
20. Andre M, Lau LS, Pokharel MD, Ramelow J, Owens F, Souchak J, et al. From Alpha to Omicron: How Different Variants of Concern of the SARS-Coronavirus-2 Impacted the World. Biology (Basel). 2023;12(9).
21. Carabelli AM, Peacock TP, Thorne LG, Harvey WT, Hughes J, de Silva TI, et al. SARS-CoV-2 variant biology: immune escape, transmission and fitness. Nature Reviews Microbiology. 2023;21(3):162-77.
22. Young BE, Fong SW, Chan YH, Mak TM, Ang LW, Anderson DE, et al. Effects of a major deletion in the SARS-CoV-2 genome on the severity of infection and the inflammatory response: an observational cohort study. Lancet. 2020;396(10251):603-11.
23. Su Y, Anderson D, Young B, Linster M, Zhu F, Jayakumar J, et al. Discovery and genomic characterization of a 382-nucleotide deletion in ORF7b and ORF8 during the early evolution of SARS-CoV-2. mBio 11 (4): e01610-20. 2020.
24. Wu F, Zhao S, Yu B, Chen Y-M, Wang W, Song Z-G, et al. A new coronavirus associated with human respiratory disease in China. Nature. 2020;579(7798):265-9.
25. Rambaut A, Holmes EC, O'Toole Á, Hill V, McCrone JT, Ruis C, et al. A dynamic nomenclature proposal for SARS-CoV-2 lineages to assist genomic epidemiology. Nat Microbiol. 2020;5(11):1403-7.
26. Frampton D, Rampling T, Cross A, Bailey H, Heaney J, Byott M, et al. Genomic characteristics and clinical effect of the emergent SARS-CoV-2 B.1.1.7 lineage in London, UK: a whole-genome sequencing and hospital-based cohort study. Lancet Infect Dis. 2021;21(9):1246-56.
27. Raman R, Patel KJ, Ranjan K. COVID-19: Unmasking Emerging SARS-CoV-2 Variants, Vaccines and Therapeutic Strategies. Biomolecules. 2021;11(7).
28. Guo K, Barrett BS, Morrison JH, Mickens KL, Vladar EK, Hasenkrug KJ, et al. Interferon resistance of emerging SARS-CoV-2 variants. Proceedings of the National Academy of Sciences. 2022;119(32):e2203760119.
29. Hassan SS, Kodakandla V, Redwan EM, Lundstrom K, Pal Choudhury P, Abd El-Aziz TM, et al. An issue of concern: unique truncated ORF8 protein variants of SARS-CoV-2. PeerJ. 2022;10:e13136.
30. Hachim A, Kavian N, Valkenburg SA. Antibody landscapes of SARS-CoV-2 can reveal novel vaccine and diagnostic targets. Current Opinion in Virology. 2021;50:139-46.
31. Domingo P, de Benito N. Alpha variant SARS-CoV-2 infection: How it all starts. EBioMedicine. 2021;74:103703.
32. Lamers MM, Breugem TI, Mykytyn AZ, Wang Y, Groen N, Knoops K, et al. Human organoid systems reveal correlates of fitness for SARS-CoV-2 B.1.1.7. bioRxiv. 2021:2021.05.03.441080.
33. Korobova ZR, Arsentieva NA, Liubimova NE, Batsunov OK, Dedkov VG, Gladkikh AS, et al. Cytokine Profiling in Different SARS-CoV-2 Genetic Variants. Int J Mol Sci. 2022;23(22).
34. Faria NR, Mellan TA, Whittaker C, Claro IM, Candido DDS, Mishra S, et al. Genomics and epidemiology of the P.1 SARS-CoV-2 lineage in Manaus, Brazil. Science. 2021;372(6544):815-21.
35. Giovanetti M, Fonseca V, Wilkinson E, Tegally H, San EJ, Althaus CL, et al. Replacement of the Gamma by the Delta variant in Brazil: Impact of lineage displacement on the ongoing pandemic. Virus Evolution. 2022;8(1).
36. Arduini A, Laprise F, Liang C. SARS-CoV-2 ORF8: A Rapidly Evolving Immune and Viral Modulator in COVID-19. Viruses. 2023;15(4).
37. de Oliveira MHS, Lippi G, Henry BM. Sudden rise in COVID-19 case fatality among young and middle-aged adults in the south of Brazil after identification of the novel B.1.1.28.1 (P.1) SARS-CoV-2 strain: analysis of data from the state of Parana. medRxiv. 2021:2021.03.24.21254046.
38. Zavascki AP, Vieceli T, Wink PL, Volpato FCZ, Monteiro FL, Willig JB, et al. Evaluation of Clinical Course of Gamma (P.1) Variant of Concern versus Lineages in

Hospitalized Patients with COVID-19 in a Reference Center in Brazil. Am J Trop Med Hyg. 2022;107(2):245-51.
39. Hojo-Souza NS, Freitas VLS, Guidoni DL, Souza FSH. Clinical symptom profile of hospitalized COVID-19 Brazilian patients according to SARS-CoV-2 variants. Epidemiol Health. 2023;45:e2023079.
40. Spira B. The Impact of the Highly Virulent SARS-CoV-2 Gamma Variant on Young Adults in the State of São Paulo: Was It Inevitable? Cureus. 2022;14(7):e26486.
41. Arabi M, Al-Najjar Y, Mhaimeed N, Salameh MA, Paul P, AlAnni J, et al. Severity of the Omicron SARS-CoV-2 variant compared with the previous lineages: A systematic review. J Cell Mol Med. 2023;27(11):1443-64.
42. Relan P, Motaze NV, Kothari K, Askie L, Le Polain de Waroux O, Van Kerkhove MD, et al. Severity and outcomes of Omicron variant of SARS-CoV-2 compared to Delta variant and severity of Omicron sublineages: a systematic review and metanalysis. BMJ Global Health. 2023;8(7):e012328.
43. Tamura T, Irie T, Deguchi S, Yajima H, Tsuda M, Nasser H, et al. Virological characteristics of the SARS-CoV-2 Omicron XBB.1.5 variant. Nature Communications. 2024;15(1):1176.
44. Nextstrain. SARS-CoV-2: Global overview 2024 [Available from: https://nextstrain.org/ncov/gisaid/global/6m?gt=ORF8.8%2A.
45. Markov PV, Ghafari M, Beer M, Lythgoe K, Simmonds P, Stilianakis NI, et al. The evolution of SARS-CoV-2. Nature Reviews Microbiology. 2023;21(6):361-79.
46. Ahn JH, Kim J, Hong SP, Choi SY, Yang MJ, Ju YS, et al. Nasal ciliated cells are primary targets for SARS-CoV-2 replication in the early stage of COVID-19. J Clin Invest. 2021;131(13).
47. Khan M, Yoo SJ, Clijsters M, Backaert W, Vanstapel A, Speleman K, et al. Visualizing in deceased COVID-19 patients how SARS-CoV-2 attacks the respiratory and olfactory mucosae but spares the olfactory bulb. Cell. 2021;184(24):5932-49.e15.
48. Ortiz Bezara ME, Thurman A, Pezzulo AA, Leidinger MR, Klesney-Tait JA, Karp PH, et al. Heterogeneous expression of the SARS-Coronavirus-2 receptor ACE2 in the human respiratory tract. bioRxiv. 2020.
49. Lamers MM, Haagmans BL. SARS-CoV-2 pathogenesis. Nat Rev Microbiol. 2022;20(5):270-84.
50. Li W, Moore MJ, Vasilieva N, Sui J, Wong SK, Berne MA, et al. Angiotensin-converting enzyme 2 is a functional receptor for the SARS coronavirus. Nature. 2003;426(6965):450-4.
51. Hoffmann M, Kleine-Weber H, Schroeder S, Krüger N, Herrler T, Erichsen S, et al. SARS-CoV-2 Cell Entry Depends on ACE2 and TMPRSS2 and Is Blocked by a Clinically Proven Protease Inhibitor. Cell. 2020;181(2):271-80.e8.
52. Mykytyn AZ, Breugem TI, Riesebosch S, Schipper D, van den Doel PB, Rottier RJ, et al. SARS-CoV-2 entry into human airway organoids is serine protease-mediated and facilitated by the multibasic cleavage site. Elife. 2021;10.
53. Beumer J, Geurts MH, Lamers MM, Puschhof J, Zhang J, van der Vaart J, et al. A CRISPR/Cas9 genetically engineered organoid biobank reveals essential host factors for coronaviruses. Nat Commun. 2021;12(1):5498.
54. Wang S, Qiu Z, Hou Y, Deng X, Xu W, Zheng T, et al. AXL is a candidate receptor for SARS-CoV-2 that promotes infection of pulmonary and bronchial epithelial cells. Cell Res. 2021;31(2):126-40.
55. Kyrou I, Randeva HS, Spandidos DA, Karteris E. Not only ACE2—the quest for additional host cell mediators of SARS-CoV-2 infection: Neuropilin-1 (NRP1) as a novel SARS-CoV-2 host cell entry mediator implicated in COVID-19. Signal Transduction and Targeted Therapy. 2021;6(1):21.
56. Hou YJ, Okuda K, Edwards CE, Martinez DR, Asakura T, Dinnon KH, 3rd, et al. SARS-CoV-2 Reverse Genetics Reveals a Variable Infection Gradient in the Respiratory Tract. Cell. 2020;182(2):429-46.e14.

57. Chua RL, Lukassen S, Trump S, Hennig BP, Wendisch D, Pott F, et al. COVID-19 severity correlates with airway epithelium-immune cell interactions identified by single-cell analysis. Nat Biotechnol. 2020;38(8):970-9.
58. Barkauskas CE, Cronce MJ, Rackley CR, Bowie EJ, Keene DR, Stripp BR, et al. Type 2 alveolar cells are stem cells in adult lung. J Clin Invest. 2013;123(7):3025-36.
59. Zhao F, Ma Q, Yue Q, Chen H. SARS-CoV-2 Infection and Lung Regeneration. Clin Microbiol Rev. 2022;35(2):e0018821.
60. Roingeard P, Eymieux S, Burlaud-Gaillard J, Hourioux C, Patient R, Blanchard E. The double-membrane vesicle (DMV): a virus-induced organelle dedicated to the replication of SARS-CoV-2 and other positive-sense single-stranded RNA viruses. Cell Mol Life Sci. 2022;79(8):425.
61. Wolff G, Melia CE, Snijder EJ, Bárcena M. Double-Membrane Vesicles as Platforms for Viral Replication. Trends Microbiol. 2020;28(12):1022-33.
62. Zhang J, Lan Y, Sanyal S. Membrane heist: Coronavirus host membrane remodeling during replication. Biochimie. 2020;179:229-36.
63. V'kovski P, Kratzel A, Steiner S, Stalder H, Thiel V. Coronavirus biology and replication: implications for SARS-CoV-2. Nature Reviews Microbiology. 2021;19(3):155-70.
64. Sola I, Almazán F, Zúñiga S, Enjuanes L. Continuous and Discontinuous RNA Synthesis in Coronaviruses. Annu Rev Virol. 2015;2(1):265-88.
65. Kim D, Lee J-Y, Yang J-S, Kim JW, Kim VN, Chang H. The Architecture of SARS-CoV-2 Transcriptome. Cell. 2020;181(4):914-21.e10.
66. Jungreis I, Sealfon R, Kellis M. SARS-CoV-2 gene content and COVID-19 mutation impact by comparing 44 Sarbecovirus genomes. Nature Communications. 2021;12(1):2642.
67. Bracquemond D, Muriaux D. Betacoronavirus Assembly: Clues and Perspectives for Elucidating SARS-CoV-2 Particle Formation and Egress. mBio. 2021;12(5):10.1128/mbio.02371-21.
68. Dutta M, Voth GA. Understanding the assembly and budding mechanisms of SARS CoV-2 M and N proteins. Biophysical Journal. 2024;123(3):374a.
69. Boson B, Legros V, Zhou B, Siret E, Mathieu C, Cosset FL, et al. The SARS-CoV-2 envelope and membrane proteins modulate maturation and retention of the spike protein, allowing assembly of virus-like particles. J Biol Chem. 2021;296:100111.
70. Xu R, Shi M, Li J, Song P, Li N. Construction of SARS-CoV-2 Virus-Like Particles by Mammalian Expression System. Front Bioeng Biotechnol. 2020;8:862.
71. Sicari D, Chatziioannou A, Koutsandreas T, Sitia R, Chevet E. Role of the early secretory pathway in SARS-CoV-2 infection. Journal of Cell Biology. 2020;219(9).
72. Sergio MC, Ricciardi S, Guarino AM, Giaquinto L, De Matteis MA. Membrane remodeling and trafficking piloted by SARS-CoV-2. Trends in Cell Biology.
73. Ghosh S, Dellibovi-Ragheb TA, Kerviel A, Pak E, Qiu Q, Fisher M, et al. β-Coronaviruses Use Lysosomes for Egress Instead of the Biosynthetic Secretory Pathway. Cell. 2020;183(6):1520-35.e14.
74. Pereira F. Evolutionary dynamics of the SARS-CoV-2 ORF8 accessory gene. Infect Genet Evol. 2020;85:104525.
75. Flower TG, Buffalo CZ, Hooy RM, Allaire M, Ren X, Hurley JH. Structure of SARS-CoV-2 ORF8, a rapidly evolving immune evasion protein. 2021;118(2):e2021785118.
76. Geng H, Subramanian S, Wu L, Bu H-F, Wang X, Du C, et al. SARS-CoV-2 ORF8 Forms Intracellular Aggregates and Inhibits IFNγ-Induced Antiviral Gene Expression in Human Lung Epithelial Cells. 2021;12(2108).
77. Liu P, Wang X, Sun Y, Zhao H, Cheng F, Wang J, et al. SARS-CoV-2 ORF8 reshapes the ER through forming mixed disulfides with ER oxidoreductases. Redox Biol. 2022;54:102388.
78. Matsuoka K, Imahashi N, Ohno M, Ode H, Nakata Y, Kubota M, et al. SARS-CoV-2 accessory protein ORF8 is secreted extracellularly as a glycoprotein homodimer. J Biol Chem. 2022;298(3):101724.

79. Stukalov A, Girault V, Grass V, Karayel O, Bergant V, Urban C, et al. Multilevel proteomics reveals host perturbations by SARS-CoV-2 and SARS-CoV. Nature. 2021;594(7862):246-52.
80. Zhou Y, Liu Y, Gupta S, Paramo MI, Hou Y, Mao C, et al. A comprehensive SARS-CoV-2–human protein–protein interactome reveals COVID-19 pathobiology and potential host therapeutic targets. Nature Biotechnology. 2023;41(1):128-39.
81. Gordon DE, Hiatt J, Bouhaddou M, Rezelj VV, Ulferts S, Braberg H, et al. Comparative host-coronavirus protein interaction networks reveal pan-viral disease mechanisms. Science. 2020;370(6521).
82. Wu X, Manske MK, Ruan GJ, Witter TL, Nowakowski KE, Abeykoon JP, et al. Secreted ORF8 induces monocytic pro-inflammatory cytokines through NLRP3 pathways in patients with severe COVID-19. iScience. 2023;26(6):106929.
83. Lin X, Fu B, Xiong Y, Xing N, Xue W, Guo D, et al. Unconventional secretion of unglycosylated ORF8 is critical for the cytokine storm during SARS-CoV-2 infection. PLoS Pathog. 2023;19(1):e1011128.
84. Lee JS, Shin E-C. The type I interferon response in COVID-19: implications for treatment. Nature Reviews Immunology. 2020;20(10):585-6.
85. Pittet JF, Griffiths MJ, Geiser T, Kaminski N, Dalton SL, Huang X, et al. TGF-beta is a critical mediator of acute lung injury. J Clin Invest. 2001;107(12):1537-44.
86. McDonald LT. Healing after COVID-19: are survivors at risk for pulmonary fibrosis? Am J Physiol Lung Cell Mol Physiol. 2021;320(2):L257-l65.
87. Zhang Y, Chen Y, Li Y, Huang F, Luo B, Yuan Y, et al. The ORF8 protein of SARS-CoV-2 mediates immune evasion through down-regulating MHC-I. Proc Natl Acad Sci U S A. 2021;118(23).
88. Jheng J-R, Ho J-Y, Horng J-T. ER stress, autophagy, and RNA viruses. Frontiers in Microbiology. 2014;5:388.
89. Fung TS, Huang M, Liu DX. Coronavirus-induced ER stress response and its involvement in regulation of coronavirus-host interactions. Virus Res. 2014;194:110-23.
90. Nguyen LC, Renner DM, Silva D, Yang D, Parenti NA, Medina KM, et al. SARS-CoV-2 Diverges from Other Betacoronaviruses in Only Partially Activating the IRE1α/XBP1 Endoplasmic Reticulum Stress Pathway in Human Lung-Derived Cells. mBio. 2022;13(5):e0241522.
91. Oyarzún-Arrau A, Alonso-Palomares L, Valiente-Echeverría F, Osorio F, Soto-Rifo R. Crosstalk between RNA Metabolism and Cellular Stress Responses during Zika Virus Replication. Pathogens. 2020;9(3).
92. Wang Y, Grunewald M, Perlman S. Coronaviruses: An Updated Overview of Their Replication and Pathogenesis. Methods Mol Biol. 2020;2203:1-29.
93. Travers KJ, Patil CK, Wodicka L, Lockhart DJ, Weissman JS, Walter P. Functional and genomic analyses reveal an essential coordination between the unfolded protein response and ER-associated degradation. Cell. 2000;101(3):249-58.
94. Oslowski CM, Urano F. Measuring ER stress and the unfolded protein response using mammalian tissue culture system. Methods Enzymol. 2011;490:71-92.
95. Liu X, Huuskonen S, Laitinen T, Redchuk T, Bogacheva M, Salokas K, et al. SARS-CoV-2-host proteome interactions for antiviral drug discovery. Mol Syst Biol. 2021;17(11):e10396.
96. Davies JP, Almasy KM, McDonald EF, Plate L. Comparative Multiplexed Interactomics of SARS-CoV-2 and Homologous Coronavirus Nonstructural Proteins Identifies Unique and Shared Host-Cell Dependencies. ACS Infectious Diseases. 2020;6(12):3174-89.
97. Mufrrih M, Chen B, Chan SW. Zika Virus Induces an Atypical Tripartite Unfolded Protein Response with Sustained Sensor and Transient Effector Activation and a Blunted BiP Response. mSphere. 2021;6(3):e0036121.
98. Siwecka N, Rozpędek-Kamińska W, Wawrzynkiewicz A, Pytel D, Diehl JA, Majsterek I. The Structure, Activation and Signaling of IRE1 and Its Role in Determining Cell Fate. Biomedicines. 2021;9(2).

99. Harding HP, Novoa I, Zhang Y, Zeng H, Wek R, Schapira M, et al. Regulated translation initiation controls stress-induced gene expression in mammalian cells. Mol Cell. 2000;6(5):1099-108.
100. Avivar-Valderas A, Salas E, Bobrovnikova-Marjon E, Diehl JA, Nagi C, Debnath J, et al. PERK integrates autophagy and oxidative stress responses to promote survival during extracellular matrix detachment. Mol Cell Biol. 2011;31(17):3616-29.
101. Kolpikova EP, Tronco AR, Hartigh ABD, Jackson KJ, Iwawaki T, Fink SL. IRE1α Promotes Zika Virus Infection via XBP1. Viruses. 2020;12(3).
102. Davies JP, Sivadas A, Keller KR, Roman BK, Wojcikiewicz RJH, Plate L. Expression of SARS-CoV-2 Nonstructural Proteins 3 and 4 Can Tune the Unfolded Protein Response in Cell Culture. J Proteome Res. 2024;23(1):356-67.
103. Tan X, Cai K, Li J, Yuan Z, Chen R, Xiao H, et al. Coronavirus subverts ER-phagy by hijacking FAM134B and ATL3 into p62 condensates to facilitate viral replication. Cell Reports. 2023;42(4):112286.
104. Kwon J, Kim J, Kim KI. Crosstalk between endoplasmic reticulum stress response and autophagy in human diseases. Anim Cells Syst (Seoul). 2023;27(1):29-37.
105. Choi Y, Bowman JW, Jung JU. Autophagy during viral infection — a double-edged sword. Nature Reviews Microbiology. 2018;16(6):341-54.
106. Teo QW, van Leur SW, Sanyal S. Escaping the Lion's Den: redirecting autophagy for unconventional release and spread of viruses. Febs j. 2021;288(13):3913-27.
107. Reggiori F, Molinari M. ER-phagy: mechanisms, regulation, and diseases connected to the lysosomal clearance of the endoplasmic reticulum. Physiol Rev. 2022;102(3):1393-448.
108. Gubas A, Dikic I. ER remodeling via ER-phagy. Mol Cell. 2022;82(8):1492-500.
109. Stolz A, Grumati P. The various shades of ER-phagy. Febs j. 2019;286(23):4642-9.
110. Mochida K, Nakatogawa H. ER‐phagy: selective autophagy of the endoplasmic reticulum. EMBO reports. 2022;23(8):e55192.
111. Lennemann NJ, Coyne CB. Dengue and Zika viruses subvert reticulophagy by NS2B3-mediated cleavage of FAM134B. Autophagy. 2017;13(2):322-32.
112. Zhang J, Lan Y, Sanyal S. Modulation of Lipid Droplet Metabolism-A Potential Target for Therapeutic Intervention in Flaviviridae Infections. Front Microbiol. 2017;8:2286.
113. Qu Y, Wang W, Xiao MZX, Zheng Y, Liang Q. The interplay between lipid droplets and virus infection. J Med Virol. 2023;95(7):e28967.
114. Zhang J, Lan Y, Li MY, Lamers MM, Fusade-Boyer M, Klemm E, et al. Flaviviruses Exploit the Lipid Droplet Protein AUP1 to Trigger Lipophagy and Drive Virus Production. Cell Host & Microbe. 2018;23(6):819-31.e5.
115. Wang W, Qu Y, Wang X, Xiao MZX, Fu J, Chen L, et al. Genetic variety of ORF3a shapes SARS-CoV-2 fitness through modulation of lipid droplet. Journal of Medical Virology. 2023;95(3):e28630.
116. Jarc E, Petan T. A twist of FATe: Lipid droplets and inflammatory lipid mediators. Biochimie. 2020;169:69-87.
117. Bello-Perez M, Hurtado-Tamayo J, Mykytyn AZ, Lamers MM, Requena-Platek R, Schipper D, et al. SARS-CoV-2 ORF8 accessory protein is a virulence factor. mBio. 2023;14(5):e0045123.
118. Hassan SS, Aljabali AAA, Panda PK, Ghosh S, Attrish D, Choudhury PP, et al. A unique view of SARS-CoV-2 through the lens of ORF8 protein. Comput Biol Med. 2021;133:104380.
119. Flower TG, Buffalo CZ, Hooy RM, Allaire M, Ren X, Hurley JH. Structure of SARS-CoV-2 ORF8, a rapidly evolving immune evasion protein. Proceedings of the National Academy of Sciences. 2021;118(2):e2021785118.
120. Valcarcel A, Bensussen A, Álvarez-Buylla ER, Díaz J. Structural Analysis of SARS-CoV-2 ORF8 Protein: Pathogenic and Therapeutic Implications. Front Genet. 2021;12:693227.

121. Wu X, Xia T, Shin WJ, Yu KM, Jung W, Herrmann A, et al. Viral Mimicry of Interleukin-17A by SARS-CoV-2 ORF8. mBio. 2022;13(2):e0040222.
122. Lin X, Fu B, Yin S, Li Z, Liu H, Zhang H, et al. ORF8 contributes to cytokine storm during SARS-CoV-2 infection by activating IL-17 pathway. iScience. 2021;24(4):102293.
123. Wu F, Chen X, Ma Y, Wu Y, Li R, Huang Y, et al. Glycosylated, Lipid-Binding, CDR-Like Domains of SARS-CoV-2 ORF8 Indicate Unique Sites of Immune Regulation. Microbiol Spectr. 2023;11(4):e0123423.
124. Geng H, Subramanian S, Wu L, Bu HF, Wang X, Du C, et al. SARS-CoV-2 ORF8 Forms Intracellular Aggregates and Inhibits IFNγ-Induced Antiviral Gene Expression in Human Lung Epithelial Cells. Front Immunol. 2021;12:679482.
125. Kee J, Thudium S, Renner DM, Glastad K, Palozola K, Zhang Z, et al. SARS-CoV-2 disrupts host epigenetic regulation via histone mimicry. Nature. 2022;610(7931):381-8.
126. Gordon DE, Jang GM, Bouhaddou M, Xu J, Obernier K, White KM, et al. A SARS-CoV-2 protein interaction map reveals targets for drug repurposing. Nature. 2020;583(7816):459-68.
127. Lu Y, Michel HA, Wang PH, Smith GL. Manipulation of innate immune signaling pathways by SARS-CoV-2 non-structural proteins. Front Microbiol. 2022;13:1027015.
128. Cheng Y, Peng X. In silico study on the effects of disulfide bonds in ORF8 of SARS-CoV-2. Phys Chem Chem Phys. 2022;24(27):16876-83.
129. Assadizadeh M, Azimzadeh Irani M. Oligomer formation of SARS-CoV-2 ORF8 through 73YIDI76 motifs regulates immune response and non-infusion antiviral interactions. Front Mol Biosci. 2023;10:1270511.
130. Suriawinata E, Mehta KJ. Iron and iron-related proteins in COVID-19. Clinical and Experimental Medicine. 2023;23(4):969-91.
131. Samavarchi-Tehrani P, Abdouni H, Knight JDR, Astori A, Samson R, Lin Z-Y, et al. A SARS-CoV-2 – host proximity interactome. bioRxiv. 2020:2020.09.03.282103.
132. Choi H, Larsen B, Lin Z-Y, Breitkreutz A, Mellacheruvu D, Fermin D, et al. SAINT: probabilistic scoring of affinity purification–mass spectrometry data. Nature Methods. 2011;8(1):70-3.
133. Puri C, Gratian MJ, Rubinsztein DC. Mammalian autophagosomes form from finger-like phagophores. Developmental Cell. 2023;58(23):2746-60.e5.
134. Dietl P, Frick M. Channels and Transporters of the Pulmonary Lamellar Body in Health and Disease. Cells. 2021;11(1).
135. Ridsdale R, Na C-L, Xu Y, Greis KD, Weaver T. Comparative Proteomic Analysis of Lung Lamellar Bodies and Lysosome-Related Organelles. PLOS ONE. 2011;6(1):e16482.
136. Sever N, Miličić G, Bodnar NO, Wu X, Rapoport TA. Mechanism of Lamellar Body Formation by Lung Surfactant Protein B. Mol Cell. 2021;81(1):49-66.e8.
137. Morishita H, Kanda Y, Kaizuka T, Chino H, Nakao K, Miki Y, et al. Autophagy Is Required for Maturation of Surfactant-Containing Lamellar Bodies in the Lung and Swim Bladder. Cell Rep. 2020;33(10):108477.
138. Chintagari NR, Mishra A, Su L, Wang Y, Ayalew S, Hartson SD, et al. Vacuolar ATPase Regulates Surfactant Secretion in Rat Alveolar Type II Cells by Modulating Lamellar Body Calcium. PLOS ONE. 2010;5(2):e9228.
139. Vats S, Galli T. Introducing secretory reticulophagy/ER-phagy (SERP), a VAMP7-dependent pathway involved in neurite growth. Autophagy. 2021;17(4):1037-9.
140. Miao G, Zhao H, Li Y, Ji M, Chen Y, Shi Y, et al. ORF3a of the COVID-19 virus SARS-CoV-2 blocks HOPS complex-mediated assembly of the SNARE complex required for autolysosome formation. Dev Cell. 2021;56(4):427-42.e5.
141. Moriyama M, Lucas C, Monteiro VS, Iwasaki A. Enhanced inhibition of MHC-I expression by SARS-CoV-2 Omicron subvariants. Proc Natl Acad Sci U S A. 2023;120(16):e2221652120.
142. Díaz J. SARS-CoV-2 Molecular Network Structure. Front Physiol. 2020;11:870.
143. Gómez de San José N, Massa F, Halbgebauer S, Oeckl P, Steinacker P, Otto M. Neuronal pentraxins as biomarkers of synaptic activity: from physiological functions to

pathological changes in neurodegeneration. J Neural Transm (Vienna). 2022;129(2):207-30.
144. Li W, Tsen F, Sahu D, Bhatia A, Chen M, Multhoff G, et al. Extracellular Hsp90 (eHsp90) as the actual target in clinical trials: intentionally or unintentionally. Int Rev Cell Mol Biol. 2013;303:203-35.
145. Ralchev Ralchev N, Lyubenova Bradyanova S, Valerieva Doneva Y, Mihaylova N, Vikentieva Elefterova-Florova E, Ivanov Tchorbanov A, et al. Exploring the Role of CD74 and D-Dopachrome Tautomerase in COVID-19: Insights from Transcriptomic and Serum Analyses. J Clin Med. 2023;12(15).
146. Song S, Liu B, Habibie H, van den Bor J, Smit MJ, Gosens R, et al. D-dopachrome tautomerase contributes to lung epithelial repair via atypical chemokine receptor 3-dependent Akt signaling. EBioMedicine. 2021;68:103412.
147. Bleilevens C, Soppert J, Hoffmann A, Breuer T, Bernhagen J, Martin L, et al. Macrophage Migration Inhibitory Factor (MIF) Plasma Concentration in Critically Ill COVID-19 Patients: A Prospective Observational Study. Diagnostics (Basel). 2021;11(2).
148. Nasser SMT, Rana AA, Doffinger R, Kafizas A, Khan TA, Nasser S. Elevated free interleukin-18 associated with severity and mortality in prospective cohort study of 206 hospitalised COVID-19 patients. Intensive Care Medicine Experimental. 2023;11(1):9.
149. Satış H, Özger HS, Aysert Yıldız P, Hızel K, Gulbahar Ö, Erbaş G, et al. Prognostic value of interleukin-18 and its association with other inflammatory markers and disease severity in COVID-19. Cytokine. 2021;137:155302.
150. Claude-Taupin A, Bissa B, Jia J, Gu Y, Deretic V. Role of autophagy in IL-1β export and release from cells. Semin Cell Dev Biol. 2018;83:36-41.
151. Ganesan D, Cai Q. Understanding amphisomes. Biochem J. 2021;478(10):1959-76.
152. Raymond A-A, de Peredo AG, Stella A, Ishida-Yamamoto A, Bouyssie D, Serre G, et al. Lamellar Bodies of Human Epidermis: Proteomics Characterization by High Throughput Mass Spectrometry and Possible Involvement of CLIP-170 in their Trafficking/Secretion. Molecular & Cellular Proteomics. 2008;7(11):2151-75.
153. Ji X, Ji H-L. Metabolic signatures of acute respiratory distress syndrome: COVID versus non-COVID. American Journal of Physiology-Lung Cellular and Molecular Physiology. 2024;326(5):L596-L603.
154. Farrugia MA, Puglielli L. Nε-lysine acetylation in the endoplasmic reticulum - a novel cellular mechanism that regulates proteostasis and autophagy. J Cell Sci. 2018;131(22).
155. Annaert W, Kaether C. Bring it back, bring it back, don't take it away from me - the sorting receptor RER1. J Cell Sci. 2020;133(17).
156. Wojnacki J, Nola S, Bun P, Cholley B, Filippini F, Pressé MT, et al. Role of VAMP7-Dependent Secretion of Reticulon 3 in Neurite Growth. Cell Rep. 2020;33(12):108536.
157. Kratzel A, Thiel V. RTN3 and RTN4: Architects of SARS-CoV-2 replication organelles. J Cell Biol. 2023;222(7).
158. Adler KB, Tuvim MJ, Dickey BF. Regulated Mucin Secretion from Airway Epithelial Cells. Frontiers in Endocrinology. 2013;4.
159. Raiford KL, Park J, Lin K-W, Fang S, Crews AL, Adler KB. Mucin granule-associated proteins in human bronchial epithelial cells: the airway goblet cell "granulome". Respiratory Research. 2011;12(1):118.
160. Syed ZA, Zhang L, Tran DT, Bleck CKE, Ten Hagen KG. Regulated Restructuring of Mucins During Secretory Granule Maturation In Vivo. Proc Natl Acad Sci U S A. 2022;119(43):e2209750119.
161. Zimmermann L, Zhao X, Makroczyova J, Wachsmuth-Melm M, Prasad V, Hensel Z, et al. SARS-CoV-2 nsp3 and nsp4 are minimal constituents of a pore spanning replication organelle. Nature Communications. 2023;14(1):7894.

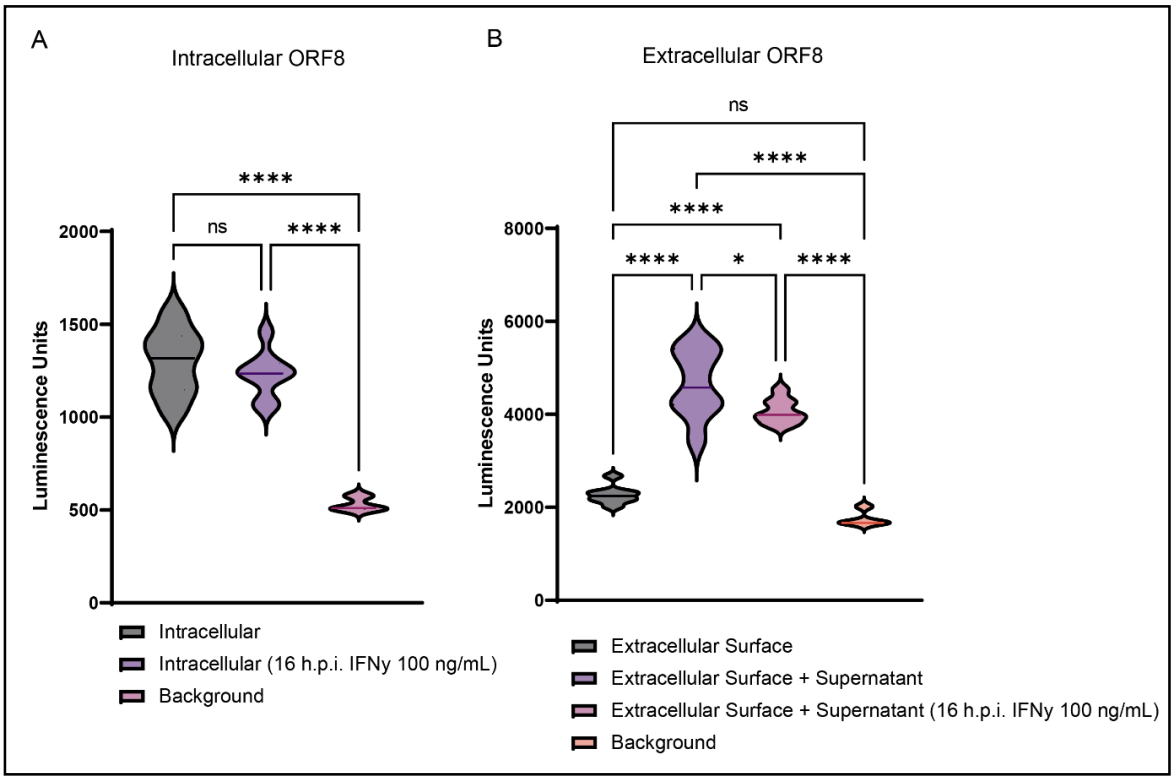
162. Ricciardi S, Guarino AM, Giaquinto L, Polishchuk EV, Santoro M, Di Tullio G, et al. The role of NSP6 in the biogenesis of the SARS-CoV-2 replication organelle. Nature. 2022;606(7915):761-8.
163. Mironov AA, Savin MA, Beznoussenko GV. COVID-19 Biogenesis and Intracellular Transport. Int J Mol Sci. 2023;24(5).
164. Lei J, Kusov Y, Hilgenfeld R. Nsp3 of coronaviruses: Structures and functions of a large multi-domain protein. Antiviral Res. 2018;149:58-74.
165. Hagemeijer MC, Monastyrska I, Griffith J, van der Sluijs P, Voortman J, van Bergen en Henegouwen PM, et al. Membrane rearrangements mediated by coronavirus nonstructural proteins 3 and 4. Virology. 2014;458-459:125-35.
166. Dias SSG, Soares VC, Ferreira AC, Sacramento CQ, Fintelman-Rodrigues N, Temerozo JR, et al. Lipid droplets fuel SARS-CoV-2 replication and production of inflammatory mediators. PLoS Pathog. 2020;16(12):e1009127.
167. Klein S, Cortese M, Winter SL, Wachsmuth-Melm M, Neufeldt CJ, Cerikan B, et al. SARS-CoV-2 structure and replication characterized by in situ cryo-electron tomography. Nature Communications. 2020;11(1):5885.
168. Eymieux S, Rouillé Y, Terrier O, Seron K, Blanchard E, Rosa-Calatrava M, et al. Ultrastructural modifications induced by SARS-CoV-2 in Vero cells: a kinetic analysis of viral factory formation, viral particle morphogenesis and virion release. Cell Mol Life Sci. 2021;78(7):3565-76.
169. Keramidas P, Pitou M, Papachristou E, Choli-Papadopoulou T. Insights into the Activation of Unfolded Protein Response Mechanism during Coronavirus Infection. Curr Issues Mol Biol. 2024;46(5):4286-308.
170. Williams JM, Chen Y-J, Cho WJ, Tai AW, Tsai B. Reticulons promote formation of ER-derived double-membrane vesicles that facilitate SARS-CoV-2 replication. Journal of Cell Biology. 2023;222(7).
171. Shin W-J, Ha DP, Machida K, Lee AS. The stress-inducible ER chaperone GRP78/BiP is upregulated during SARS-CoV-2 infection and acts as a pro-viral protein. Nature Communications. 2022;13(1):6551.
172. Li X, Kuang E. Reticulophagy Reprograms the Endoplasmic Reticulum for SARS-CoV-2 Replication. Frontiers in Cell and Developmental Biology. 2022;10.
173. Grumati P, Morozzi G, Hölper S, Mari M, Harwardt M-LIE, Yan R, et al. Full length RTN3 regulates turnover of tubular endoplasmic reticulum via selective autophagy. eLife. 2017;6:e25555.
174. Pasteur I. Real-time RT-PCR assays for the detection of SARS-CoV-2. WHO.int2020 [Available from: https://www.who.int/docs/default-source/coronaviruse/real-time-rt-pcr-assays-for-the-detection-of-sars-cov-2-institut-pasteur-paris.pdf.
175. Lai M, De Carli A, Filipponi C, Iacono E, La Rocca V, Lottini G, et al. Lipid balance remodelling by human positive-strand RNA viruses and the contribution of lysosomes. Antiviral Research. 2022;206:105398.
176. Zhang L, Zhang ZP, Zhang XE, Lin FS, Ge F. Quantitative proteomics analysis reveals BAG3 as a potential target to suppress severe acute respiratory syndrome coronavirus replication. J Virol. 2010;84(12):6050-9.
177. Qin C-F, Li M-Y, Deng K, Cheng X-H, Siu LY-L, Naik TS, et al. Targeting ARF4-mediated intracellular transport as broad-spectrum antivirals. 2024.
178. van Leur SW, Lan Y, Fernando JA, Wong HH, Kampmann M, Siu L, et al. Viral subversion of selective autophagy is critical for biogenesis of virus replication organelles. Nature Communications. 2023;14(1):2698.
179. May DG, Martin-Sancho L, Anschau V, Liu S, Chrisopulos RJ, Scott KL, et al. A BioID-Derived Proximity Interactome for SARS-CoV-2 Proteins. Viruses. 2022;14(3).
180. Bills C, Xie X, Shi PY. The multiple roles of nsp6 in the molecular pathogenesis of SARS-CoV-2. Antiviral Res. 2023;213:105590.
181. Daniloski Z, Jordan TX, Wessels HH, Hoagland DA, Kasela S, Legut M, et al. Identification of Required Host Factors for SARS-CoV-2 Infection in Human Cells. Cell. 2021;184(1):92-105.e16.

182. Sun X, Liu Y, Huang Z, Xu W, Hu W, Yi L, et al. SARS-CoV-2 non-structural protein 6 triggers NLRP3-dependent pyroptosis by targeting ATP6AP1. Cell Death & Differentiation. 2022;29(6):1240-54.
183. Li J, Gui Q, Liang F-X, Sall J, Zhang Q, Duan Y, et al. The REEP5/TRAM1 complex binds SARS-CoV-2 NSP3 and promotes virus replication. Journal of Virology. 2023;97(10):e00507-23.
184. Garvanska DH, Alvarado RE, Mundt FO, Lindqvist R, Duel JK, Coscia F, et al. The NSP3 protein of SARS-CoV-2 binds fragile X mental retardation proteins to disrupt UBAP2L interactions. EMBO reports. 2024;25(2):902-26-26.
185. Li M, Hou Y, Zhou Y, Yang Z, Zhao H, Jian T, et al. LLPS of FXR proteins drives replication organelle clustering for β-coronaviral proliferation. Journal of Cell Biology. 2024;223(6):e202309140.
186. Pahmeier F, Lavacca TM, Goellner S, Neufeldt CJ, Prasad V, Cerikan B, et al. Identification of host dependency factors involved in SARS-CoV-2 replication organelle formation through proteomics and ultrastructural analysis. J Virol. 2023;97(11):e0087823.
187. Zhang N, Wang S, Wong CCL. Proteomics research of SARS-CoV-2 and COVID-19 disease. Med Rev (2021). 2022;2(4):427-45.
188. Ji M, Li M, Sun L, Zhao H, Li Y, Zhou L, et al. VMP1 and TMEM41B are essential for DMV formation during β-coronavirus infection. J Cell Biol. 2022;221(6).
189. Schneider WM, Luna JM, Hoffmann HH, Sánchez-Rivera FJ, Leal AA, Ashbrook AW, et al. Genome-Scale Identification of SARS-CoV-2 and Pan-coronavirus Host Factor Networks. Cell. 2021;184(1):120-32.e14.
190. Zhen Y, Stenmark H. Autophagosome Biogenesis. Cells. 2023;12(4):668.
191. Rodrigues TS, de Sá KSG, Ishimoto AY, Becerra A, Oliveira S, Almeida L, et al. Inflammasomes are activated in response to SARS-CoV-2 infection and are associated with COVID-19 severity in patients. J Exp Med. 2021;218(3).
192. Sun X, Yu J, Wong SH, Chan MTV, Zhang L, Wu WKK. SARS-CoV-2 targets the lysosome to mediate airway inflammatory cell death. Autophagy. 2022;18(9):2246-8.
193. Morita K, Hama Y, Mizushima N. TMEM41B functions with VMP1 in autophagosome formation. Autophagy. 2019;15(5):922-3.
194. van Leur SW, Heunis T, Munnur D, Sanyal S. Pathogenesis and virulence of flavivirus infections. Virulence. 2021;12(1):2814-38.
195. Ryan SJ, Carlson CJ, Mordecai EA, Johnson LR. Global expansion and redistribution of Aedes-borne virus transmission risk with climate change. PLoS Negl Trop Dis. 2019;13(3):e0007213.
196. Bhatt S, Gething PW, Brady OJ, Messina JP, Farlow AW, Moyes CL, et al. The global distribution and burden of dengue. Nature. 2013;496(7446):504-7.
197. Agrelli A, de Moura RR, Crovella S, Brandão LAC. ZIKA virus entry mechanisms in human cells. Infection, Genetics and Evolution. 2019;69:22-9.
198. Gollins SW, Porterfield JS. The uncoating and infectivity of the flavivirus West Nile on interaction with cells: effects of pH and ammonium chloride. J Gen Virol. 1986;67 (Pt 9):1941-50.
199. Cortese M, Goellner S, Acosta EG, Neufeldt CJ, Oleksiuk O, Lampe M, et al. Ultrastructural Characterization of Zika Virus Replication Factories. Cell Rep. 2017;18(9):2113-23.
200. Neufeldt CJ, Cortese M. Membrane architects: how positive-strand RNA viruses restructure the cell. J Gen Virol. 2022;103(8).
201. Qin ZL, Yao QF, Ren H, Zhao P, Qi ZT. Lipid Droplets and Their Participation in Zika Virus Infection. Int J Mol Sci. 2022;23(20).
202. Khromykh AA, Varnavski AN, Sedlak PL, Westaway EG. Coupling between replication and packaging of flavivirus RNA: evidence derived from the use of DNA-based full-length cDNA clones of Kunjin virus. J Virol. 2001;75(10):4633-40.
203. Welsch S, Miller S, Romero-Brey I, Merz A, Bleck CKE, Walther P, et al. Composition and Three-Dimensional Architecture of the Dengue Virus Replication and Assembly Sites. Cell Host & Microbe. 2009;5(4):365-75.

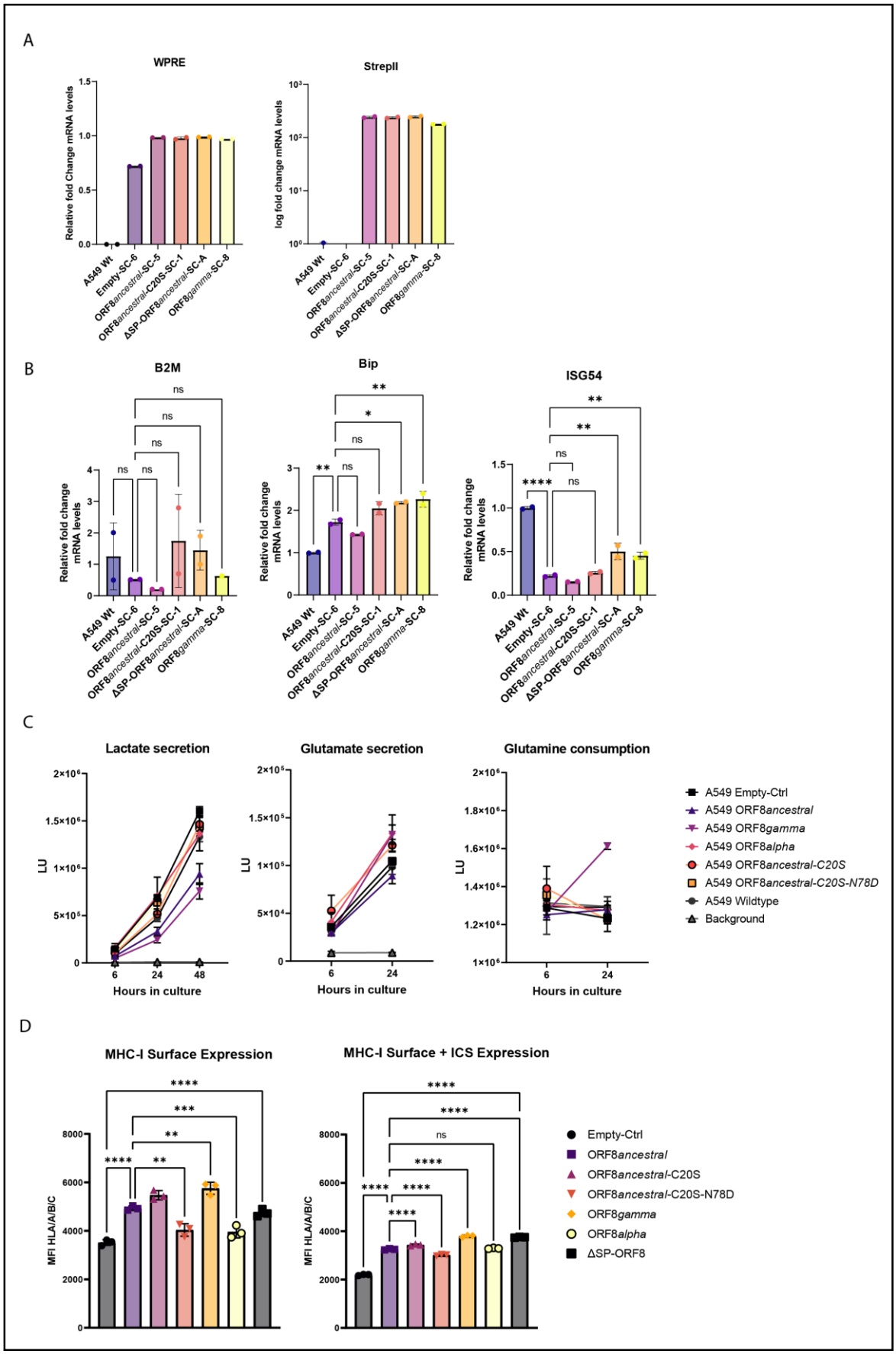
204. Neufeldt CJ, Cortese M, Scaturro P, Cerikan B, Wideman JG, Tabata K, et al. ER-shaping atlastin proteins act as central hubs to promote flavivirus replication and virion assembly. Nat Microbiol. 2019;4(12):2416-29.
205. Li MY, Grandadam M, Kwok K, Lagache T, Siu YL, Zhang JS, et al. KDEL Receptors Assist Dengue Virus Exit from the Endoplasmic Reticulum. Cell Rep. 2015;10(9):1496-507.
206. Li MY, Naik TS, Siu LYL, Acuto O, Spooner E, Wang P, et al. Lyn kinase regulates egress of flaviviruses in autophagosome-derived organelles. Nat Commun. 2020;11(1):5189.
207. Klemm EJ, Spooner E, Ploegh HL. Dual role of ancient ubiquitous protein 1 (AUP1) in lipid droplet accumulation and endoplasmic reticulum (ER) protein quality control. J Biol Chem. 2011;286(43):37602-14.
208. Das R, Liang YH, Mariano J, Li J, Huang T, King A, et al. Allosteric regulation of E2:E3 interactions promote a processive ubiquitination machine. Embo j. 2013;32(18):2504-16.
209. Das R, Mariano J, Tsai YC, Kalathur RC, Kostova Z, Li J, et al. Allosteric activation of E2-RING finger-mediated ubiquitylation by a structurally defined specific E2-binding region of gp78. Mol Cell. 2009;34(6):674-85.
210. Zhang T, Xu Y, Liu Y, Ye Y. gp78 functions downstream of Hrd1 to promote degradation of misfolded proteins of the endoplasmic reticulum. Mol Biol Cell. 2015;26(24):4438-50.
211. Smith CE, Tsai YC, Liang YH, Khago D, Mariano J, Li J, et al. A structurally conserved site in AUP1 binds the E2 enzyme UBE2G2 and is essential for ER-associated degradation. PLoS Biol. 2021;19(12):e3001474.
212. Kikkert M, Doolman R, Dai M, Avner R, Hassink G, van Voorden S, et al. Human HRD1 Is an E3 Ubiquitin Ligase Involved in Degradation of Proteins from the Endoplasmic Reticulum*. Journal of Biological Chemistry. 2004;279(5):3525-34.
213. Ju T, Bocik W, Majumdar A, Tolman JR. Solution structure and dynamics of human ubiquitin conjugating enzyme Ube2g2. Proteins. 2010;78(5):1291-301.
214. Bernales S, McDonald KL, Walter P. Autophagy counterbalances endoplasmic reticulum expansion during the unfolded protein response. PLoS Biol. 2006;4(12):e423.
215. Hill ME, Kumar A, Wells JA, Hobman TC, Julien O, Hardy JA. The Unique Cofactor Region of Zika Virus NS2B-NS3 Protease Facilitates Cleavage of Key Host Proteins. ACS Chem Biol. 2018;13(9):2398-405.
216. Yan L, Liu W, Zhang H, Liu C, Shang Y, Ye Y, et al. Ube2g2-gp78-mediated HERP polyubiquitylation is involved in ER stress recovery. J Cell Sci. 2014;127(Pt 7):1417-27.
217. Loi M, Raimondi A, Morone D, Molinari M. ESCRT-III-driven piecemeal micro-ER-phagy remodels the ER during recovery from ER stress. Nat Commun. 2019;10(1):5058.
218. Fumagalli F, Noack J, Bergmann TJ, Cebollero E, Pisoni GB, Fasana E, et al. Translocon component Sec62 acts in endoplasmic reticulum turnover during stress recovery. Nat Cell Biol. 2016;18(11):1173-84.
219. Tapia D, Jiménez T, Zamora C, Espinoza J, Rizzo R, González-Cárdenas A, et al. KDEL receptor regulates secretion by lysosome relocation- and autophagy-dependent modulation of lipid-droplet turnover. Nat Commun. 2019;10(1):735.
220. Savarino A, Boelaert JR, Cassone A, Majori G, Cauda R. Effects of chloroquine on viral infections: an old drug against today's diseases? Lancet Infect Dis. 2003;3(11):722-7.
221. Zhou W, Wang H, Yang Y, Chen ZS, Zou C, Zhang J. Chloroquine against malaria, cancers and viral diseases. Drug Discov Today. 2020;25(11):2012-22.
222. Wahaab A, Mustafa BE, Hameed M, Stevenson NJ, Anwar MN, Liu K, et al. Potential Role of Flavivirus NS2B-NS3 Proteases in Viral Pathogenesis and Anti-flavivirus Drug Discovery Employing Animal Cells and Models: A Review. Viruses. 2021;14(1).
223. Cao YQ, Yuan L, Zhao Q, Yuan JL, Miao C, Chang YF, et al. Hsp40 Protein DNAJB6 Interacts with Viral NS3 and Inhibits the Replication of the Japanese Encephalitis Virus. Int J Mol Sci. 2019;20(22).

224. Krols M, Asselbergh B, De Rycke R, De Winter V, Seyer A, Müller FJ, et al. Sensory neuropathy-causing mutations in ATL3 affect ER-mitochondria contact sites and impair axonal mitochondrial distribution. Hum Mol Genet. 2019;28(4):615-27.
225. Kim I-J, Lee Y-h, Khalid MM, Chen IP, Zhang Y, Ott M, et al. SARS-CoV-2 protein ORF8 limits expression levels of Spike antigen and facilitates immune evasion of infected host cells. Journal of Biological Chemistry. 2023;299(8).
226. Ji M, Li M, Sun L, Deng H, Zhao YG. DMV biogenesis during β-coronavirus infection requires autophagy proteins VMP1 and TMEM41B. Autophagy. 2023;19(2):737-8.
227. D'Avila H, Lima CNR, Rampinelli PG, Mateus LCO, Sousa Silva RVd, Correa JR, et al. Lipid Metabolism Modulation during SARS-CoV-2 Infection: A Spotlight on Extracellular Vesicles and Therapeutic Prospects. International Journal of Molecular Sciences. 2024;25(1):640.
228. Li X, Wang L, Hao J, Zhu Q, Guo M, Wu C, et al. The Role of Autophagy in Lamellar Body Formation and Surfactant Production in Type 2 Alveolar Epithelial Cells. Int J Biol Sci. 2022;18(3):1107-19.
229. Weaver TE, Na C-L, Stahlman M. Biogenesis of lamellar bodies, lysosome-related organelles involved in storage and secretion of pulmonary surfactant. Seminars in Cell & Developmental Biology. 2002;13(4):263-70.
230. Li T, Zhao H, Guo G, Xia S, Wang L. VMP1 affects endoplasmic reticulum stress sensitivity via differential modulation of the three unfolded protein response arms. Cell Rep. 2023;42(3):112209.
231. Khaminets A, Heinrich T, Mari M, Grumati P, Huebner AK, Akutsu M, et al. Regulation of endoplasmic reticulum turnover by selective autophagy. Nature. 2015;522(7556):354-8.
232. Knupp J, Pletan ML, Arvan P, Tsai B. Autophagy of the ER: the secretome finds the lysosome. The FEBS Journal. 2023;290(24):5656-73.
233. Wu Y, Wu Z, Jin Q, Liu J, Xu P. Identification and Analysis of Biomarkers Associated with Lipophagy and Therapeutic Agents for COVID-19. Viruses. 2024;16(6):923.
234. Kohyama M, Suzuki T, Nakai W, Ono C, Matsuoka S, Iwatani K, et al. SARS-CoV-2 ORF8 is a viral cytokine regulating immune responses. Int Immunol. 2023;35(1):43-52.

Appendices

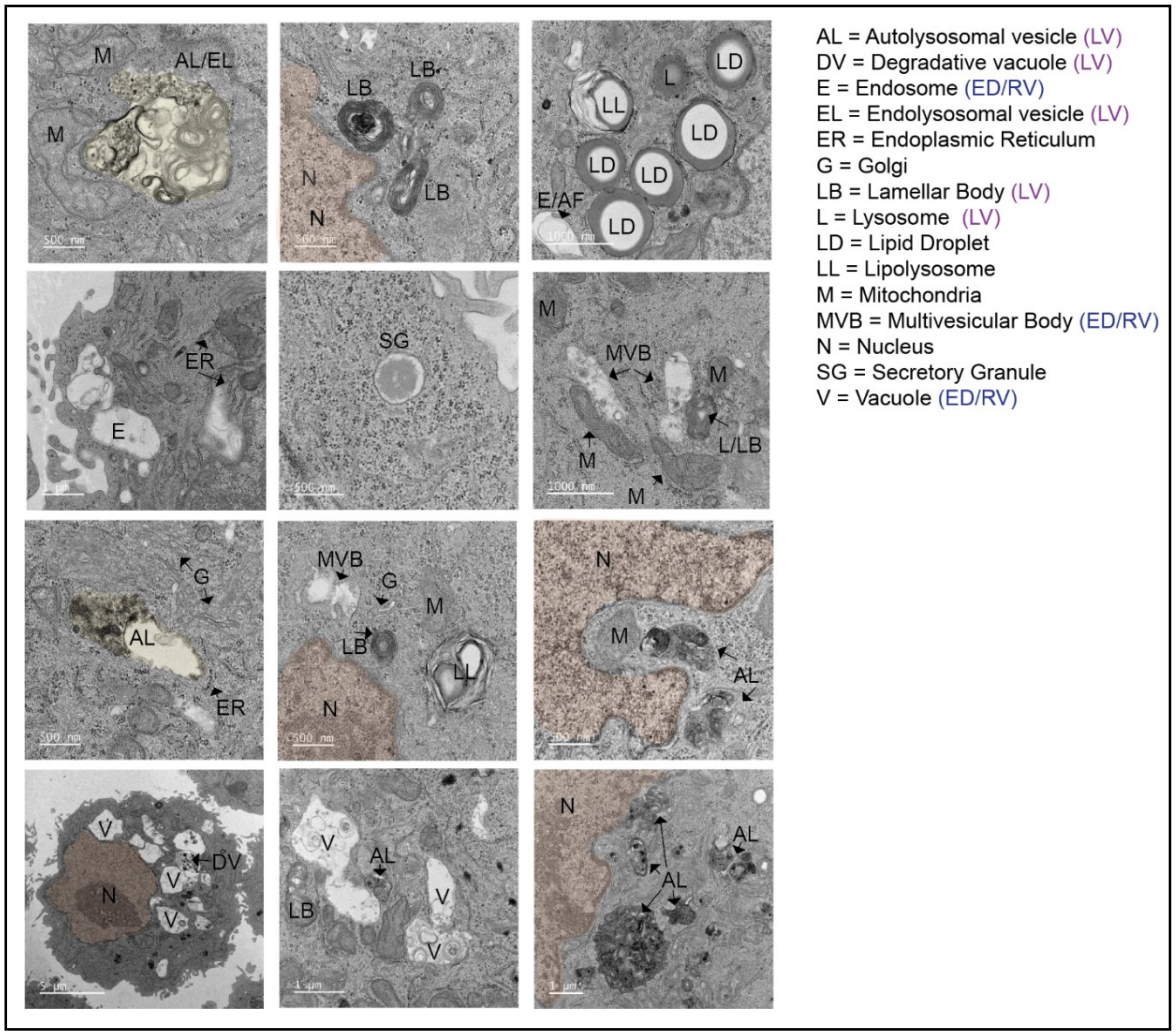


Supplementary Figure 2.1 IFNγ-stimulation restricts ORF8 secretion in 293T cells. 293T cells were stably transduced with pTetOne-ORF8-'C-term-HiBiT and assessed for cell surface, extracellular and intracellular levels of ORF8 using the Nano-Glo® HiBiT Extracellular and Lytic Detection Systems (Promega, UK). Cells were seeded in three sets of biological duplicates with technical quadruplicates. After 24 hours, the cells were stimulated with Doxycyline (250ng/mL). At 32 hours post induction, the cells were either mock or IFNγ-stimulated. After a 16-hour IFNγ-treatment, one set of cells was washed and used for A) assessing the intracellular MHC-I levels. For the other sets, the cells were either changed for fresh medium or directly assessed for B) extracellular detection of ORF8, providing the cell surface and total extracellular amounts of ORF8 respectively. Medium without cells was used as a control for extracellular detection,; non-stimulated cells were used as a control for intracellular detection. Data represents mean ± SD; *P < 0.05; **P < 0.01; ***P < 0.001; ****P <0.0001 (measured by ANOVA followed by Tukey's comparison test).

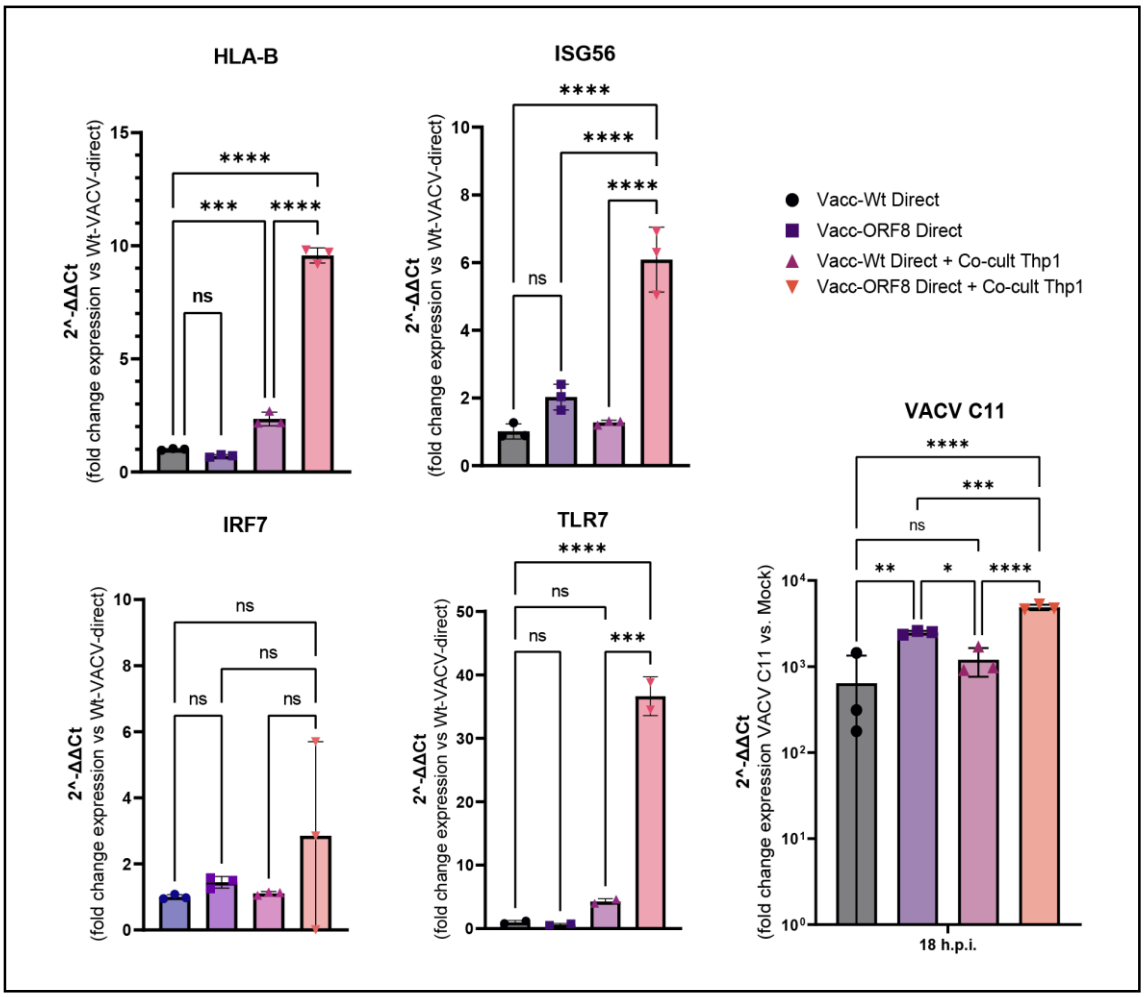


Supplementary Figure 2.2 Characteristics of A549-ORF8 variant single clones. A) Single clone lentiviral introduction of ORF8-StrepII constructs in A549 cells, assessed by RT-qPCR using WPRE and StrepII-probes. B) Changes in mRNA levels of some key immune markers during stable

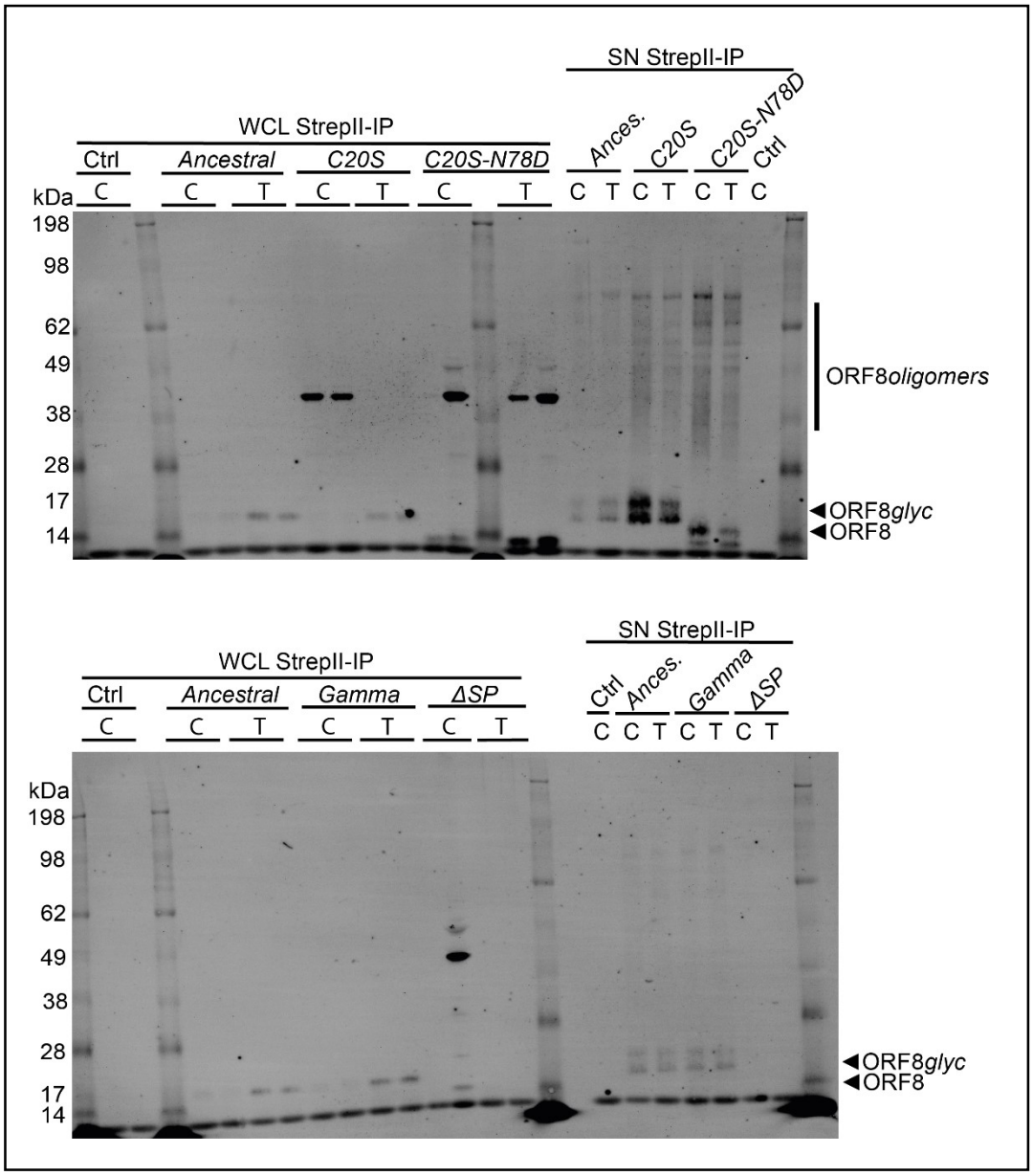
expression of ORF8 variants; probing for B2M, ISG54 and assessing cellular stress by BiP/HSPA5 levels relative to GAPDH. C) Luciferase read-out of Lactate-Glo™and Glutamine/Glutamate-Glo™ assays (Promega, UK) performed on the A549 single clones to report on glycolysis and glutaminolysis. D) FACS analysis of MHC-I cell surface and intracellular (ICS) expression, reported as mean fluorescence intensity (MFI) using live/dead and W6/32-staining. RT-qPCR was reported from two biological replicates with 3 technical replicates. The metabolism assays were performed in biological duplicate. FACS was performed in technical triplicates. Statistical significance was determined using Dunnett's multiple comparisons tests or for FACS with the Tukey's comparison. Significant differences are denoted as follows: *p < 0.05, **p < 0.01, ***p < 0.001, ****p < 0.0001.



Supplementary Figure 2.3 Organelle identification for TEM quantification. This figure illustrates examples of how organelle and vesicle identification was performed on TEM images. Abbreviations are listed on the right side of the figure. Vesicles are categorized for quantification into early degradative/recycling vesicles (ED/RV) and late degradative/lysosomal vesicles (LV), with these categories clearly marked. Secretory vesicles, including secretory granules and exosomes, are excluded from this categorization.



Supplementary Figure 2.4 Cell-cell communication during infection affects ORF8's role in immune-modulation. A549 cells were infected with recombinant Lister Vaccinia strains; expressing ORF8 (rVACV-ORF8) or wildtype Lister (rVACV-Wt). After 18 hours of infection the cells were changed for fresh medium or co-cultured with uninfected Thp1 cells in fresh medium for 24 hours. The cells were washed and the adherent cells were assessed for mRNA levels of immune markers ISG56, TLR7, IRF7 and for MHC-I subtype HLA-B. The intracellular VACVgenome copies were assessed prior to co-culture by measuring the VACV early gene C11 mRNA levels.



Supplementary Figure 2.5 Thapsigargin treatment leads to intracellular ORF8 accumulation across variants, except ΔSP-ORF8. Single clone A549 stable cell lines expressing variants of ORF8 were control-treated or treated with 2 uM thapsigargin for 12 hours. Lysates and concentrated supernatant were immunoprecipitated using MagStrep ""type3"" XT beads. The proteins were resolved by SDS-PAGE and stained for ORF8 using StrepII-tag antibody.

Supplementary Table 3.1 Reported interactors of SARS-CoV2 ORF8. Proteins are included if reported in at least two proteomic screens. In bold are proteins identified in the ORF8variant interactome of Chapter 3 that are discussed themselves or the process they are associated with.

Gene	Protein Name	Proteomic screen
AHSA1	Heat shock 90 kDa protein 1 co-chaperone	(95, 126)
ADAMTS1	A Disintegrin And Metalloproteinase With Thrombospondin Motifs 1	(80, 126)
ALDH3A2	Aldehyde Dehydrogenase 3 Family Member A2	(95, 126)
ALG1	Alpha-1,3-mannosyl-glycoprotein 4-alpha-mannosyltransferase	(95, 126)
ARCN1	ARCN1 Coatomer Protein Complex Subunit 1	(95, 126)
ASPH	Aspartate Beta-Hydroxylase	(80, 95, 126)
B3GALT6	Beta-1,3-Galactosyltransferase 6	(95, 126)
B4GAT1	Beta-1,4-Galactosyltransferase 1	(95, 126)
BSG	Basigin	(95, 126)
CALR	Calreticulin	(80, 95, 126)
CANX	Calnexin	(80, 95, 126)
CCDC47	Coiled-Coil Domain-Containing Protein 47	(80, 95, 126)
CDC42	Cell Division Control Protein 42	(95, 126)
CDKAL1	Cyclin-Dependent Kinase 5 Regulatory Subunit Associated Protein 1	(95, 126)
CHID1	Chitinase Domain Containing 1	(80, 126)
CHPF2	Chondroitin Sulfate N-Acetylgalactosaminyltransferase 2	(95, 126)
CHST14	Carbohydrate Sulfotransferase 14	(95, 126)
CNNM3	Cyclin And CBS Domain Diphtheria Toxin-Like 3	(79, 126)
COL6A1	Collagen Type VI Alpha 1 Chain	(95, 126)
COLGALT1	Collagen Beta-1,4-Galactosyltransferase 1	(95, 126)
COPA	Coatomer Protein Complex Subunit Alpha	(95, 126)
COPB1	Coatomer Protein Complex Subunit Beta 1	(95, 126)
COPB2	Coatomer Protein Complex Subunit Beta 2	(95, 126)
CTSC	Cathepsin C	(95, 126)
DDOST	Dolichyl-Phosphate Mannose-Protein Dolichyl-Phosphate Mannosyltransferase	(95, 126)
DHCR7	7-Dehydrocholesterol Reductase	(95, 126)
DHRS7B	Dehydrogenase/Reductase 7B	(95, 126)
DNAJB11	DnaJ Heat Shock Protein Family Member B11	(80, 95, 126)
DNAJC3	DnaJ Heat Shock Protein Family Member C3	(80, 95, 126)
EDEM3	ER Degradation Enhancing Alpha-Mannosidase 3	(95, 126)
EMC1	ER Membrane Protein Complex 1	(80, 126)
EMD	Emerin	(95, 126)
ERLEC1	Endoplasmic Reticulum Lectin 1	(95, 126)
ERO1A	Endoplasmic Reticulum Oxidoreductase 1 Alpha	(95, 126)
ERP44	Endoplasmic Reticulum Protein 44	(80, 95, 126)
EXT2	Exostosin 2	(95, 126)
FGA	Fibrinogen Alpha Chain	(79, 80)
FKBP10	FK506 Binding Protein 10	(95, 126)
FKBP7	FK506 Binding Protein 7	(95, 126)
GALNT2	Polypeptide N-Acetylgalactosaminyltransferase 2	(95, 126)
GALNT7	Polypeptide N-Acetylgalactosaminyltransferase 7	(95, 126)
GANAB	Alpha-Glucosidase	(95, 126)

GGH	Gamma-Glutamyl Hydrolase	(79, 126)
GLA	Gamma-Carboxylase	(95, 126)
GLB1	Galactosylceramidase	(95, 126)
GLG1	Glycogenin-1	(80, 126)
GPX8	Glutathione Peroxidase 8	(95, 126)
HACD3	3-Hydroxyacyl-CoA Dehydratase 3	(95, 126)
HADHB	Hydroxyacyl-CoA Dehydrogenase Beta Subunit	(95, 126)
HLA-A	Major Histocompatibility Complex, Class I, A	(95, 126)
HLA-C	Major Histocompatibility Complex, Class I, C	(95, 126)
HSD17B12	Hydroxysteroid 17-Beta Dehydrogenase 12	(95, 126)
HSP90B1	Heat Shock Protein 90 Beta Family Member 1	(80, 95, 126)
HSPA5	Heat Shock Protein Family A Member 5	(80, 95, 126)
HSPD1	Heat Shock Protein Family D Member 1	(95, 126)
HYOU1	Hypoxia Up-Regulated Protein 1	(80, 95, 126)
ITGB1	Integrin Beta 1	(80, 126)
LMAN2	Lectin, Mannose-Binding 2	(95, 126)
LMAN2L	Lectin, Mannose-Binding 2-Like	(95, 126)
LPCAT1	Lysophosphatidylcholine Acyltransferase 1	(95, 126)
MGAT2	Mannosyl-Glycoprotein 2 Beta-1,2-N-Acetylglucosaminyltransferase	(95, 126)
MOGS	Mannosyl-Oligosaccharide Glucosidase	(95, 126)
NCLN	Nucleolin	(95, 126)
NME3	NME/NM23 Family Member 3	(79, 126)
NPTX1	Neuronal Pentraxin 1	(79, 126)
P3H1	Prolyl 3-Hydroxylase 1	(95, 126)
P4HA1	Prolyl 4-Hydroxylase Alpha 1	(95, 126)
P4HA2	Prolyl 4-Hydroxylase Alpha 2	(95, 126)
P4HB	Protein Disulfide Isomerase	(95, 126)
PCSK6	Proprotein Convertase Subtilisin/Kexin Type 6	(95, 126)
PDIA3	Protein Disulfide Isomerase Family A, Member 3	(79, 95, 126)
PDIA4	Protein Disulfide Isomerase Family A, Member 4	(95, 126)
PDIA5	Protein Disulfide Isomerase Family A, Member 5	(95, 126)
PGRMC1	Progesterone Receptor Membrane Component 1	(95, 126)
PIGK	Phosphatidylinositol Glycan Anchor Biosynthesis Class K	(95, 126)
PIGX	Phosphatidylinositol Glycan Anchor Biosynthesis Class X	(95, 126)
PLD3	Phospholipase D3	(95, 126)
PLOD1	Procollagen-Lysine, 2-Oxoglutarate 5-Dioxygenase 1	(95, 126)
PLOD2	Procollagen-Lysine, 2-Oxoglutarate 5-Dioxygenase 2	(95, 126)
PLOD3	Procollagen-Lysine, 2-Oxoglutarate 5-Dioxygenase 3	(95, 126)
POFUT1	Protein O-Fucosyltransferase 1	(95, 126)
PPP6C	Protein Phosphatase 6C	(95, 126)
PPT1	Palmitoyl-Protein Thioesterase 1	(95, 126)
PREB	Pre-B Cell Receptor Beta	(95, 126)
PTGES2	Prostaglandin E Synthase 2	(95, 126)
QPCTL	Glutaminyl Peptide Cyclotransferase	(95, 126)
RCN1	Reticulocalbin 1	(95, 126)
RCN2	Reticulocalbin 2	(95, 126)
RPN1	Proteasome 26S Subunit ATPase 1	(95, 126)
RPN2	Proteasome 26S Subunit ATPase 2	(95, 126)
RTCB	RNA 3'-Phosphatase	(95, 126)

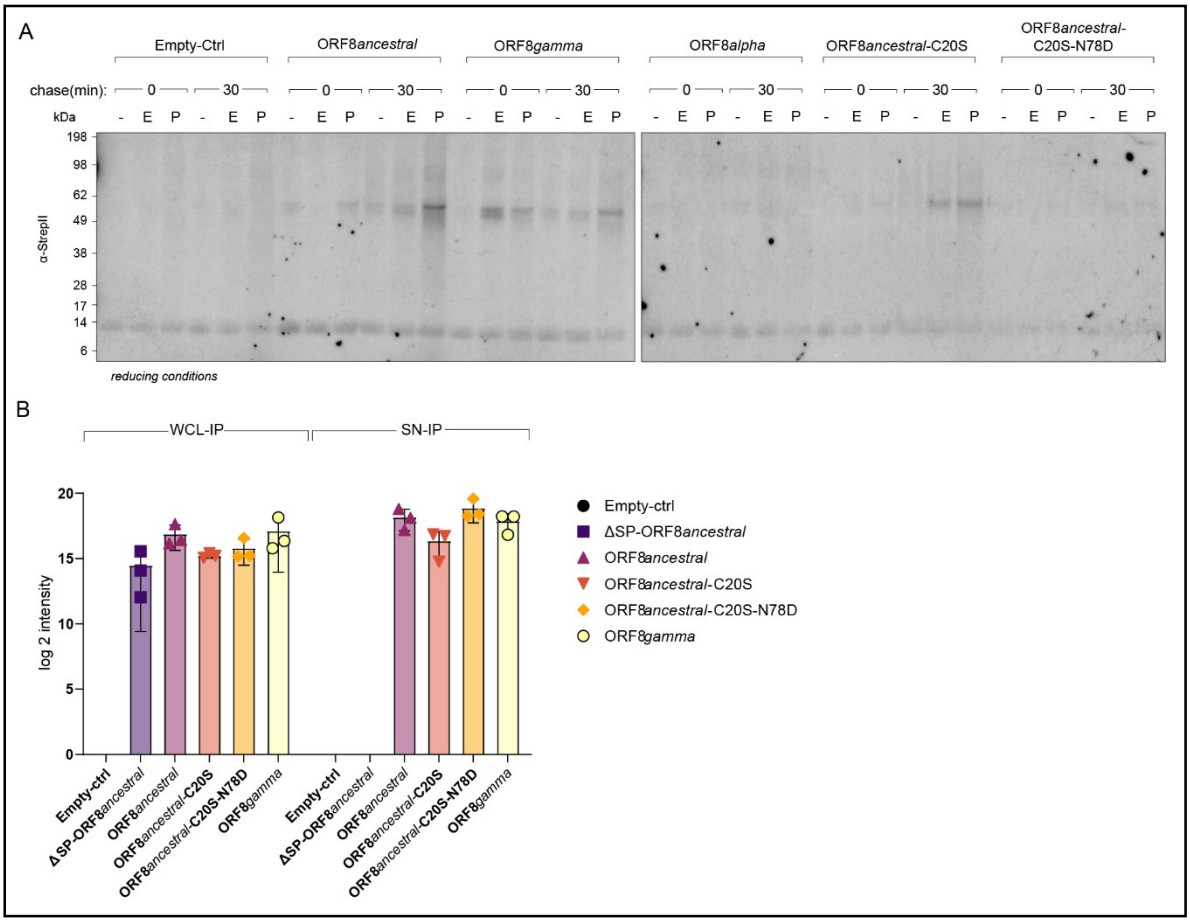
RUVBL1	RuvB-like 1	(95, 126)
SDF2	Stromal Cell-Derived Factor 2	(95, 126)
SDF2L1	Stromal Cell-Derived Factor 2-Like 1	(95, 126)
SDF4	Stromal Cell-Derived Factor 4	(95, 126)
SEC22B	SEC22B Vesicle Transport Protein	(95, 126)
SEC61A1	Sec61 Alpha Subunit	(95, 126)
SELENOF	Selenoprotein F	(95, 126)
SERPINH1	Serpin Family H Member 1	(79, 126)
SIL1	Sil1 Protein	(95, 126)
SLC1A5	Solute Carrier Family 1 Member 5	(95, 126)
SPCS2	Signal Peptide-Cleaving Enzyme 2	(95, 126)
SPCS3	Signal Peptide-Cleaving Enzyme 3	(95, 126)
SQSTM1	Sequestosome 1	(80, 126)
STT3A	STT3 Oligosaccharyltransferase 1	(95, 126)
SUMF2	Sulfatase-Modifying Factor 2	(95, 126)
TCP1	T-complex Protein 1	(95, 126)
TCTN3	Tectonic 3	(79, 126)
TECR	Tetrahydrofolate Deformylase	(95, 126)
TMED10	Transmembrane Protein 10	(95, 126)
TMED7	Transmembrane Protein 7	(95, 126)
TMED9	Transmembrane Protein 9	(95, 126)
TMEM165	Transmembrane Protein 165	(95, 126)
TMEM30A	Transmembrane Protein 30A	(95, 126)
TMEM33	Transmembrane Protein 33	(95, 126)
TMPO	Thymopoietin	(95, 126)
TMX1	Thioredoxin-Related Transmembrane Protein 1	(95, 126)
TMX4	Thioredoxin-Related Transmembrane Protein 4	(95, 126)
TOR1A	Torsin Family 1 Member A	(95, 126)
TOR1AIP2	Torsin 1 Interacting Protein 2	(95, 126)
TOR1B	Torsin Family 1 Member B	(79, 95, 126)
TXNDC5	Thioredoxin Domain Containing 5	(95, 126)
UBR4	Ubiquitin Protein Ligase E3 Component 4	(80, 126)
UGGT1	UDP-Glucose Glycoprotein Glucosyltransferase 1	(95, 126)
UGGT2	UDP-Glucose Glycoprotein Glucosyltransferase 2	(79, 95, 126)
WLS	Wntless	(95, 126)

Supplementary Table 3.2 Reactome and KEGG pathway enrichment of consensus ORF8 interactome described in Supp.Table 3.1. Significant enrichment was assumed at FDR<0.01 and p-value<0.05.

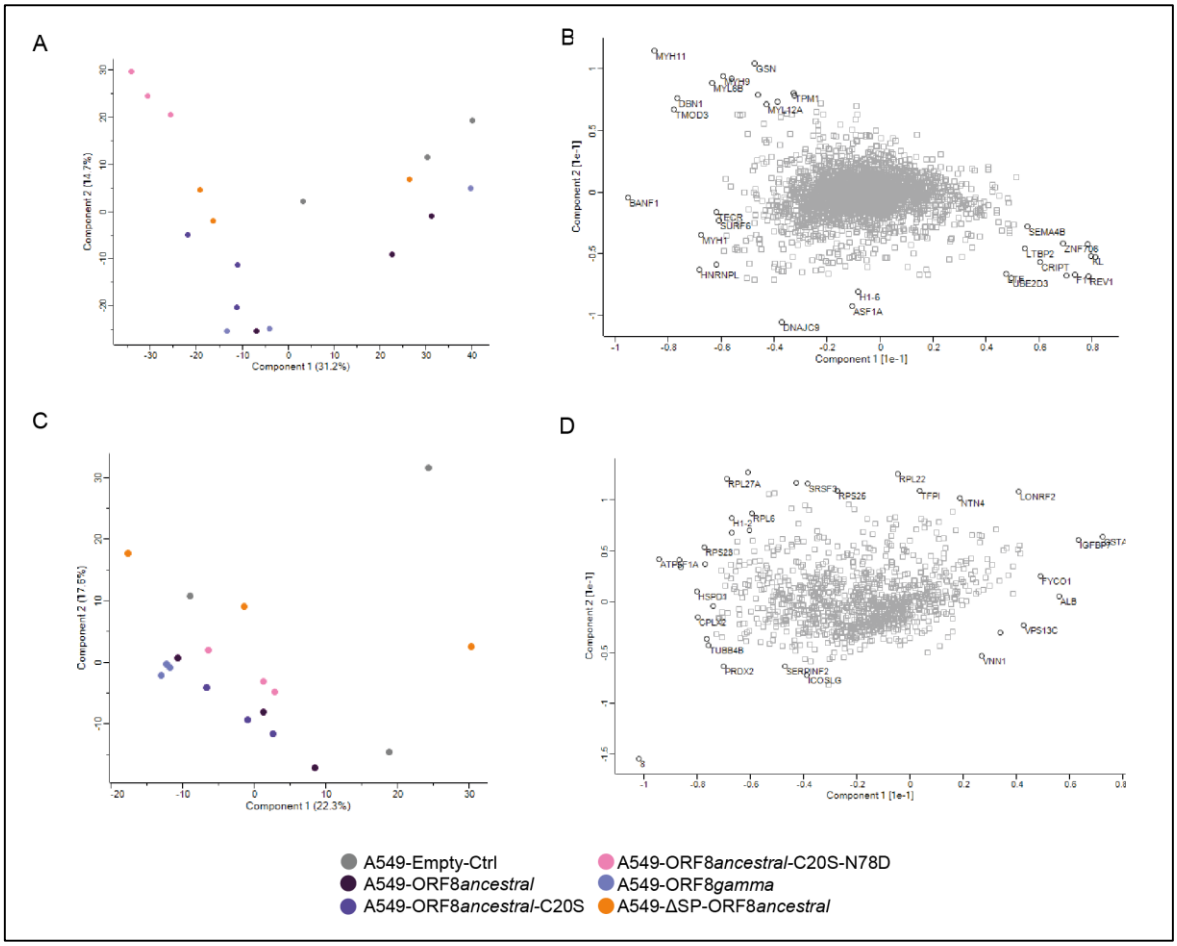
Pathway description (associated genes)	**Category**	**Significance (p-value)**	**FDR value**
Protein processing in endoplasmic reticulum ERLEC1|RPN2|SEC61A1|CANX|UGGT1|PREB|RPN1|HSP90B1|PDIA3|LMAN2|EDEM3|CALR|HSPA5|P4HB|GANAB|UGGT2|TXNDC5|STT3A|ERO1L|DDOST|DNAJB11|DNAJC3|HYOU1	KEGG Pathways	5.72E-24	1.92E-21
Asparagine N-linked glycosylation CTSC|RPN2|CANX|COPB1|UGGT1|PREB|ALG1|ARCN1|RPN1|PDIA3|TMED10|LMAN2|GLB1|MGAT2|EDEM3|CALR|COPB2|TMED9|GANAB|COPA|UGGT2|LMAN2L|STT3A|DDOST|TMED7|SEC22B	Reactome Pathways	3.44E-22	7.46E-19
Metabolism of proteins RCN1|CTSC|RPN2|SEC61A1|CANX|COPB1|UGGT1|PREB|ALG1|SPCS2|ARCN1|GALNT7|ADAMTS1|RPN1|PIGX|HSP90B1|PDIA3|TMED10|LMAN2|GLB1|MGAT2|B3GNT1|TCP1|EDEM3|RUVBL1|CALR|PDIA5|HSPA5|P4HB|COPB2|TMED9|GANAB|GALNT2|COPA|PIGK|UGGT2|LMAN2L|STT3A|ERO1L|HLA-A|DDOST|TMED7|DNAJB11|SPCS3|SEC22B|DNAJC3|HYOU1	Reactome Pathways	2.05E-17	2.23E-14
Post-translational protein modification RCN1|CTSC|RPN2|CANX|COPB1|UGGT1|PREB|ALG1|ARCN1|GALNT7|ADAMTS1|RPN1|PIGX|HSP90B1|PDIA3|TMED10|LMAN2|GLB1|MGAT2|B3GNT1|EDEM3|RUVBL1|CALR|P4HB|COPB2|TMED9|GANAB|GALNT2|COPA|PIGK|UGGT2|LMAN2L|STT3A|HLA-A|DDOST|TMED7|SEC22B|DNAJC3	Reactome Pathways	9.60E-16	6.95E-13
Metabolic pathways CHPF2|PLOD1|TECR|GLA|NME3|PLOD3|RPN2|COLGALT1|PTPLAD1|ALG1|P4HA1|GALNT7|HSD17B12|PLOD2|LPCAT1|RPN1|GLB1|MGAT2|B3GNT1|HADHB|GANAB|PTGES2|ALDH3A2|DHCR7|GALNT2|PIGK|B3GALT6|STT3A|EXT2|P4HA2|PLD3|DDOST|GPX8	KEGG Pathways	1.61E-11	2.70E-09
Collagen biosynthesis and modifying enzymes PLOD1|PLOD3|LEPRE1|COLGALT1|P4HA1|PLOD2|P4HB|COL6A1|P4HA2|SERPINH1	Reactome Pathways	2.93E-11	1.59E-08
Transport to the Golgi and subsequent modification CTSC|COPB1|PREB|ARCN1|TMED10|LMAN2|MGAT2|COPB2|TMED9|COPA|LMAN2L|TMED7|SEC22B	Reactome Pathways	1.49E-10	6.48E-08
ER to Golgi Anterograde Transport CTSC|COPB1|PREB|ARCN1|TMED10|LMAN2|COPB2|TMED9|COPA|LMAN2L|TMED7|SEC22B	Reactome Pathways	2.69E-10	9.73E-08
Calnexin/calreticulin cycle CANX|UGGT1|PDIA3|EDEM3|CALR|GANAB|UGGT2	Reactome Pathways	8.22E-10	2.23E-07

Maturation of spike protein RPN2|CANX|RPN1|MGAT2|GANAB|STT3A|DDOST	Reactome Pathways	1.28E-09	3.09E-07
Vesicle-mediated transport CTSC|COPB1|TOR1B|PREB|ARCN1|HSP90B1|TMED10|LMAN2|CALR|COPB2|TMED9|TOR1A|GALNT2|COPA|LMAN2L|TXNDC5|TMED7|SEC22B|HYOU1	Reactome Pathways	1.88E-08	3.49E-06
Antigen Presentation: Folding, assembly and peptide loading of class I MHC CANX|PDIA3|CALR|HSPA5|HLA-C|HLA-A	Reactome Pathways	2.53E-08	4.22E-06
N-Glycan biosynthesis RPN2|ALG1|RPN1|MGAT2|GANAB|STT3A|DDOST	KEGG Pathways	4.52E-08	5.07E-06
Neutrophil degranulation PGRMC1|GLA|CTSC|TMEM30A|COPB1|GGH|ERP44|LPCAT1|GLB1|PTGES2|UBR4|HLA-C|TXNDC5|HLA-A|DDOST|DNAJC3	Reactome Pathways	3.31E-08	5.14E-06
Extracellular matrix organization PLOD1|PLOD3|LEPRE1|COLGALT1|P4HA1|PLOD2|ADAMTS1|P4HB|BSG|COL6A1|ITGB1|P4HA2|SERPINH1	Reactome Pathways	4.74E-08	6.86E-06
Cargo concentration in the ER CTSC|PREB|TMED10|LMAN2|LMAN2L|SEC22B	Reactome Pathways	1.08E-07	1.46E-05
Unfolded Protein Response (UPR) PREB|HSP90B1|CALR|PDIA5|HSPA5|DNAJB11|DNAJC3|HYOU1	Reactome Pathways	1.44E-07	1.85E-05
Golgi-to-ER retrograde transport COPB1|ARCN1|TMED10|COPB2|TMED9|GALNT2|COPA|TMED7|SEC22B	Reactome Pathways	1.46E-07	1.85E-05
Various types of N-glycan biosynthesis RPN2|ALG1|RPN1|MGAT2|STT3A|DDOST	KEGG Pathways	2.28E-07	1.91E-05
COPI-dependent Golgi-to-ER retrograde traffic COPB1|ARCN1|TMED10|COPB2|TMED9|COPA|TMED7|SEC22B	Reactome Pathways	2.11E-07	2.41E-05
IRE1alpha activates chaperones PREB|PDIA5|HSPA5|DNAJB11|DNAJC3|HYOU1	Reactome Pathways	9.88E-07	1.00E-04
Membrane Trafficking CTSC|COPB1|TOR1B|PREB|ARCN1|TMED10|LMAN2|COPB2|TMED9|TOR1A|GALNT2|COPA|LMAN2L|TXNDC5|TMED7|SEC22B	Reactome Pathways	1.19E-06	1.20E-04
Antigen processing and presentation CANX|PDIA3|CALR|HSPA5|HLA-C|HLA-A	KEGG Pathways	3.43E-06	2.30E-04
Diseases of glycosylation ALG1|ADAMTS1|GLB1|CHST14|MGAT2|B3GNT1|B3GALT6|EXT2	Reactome Pathways	3.04E-06	2.90E-04
COPI-mediated anterograde transport COPB1|ARCN1|TMED10|COPB2|TMED9|COPA|TMED7	Reactome Pathways	3.49E-06	3.20E-04
SARS-CoV Infections RPN2|CANX|RPN1|MGAT2|GANAB|STT3A|ITGB1|DDOST	Reactome Pathways	3.70E-06	3.20E-04
COPII-mediated vesicle transport CTSC|PREB|TMED10|LMAN2|LMAN2L|SEC22B	Reactome Pathways	4.77E-06	3.80E-04

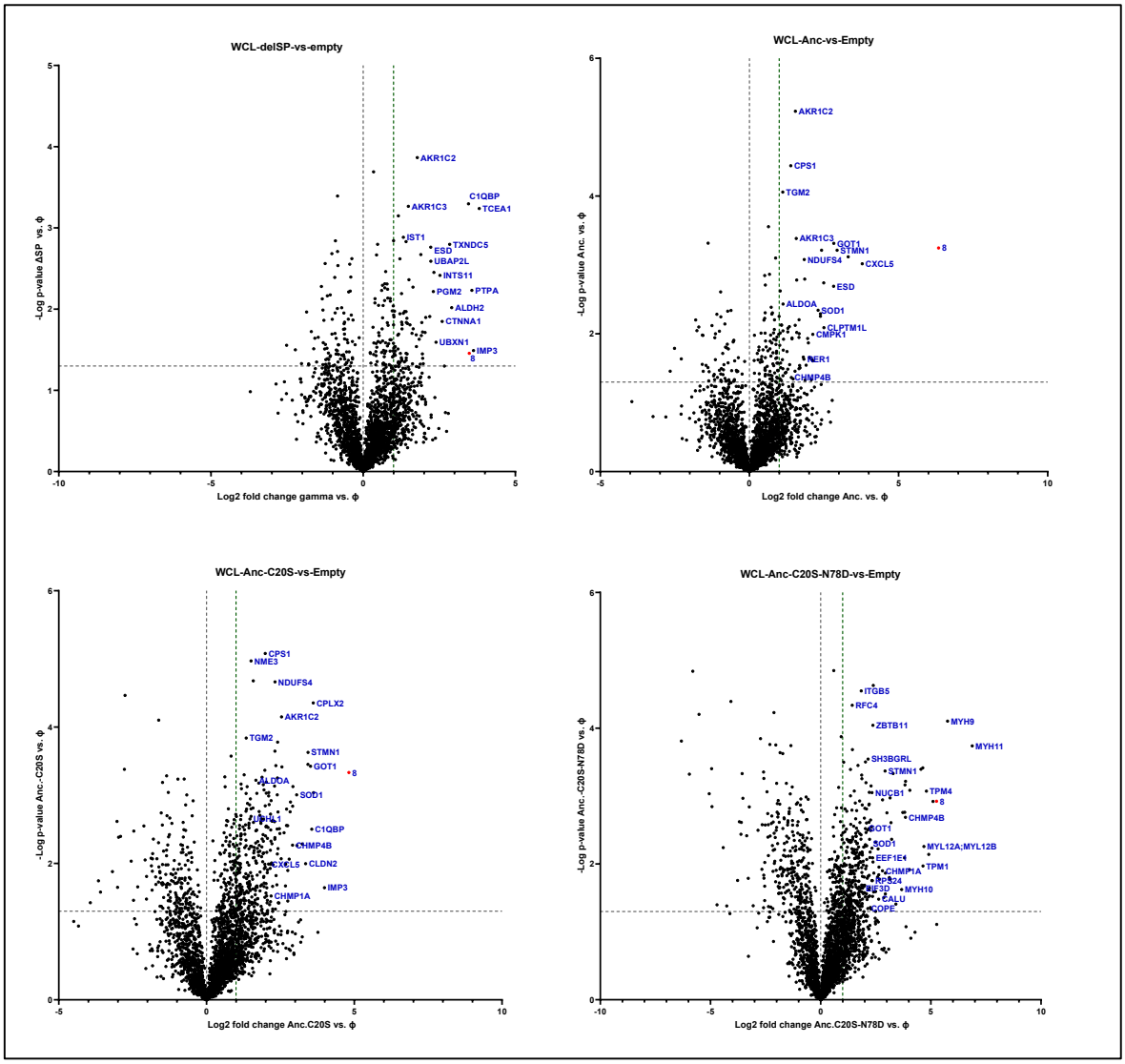
Other types of O-glycan biosynthesis PLOD3|COLGALT1|GALNT7|GALNT2|POFUT1	KEGG Pathways	9.51E-06	5.30E-04
Immune System PGRMC1|GLA|CTSC|TMEM30A|SEC61A1|CANX|COPB1|GGH|ERP44|LPCAT1|HSP90B1|PDIA3|GLB1|TCP1|CALR|HSPA5|P4HB|PTGES2|UBR4|HLA-C|TXNDC5|SQSTM1|ITGB1|HLA-A|PLD3|DDOST|SEC22B|DNAJC3	Reactome Pathways	1.08E-05	8.40E-04
Protein export SEC61A1|SPCS2|HSPA5|SPCS3	KEGG Pathways	1.87E-05	9.00E-04
ER-Phagosome pathway SEC61A1|PDIA3|CALR|HLA-C|HLA-A|SEC22B	Reactome Pathways	1.32E-05	9.90E-04
XBP1(S) activates chaperone genes PREB|PDIA5|DNAJB11|DNAJC3|HYOU1	Reactome Pathways	1.56E-05	0.0011
Fatty acid elongation TECR|PTPLAD1|HSD17B12|HADHB	KEGG Pathways	2.51E-05	0.0011
Phagosome SEC61A1|CANX|CALR|HLA-C|ITGB1|HLA-A|SEC22B	KEGG Pathways	3.06E-05	0.0011
Lysine degradation PLOD1|PLOD3|COLGALT1|PLOD2|ALDH3A2	KEGG Pathways	4.23E-05	0.0014
Innate Immune System PGRMC1|GLA|CTSC|TMEM30A|COPB1|GGH|ERP44|LPCAT1|HSP90B1|GLB1|PTGES2|UBR4|HLA-C|TXNDC5|HLA-A|PLD3|DDOST|DNAJC3	Reactome Pathways	4.30E-05	0.0029
ATF6 (ATF6-alpha) activates chaperone genes HSP90B1|CALR|HSPA5	Reactome Pathways	5.61E-05	0.0037
SRP-dependent cotranslational protein targeting to membrane RPN2|SEC61A1|SPCS2|RPN1|DDOST|SPCS3	Reactome Pathways	6.76E-05	0.0043
Glycosaminoglycan metabolism CHPF2|GLB1|CHST14|B3GNT1|B3GALT6|EXT2	Reactome Pathways	1.20E-04	0.0073



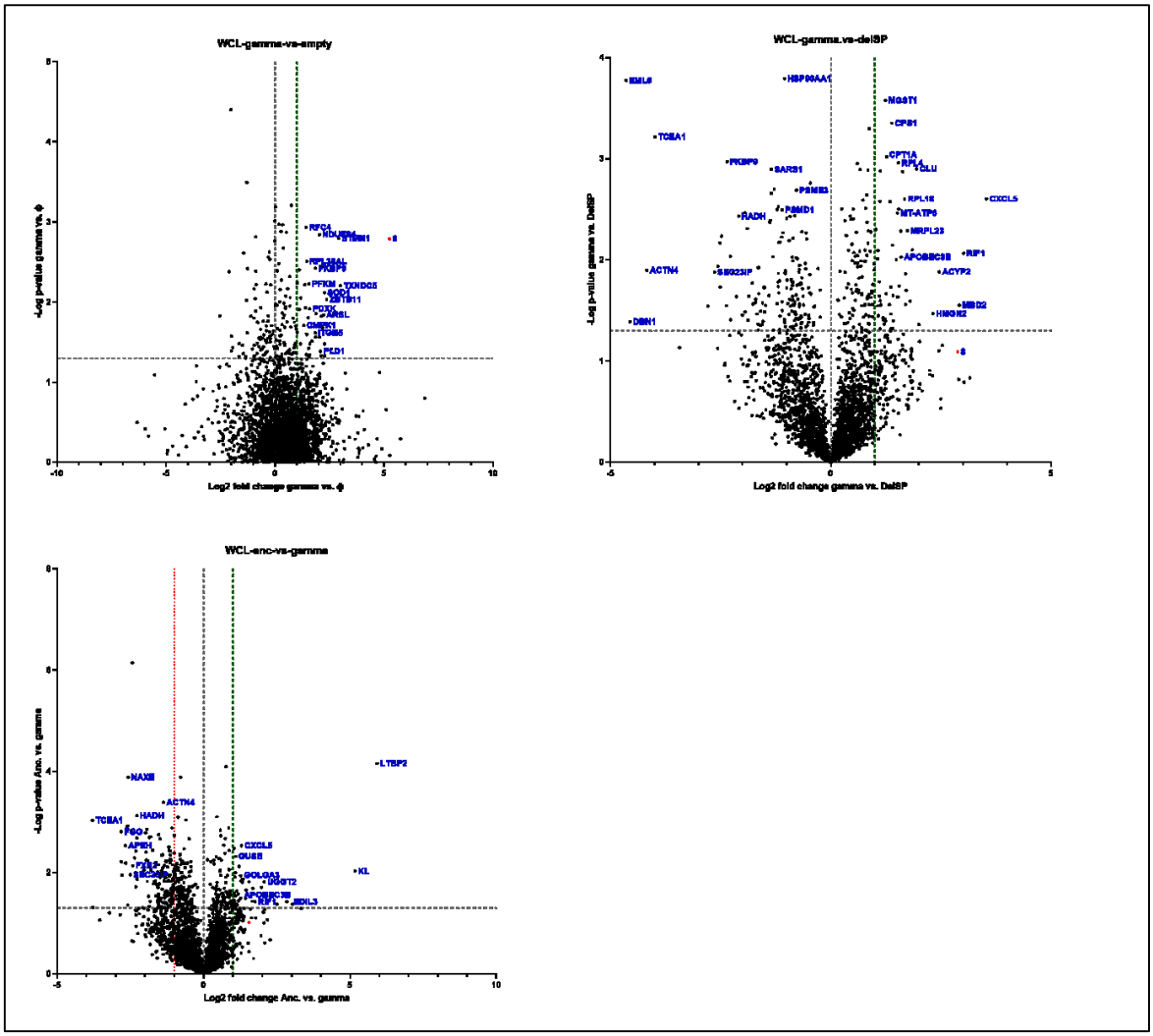
Supplementary Figure 3.1 ORF8 is rapidly secreted as tetramer and detected by autoradiogram in [35S]-pulse-chase assay and mass spectrometry. A) A549-stable cell lines ORF8*ancestral*, -C20S, -C20S-N78D, ORF8*gamma*, -*alpha* and Empty-Ctrl were subjected to standard [35S]-pulse-chase with 0 and 30 min chase. ORF8 was immunoprecipitated from the supernatant and visualized using autoradiography. The IPs were treated with EndoH (E), PNGase (P) to detect glycosylation status of the secreted products. B) MagStrep-beads-antigen complexes were processed by the Target Discovery Institute, University of Oxford, for mass spectrometry analysis. The raw data were analyzed using DIA-NN in library-free mode against the StrepII-tagged ORF8*ancestral* tryptic peptides. ORF8 detection was visualized as log2 intensity of three biological replicates.



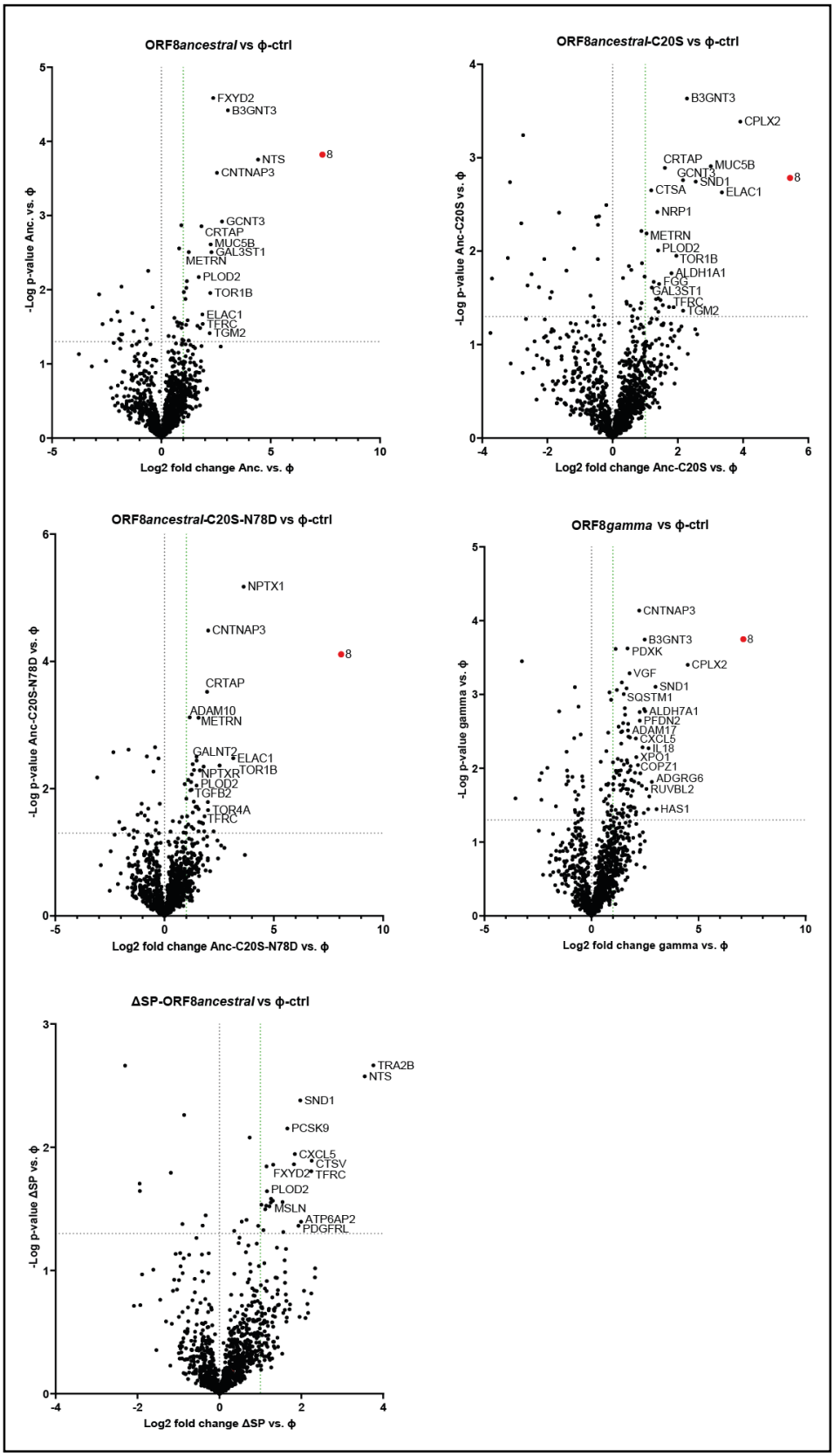
Supplementary Figure 3.2 Visualization of PCA loadings and analysis. A) PCA analysis and B) loadings of the intracellular interactome samples; C) PCA analysis and D) loadings of the extracellular interactome samples submitted for MS analysis. Samples were prepared in biological triplicates of A549-stable cell lines ORF8*ancestral*, -C20S, -C20S-N78D, ORF8*gamma*, -*alpha* and Empty-Ctrl. The graphs were generated using Perseus software (v2.1).



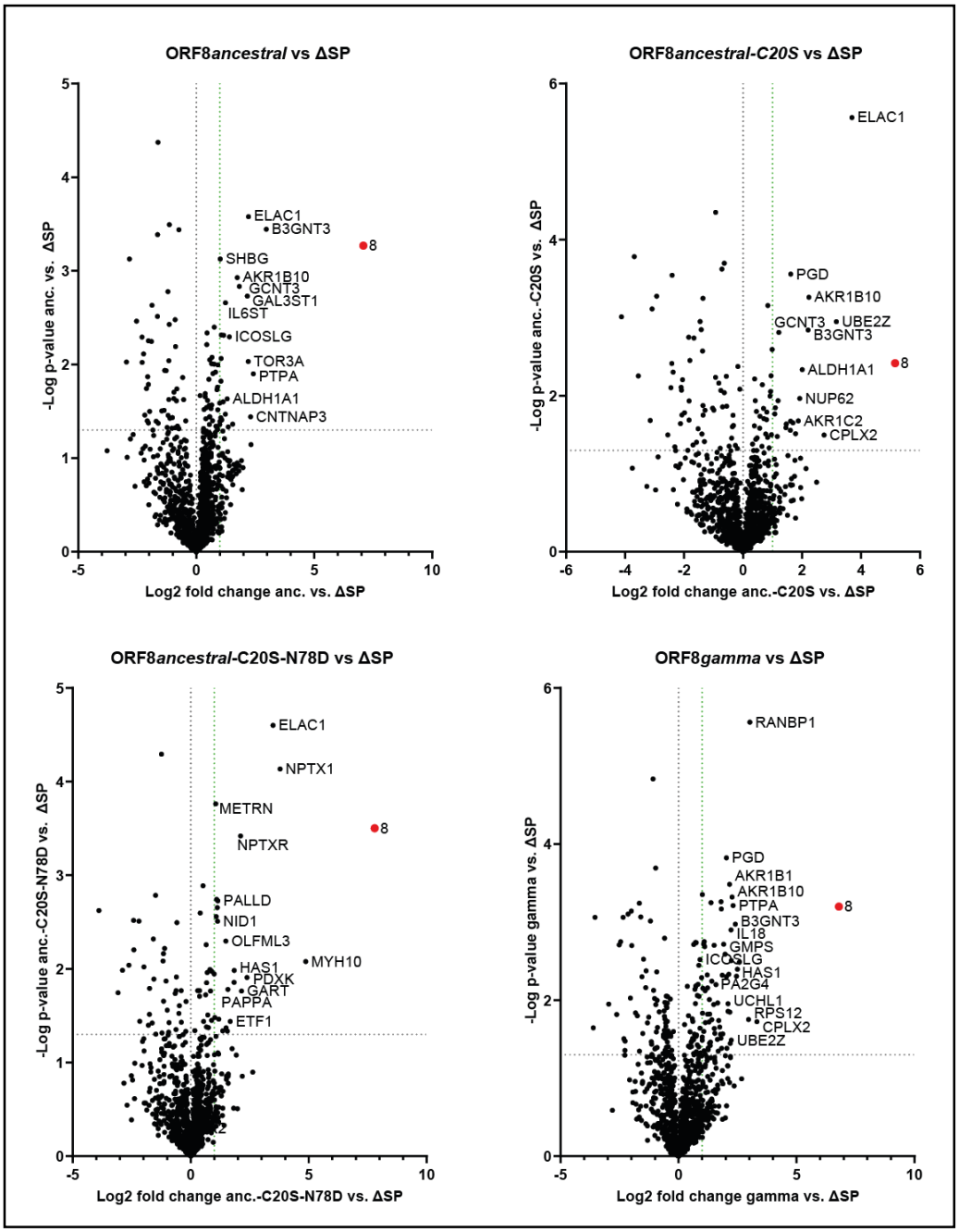
Supplementary Figure 3.3 Volcano plots of intracellular interactomes of ORF8 variants in comparison to Empty-Ctrl A549 cells. Protein intensities were log2-transformed and analysed in Perseus (v2.1). Cut-offs are indicated for p<0.05 (student p-value >1.3) and fold change larger than 2 (log 2 fold >1).



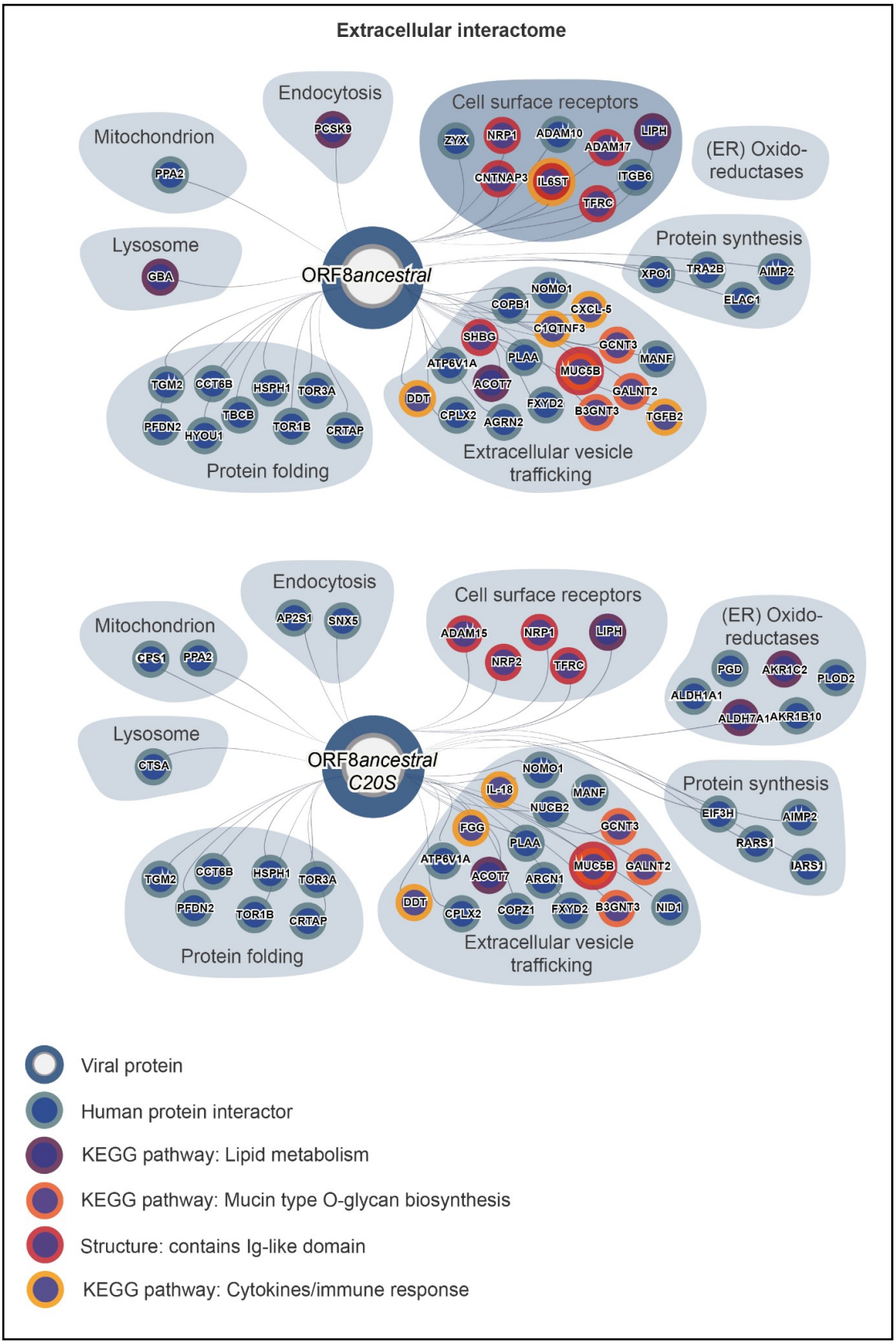
Supplementary Figure 3.4 Volcano plots of the intracellular interactome of ORF8*gamma* in comparison to Empty-Ctrl, ΔSP and ORF8*ancestral* A549 cells. Protein intensities were log2-transformed and analysed in Perseus (v2.1). Cut-offs are indicated for p<0.05 (student p-value >1.3) and fold change larger than 2 (log 2 fold >1).



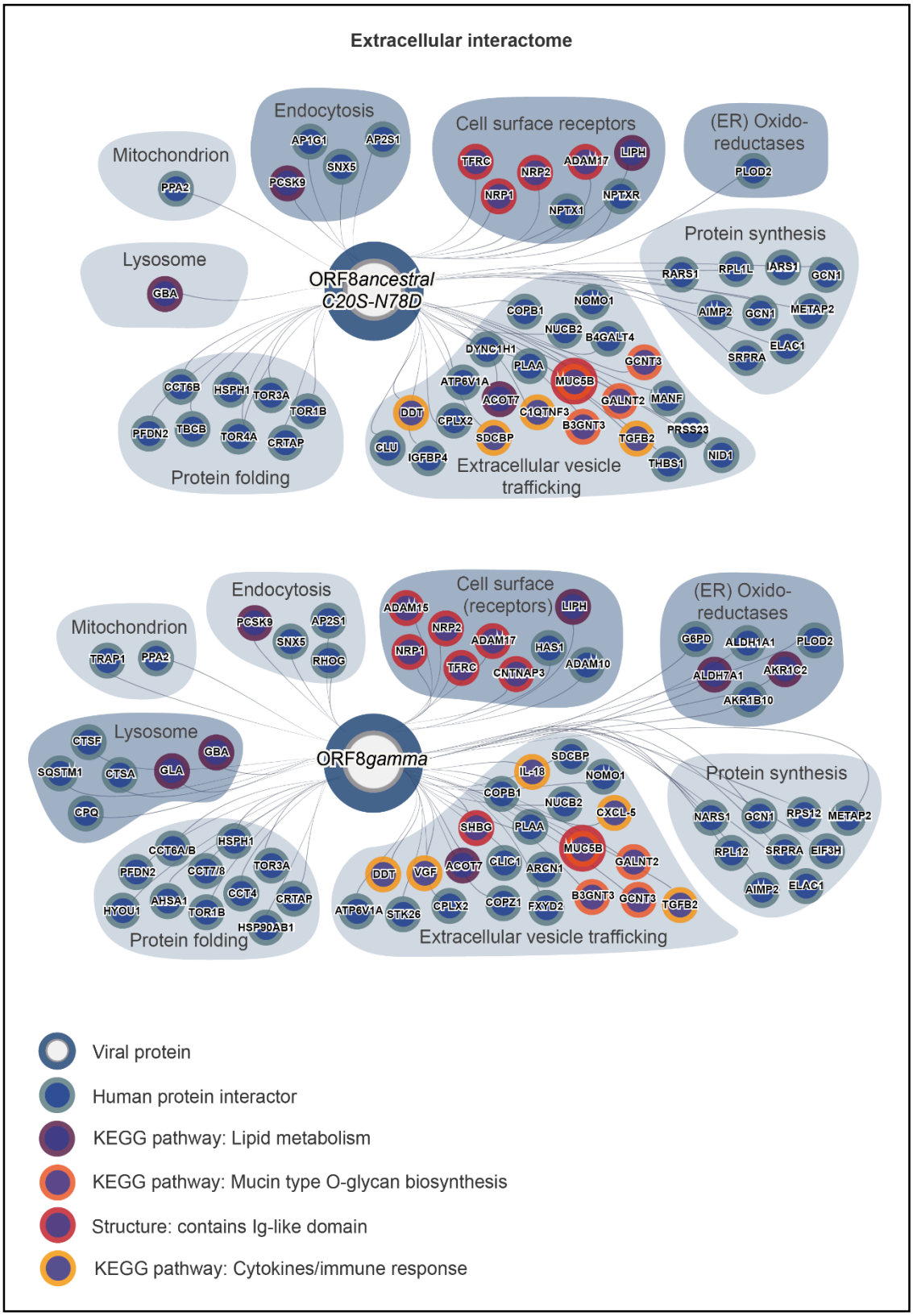
Supplementary Figure 3.5 Volcano plots of extracellular interactomes of ORF8 variants in comparison to Empty-Ctrl A549 cells. Protein intensities were log2-transformed and analysed in Perseus (v2.1). Cut-offs are indicated for p<0.05 (student p-value >1.3) and fold change larger than 2 (log2 FC >1).



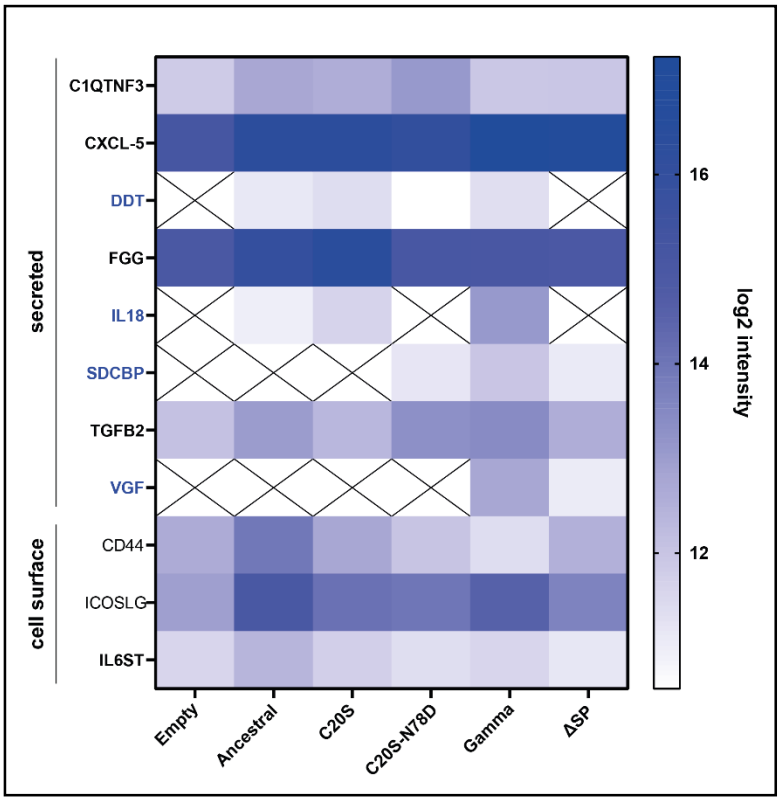
Supplementary Figure 3.6 Volcano plots of extracellular interactomes of ORF8 variants in comparison to ΔSP-ORF8 A549 cells. Protein intensities were log2-transformed and analysed in Perseus (v2.1). Cut-offs are indicated for p<0.05 (student p-value >1.3) and fold change larger than 2 (log2 FC >1).



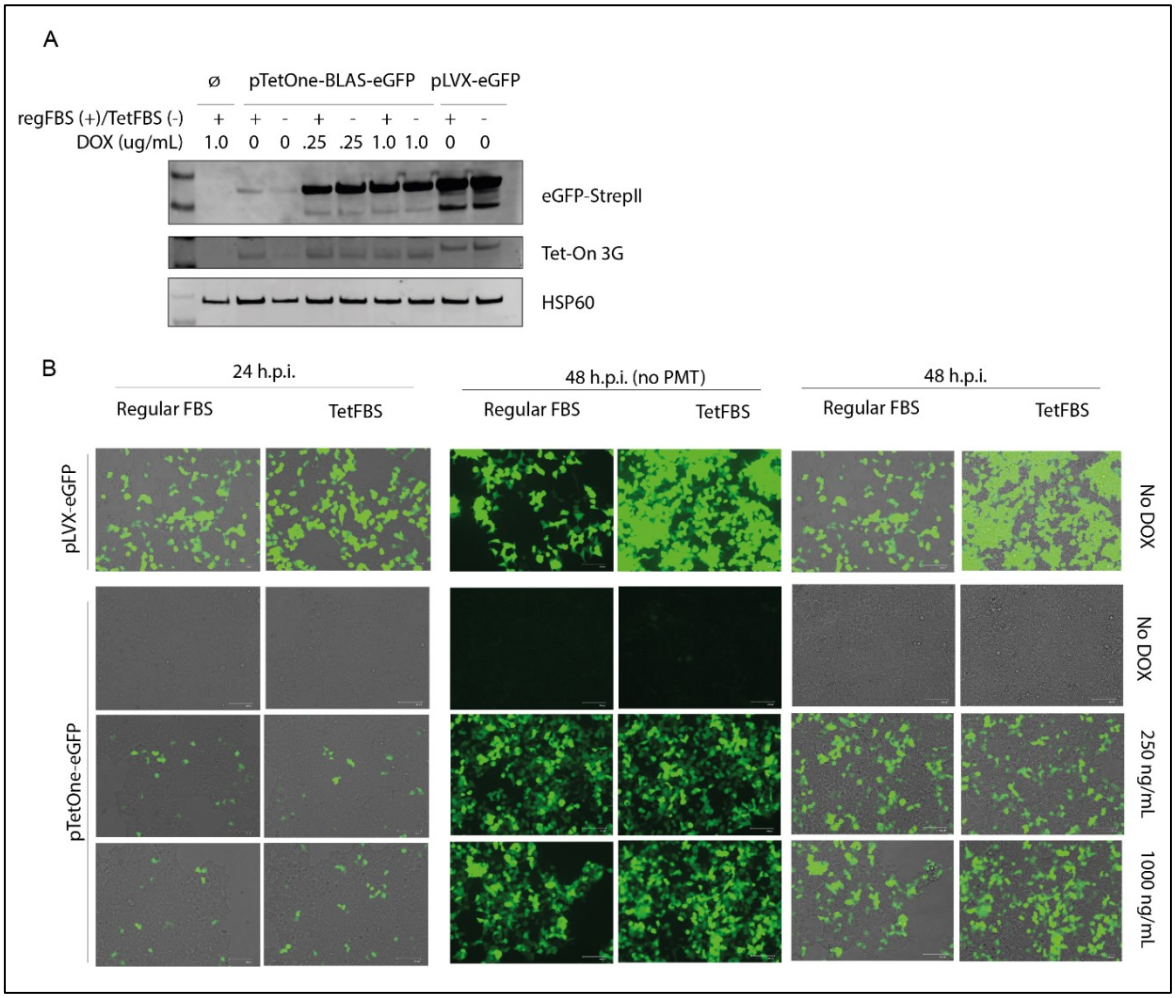
Supplementary Figure 3.7 Extracellular interactomes of ORF8*ancestral* and ORF8*ancestral*-C20S show an enrichment for extracellular vesicle trafficking, mucus-secretion and immune response markers. Protein intensities were log2-transformed and analysed in Perseus (v2.1). Uniquely identified protein interactors (not present in all three control replicates) and significantly enriched interactors were included in the visualization. KEGG pathways and subcellular localization were assigned using String.db (v12). Proteins reported to contain an Ig-like domain were highlighted.



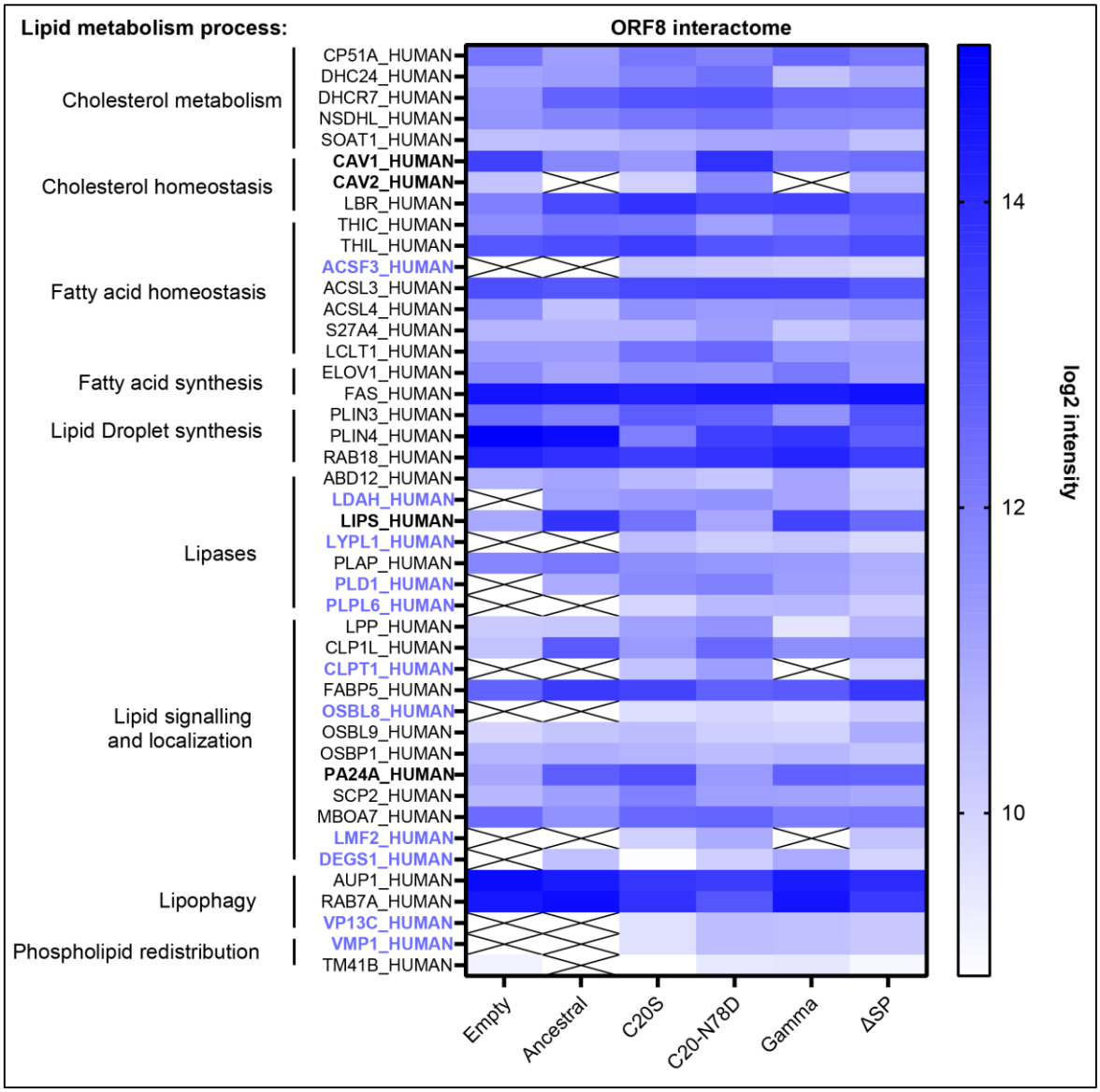
Supplementary Figure 3.8 Extracellular interactomes of ORF8*ancestral*-C20S-N78D and ORF8*gamma* show an enrichment for extracellular vesicle trafficking, mucus-secretion and immune response markers. Protein intensities were log2-transformed and analysed in Perseus (v2.1). Uniquely identified protein interactors (not present in all three control replicates) and significantly enriched interactors were included in the visualization. KEGG pathways and subcellular localization were assigned using String.db (v12). Proteins reported to contain an Ig-like domain were highlighted.



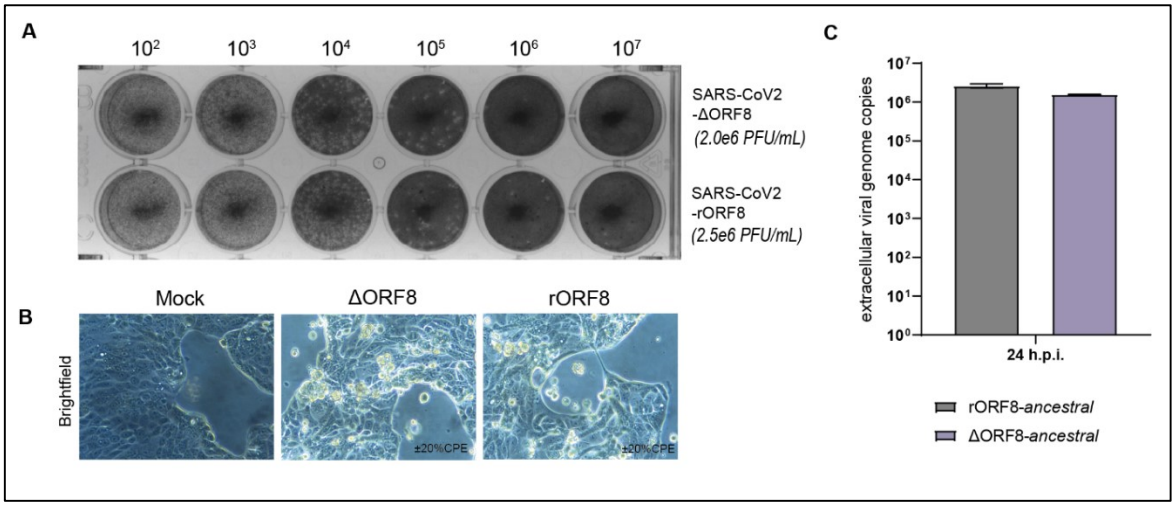
Supplementary Figure 3.9 Extracellular interactors of ORF8 involved in the immune response. Protein intensities were log2-transformed and analysed in Perseus (v2.1). Uniquely identified protein interactors (not present in all three control replicates) are marked in blue, significantly enriched interactors are in bold. In regular text, interactors are indicated that are not significantly enriched compared to the empty control but are significant compared to ΔSP (ICOSLG and CD44).



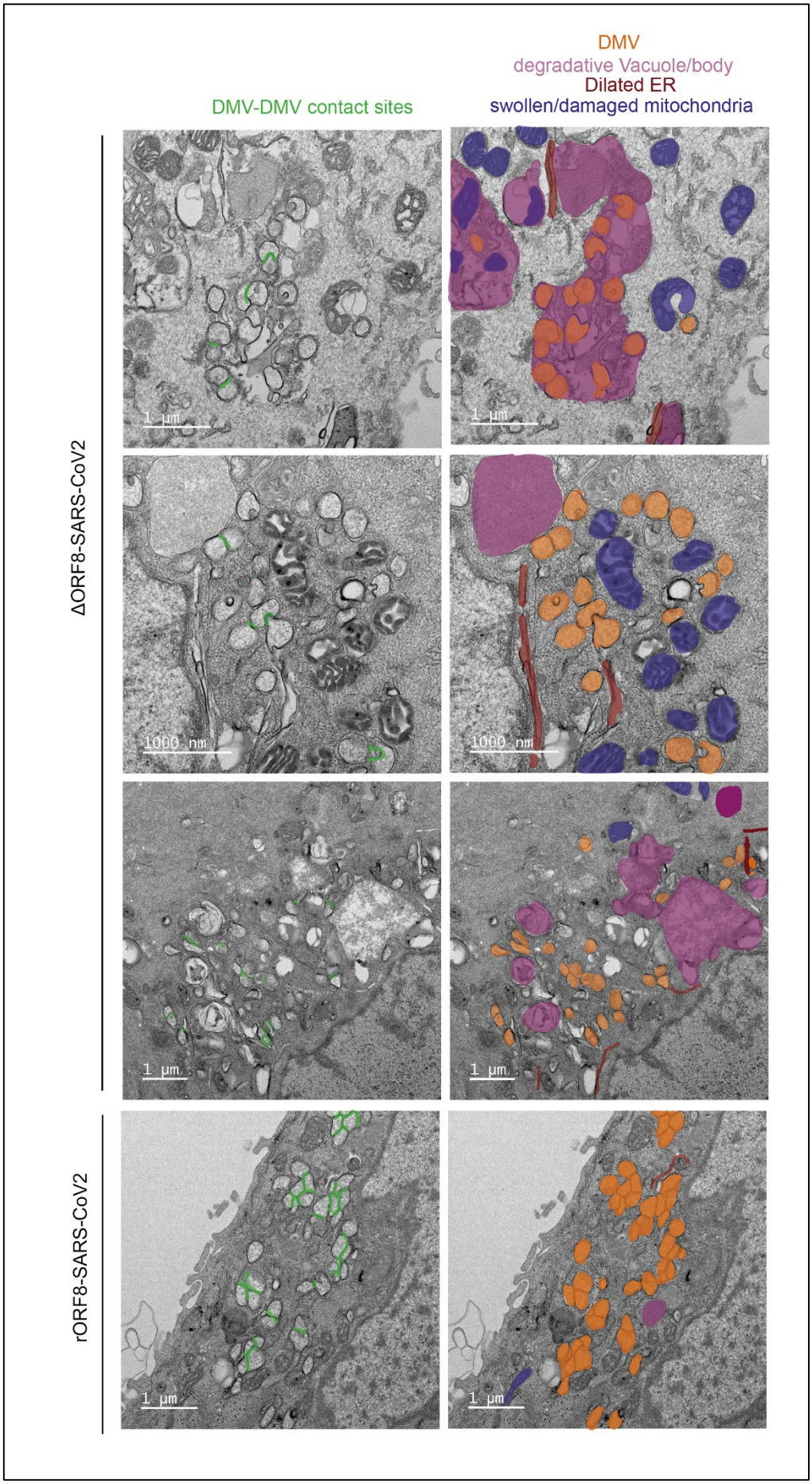
Supplementary Figure 4.1 Inducibility optimization of stably transduced TetOne-constructs. A) Western blot analysis of TetOne-eGFP and pLVX-eGFP expression in 293T cells 48 hours post induction with the indicated Doxycycline amounts (0, 250 or 1000 ng/mL) in either TetFBS (TakaraBio) (-) or regular FBS (+). B) Visualization of eGFP expression at 24 and 48 hours post induction, using the FLoid™ Cell Imaging Station (Thermo Fisher). Cells were visualized on brightfield and green channel (Ex/Em: 482-18/446-33) for the eGFP signal.



Supplementary Figure 4.2 ORF8 interferes in lipid metabolism. The ORF8 interactome studies from chapter 4 was investigated for significant changes in lipid metabolism. In blue are lipid metabolism-associated proteins found as unique intracellular interactors of ORF8. In **bold** are proteins significantly altered. Significance is determined at -1 < log2 FC > 1 and $p < 0.05$; 'unique' indicates absence in any of the three empty control replicates. Statistical analysis was performed using Student's T-test in Perseus (v2.1.0.0). The proteins were subdivided based on the main process they are involved in, based on KEGG and reactome pathways, biological process and molecular function. This information was retrieved from https://string-db.org (v.12.).



Supplementary Figure 4.3 ORF8 deletion does not significantly interfere with SARS-CoV2 viral production. Calu-3 cells were infected at MOI 0.5 with rORF8-SARS-CoV2*ancestral* or ΔORF8-SARS-CoV2*ancestral* for 24 hours prior to preparation for transmission electron microscopy. A) Viral titres of the TEM samples were determined using standard plaque assay on VeroE6 cells. Plaque forming units were counted at 2 different serial dilutions and in technical duplicates and estimated at 2.0e6 PFU/mL and 2.5e6 pfu/mL for SARS-CoV2-ΔORF8 and –rORF8, respectively. B) extracellular viral genomes were quantitated by RT-qPCR probing for SARS-CoV2 nucleocapsid and using a standard curve of a virus stock of known titre. C) Cytopathic effects were visualized by brightfield imaging at 24 hours post infection.


DMV
degradative Vacuole/body
Dilated ER
swollen/damaged mitochondria
DMV-DMV contact sites
ΔORF8-SARS-CoV2
rORF8-SARS-CoV2
1 µm
1000 nm

Supplementary Figure 4.4 SARS-CoV2 DMVs are increasingly engulfed and have less DMV-DMV contact in absence of ORF8. Calu-3 cells were infected at MOI 0.5 with rORF8-SARS-CoV2*ancestral* or ΔORF8-SARS-CoV2*ancestral*. After 24 hours, the cells were fixed in 4%PFA, 2.5%gluteraldehyde in 0.1M PIPES buffer and processed by the Dunn School BioImaging facility (University of Oxford). Images were obtained on the JEOL 1400 TEM using the Gatan Rio CMOS detector. Representative images of rORF8-SARS-CoV2*ancestral*- or ΔORF8-SARS-CoV2*ancestral*-infected cells are shown highlighting DMV's (orange), that are commonly found within degradative vesicles in the case of ΔORF8-SARS-CoV2*ancestral*-infection. Some key significant morphological changes are indicated: dilated ER (red), elongated/swollen/damaged mitochondria (blue), vacuoles/degradative vesicles (purple), DMV-DMV-contact sites (green).

Acknowledgements

First, I'd like to thank **Sumana, Asmaa, Iolanthe, Tiaan** and **Deeksha**, who have been part of the research projects presented in this thesis. It has been great to set out these projects together, to brainstorm and to get lost in the intricacies of these viral manipulation processes together. A special thanks to **Iolanthe**, my Master Research Project supervisor at the HKU-Pasteur Research Pole, who has been a true mentor and friend throughout.

Similarly, this project would not have been possible without the extraordinary help of the core facilities at the University of Oxford. With a special thank you to **Errin** and **Charlotte** (Electron Microscopy unit, Dunn School BioImaging facility), **Vasiliki** and **Bobby** (Flow Cytometry unit, Dunn School BioImaging facility), **Sarah, Roman, Iolanda** (Target Discovery Institute) and **Zhu** (NDM), and **Michelle** (Dunn School BSL3).

I'd like to thank all the past and present members of the team: **Tiaan, Vicky, Deeksha, Oscar, Asmaa, Addie, Dorian, Theo, Karolina,** and **Sumana**; it has been a great experience to be part of this crazy lab. Our reputation on OMPI1 was notoriously marked by our constant chatter, which I guess was just a sign that we were having a great time together. Everyone on OMPI1, thank you for dealing with our group and for helping me during my PhD, specifically, **Rebecca**, for being my lifeline for snacks and advice.

A special mention goes out to **Deeksha**. As the OG members of the lab, we faced the challenge of setting up the lab during the COVID-19 pandemic and I honestly think I would have drowned that first year if you weren't there. You truly treated me like family throughout the PhD. Even getting your whole family involved to help me move multiple times (**Arjun** was definitely my favourite mover, sorry not sorry), which I am so grateful for.

Similarly, **Asmaa**, it has been so special to create a project together in Hong Kong and to actually be able to execute it alongside each other here in Oxford. Our fiery brainstorming sessions may have scared the rest of the lab, but I am so grateful for them

and for having you alongside me on this project. Moreover, I'd like to thank **Sumana**, who has always given me the freedom and support to delve into any project I found interesting, regardless of whether she thought I was crazy for it. Finally, a special shout-out to my students **Jamie** and **Omar**, who have been amazing to work with and weren't afraid to dive into the complexity of ORF8 with me.

Then, I'd like to thank my Dunn Family; **Annie, Anne-Sofie** and **Lachlan**. When we joined the Dunn School in October 2020 in the middle of the pandemic, you were my rock or more my excuse to drink wine together. We established a wine club, using it as an excuse to hang out together at the Dunn School, when we couldn't hang out anywhere else. It really kept us sane during the lockdowns and we've built the most amazing friendship. Moreover, we have always been able to discuss and brainstorm about our PhDs together. This even led to Lachlan and I working together for multiple small projects. Of which, **Lachlan**'s help in setting up SARS-CoV2 ORF8 mammalian protein production was incredibly appreciated. I am so excited to see where we all end up.

Similarly, during the mandatory quarantine at the start of my PhD, I met the most amazing people in college, the St. Giles Girls, **Nina** and **Divya**. They took me in when I was struggling with lockdown and my assigned housing at Somerville. Together, we navigated the lockdowns and created unforgettable memories, coming up with the strangest activities like Bob Ross night, a basement digging adventure (our lungs will probably not forget this one either) and pageant- and space night. Both of you have been a constant support throughout my PhD. Divya is now killing it with a Postdoc at Harvard and Nina with her PhD here at Oxford. Your drive and achievements have been and will continue to be truly inspirational to me.

Then a special mention for **Fe**. Along with **Clare**, you were my tennis buddy in Year 1 and one of my first friends in town. When the October lockdown hit, we realised that although tennis stopped, this couldn't stop us from hanging out and you quickly became one of my best friends in town. I truly cannot imagine my Oxford time without you. It was

also you who introduced me to **JB, Ian, Nathania, Hannah**, and **Ziggy**— who made my time in Oxford so enjoyable.

Hannah and **Ziggy**, as my housemates with **Fe** this year, who created a true home, where we cook and eat breakfast together and indulged in Single's Inferno, the Great British Bake-Off or whatever our crazy YouTube algorithm recommended to us. And most importantly, it was a place where there was always someone looking out for you.

Similarly, I should probably apologize to **JB, Ian, Nathania** and **Fe** for channelling my PhD frustrations into my serve and backhand on the tennis court. I'm incredibly grateful for being welcomed into this circle of friends and I will never forget our many tennis sessions, our time at Wimbledon, our Mario & Margs nights and even our real-life Mario karting. Most importantly I will miss our long Sunday afternoon hangouts to get away from our PhDs.

Through **Nina**, I also met **Julia, Anja** and **Annie**, who were kicking ass in the Oxford Blues boat whilst also completing amazing degrees and being great friends. You are amazing and I am so glad we met during our time in Oxford. I'm sure we will continue to find each other around the world, even if just for a quick cocktail and ice cream in SF.

And finally **Lizzy, Christina** and **Nick,** for all our chaotic and early Sunday morning tennis sessions, for being my source for all Jericho-related gossip, for our crazy laughing fits and just lovely times. Even though you've all moved to different parts of the world, the fact that we've already managed to catch up over breakfast in Paris and tennis in Brisbane, shows that we'll always find each other, no matter where we are in the world.

I'm also incredibly grateful to have been writing this thesis at the same time as **Ziggy** and 'broertje' **Paul**. The thesis writing process can be quite strange, but sharing the experience with you both—discussing our challenges or even just simply enjoying coffee breaks together—made it so much more bearable.

I would like to give the biggest thanks to my family, you have truly been the best support I can imagine. My parents, **Papa en Mama**, and my sister **Eefje**, for supporting me through-and-through and for dealing with my weekly PhD venting session. Thank you for always being so supportive of whichever career path I choose. Similarly, my grandparents, **Opa en Oma**, and godparents, **Tante Ine en Ome Antoon**; who have encouraged me so much throughout my PhD.

Likewise, the I&I girlies - **Raquel, Amy, Katie, Muriel, Marta, Anna** (and honorary member Tim) – as well as my 2xDeCadent bestuursvriendjes - **Lisa, Barry, Hessel** en **Donna** - and my high school friends - **Yasna, Renee, Nathalie, Amber, Koen**, **Sanne en Naomi** - who even if it has been more than 6 months since I last saw them; they always made me feel as if we were together just yesterday. Your friendships have been a vital source of support during this PhD. I will, for example, never forget how **Yasna** and **Nathalie** hosted me for an Amsterdam staycation, when I couldn't afford a summer break during the PhD. Or when the '**Bestuursvriendjes**' came right after lockdown or **Marta** hosted us in Paris to break away from our final year of PhD stress.

And finally a special mention to **Mart**, my previous MSc. supervisor, who has been such a great support during this PhD. I truly appreciate our brainstorms, that we always check in on each other and for inspiring my work.

I truly appreciate every single one of you, I could not have done it without you!